Optimization of Unbalanced Distribution Grid Operations using Distributed Energy Resources

by

Kshitij Girigoudar

A dissertation submitted in partial fulfillment of
the requirements for the degree of

Doctor of Philosophy
(Electrical & Computer Engineering)

at the
UNIVERSITY OF WISCONSIN–MADISON
2022

Date of final oral examination: 08/18/2022

The dissertation is approved by the following members of the Final Oral Committee:

Line Roald, Assistant Professor, Electrical and Computer Engineering
Bernard Lesieutre, Professor, Electrical and Computer Engineering
Dominic Groß, Assistant Professor, Electrical and Computer Engineering
Stephen Wright, Professor, Computer Sciences
Daniel Molzahn, Assistant Professor, Electrical and Computer Engineering, Georgia Tech

To my parents.

For their unconditional love, encouragement and support.

Acknowledgments

An endeavour over a long period can be successful only with the advice and guidance of many well-wishers. I take this opportunity to express my deep sense of gratitude and appreciation for all those who encouraged me to the successful completion of this PhD.

First and foremost, I would like to express my sincerest gratitude to my advisor and mentor, Prof. Line Roald, for her esteemed guidance, support and creative inputs in every step of this PhD. I could not have asked for a better advisor. Her patience, motivation and immense knowledge helped me to a great extent in the work done over the past four years. I am extremely grateful to Line for taking me on as a student and I have gained a lot of valuable knowledge from her regarding independent research, technical writing, teaching, and presentation skills.

I would also like to sincerely thank my committee members Prof. Bernard Lesieutre, Prof. Dominic Groß, Prof. Daniel Molzahn, and Prof. Stephen Wright for taking the time to review this thesis. Their invaluable expertise, insightful comments, and constructive feedback not only served to improve the quality of this work, but also provided inspiring directions for future work.

I thank all my friends and colleagues in the WISPO research group for their versatile support, numerous suggestions and stimulating discussions.

Finally, my heartfelt thanks go to my family. Without their unwavering support and the sacrifices made by them, this thesis would not have been possible. My father is my role model and I would like to thank him for teaching me how to remain calm and composed under pressure. My mother is my biggest superhero, and I am grateful to her for teaching me the value of perseverance and how to have a strong mind. Last, but not the least, I would like to thank my lovely wife, Abitha for being my emotional support throughout this journey, for repeatedly proofreading (even after hard and stressful days at work), and for making jokes when things got too serious.

Abstract

Among the various major components of the electric power system, distribution grids have not received a lot of attention from the research community. While novel analysis and optimization techniques have been developed for the operation of large transmission systems, the distribution grids continued to act as a passive interconnection between the transmission systems and consumers without a lot of analysis. Today's distribution grids are experiencing a significant transformation due to an increasing amount of smart electric loads and distributed energy resources (DERs), such as electric vehicles, smart home appliances, rooftop solar photovoltaic (PV) systems and energy storage. Growing penetration of DERs can increase the power injection variability in distribution grids, which lead to power quality issues such as voltage unbalance. High voltage unbalance can increase network losses and lead to failure of three-phase equipment such as induction motor loads connected to the grid. Apart from voltage unbalance, increasing deployment of DERs might result in large voltage variations and increase in the voltage magnitudes at the customers' end. DERs such as solar PV systems with power electronic inverters can be employed as a cost-effective solution to provide reactive power support and minimize voltage violations as well as unbalance. However, the intermittent nature of these DERs as well as load forecasting errors can increase uncertainty in distribution grids. Furthermore, DERs are managed by different entities such as distribution utility or third-party aggregators whose objectives are conflicting with each other. This makes it challenging to effectively and precisely control DER behavior to optimize grid operations.

This work introduces an optimization-based approach to improve power quality in unbalanced distribution grids and effectively exploit the considerable flexibility offered by DERs in response to uncertainty. Organizations such as IEC, NEMA and IEEE define voltage unbalance in their power quality standards and these definitions are not consistent. To address this issue, bounds are derived on the maximum difference among the definitions of voltage unbalance to understand how one definition can be used to ensure safe bounds on the voltage unbalance defined by another definition. Next, an unbalanced distribution grid is modelled in the phase domain and a three-phase optimal power flow (OPF) formulation is developed to identify DER control actions that mitigate voltage unbalance. A major challenge to efficiently solving the three-phase OPF problem is computation time. To reduce the computational complexity, three linear power flow models which are well suited to analyze voltage unbalance are utilized as part of a successive approximation approach to provide good quality solutions that are feasible for three-phase AC power flow. The OPF formulation is then extended to examine the impact of uncertainty on distribution grid operations by leveraging a chance-constrained optimization approach. A reformulation based on constraint tightening is discussed to efficiently solve the problem and identify a set of DER control actions that can be utilized across a range of highly uncertain scenarios. Finally, the challenges of harnessing the flexibility offered by DERs that are controlled by different entities in the grid is addressed. A bilevel optimization approach is proposed to determine a feasible region of aggregate power that represents the collective DER and load flexibility in the network. This aggregate power flexibility range can help reduce burdens on transmission system resources while maintaining power quality in distribution grids.

Contents

Page

Page

Page

Page

List of Tables

List of Figures

Figure Page

Figure Page

Nomenclature

Abbreviations

DER	Distributed energy resources
DSO	Distribution system operator
EV	Electric vehicles
PV	Photovoltaic
LVUR	Line voltage unbalance rate
PVUR	Phase voltage unbalance rate
VUF	Voltage unbalance factor
IEC	International Electrotechnical Commission
IEEE	Institute of Electrical and Electronics Engineers
NEMA	National Electrical Manufacturers Association
ZIP	Load model comprising of constant impedance (Z), constant current (I) and constant power (P) components
AC	Alternating current
DC	Direct current
OPF	Optimal power flow

FBS	Forward backward sweep
FOT	First-order Taylor
FP	Fixed-point
KCL	Kirchoff's current law
KVL	Kirchoff's voltage law
LDF	Three-phase LinDistFlow approximation model
SDP	Semidefinite Programming
SOCP	Second-order Cone Programming

Voltage Unbalance: Parameters

$v = \|v\|\angle\theta$	Polar representation of complex phasor v where $\|v\|$ and θ are phasor magnitude and angle, respectively
$v = v_{\mathrm{d}} + jv_{\mathrm{q}}$	Rectangular representation of complex phasor v where v_{d} and v_{q} are real and imaginary components, respectively; $j = \sqrt{-1}$
v^a, v^b, v^c	Three phase-to-neutral voltage phasors
v^{ab}, v^{bc}, v^{ca}	Three phase-to-phase voltage phasors
v^-, v^+	Negative and positive sequence voltage phasors
$v_{\mathrm{P}}, v_{\mathrm{L}}$	Balanced phase-to-neutral and phase-to-phase voltage magnitudes
$v_{\mathrm{P}}^{\mathrm{avg}}, v_{\mathrm{L}}^{\mathrm{avg}}$	Average phase-to-neutral and phase-to-phase voltage magnitudes
$\Delta v_{\mathrm{P}}^{\mathrm{max}}$	Maximum deviation of phase-to-neutral voltage magnitude from $v_{\mathrm{P}}^{\mathrm{avg}}$
$\Delta v_{\mathrm{L}}^{\mathrm{max}}$	Maximum deviation of phase-to-phase voltage magnitude from $v_{\mathrm{L}}^{\mathrm{avg}}$

$u_{\text{VUF}}, u_{\text{LVUR}}, u_{\text{PVUR}}$	Voltage unbalance limits for VUF, LVUR and PVUR

Distribution Grid: Topology

$\mathcal{N}$	Set of three-phase nodes excluding slack node, $\lvert\mathcal{N}\rvert = n$
$\mathcal{N}_0$	Set of three-phase nodes, $\lvert\mathcal{N}_0\rvert = n + 1$
$\mathcal{G}$	Set of nodes with generators
$\mathcal{L}_\Delta$	Set of nodes with delta-connected loads
$\mathcal{L}_y$	Set of nodes with wye-connected loads
$\mathcal{N}_k$	Set of downstream nodes connected to node k
$\Phi \in \{a, b, c\}$	Set of phases
$\Phi_\Delta \in \{ab, bc, ca\}$	Set of phase-to-phase connections
$\phi \in \Phi$	Index for single-phase connections
$\phi_\Delta \in \Phi_\Delta$	Index for phase-to-phase connections
$i, k, l \in \mathcal{N}_0$	Three-phase node index
$\omega \in \Omega$	Index for uncertainty realization
Ω	Uncertainty set, $\lvert\Omega\rvert = M$

Distribution Grid Modelling: Parameters

$b_{ik}^{aa}, b_{ik}^{bb}, b_{ik}^{cc}$	Shunt self susceptance for three-phase branch ik
$z_{ik}^{aa}, z_{ik}^{bb}, z_{ik}^{cc}$	Series self impedance for three-phase branch ik
$z_{ik}^{ab}, z_{ik}^{bc}, z_{ik}^{ca}$	Series mutual impedance for three-phase branch ik
$Y_{ik,\text{se}} \in \mathbb{C}^{3\times3}$	Series branch admittance matrix for branch ik

$Y_{ik,\mathrm{sh}} \in \mathbb{C}^{3\times3}$	Shunt branch admittance matrix for branch ik
$Y_{ik} \in \mathbb{C}^{3\times3}$	Branch admittance matrix for branch ik
$B_{ik} \in \mathbb{R}^{3\times3}$	Imaginary component of Y_{ik} for branch ik
$G_{ik} \in \mathbb{R}^{3\times3}$	Real component of Y_{ik} for branch ik
$Y_{\mathrm{pr}} \in \mathbb{C}^{6\times6}$	Primitive admittance matrix of three-phase transformer
$C_{\mathrm{tf}} \in \mathbb{Z}^{6\times6}$	Connection matrix mapping voltage difference across three-phase transformer windings to node voltages
$Y_{\mathrm{pp}}, Y_{\mathrm{ss}} \in \mathbb{C}^{3\times3}$	Primary and secondary self admittance submatrices of Y_{pr}
$Y_{\mathrm{ps}}, Y_{\mathrm{sp}} \in \mathbb{C}^{3\times3}$	Mutual admittance submatrices of Y_{pr}
y_{t}	Transformer leakage admittance
$Y_{\mathrm{T}} \in \mathbb{C}^{6\times6}$	Transformer admittance matrix
t_a, t_b, t_c	Tap ratios of three-phase voltage regulator
y_{r}	Voltage regulator admittance
$Y_{\mathrm{R}} \in \mathbb{C}^{6\times6}$	Voltage regulator admittance matrix
$Y \in \mathbb{C}^{3(n+1)\times3(n+1)}$	Overall node admittance matrix
$\lvert Y\rvert, \Psi \in \mathbb{R}^{3(n+1)\times3(n+1)}$	Magnitude and angle components of Y
$G, B \in \mathbb{R}^{3(n+1)\times3(n+1)}$	Conductance and susceptance components of Y

Three-phase OPF: Parameters

$P_{\mathrm{G},i}, Q_{\mathrm{G},i} \in \mathbb{R}^3$	Active and reactive components of generation at node $i \in \mathcal{G}$
$P_{\mathrm{LY},i}, Q_{\mathrm{LY},i} \in \mathbb{R}^3$	Active and reactive components of wye-connected load at node $i \in \mathcal{L}_{\mathrm{Y}}$

$P_{\mathrm{L},i}, Q_{\mathrm{L},i} \in \mathbb{R}^3$	Active and reactive components of total load demand at node $i \in \mathcal{N}_0$
$P_{\mathrm{L}\Delta,i}, Q_{\mathrm{L}\Delta,i} \in \mathbb{R}^3$	Active and reactive components of delta-connected load at node $i \in \mathcal{L}_\Delta$
$P_i, Q_i \in \mathbb{R}^3$	Active and reactive injection vector at node $i \in \mathcal{N}_0$
$P, Q \in \mathbb{R}^{3n}$	Overall active and reactive power injections at all nodes except slack node
$P_{\mathrm{G}}, Q_{\mathrm{G}} \in \mathbb{R}^{3n}$	Overall active and reactive components of generation at all nodes except slack node
$P_{\mathrm{L}}, Q_{\mathrm{L}} \in \mathbb{R}^{3n}$	Overall active and reactive components of load demand at all nodes except slack node
$P_{\Delta\mathrm{Y},i}, Q_{\Delta\mathrm{Y},i} \in \mathbb{R}^3$	Active and reactive components of wye-equivalent delta-connected load at node $i \in \mathcal{L}_\Delta$
$\underline{v}, \overline{v}$	Lower and upper voltage magnitude limits
$\lvert s^{\phi}_{\mathrm{G},i} \rvert$	Apparent power limit of solar PV inverter at node $i \in \mathcal{G}, \phi \in \Phi$
$\Gamma \in \mathbb{Z}^{3\times 3}$	Transformation matrix converting phase-to-phase current phasors to phase-to-neutral current phasors
$I_{\mathrm{d},ki}, I_{\mathrm{q},ki} \in \mathbb{R}^3$	Real and imaginary components of phase-to-neutral current flowing in branch ki
$i^{\phi}_{\mathrm{d}i}, i^{\phi}_{\mathrm{q}i}$	Real and imaginary components of phase-to-neutral current injection at node $i \in \mathcal{N}_0, \phi \in \Phi$
$H \in \mathbb{Z}^{3n\times 3n}$	Delta to wye transformation block diagonal matrix
$J \in \mathbb{R}^{3n\times 3n}$	Jacobian matrix ignoring slack node
$Y_{\mathrm{LL}} \in \mathbb{C}^{3n\times 3n}$	Submatrix of Y ignoring slack node
$\mathrm{w} \in \mathbb{C}^{3n}$	No-load voltage at all nodes except slack node

$V^{(\kappa)} \in \mathbb{C}^{3n}$	Voltage estimate at all nodes except slack node at iteration κ
$P^{(\kappa)}, Q^{(\kappa)} \in \mathbb{R}^{3n}$	Active and reactive power injections corresponding to $V^{(\kappa)}$
$S_\Delta \in \mathbb{C}^{3n}$	Complex delta-connected injections at all nodes except slack node
$S_\mathrm{Y} \in \mathbb{C}^{3n}$	Complex wye-connected injections at all nodes except slack node

Three-phase OPF: Variables

$\lvert\boldsymbol{V}\rvert, \boldsymbol{\Theta} \in \mathbb{R}^{3n}$	Polar form: overall phase-to-neutral voltage magnitude and angle vector
$\lvert\boldsymbol{V}_i\rvert, \boldsymbol{\Theta}_i \in \mathbb{R}^3$	Polar form: phase-to-neutral voltage magnitude and angle vector at node $i \in \mathcal{N}_0$
$\lvert\boldsymbol{v}_i^\phi\rvert, \boldsymbol{\theta}_i^\phi$	Polar form: phase-to-neutral voltage magnitude and angle at node $i \in \mathcal{N}_0,\ \phi \in \Phi$
$\boldsymbol{V}_{\mathbf{d}i}, \boldsymbol{V}_{\mathbf{q}i} \in \mathbb{R}^3$	Rectangular form: real and imaginary components of phase-to-neutral voltage phasor at node $i \in \mathcal{N}$
$\boldsymbol{v}_{\mathbf{d}i}^\phi, \boldsymbol{v}_{\mathbf{q}i}^\phi$	Rectangular form: real and imaginary components of phase-to-neutral voltage phasor at node $i \in \mathcal{N},\ \phi \in \Phi$
$\boldsymbol{V}_\mathbf{d}, \boldsymbol{V}_\mathbf{q} \in \mathbb{R}^{3n}$	Rectangular form: overall real and imaginary components of phase-to-neutral voltage phasor
$\boldsymbol{p}_{\mathbf{G},i}^\phi, \boldsymbol{q}_{\mathbf{G},i}^\phi$	Active and reactive power injection of generators $\forall i \in \mathcal{N}$
$\lvert\boldsymbol{V}_{\Delta,i}\rvert \in \mathbb{R}^3$	Phase-to-phase voltage magnitude at node $i \in \mathcal{N}_0$
$\lvert\boldsymbol{v}_{\Delta,i}^{\phi_\Delta}\rvert$	Phase-to-phase voltage magnitude at node $i \in \mathcal{N},\ \phi_\Delta \in \Phi_\Delta$
$\boldsymbol{i}_{\Delta\mathbf{d},i}^{\phi_\Delta}, \boldsymbol{i}_{\Delta\mathbf{q},i}^{\phi_\Delta}$	Real and imaginary components of phase-to-phase current drawn by delta-connected load at node $i \in \mathcal{L}_\Delta, \phi_\Delta \in \Phi_\Delta$
$\boldsymbol{z}_{\mathbf{L},i}$	Maximum phase-to-phase voltage magnitude deviation at node $i \in \mathcal{N}$

$\boldsymbol{z}_{\mathbf{L},i}^{\phi_\Delta}$	Absolute phase-to-phase voltage magnitude deviation vector at node $i \in \mathcal{N}, \phi_\Delta \in \Phi_\Delta$
$\boldsymbol{z}_{\mathbf{P},i}$	Maximum phase-to-neutral voltage magnitude deviation at node $i \in \mathcal{N}$
$\boldsymbol{z}_{\mathbf{P},i}^{\phi}$	Absolute phase-to-neutral voltage magnitude deviation vector at node $i \in \mathcal{N}, \phi \in \Phi$

Random Variables

$p_{\mathrm{G},i,\omega}^{\phi}, P_{\mathrm{G},i,\omega}$	Uncertain active power generation of solar PV
$p_{\mathrm{L},i,\omega}^{\phi}, P_{\mathrm{L},i,\omega}$	Uncertain active power load demand
$p_{i,\omega}^{\phi}, P_{i,\omega}$	Uncertain active power injection
$q_{\mathrm{L},i,\omega}^{\phi}, Q_{\mathrm{L},i,\omega}$	Uncertain reactive power load demand
$q_{i,\omega}^{\phi}, Q_{i,\omega}$	Uncertain reactive power injection
$\delta p_{\mathrm{G},i,\omega}^{\phi}, \delta P_{\mathrm{G},i,\omega}$	Deviation of uncertain active power generation from average value
$\delta p_{\mathrm{L},i,\omega}^{\phi}, \delta P_{\mathrm{L},i,\omega}$	Deviation of uncertain active power load demand from average value

Three-phase OPF: Parameters Considering Uncertainty

$\bar{p}_{\mathrm{G},i}^{\phi}, \bar{P}_{\mathrm{G},i}$	Average active power generation of solar PV
$\bar{p}_{\mathrm{L},i}^{\phi}, \bar{P}_{\mathrm{L},i}$	Average active power load demand
$\bar{p}_{i,\omega}^{\phi}, \bar{P}_{i,\omega}$	Average active power injection
$\bar{q}_{\mathrm{L},i}^{\phi}, \bar{Q}_{\mathrm{L},i}$	Average reactive power load demand
$\bar{q}_{i,\omega}^{\phi}, \bar{Q}_{i,\omega}$	Average reactive power injection
$\gamma_{\mathrm{L},i}^{\phi}, \Gamma_{\mathrm{L},i}$	Power ratio of load demand

$\epsilon_q \in [0,1]$	Violation probability of solar PV inverter reactive power limits
$\epsilon_v \in [0,1]$	Violation probability of voltage magnitude limits
$\overline{\lambda}^{\phi}_{q,i}, \overline{\Lambda}_q$	Upper reactive power constraint tightening
$\overline{\lambda}^{\phi}_{v,i}, \overline{\Lambda}_v$	Upper voltage constraint tightening
$\overline{q}^{\phi}_{\mathrm{G},i}, \underline{q}^{\phi}_{\mathrm{G},i}$	Upper and lower PV inverter limits w.r.t. average generation
$\underline{\lambda}^{\phi}_{q,i}, \underline{\Lambda}_q$	Lower reactive power constraint tightening
$\underline{\lambda}^{\phi}_{v,i}, \underline{\Lambda}_v$	Lower voltage constraint tightening
$\hat{E}^{\phi}_{\overline{v},i}$	Constraint empirical violation probability
$\hat{E}^{\max}_{\overline{v}}$	Worst case empirical violation probability for upper voltage constraint
$Y^{\phi}_{\overline{v},i}$	Constraint violation indicator random variable

Three-phase OPF: Variables Considering Uncertainty

$\lvert\boldsymbol{v}^{\phi}_{i,\omega}\rvert, \lvert\boldsymbol{V}_{i,\omega}\rvert$	Voltage magnitude corresponding to uncertain power injections
$\boldsymbol{\theta}^{\phi}_{i,\omega}, \boldsymbol{\Theta}_{i,\omega}$	Voltage angle corresponding to uncertain power injections
$\boldsymbol{p}^{\phi}_{\mathbf{G},0,\omega}, \boldsymbol{P}_{\mathbf{G},0,\omega}$	Active power injection at substation corresponding to uncertain power injections
$\boldsymbol{q}^{\phi}_{\mathbf{G},0,\omega}, \boldsymbol{Q}_{\mathbf{G},0,\omega}$	Reactive power injection at substation corresponding to uncertain power injections
$\boldsymbol{v}^{+}_{\mathbf{d}l,\omega}, \boldsymbol{v}^{+}_{\mathbf{q}l,\omega}$	Real and imaginary components of positive sequence voltage phasor $\boldsymbol{v}^{+}_{l,\omega}$ corresponding to uncertain power injections
$\boldsymbol{v}^{-}_{\mathbf{d}l,\omega}, \boldsymbol{v}^{-}_{\mathbf{q}l,\omega}$	Real and imaginary components of negative sequence voltage phasor $\boldsymbol{v}^{-}_{l,\omega}$ corresponding to uncertain power injections

Three-phase OPF: Bilevel Problem Variables

$\boldsymbol{X}_{\mathbf{l}}, \boldsymbol{X}_{\mathbf{u}}$	Bilevel problem lower-level and upper-level variable vectors
$\Delta \boldsymbol{p}$	Aggregate active power flexibility of distribution grid
$\Delta \boldsymbol{p}^{+}, \Delta \boldsymbol{p}^{-}$	Maximum and minimum limits on aggregate active power flexibility
$\Delta \boldsymbol{p}^{\phi}_{\mathbf{G},i}, \Delta \boldsymbol{p}^{\phi}_{\mathbf{L},i}$	Active power flexibility of generators and loads at node $i \in \mathcal{N},\ \phi \in \Phi$
$\boldsymbol{\gamma}^{\phi}_{\mathbf{G},i}$	Power ratio of solar PV inverters at node $i \in \mathcal{N},\ \phi \in \Phi$ in constant power factor mode
$\overline{\boldsymbol{q}}^{\phi}_{\mathbf{G},i}$	Maximum allowable reactive power of solar PV inverters at node $i \in \mathcal{N},\ \phi \in \Phi$ in voltage-reactive power mode
$\hat{\boldsymbol{p}}^{\phi}_{\mathbf{G},i}, \hat{\boldsymbol{q}}^{\phi}_{\mathbf{G},i}$	Current operating point: active and reactive power injection of generators $\forall i \in \mathcal{N},\ \phi \in \Phi$
$\hat{\boldsymbol{p}}^{\phi}_{\mathbf{L},i}, \hat{\boldsymbol{q}}^{\phi}_{\mathbf{L},i}$	Current operating point: active and reactive power load demand $\forall i \in \mathcal{N},\ \phi \in \Phi$
$\hat{\boldsymbol{V}}_{\mathbf{d}i}, \hat{\boldsymbol{V}}_{\mathbf{q}i} \in \mathbb{R}^3$	Current operating point: real and imaginary components of phase-to-neutral voltage phasor at node $i \in \mathcal{N}$
$\hat{\boldsymbol{v}}^{\phi}_{\mathbf{d}i}, \hat{\boldsymbol{v}}^{\phi}_{\mathbf{q}i}$	Current operating point: real and imaginary components of phase-to-neutral voltage phasor at node $i \in \mathcal{N},\ \phi \in \Phi$
$\hat{\boldsymbol{V}}_{\mathbf{d}}, \hat{\boldsymbol{V}}_{\mathbf{q}} \in \mathbb{R}^{3n}$	Current operating point: overall real and imaginary components of phase-to-neutral voltage phasor
$\lvert\hat{\boldsymbol{v}}^{\phi}_{i}\rvert$	Current operating point: phase-to-neutral voltage magnitude at node $i \in \mathcal{N},\ \phi \in \Phi$

Chapter 1

Introduction

The power grid infrastructure is currently undergoing major changes all over the world with many countries adopting incentives and policies that promote deployment of low-emission renewable energy sources. As the electric power system transitions from a centrally controlled electric grid with unidirectional delivery of power (i.e. from large central power plants to end consumers) into one that includes distributed generation and control systems, we require novel approaches to optimize the operation of the grid such that system performance as well as power quality is preserved. In this thesis, we will focus on how this transition impacts the operation of distribution grids.

1.1 Motivation

The increasing deployment of distributed energy resources (DERs) is creating both opportunities and challenges for distribution grid operations. End consumers might install solar photovoltaic (PV) systems which will generate electricity and may lead to a bidirectional flow of power in the network as well as voltage variations at the consumer end. Furthermore, the electricity consumption is expected to rise due to electrification of heating, ventilation and air conditioning as well as the charging of electric vehicles (EVs). The characteristics of these intermittent sources require distribution system operators (DSOs) to employ different, and sometimes more expensive steps to manage generation and load while maintaining system reliability. At the same time, the presence of DERs provide new opportunities for control and flexibility in adjusting power generation or consumption that can be utilized by DSOs to optimize the grid operations. For example, distribution

utilities can control the active and reactive power outputs of DERs such as solar PV installations or battery storage systems to improve power quality, manage grid constraints and minimize cost of electricity distribution.

The integration of DERs is expected to have a major impact on the design and operation of distribution grids. A critical issue due to the large-scale DER installations is the expected degradation in power quality [2]. While there is no standard definition of power quality in the existing literature, it generally refers to the electrical interaction between the distribution grid and the equipment or customers connected to the grid. Any deviation from the ideal voltage and current characteristics specified for the grid can be considered as a power quality issue [2]. Most of the emphasis on power quality is typically assigned to the deviations from ideal voltage characteristics since they frequently lead to voltage violations and interruptions in the grid operation [2]. At the distribution level, DERs such as solar PV and plug-in EVs are typically not equally distributed throughout the feeder. This can lead to major power quality issues such as voltage unbalance. High unbalance can result in damage of three-phase devices such as induction motors [3] and transformers [4]. In addition, it can also increase the cost of infrastructure upgrades due to the higher current flowing in the three-phase lines to accommodate the excess unbalance [4]. Traditional practices such as reassigning individual customers to different phases [5] cannot mitigate temporary unbalances which can be significant due to intermittent distributed generation as well as large single-phase seasonal loads [6].

Apart from voltage unbalance, the deployment of DERs will have a major impact on voltage variations and lead to increase in the voltage magnitudes at the customers' end. This will lead to transformers and distribution lines operating close to their maximum limits [2]. Although these scenarios can be avoided by placing additional transformers or distribution lines with larger cross-section area, they increase the investment cost.

Another major challenge for DSOs is the intermittent nature of power injections of DERs such as solar photovoltaic (PV) systems as well as load variability which increases uncertainty in the grid. The outputs of DERs and load demands are still difficult to predict accurately especially for the long term due to their inherent volatility. In addition, distribution grids are also characterized by

limited real-time measurement availability which further aggravate the estimation errors of DER generation and load demand [7]. Therefore, uncertainty has become a salient feature of the modern distribution grid and it is essential to accurately model the impact of uncertainty on distribution grid operation. This will help in maximizing the DER hosting capacity of the grid while ensuring that the network is secure.

Typically, all DERs connected to the distribution grid are not controlled by a single entity. Apart from DSOs managing some of the DERs, there are various third-party entities such as aggregators who control DERs with objectives that conflict with the control objectives of the DSO. If there is no proper coordination between these various entities with possibly contradictory interests, DERs are prone to be underutilized and it might not be possible to harness the true flexibility offered by these resources.

All the challenges mentioned above emphasize the requirement of better modeling and analytical tools to optimize operation of the distribution grids using DERs. Conventional tools used to analyze transmission networks are inadequate for distribution grids since they assume a perfectly balanced, single-phase equivalent model of the system. Some of the prominent characteristics of distribution grids [8] that make them different from transmission systems are

- Radial structure with large number of branches/buses
- Untransposed lines with high R/X ratio
- Three-phase, unbalanced systems with grounded or ungrounded operation
- Unbalanced loads which are also voltage-dependent

Furthermore, the number of simulation tools available specifically to analyze and optimize distribution grid operations are limited since there was no crucial demand for research in this area. Therefore, an optimization framework that considers an unbalanced, three-phase model of the distribution grid will be beneficial for system operators to harness the full flexibility of DERs while ensuring that power quality standards are met throughout the whole network.

The main goal of our research work is to develop efficient optimization-based methods to improve power quality in distribution grids. Our aim is to develop a framework that enables DSOs,

individual DER owners and third-party entities (such as DER aggregators) to mutually share the benefits offered by DERs while ensuring that the grid is secure. First, we focus on tackling voltage unbalance which is becoming one of the major power quality issues due to large deployments of single-phase rooftop solar PV systems. In order to mitigate voltage unbalance and avoid voltage violations, we utilize the reactive power capabilities of solar PV inverters. These power electronic devices are able to provide reactive power support without undesirable curtailment of active power as they are not always operating at their maximum apparent power capacity. By reducing unbalance and eliminating voltage violations, distribution grids can be operated in a more efficient and reliable manner. Next, we consider the impact of uncertainty in distribution grids. We propose different methods to maintain power quality and maximize the flexibility offered by DERs in response to uncertain parameters (load demand, DER outputs etc.) in the grid. We explore the different ways in which uncertainty can be incorporated in the optimization framework to ensure that the resulting solutions are realistic and practical.

While we reference various previous works when developing our formulations, the proposed methods will be more practical due to our consideration of large-scale, realistic networks with various DERs using actual measurement data, more cost efficient because we use existing equipment such as solar PV inverters, and more robust since we will consider uncertainty associated with the DERs and loads.

1.2 State of the Art in Distribution Grid Analysis

In this section, we provide a brief summary of the existing literature and introduce the state-of-the-art tools for distribution grid analysis. A more comprehensive review of the existing methods related to our research is provided at the beginning of each chapter.

1.2.1 Power Flow

The main objective of power flow is to determine the steady-state behaviour of a network for a given generation and load consumption. Power-flow studies determine voltages at various buses, line flows through branches and losses in the system to analyze whether the network is

able to function properly. In addition to this, they are also crucial to design and plan electric grid expansions.

Typically, the Newton–Raphson method and its variants which rely on the calculation of the Jacobian and bus admittance matrices are employed for the power flow analysis of transmission systems. However, they do not exhibit similar performance for radial distribution grids since the Jacobian and bus admittance matrices are no longer diagonally dominant and convergence problems arise in power flow solutions that depend on the inverse of these matrices [8]. In terms of analysis for three-phase systems, [9] proposed an iterative approach using Newton–Raphson method in the polar coordinate frame where voltage phasors were represented by their magnitude and angle components. In addition to this, the power flow problem was also presented in the rectangular coordinate frame where voltage phasors were represented by their real and imaginary components. By assessing the performance of both power flow formulations, [9] concluded that the rectangular coordinate implementation had better convergence rate than the polar coordinate frame especially for ill-conditioned systems. In [10], a model based on three-phase current injections which exploits the structure of the Jacobian matrix was presented using the rectangular coordinate frame.

Since the Newton-Raphson method showed poor convergence in distribution system studies, other approaches were developed to perform distribution power flow analysis. The method of symmetrical components is a common approach to simplify analysis of unbalanced three-phase power systems by expressing the asymmetrical voltage phasors as linear combinations of symmetrical phasors. A three-phase power flow problem formulation using symmetrical components was proposed in [11] and numerical simulations verified that the results were as fast as the conventional Newton–Raphson method in the phase domain. However, it only included branches comprising of distribution lines without any models for other major components such as transformers and voltage regulators. In [12], a fixed-point interpretation of the power flow equations was presented. The conditions that guarantee uniqueness of the power flow solutions were theoretically derived and corroborated through simulations in [12]. Another approach to solve three-phase power flow for unbalanced distribution grids is the forward-backward sweep method. This method takes advantage of the radial topology and consists of two computational steps, a forward sweep for bus

voltage calculations and a backward sweep to determine branch currents [13, 14]. The work in [8] extended a balanced, single-phase equivalent analysis to a three-phase power flow method using the forward-backward sweep approach, However, the grid model only included three-phase distribution lines and constant power loads.

Distribution grids with large installation of DERs require advanced modeling and simulation tools to analyze the operation of the network. There are few open-source power flow solvers available for distribution grid analysis and used extensively by grid planners, distribution grid operators and research institutions. The two most commonly used software tools which are easily integrated with other software platforms are the following:

- *OpenDSS* is a free and powerful tool used for simulating distribution grids which includes various models for distributed generation [15]. Most of the major distribution grid components such as transformers, distribution lines and cables, motors, capacitor banks etc. can be modelled on this platform. This software supports power flow analysis using Newton and fixed-point methods [16].

- *GridLAB-D* is one of the first open source and flexible simulation platforms focusing on distribution grid modelling [17]. This software also supports models of major distribution grid components similar to OpenDSS. Furthermore, GridLAB-D provides options to perform the power flow analysis using either Newton-Raphson or forward-backward sweep methods [16].

Both OpenDSS and GridLAB-D are capable of simulating unbalanced distribution networks especially with time-varying data. While GridLAB-D has fewer features to visualize distribution networks and display power flow results compared to OpenDSS, it supports more residential end-user load models (heater, electric vehicle charger, refrigerator, dryer etc.) and different PV system models whose generation is determined based on geographical PV irradiance data [16]. Since these features are not available in OpenDSS, it might be easier to obtain more realistic distribution grid models in GridLAB-D. Therefore, we use GridLAB-D as our source for system data and also for benchmarking purposes.

1.2.2 Optimal Power Flow

Generally, optimal power flow (OPF) is a nonlinear and non-convex optimization problem that optimizes operating conditions and control actions while ensuring that power flow equations and other engineering constraints are satisfied in the electrical power system. For distribution grids, an unbalanced three-phase OPF problem must be solved to alleviate various power quality and security issues and minimize grid investments. Typically, the OPF problem can be summarized as

$$\begin{aligned} \min \quad & \text{Objective Function} \\ \text{s.t.} \quad & \text{Engineering constraints,} \\ & \text{Power flow.} \end{aligned}$$

where we minimize an objective function subject to various constraints of the network. The optimization problem comprises of two types of variables: 1) continuous variables which include power injections of controllable loads and DERs such as solar PV and battery systems, voltage at all buses etc. and 2) discrete variables which are assigned to the switching actions of other controllable devices in the distribution grid such as capacitors, transformer and voltage regulator taps [18]. In this thesis, the controllable devices are solar PV systems and hence we only need to consider continuous variables in our OPF problem formulation. More specifically, the control actions to minimize the objective function are the power injections of solar PV systems.

For transmission systems, one of the most commonly used objective function is operating cost. For distribution grids, there are variety of different objective function choices such as load adjustment or curtailment, tap position and capacitor switching, carbon emissions, social welfare etc. [18]. We will consider two critical objective functions in our work related to power quality which are voltage unbalance and network losses. While minimizing network losses helps in reducing the cost of electricity distribution, minimizing voltage unbalance will improve power quality and ensure secure operation of equipment connected to the distribution grid.

The engineering constraints include both physical and operational limits that need to be enforced for stable operation of the grid. These constraints define the feasible region of our optimization problem and can generally be classified into two categories, inequality and equality

constraints. The inequality constraints usually include limits on the voltage magnitude, power injections by generators (i.e. DERs such as solar PV, battery systems etc.) based on their maximum capacity, current constraints to limit the power flow over the line, capacitor and transformer tap switching constraints which require discrete variables etc. [18]. Recall that power quality issues related to voltage are more prevalent in distribution grids compared to power quality issues related to current [2]. Hence, we do not consider current constraints in our work, but enforce the voltage magnitude limits.

The power flow problem described in the previous section is typically included in the OPF as equality constraints. These equality constraints are nonlinear and make the optimization problem hard to solve. Novel techniques which involve approximations and relaxations of the nonlinear AC power flow equations were developed for transmission systems. These strategies based on the simplified OPF formulations have been extended for balanced distribution grid models. In [19], loss minimization and voltage regulation are addressed by utilizing second order cone relaxations of the power flow constraints. The method proposed in [20] considers an OPF strategy for voltage regulation using semidefinite programming (SDP) and derive the conditions under which the semidefinite relaxation is tight for balanced circuits.

There are several works focusing on developing strategies for coordinating and optimizing control actions of DERs in unbalanced distribution grids. While we only mention some examples here, a more detailed literature review is provided in Chapters 4 and 5. In [21], an unbalanced OPF approach is utilized to optimize load shedding and operate smart grids in real time. The optimization problem was solved using a quasi-Newton method coupled with OpenDSS to calculate the three-phase power flow. A three-phase OPF model was developed in [22] using discrete variables to include capacitors switching and regulator taps changes. Since the proposed problem did not scale well, the discrete values were relaxed and a nonlinear optimization problem was solved by GAMS. In [23], a three-phase OPF approach using the three-phase current injection model in rectangular coordinate frame was proposed. While recent work on SDP relaxations [24] for unbalanced systems has been proposed, this approach does not scale well for large networks or guarantee solutions that are AC feasible. Furthermore, most of the above mentioned approaches are not suitable

for analyzing or mitigating voltage unbalance in distribution grids because they make assumptions about the system being nearly balanced (e.g., the voltage magnitudes at all three phases of a node are equal).

While open-source tools such as OpenDSS and GridLAB-D discussed in the previous section do not have optimization capabilities, there are some packages that support three-phase OPF formulations such as

- *PowerModelsDistribution.jl* is a Julia [25] package using JuMP [26] for steady-state optimization of distribution grids [27]. It provides a common platform for testing and benchmarking multiple three-phase OPF formulations based on variable space, coordinates (polar or rectangular) and approximations of power balance equations.

- *GridAPPS-D* is an open-source platform developed for application development and data integration [28]. Although the GridAPPS-D platform supports modelling of various DERs, most of the proposed applications focus on decentralized OPF approach to control smart inverters and coordinate switching devices such as capacitors and regulators to achieve system-level objectives.

1.2.3 Considering Uncertainty in Load and DER Power Injections

The OPF problem described in the previous section is typically handled as a deterministic optimization problem on the basis of a forecasted point for the load and renewable generation. However, the uncertainty in power systems has been rising in the recent years and is projected to increase further in the near future. We need to account for this uncertainty by treating the OPF problem as a stochastic optimization problem. The main reason for the increasing uncertainty is the higher power injection uncertainty of DERs and load variability. This can be particularly challenging at the distribution grid level, where limited real-time measurements are available and DERs are typically not equally distributed among the three phases of the feeder. An important question becomes how to coordinate DER control actions and maintain power quality of distribution grids under uncertainty.

Several approaches for stochastic OPF with uncertainty in load demand and renewable energy generation have been well documented in the context of transmission systems [29, 30, 31, 32, 33]. However, these proposed methods often employ DC power flow approximations and single-phase equivalents to represent the power flow physics, which are not applicable to distributions grids that are unbalanced and exhibit large R/X ratios. In addition, the primary focus of transmission operations is system balancing and congestion management. On the other hand, distribution utilities tend to focus on power quality issues that affect end consumers such as managing voltage magnitudes and voltage unbalance. In order to do this efficiently, several stochastic OPF models have been developed especially for distribution grids. Some of these methods include stochastic approximation techniques [34], distributionally robust methods [7, 35, 36], and chance-constrained formulations [37]. A more comprehensive literature review is provided in Chapter 6. The above mentioned strategies are different in the way uncertainty is incorporated into the system model and they prepare the power system for a wide range of uncertainty realizations. While some approaches are computationally complex and exhibit better accuracy, other methods are computationally simpler at the cost of a lower accuracy. In most methods, incorporating uncertainty in the optimization model will either lead to highly conservative and expensive solutions. Therefore, one of the most important factors to consider when solving an OPF problem that includes uncertainty is to find a suitable trade-off between cost and security. This is usually determined by how we define the uncertainty set (robust optimization), the type of scenarios that are taken into account (stochastic programming) or the acceptable violation probability (chance constraints) [38].

1.2.4 Aggregate Power Flexibility

As mentioned previously, majority of DERs in distribution grids are controlled by third-party entities such as aggregators. Typically, these aggregators have limited knowledge about the network and as a result, they control DERs without considering the grid constraints. From the perspective of the DSO who might not have direct control over these resources, DERs represent a

combination of renewable generation and loads with uncertain and dynamic response characteristics. Without proper coordination between the DSO and aggregators, it is not possible to leverage all the flexibility offered by the DERs.

One way for DSOs to account for the uncertain DER responses is to identify secure operating ranges which can be easily communicated to aggregators. An example of such easy to communicate operating ranges could be a feasible region of aggregate power that defines the collective DER and load variability in the network. This feasible region is referred to as the aggregate power flexibility and it determines the ability of the distribution grid to exchange power with the transmission system at the point of interconnection (i.e. substation interface) without the risk of grid constraint violations. A major advantage of accurately identifying the aggregate power flexibility is that it allows distribution grids to actively contribute as virtual power plants in the operation and control of transmission systems [39]. Since DERs are mostly connected to the grid via power electronic inverters, the aggregate power can be regulated quickly with a large ramping rate in response to the command signals. As a result, a distribution grid with a precise aggregate feasible region has the capability to provide ancillary services to the bulk transmission system, such as reserve and regulation services. Several works in literature propose methods for distribution-level power aggregation [40, 41, 42]. While determining the aggregate power flexibility is only part of the problem, it is important to guarantee disaggregation feasibility so that any aggregate power trajectory inside the feasible region can be utilized to dispatch DERs appropriately without causing any grid constraints violations. There are only a few works in literature [43, 44, 45, 46] which develop distribution system-level aggregate power flexibility while considering both aggregation optimality and disaggregation feasibility. We provide a more detailed literature review in Chapter 7.

1.3 Thesis Organization

This thesis attempts to optimize the operations of unbalanced distribution grids by using DERs to maintain power quality and provide flexibility in response to uncertainty. On one hand, we introduce a three-phase OPF approach to mitigate voltage unbalance using reactive power support from DERs such as solar PV systems. On the other hand, we propose different ways to model

uncertainty arising from DER variability or lack of direct DER control within the OPF framework and apply these models to different kinds of problems to investigate operational cost and grid security. The thesis is structured as follows:

Chapter 2 introduces the different definitions of voltage unbalance adopted by IEC, NEMA and IEEE in their power quality standards and emphasizes that these definitions are partially inconsistent with one another. This chapter highlights the relationships between the three most commonly used voltage unbalance definitions. We perform empirical evaluations to characterize these relationships' accuracy and asses the conditions under which these relationships are inaccurate.

Chapter 3 entails the fundamentals needed for the modelling of major distribution grid components which is the first step in building a framework to optimize the operation of distribution grids. We discuss modelling of the distribution grid in the phase-domain to incorporate the three-phase unbalanced nature of the network. We discuss detailed models of major system components such as transformers and voltage-dependent loads in any configuration (wye or delta).

Chapter 4 provides a detailed description of the three-phase OPF formulation which is flexible enough to represent the various voltage unbalance definitions either as objective function or constraints. The proposed method is tested on two distribution feeders and we perform an in-depth comparison of the results obtained by minimizing different voltage unbalance definitions, which show that minimizing unbalance using one standard might violate the limits set by another standard or lead to other power quality issues such as increase in network losses.

Chapter 5 extends the three-phase OPF approach by introducing three different linear power flow models used within a successive approximation framework to improve scalability of the three-phase OPF formulation. We discuss the various modifications made to the conventional three-phase OPF approach introduced in Chapter 3 in order to develop the three scalable methods and summarize the advantages as well as limitations of these scalable implementations. We demonstrate the efficacy of the approximation scheme on three-phase OPF implementation on a large, realistic distribution feeder. We benchmark the methods against the conventional nonlinear, non-convex OPF formulation, and existing approximations such as LinDist3Flow. We perform an in-depth comparison of the performance of all methods in terms of optimality, scalability and accuracy.

Furthermore, the methods are also tested in practical scenarios considering the time-varying load demand and DER outputs with measurements available only at certain time intervals after a time delay.

Chapter 6 describes a chance-constrained optimization approach to reduce the impact of uncertainty on the operation of distribution grids. We formulate the chance-constrained optimal power flow (CC-OPF) problem which minimizes voltage unbalance by controlling setpoints of DER inverters. We propose a computationally tractable reformulation of the chance-constrained problem applicable to a distribution grid setting. A detailed case study is performed using real load and DER data where we test ability of the proposed approach to enforce chance constraint satisfaction. Furthermore, we investigate how properties of the uncertainty data can influence the resulting solutions.

Chapter 7 discusses a bilevel optimization-based framework to find the optimal aggregate power flexibility that active distribution grids can provide to help reduce burdens on transmission grid resources while mitigating the risk of constraint violations in distribution grids. We propose a computationally tractable, strong duality based reformulation of the bilevel problem which can be solved efficiently using an iterative approach. The proposed method is tested on two unbalanced distribution feeders, where we investigate how the range of the feeder's aggregate power flexibility can be maximized while considering different DER reactive power control modes.

Chapter 8 concludes with a summary and main contributions of the research work. Furthermore, we propose different directions to continue research as part of the future work to make the three-phase OPF framework more realistic.

1.4 Publications

The work presented in this document has been reported by the following publications:

Journal Publications

1. K. Girigoudar, and L. Roald, "Identifying secure operating ranges for DER control using bilevel optimization," *In preparation*. 2022

2. K. Girigoudar and L. A. Roald, ”On the impact of different voltage unbalance metrics in distribution system optimization,” *Electric Power Systems Research*, vol. 189, p. 106656, 2020 [47]

Conference Publications

1. K. Girigoudar, Hou, Ashley M and L. A. Roald, ”Chance-constrained AC optimal power flow for unbalanced distribution grids,” in *Bulk Power Systems Dynamics and Control Symposium (IREP)*. 2022 [48]

2. K. Girigoudar and L. A. Roald, ”Linearized three-phase optimal power flow models for distribution grids with voltage unbalance,” in *Conference on Decision and Control (CDC)*. IEEE, 2021 [49]

3. K. Girigoudar, D. Molzahn, and L. Roald, ”On the relationships among different voltage unbalance definitions,” in *North American Power Symposium (NAPS)*. IEEE, 2019 [50]

Other Publications

The following publication has been published during the course of this PhD, but their contents are not included in the thesis:

1. K. Girigoudar, M. Yao, J. L. Mathieu, and L. A. Roald, ”Integration of centralized and distributed methods to mitigate voltage unbalance using solar inverters”, submitted to *IEEE Transactions on Smart Grids*. 2022

Chapter 2

Voltage Unbalance

Increasing deployment of distributed energy resources (DERs) such as rooftop solar photovoltaic (PV) systems and electric vehicles (EVs) are leading to greater load variability in distribution systems. High penetrations of DERs, which are typically not allocated evenly between phases [51], can result in problems such as voltage unbalance and make it challenging for distribution system operators to maintain acceptable power quality throughout the network. Unbalanced voltages may cause damage or derating of expensive three-phase equipment such as motor loads [3]. Furthermore, voltage unbalance can also lead to non-zero neutral currents in four-wire systems which affect protection devices [52] and increase network losses [53]. Various organizations such as IEC [54], NEMA [55], and IEEE [56] propose different voltage unbalance definitions in their power quality standards. These definitions are also used to define the maximum voltage unbalance limits for both equipment manufacturers, who design equipment by ensuring no permanent damage is caused due to voltage unbalance as well as for grid operators, who need to maintain acceptable power quality throughout the system. However, the associated voltage unbalance definitions are partially inconsistent. The IEC standard [54] defines voltage unbalance using symmetrical components [57], which require measurement of both voltage magnitude and phase angle. The NEMA [55] and IEEE [56] standards use definitions based on phase-to-phase and phase-to-neutral voltage magnitudes, respectively.

There are a number of papers comparing the voltage unbalance definitions. Three definitions of voltage unbalance (IEEE 1159, IEEE 141-1993, and NEMA) are numerically compared in [58] and [59]. These papers conclude that for unbalances below 5%, the voltage unbalance definitions agree reasonably well. However, the numerical comparisons show that there are some differences

which imply that operating points satisfying one standard might might violate other standards. In [60] and [61], several approximations of the IEC definition based only on phase-to-phase voltage magnitude measurements are evaluated. However, the expressions derived are nonlinear and no clear bounds on the error with respect to the IEC definition are provided.

2.1 Main Contributions

In this chapter, we derive the analytical relationships among the voltage unbalance definitions and numerically verify the accuracy of these relationships. Additionally, we also assess the conditions when these relationships are inaccurate. Relative to existing literature, we do not just numerically compare the different voltage unbalance definitions which might be useful to analyze one definition as an approximation for the others. Instead, we focus on deriving bounds for the *maximum* difference among the voltage unbalance definitions. This is helpful to understand how we can use one voltage unbalance definition (which might for example, require fewer real time measurements) to deduce acceptable bounds on the voltage unbalance defined by another standard.

2.2 Voltage Unbalance Definitions

Voltage unbalance occurs in three-phase power systems due to unequal phase voltage magnitudes or asymmetrical phase angle displacement, or a combination of both [57]. In this section, we present the three most commonly used definitions of voltage unbalance from IEC [54], NEMA [55], and IEEE [56]. Other definitions based on approximations of the IEC definition [61] are not discussed here as they fundamentally do not represent voltage unbalance.

We use the following notation to represent phasors in polar form: $v = |v|\angle\theta$, where v represents the voltage phasor as a complex number, $|v|$ is the voltage magnitude, and θ is the phase angle. In rectangular form: $v = v_{\mathrm{d}} + jv_{\mathrm{q}}$, where $v_{\mathrm{d}}, v_{\mathrm{q}}$ denote the real and imaginary components, respectively, with $j = \sqrt{-1}$. The complex conjugate of v is denoted as v^*.

2.2.1 IEC Definition (VUF)

The Voltage Unbalance Factor (VUF) is considered to be the "true" definition of voltage unbalance. It is adopted by the IEC [54] and expressed as the ratio of negative to positive sequence voltage magnitude component using

$$\text{VUF } [\%] = \frac{|v^-|}{|v^+|} \times 100, \quad \text{where} \tag{2.1}$$
$$v^+ = \frac{v^a + \mathrm{a}\cdot v^b + \mathrm{a}^2\cdot v^c}{3},\ v^- = \frac{v^a + \mathrm{a}^2\cdot v^b + \mathrm{a}\cdot v^c}{3}.$$

v^+ and v^- are the positive and negative sequence voltage phasors, respectively; $\mathrm{a} = 1\angle 120°$; and v^a, v^b, and v^c are the three phase-to-neutral voltage phasors at phases a, b and c, respectively. The use of symmetrical components v^+ and v^- pose some practical challenges due to the need to measure both voltage magnitudes and angles for each phase as well as the associated complex algebra [58]. One of the major issues in using the IEC definition is the unavailability of phase angle measurements from RMS meters installed in the distribution systems [59]. For low- and medium-voltage systems, the IEC standard 61000-2-2 [54] limit for voltage unbalance, as defined in (2.1), is 2%.

2.2.2 IEEE Definition (PVUR)

The IEEE definition is a recommended guideline for electrical grid operators to measure unbalance [56]. It is commonly referred to as Phase Voltage Unbalance Rate (PVUR) and defined using the phase-to-neutral voltage magnitudes $|v^a|, |v^b|$ and $|v^c|$:

$$\text{PVUR } [\%] = \frac{\Delta v_{\mathrm{P}}^{\max}}{v_{\mathrm{P}}^{\mathrm{avg}}} \times 100, \tag{2.2}$$
$$\text{where } \ v_{\mathrm{P}}^{\mathrm{avg}} = \frac{|v^a| + |v^b| + |v^c|}{3},$$
$$\Delta v_{\mathrm{P}}^{\max} = \max\{||v^a| - v_{\mathrm{P}}^{\mathrm{avg}}|, ||v^b| - v_{\mathrm{P}}^{\mathrm{avg}}|, ||v^c| - v_{\mathrm{P}}^{\mathrm{avg}}|\}.$$

Motors operating near full load can be damaged by voltage unbalance exceeding 2% due to overheating [56]. Since the IEEE definition ignores phase angle information, it cannot detect voltage unbalance due to phase angle asymmetries.

2.2.3 NEMA Definition (LVUR)

Typically, motors are one of the most common three-phase loads connected to distribution systems. Motor manufacturers use the NEMA definition of voltage unbalance [55], which is also referred to as the Line Voltage Unbalance Rate (LVUR). The NEMA definition of voltage unbalance uses phase-to-phase voltage magnitudes $|v^{ab}|, |v^{bc}|$ and $|v^{ca}|$ which can be defined in terms of phase-to-neutral voltage phasors as

$$|v^{ab}| = |v^a - v^b|, \;\; |v^{bc}| = |v^b - v^c|, \;\; |v^{ca}| = |v^c - v^a|. \tag{2.3}$$

Since we are using the difference between phase-to-neutral voltage phasors in (2.3), some information about the phase-to-neutral voltage angle is inherently retained when calculating the phase-to-phase voltage magnitudes and hence, the phase angle information is not completely ignored. By using (2.3), the NEMA definition can be expressed as

$$\begin{aligned} \text{LVUR } [\%] &= \frac{\Delta v_{\text{L}}^{\max}}{v_{\text{L}}^{\text{avg}}} \times 100, \\ \text{where } \; v_{\text{L}}^{\text{avg}} &= \frac{|v^{ab}| + |v^{bc}| + |v^{ca}|}{3}, \\ \Delta v_{\text{L}}^{\max} &= \max\{||v^{ab}| - v_{\text{L}}^{\text{avg}}|, ||v^{bc}| - v_{\text{L}}^{\text{avg}}|, ||v^{ca}| - v_{\text{L}}^{\text{avg}}|\}. \end{aligned} \tag{2.4}$$

Per NEMA MG-1 [55] and ANSI C84.I [62], the maximum voltage unbalance for three-phase power systems under no-load conditions must not exceed 3%.

2.3 Comparison of Voltage Unbalance Definitions

This section provides a detailed comparison of the various voltage unbalance definitions by deriving analytical bounds which are validated through numerical simulations. For our analysis, we divide voltage unbalance into three categories:

(a) Voltage magnitude unbalance,

(b) Voltage angle unbalance,

(c) Voltage magnitude and angle unbalance.

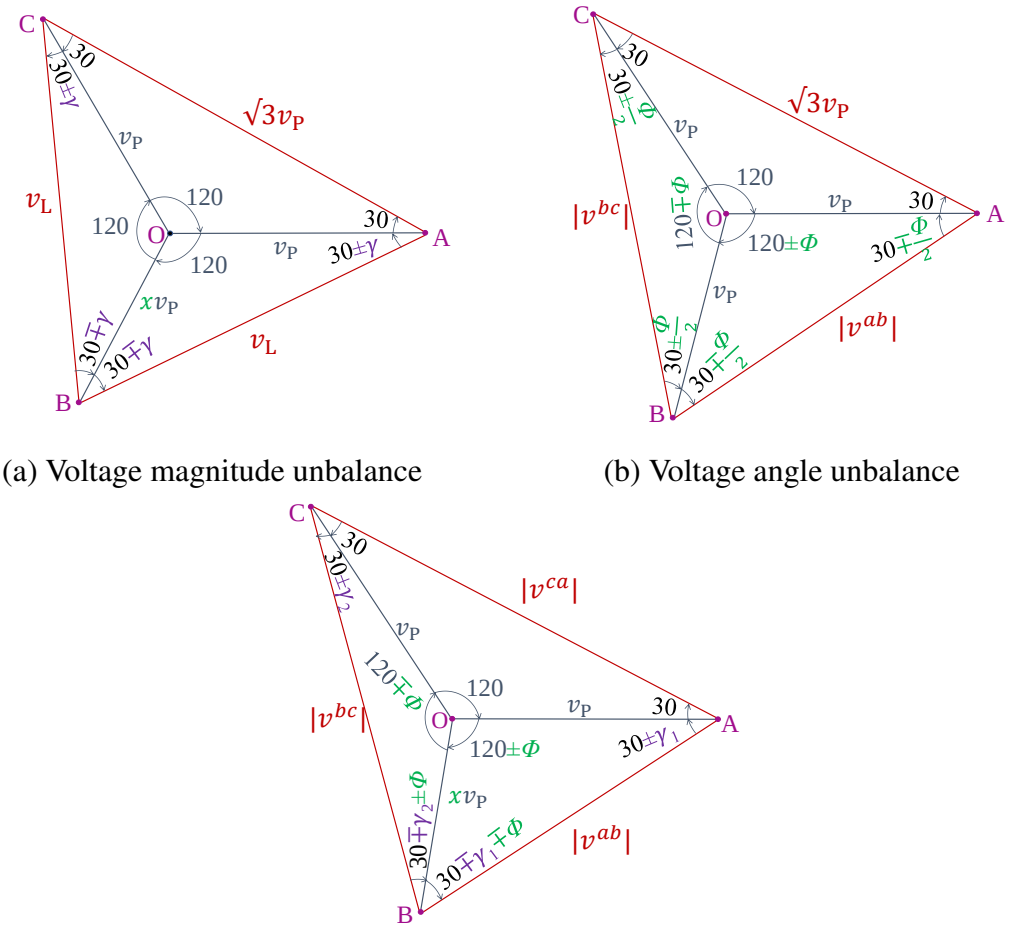

(a) Voltage magnitude unbalance

(b) Voltage angle unbalance

(c) Voltage magnitude and angle unbalance

Figure 2.1: Voltage triangles for three categories of unbalance in phase b.

Assuming phase a as the reference, we evaluate the impacts of shifting the voltage phasors associated with either phase b individually or both phases b and c. Fig. 2.1 illustrates the voltage triangle with unbalance in phase b for each of the three categories. With balanced voltage magnitude represented by v_{P}, the magnitude unbalance is defined by the multiplicative factor x and the angle unbalance is denoted by ϕ. The angles γ and γ_1, γ_2 in Fig. 2.1 can be represented as functions of both x and ϕ.

We start with the simpler voltage unbalance cases which involve either magnitude or angle unbalance. We derive analytical expressions for VUF, PVUR and LVUR by using small angle

approximations and then utilize these expressions to derive bounds on the maximum difference among the various definitions as well as characterize the relationships. Next, we verify the bounds using numerical simulations which do not involve any approximations.

For more general cases with either angle unbalance in multiple phases or combinations of magnitude and angle unbalance, the analytical expressions are complex, and hard to compare or analyze. Hence, we rely only on numerical simulations and avoid including analytical expressions for such cases.

2.3.1 Voltage Magnitude Unbalance at a Single Phase

We first investigate the voltage magnitude unbalance case (i.e., $\phi = 0°$). Let us consider a voltage magnitude unbalance in phase b (chosen arbitrarily) as shown in Fig. 2.1(a). While one of the phase-to-phase voltages has a magnitude of $\sqrt{3}v_{\mathrm{P}}$ which is similar to a perfectly balanced case, the other two phase-to-phase voltage magnitudes denoted by v_{L} are influenced by the unbalance of the phase-b-to-ground voltage magnitude. The phase-to-neutral and phase-to-phase voltage phasors are

$$\begin{aligned} v^a &= v_{\mathrm{P}}\angle 0°, & v^{ab} &= v_{\mathrm{L}}\angle(30° \pm \gamma),\\ v^b &= x \cdot v_{\mathrm{P}}\angle -120°, & v^{bc} &= v_{\mathrm{L}}\angle -(90° \pm \gamma),\\ v^c &= v_{\mathrm{P}}\angle 120°, & v^{ca} &= \sqrt{3}v_{\mathrm{P}}\angle 150°. \end{aligned}$$

2.3.1.1 IEC Definition (VUF)

We start by providing analytical expressions for the IEC definition. The magnitudes of the symmetrical components $|v^+|$ and $|v^-|$ are

$$|v^+| = \frac{|v_{\mathrm{P}}\angle 0° + x v_{\mathrm{P}}\angle 0° + v_{\mathrm{P}}\angle 0°|}{3} = \frac{v_{\mathrm{P}}\,(x+2)}{3}, \tag{2.5a}$$

$$|v^-| = \frac{|v_{\mathrm{P}}\angle 0° + x v_{\mathrm{P}}\angle 120° + v_{\mathrm{P}}\angle -120°|}{3} = \frac{v_{\mathrm{P}}}{3}\frac{|(x-1)(1-j\sqrt{3})|}{2} = \frac{v_{\mathrm{P}}|x-1|}{3}. \tag{2.5b}$$

The voltage unbalance using the IEC definition in (2.1) is

$$\mathrm{VUF} = \frac{|v^-|}{|v^+|} = \frac{|x-1|}{x+2}. \tag{2.6}$$

2.3.1.2 IEEE Definition (PVUR)

The PVUR definition (2.2) is calculated as the ratio of the maximum deviation $\Delta v_{\mathrm{P}}^{\max}$ to the average phase-to-neutral voltage $v_{\mathrm{P}}^{\mathrm{avg}}$ expressed by

$$v_{\mathrm{P}}^{\mathrm{avg}} = \frac{v_{\mathrm{P}} + v_{\mathrm{P}} + x v_{\mathrm{P}}}{3} = \frac{v_{\mathrm{P}}\,(x+2)}{3}, \tag{2.7a}$$

$$\Delta v_{\mathrm{P}}^{\max} = |x v_{\mathrm{P}} - \frac{v_{\mathrm{P}}\,(x+2)}{3}| = \frac{2 v_{\mathrm{P}} |x-1|}{3}, \tag{2.7b}$$

which gives rise to the following PVUR expression,

$$\mathrm{PVUR} = \frac{2|x-1|}{x+2}. \tag{2.8}$$

2.3.1.3 NEMA Definition (LVUR)

The LVUR voltage unbalance definition (2.4) requires the phase-to-phase voltage v_{L}. By applying the sine triangle rule to the triangle $\triangle OAB$ in Fig. 2.1(a), we can express v_{L} in terms of x as

$$\frac{v_{\mathrm{L}}}{\sin 120^\circ} = \frac{v_{\mathrm{P}}}{\sin(30^\circ \mp \gamma)} = \frac{x v_{\mathrm{P}}}{\sin(30^\circ \pm \gamma)}. \tag{2.9}$$

Using the trigonometric angle sum identities in (2.9) yields two expressions for v_{L} in terms of x and γ:

$$v_{\mathrm{L}} \sin(30^\circ \mp \gamma) = v_{\mathrm{P}} \sin 120^\circ \Rightarrow v_{\mathrm{L}} \Big(\cos\gamma \mp \sqrt{3} \sin\gamma \Big) = \sqrt{3} v_{\mathrm{P}}, \tag{2.10a}$$

$$v_{\mathrm{L}} \sin(30^\circ \pm \gamma) = x v_{\mathrm{P}} \sin 120^\circ \Rightarrow v_{\mathrm{L}} \Big(\cos\gamma \pm \sqrt{3} \sin\gamma \Big) = \sqrt{3} x v_{\mathrm{P}}. \tag{2.10b}$$

By adding (2.10a) to (2.10b) and using the small angle approximations ($\sin\gamma \approx \gamma$, $\cos\gamma \approx 1$), we can express v_{L} in terms of x using

$$v_{\mathrm{L}} = \sqrt{3} v_{\mathrm{P}} \left(\frac{x+1}{2\cos\gamma} \right) \approx \sqrt{3} v_{\mathrm{P}} \left(\frac{x+1}{2} \right). \tag{2.11}$$

Using (2.11), the maximum deviation $\Delta v_{\mathrm{L}}^{\max}$ and average phase-to-phase voltage $v_{\mathrm{L}}^{\mathrm{avg}}$ can be expressed as

$$v_{\mathrm{L}}^{\mathrm{avg}} = \frac{v_{\mathrm{L}} + v_{\mathrm{L}} + \sqrt{3} v_{\mathrm{P}}}{3} \approx \sqrt{3} v_{\mathrm{P}} \left(\frac{x+2}{3} \right), \tag{2.12a}$$

$$\Delta v_{\mathrm{L}}^{\max} = |\sqrt{3} v_{\mathrm{P}} - v_{\mathrm{L}}{}^{\mathrm{avg}}| \approx \sqrt{3} v_{\mathrm{P}} \left(\frac{|x-1|}{3} \right), \tag{2.12b}$$

which allows us to express LVUR as:

$$\text{LVUR} \approx \frac{|x-1|}{x+2}. \tag{2.13}$$

2.3.1.4 Analytical Comparison

We observe the following relationships by comparing the three definitions based on (2.6), (2.8) and (2.13):

$$\text{LVUR} \approx \text{VUF} = \frac{\text{PVUR}}{2}. \tag{2.14}$$

The LVUR expression involves small angle approximations as indicated by the $\approx$ sign. On the contrary, VUF and PVUR are exact calculations. For a given deviation in voltage magnitude $|x-1|$, the expressions for v^-, $\Delta v_{\text{P}}^{\max}$ and $\Delta v_{\text{L}}^{\max}$ in the numerators of (2.6), (2.8) and (2.13), respectively, are invariant to under-voltage ($x < 1$) or over-voltage ($x > 1$) operating conditions. Conversely, the expressions for v^+, $v_{\text{P}}^{\text{avg}}$ and $v_{\text{L}}^{\text{avg}}$ in the denominators of (2.6), (2.8) and (2.13) respectively, are directly proportional to x. Therefore, the voltage unbalance for under-voltage condition is greater compared to the over-voltage cases, which is also consistent with the observations in [60].

2.3.1.5 Numerical Validation

To verify the expressions derived previously, we run simulations to compute the voltage unbalance by varying the phase-b voltage magnitude. We vary the multiplicative factor x from 0.8 to 1.2 in steps of 0.01 to analyze both under-voltage and over-voltage operating conditions. Fig. 2.2 shows the variation of VUF (on the y-axis) for voltage magnitude unbalance in phase b only with reference to both PVUR and LVUR (on the x-axis). The dashed black line illustrates the scenario when VUF and LVUR are equal, while the dashed red line represents the scenario where PVUR is larger than VUF by a factor of 2. The orange and green dots correspond to values obtained for LVUR and PVUR, respectively.

We observe from Fig. 2.2 that PVUR is exactly twice as large as VUF which is consistent with our analytical results. The values for VUF and LVUR are almost equal, although there are

small variations due to inaccuracy of the small angle approximations. For the range of x values considered, the relative difference between LVUR and VUF $\left(\frac{|\text{LVUR}-\text{VUF}|}{\text{VUF}}\right)$ is less than 2%.

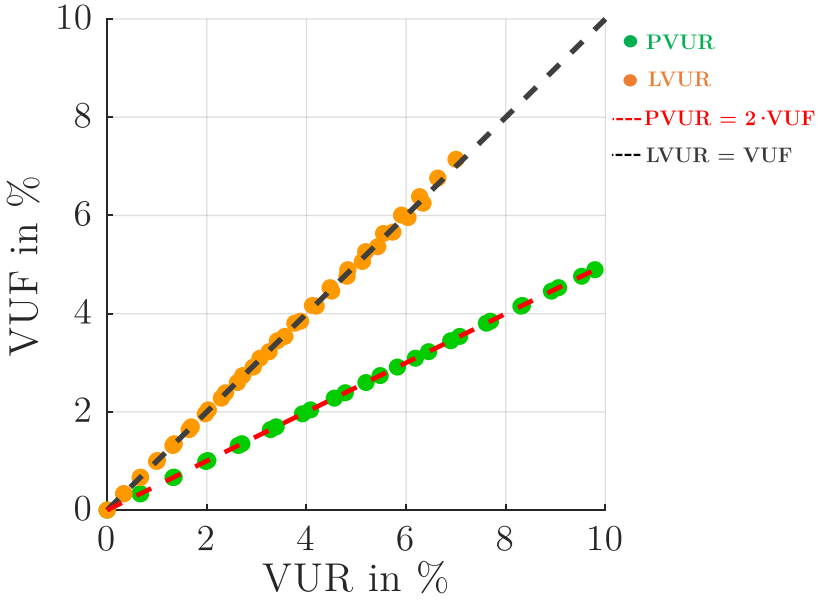

Figure 2.2: Voltage magnitude unbalance at phase b for $0.80 \leq x \leq 1.20$.

2.3.2 Voltage Magnitude Unbalance at Two Phases

Now we consider deviations in the magnitudes at phases b and c. The phase-to-neutral voltage phasors are

$$v^a = v_{\text{P}}\angle 0^\circ, \quad v^b = x_1 v_{\text{P}}\angle -120^\circ \text{ and } v^c = x_2 v_{\text{P}}\angle 120^\circ,$$

where x_1, x_2 are the two multiplicative factors. Since the voltage unbalance expressions are complex, we only include a high-level summary of this case.

2.3.2.1 IEC Definition (VUF)

The denominator and numerator for VUF in (2.1) i.e. the magnitude of the positive and negative sequence voltages are expressed as

$$|v^{+}| = \frac{|v_{\mathrm{P}}\angle 0^{\circ} + x_1 v_{\mathrm{P}}\angle 0^{\circ} + x_2 v_{\mathrm{P}}\angle 0^{\circ}|}{3} = \frac{v_{\mathrm{P}}}{3}\left(1 + x_1 + x_2\right), \tag{2.15a}$$

$$|v^{-}| = \frac{|v_{\mathrm{P}}\angle 0^{\circ} + x_1 v_{\mathrm{P}}\angle 120^{\circ} + x_2 v_{\mathrm{P}}\angle -120^{\circ}|}{3} = \frac{v_{\mathrm{P}}}{3}\sqrt{x_1^2 + x_2^2 + 1 - x_1 - x_2 - x_1 x_2}. \tag{2.15b}$$

2.3.2.2 IEEE Definition (PVUR)

The maximum deviation $\Delta v_{\mathrm{P}}^{\max}$ and average phase-to-neutral voltage $v_{\mathrm{P}}^{\mathrm{avg}}$ can be defined as

$$v_{\mathrm{P}}^{\mathrm{avg}} = \frac{|v^a| + |v^b| + |v^c|}{3} = \frac{v_{\mathrm{P}}}{3}\left(1 + x_1 + x_2\right), \tag{2.16a}$$

$$\Delta v_{\mathrm{P}}^{\max} = \max\{||v^a| - v_{\mathrm{P}}^{\mathrm{avg}}|, ||v^b| - v_{\mathrm{P}}^{\mathrm{avg}}|, ||v^c| - v_{\mathrm{P}}^{\mathrm{avg}}|\} = \frac{v_{\mathrm{P}}}{3}\max\{|y_1|, |y_2|, |y_3|\}, \tag{2.16b}$$

where $y_1 = x_1 + x_2 - 2,\ y_2 = -2x_1 + x_2 + 1$ and $y_3 = x_1 - 2x_2 + 1$ represent the three cases corresponding to the deviations of the phase-to-neutral voltage magnitudes from $v_{\mathrm{P}}^{\mathrm{avg}}$.

2.3.2.3 NEMA Definition (LVUR)

By using the sine triangle rule as well as small angle approximations and following the same procedure defined in (2.9)-(2.11), we express the phase-to-phase voltage magnitudes using

$$|v^{ab}| \approx \sqrt{3} v_{\mathrm{P}}\left(\frac{x_1 + 1}{2}\right),\ \ |v^{bc}| \approx \sqrt{3} v_{\mathrm{P}}\left(\frac{x_2 + 1}{2}\right)\ \text{ and }\ |v^{ca}| \approx \sqrt{3} v_{\mathrm{P}}\left(\frac{x_1 + x_2}{2}\right). \tag{2.17}$$

The average phase-to-phase voltage $v_{\mathrm{L}}^{\mathrm{avg}}$ can be expressed as

$$v_{\mathrm{L}}^{\mathrm{avg}} = \frac{|v^{ab}| + |v^{bc}| + |v^{ca}|}{3} \approx \sqrt{3} v_{\mathrm{P}}\left(\frac{1 + x_1 + x_2}{3}\right), \tag{2.18}$$

Since $\Delta v_{\mathrm{L}}^{\max}$ depends on the maximum deviation of the voltage magnitude from the average value, we again consider three cases,

$$\begin{aligned}\Delta v_{\mathrm{L}}^{\max} &= \max\{||v^{ab}| - v_{\mathrm{L}}^{\mathrm{avg}}|, ||v^{bc}| - v_{\mathrm{L}}^{\mathrm{avg}}|, ||v^{ca}| - v_{\mathrm{L}}^{\mathrm{avg}}|\} \\ &\approx \frac{\sqrt{3} v_{\mathrm{P}}}{6}\max\{|y_1|, |y_2|, |y_3|\},\end{aligned} \tag{2.19}$$

where $y_1, y_2 \text{ and } y_3$ represent the three cases corresponding to the deviations of the phase-to-phase voltage magnitudes from $v_{\text{L}}^{\text{avg}}$ and the expressions are already defined in (2.16b).

2.3.2.4 Analytical Comparison

Similar to the magnitude deviation in only one phase, the denominators of all three definitions of voltage unbalance defined in (2.15a), (2.16a) and (2.18) simplify to the same expressions when voltage magnitude deviations occur in two phases. Therefore, we only need to assess the differences in the numerators to analytically compare the voltage unbalance definitions. Using (2.16b) and (2.19), the relationship between PVUR and LVUR can be expressed as

$$\frac{\text{PVUR}}{\text{LVUR}} \approx \frac{\Delta v_{\text{P}}^{\max}}{\Delta v_{\text{L}}^{\max}} \approx 2 \;\Rightarrow\; \text{PVUR} \approx 2 \cdot \text{LVUR}. \tag{2.20}$$

When comparing PVUR and LVUR with VUF, we observe that a one-to-one mapping does not exist since we need to consider the three different cases corresponding to whether y_1, y_2, or y_3 defined in (2.16b) is the largest. Therefore, instead of deriving an approximate relationship, we find the bounds for VUF in terms of PVUR and LVUR. To derive an upper bound, we square the ratio between VUF and PVUR to get

$$\left(\frac{\text{VUF}}{\text{PVUR}}\right)^2 = \left(\frac{|v^-|}{\Delta v_{\text{P}}^{\max}}\right)^2 = \frac{x_1^2 + x_2^2 + 1 - x_1 - x_2 - x_1 x_2}{(\max\{|y_1|, |y_2|, |y_3|\})^2}. \tag{2.21}$$

After identifying the largest among $|y_1|, |y_2|$ and $|y_3|$, we can simplify the expressions and take the square root on both sides of (2.21). We then obtain an upper bound on VUF in terms of PVUR,

$$\frac{|v^-|}{\Delta v_{\text{P}}^{\max}} \leq \frac{1}{\sqrt{3}} \;\Rightarrow\; \text{VUF} \leq \left(\frac{1}{\sqrt{3}}\right) \cdot \text{PVUR}. \tag{2.22}$$

To derive the lower bound, we observe that the definitions of y_1, y_2, and y_3 entail that the unbalance ratio described in (2.21) is always greater than the situation when either $x_1 = 1$ or $x_2 = 1$. This means that the relationship defined in (2.14) for magnitude unbalance only in phase b is a lower bound on the more general case with voltage magnitude unbalance in two phases. By combining the upper (2.22) and lower (2.14) bounds, we get the following relationship between PVUR and VUF:

$$\left(\frac{1}{2}\right) \text{PVUR} \leq \text{VUF} \leq \left(\frac{1}{\sqrt{3}}\right) \text{PVUR}. \tag{2.23a}$$

Using (2.20) to substitute LVUR for PVUR, we obtain the approximate lower and upper bounds for VUF in terms of LVUR,

$$\text{LVUR} \lesssim \text{VUF} \lesssim \left(\frac{2}{\sqrt{3}}\right) \text{LVUR}. \tag{2.23b}$$

The $\lesssim$ sign indicates that the calculations for LVUR in (2.18) and (2.19) involve small angle approximations and are therefore not exact.

2.3.2.5 Numerical Validation

Similar to the case with unbalance in one phase, we run simulations where x_1 and x_2 vary from 0.8 to 1.2 in steps of 0.01. The results are illustrated in Fig. 2.3. The black and red lines represent the scenario where LVUR = VUF and PVUR = 2· VUF, respectively. In addition to this, we also include lines to denote the upper bounds VUF = $\frac{2}{\sqrt{3}}$· LVUR (solid blue line) and VUF = $\frac{1}{\sqrt{3}}$· PVUR (solid purple line). While most of the points fall within the predicted range, LVUR is higher than VUF for approximately 17% of the considered points. These points are below the dashed black line in the grey shaded region shown in Fig. 2.3. This scenario corresponds to cases where two phase-to-phase voltages were significantly larger than the third phase-to-phase voltage,

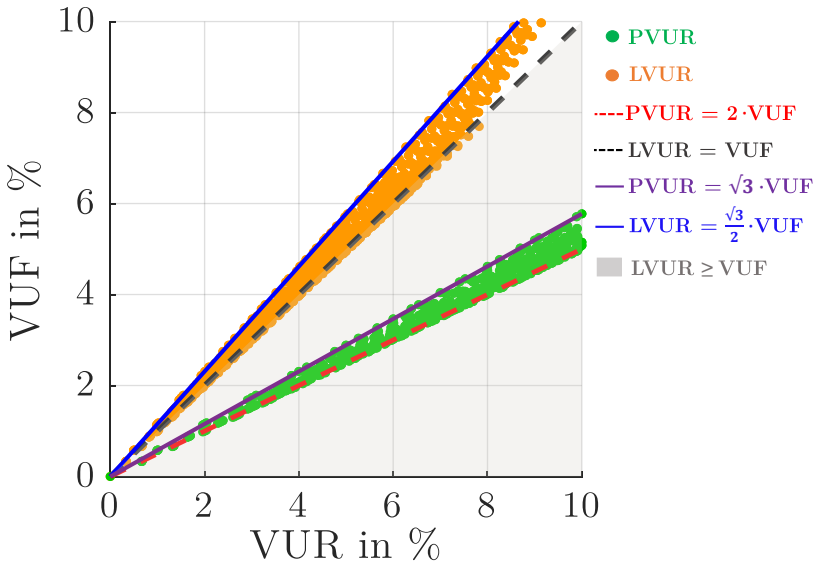

Figure 2.3: Voltage magnitude unbalance at phases b and c for $0.80 \leq x_1, x_2 \leq 1.20$.

i.e., extreme cases of over-voltage in one phase and under-voltage in other two phases, which leads to inaccurate small angle approximations. However, within the ranges of voltage magnitudes corresponding to $0.8 \leq x_1, x_2 \leq 1.2$, the errors in our bounds are negligible and we never see violations greater than 2% relative to the bounds in (2.23).

2.3.3 Voltage Angle Unbalance at a Single Phase

We next consider the voltage angle unbalance in one phase with angle displacement ϕ and balanced voltage magnitude v_{P} as illustrated in Fig. 2.1(b). The phase-to-neutral and phase-to-phase voltage phasors in this case are

$$\begin{aligned} v^a &= v_{\mathrm{P}}\angle 0^\circ, & v^{ab} &= |v^{ab}|\angle(30^\circ \mp \phi/2), \\ v^b &= v_{\mathrm{P}}\angle -(120^\circ \pm \phi), & v^{bc} &= |v^{bc}|\angle -(90^\circ \pm \phi/2), \\ v^c &= v_{\mathrm{P}}\angle(120^\circ \mp \phi), & v^{ca} &= \sqrt{3}v_{\mathrm{P}}\angle 150^\circ. \end{aligned}$$

2.3.3.1 IEC Definition (VUF)

We use the small angle approximation to calculate the magnitudes of the symmetrical voltage components, $|v^+|$ and $|v^-|$:

$$|v^+| = \frac{|v_{\mathrm{P}}\angle 0^\circ + v_{\mathrm{P}}\angle \mp\phi + v_{\mathrm{P}}\angle \mp\phi|}{3} \approx \frac{v_{\mathrm{P}}}{3}\sqrt{9+\phi^2} \approx v_{\mathrm{P}}, \tag{2.24a}$$

$$|v^-| = \frac{|v_{\mathrm{P}}\angle 0^\circ + v_{\mathrm{P}}\angle(120^\circ \mp \phi) + v_{\mathrm{P}}\angle(-120^\circ \mp \phi)|}{3} \approx \frac{v_{\mathrm{P}}}{3}\phi. \tag{2.24b}$$

2.3.3.2 IEEE Definition (PVUR)

Since the phase-to-neutral voltage magnitudes are perfectly balanced, $\Delta v_{\mathrm{P}}^{\max} = 0$. So, PVUR = 0 for any unbalance that only influences the voltage angles. Hence, we observe that PVUR does not detect phase angle unbalance.

2.3.3.3 NEMA Definition (LVUR)

To determine the expressions for LVUR, we use the small angle approximation as well as the sine triangle rule for ϕ to obtain the phase-to-phase voltage magnitudes, $|v^{ab}|$ and $|v^{bc}|$:

$$|v^{ab}| \approx v_{\mathrm{P}}(\sqrt{3} \pm \frac{\phi}{2}), \quad |v^{bc}| \approx v_{\mathrm{P}}(\sqrt{3} \mp \frac{\phi}{2}). \tag{2.25}$$

Next, we derive approximations for the maximum deviation $\Delta v_{\mathrm{L}}^{\max}$ and average phase-to-phase voltage magnitudes $v_{\mathrm{L}}^{\mathrm{avg}}$ to obtain an approximate expression for LVUR:

$$v_{\mathrm{L}}^{\mathrm{avg}} = \frac{|v^{ab}| + |v^{bc}| + \sqrt{3}v_{\mathrm{P}}}{3} \approx \sqrt{3}v_{\mathrm{P}}, \tag{2.26a}$$

$$\Delta v_{\mathrm{L}}^{\max} \approx |v_{\mathrm{P}}(\sqrt{3} \pm \frac{\phi}{2}) - \sqrt{3}v_{\mathrm{P}}| = \frac{\phi v_{\mathrm{P}}}{2}. \tag{2.26b}$$

2.3.3.4 Analytical Comparison

Using (2.24)-(2.26), we obtain the approximate relationship between LVUR and VUF as

$$\mathrm{VUF} = \frac{|v^-|}{|v^+|} \approx \frac{\phi}{3}, \ \ \mathrm{LVUR} = \frac{v_{\mathrm{L}}^{\max}}{v_{\mathrm{L}}^{\mathrm{avg}}} \approx \frac{\phi}{2\sqrt{3}} \Rightarrow \mathrm{VUF} \approx \frac{2}{\sqrt{3}}\mathrm{LVUR}. \tag{2.27}$$

2.3.3.5 Numerical Validation

The relationship defined in (2.27) is verified by numerical simulations. Assuming phase a as the reference, the angle displacement in phase b is varied in the range $-20^\circ \leq \phi \leq 20^\circ$ in steps of 1°. The results for unbalance in phase b are represented in Fig. 2.4. With PVUR = 0 for any value of ϕ and almost all points lying on the solid blue line representing LVUR $= \frac{\sqrt{3}}{2}$ VUF, the numerical simulations verifies the analytical results.

2.3.4 Voltage Angle Unbalance at Two Phases

We further assess the relationships among the definitions for voltage angle unbalance in two phases by introducing two angle deviations, ϕ_1 and ϕ_2 for phases b and c, respectively. The phase-to-neutral voltage phasors are

$$v^a = v_{\mathrm{P}}\angle 0^\circ, \ \ v^b = v_{\mathrm{P}}\angle -(120^\circ \pm \phi_1) \ \text{ and } \ v^c = v_{\mathrm{P}}\angle(120^\circ \pm \phi_2).$$

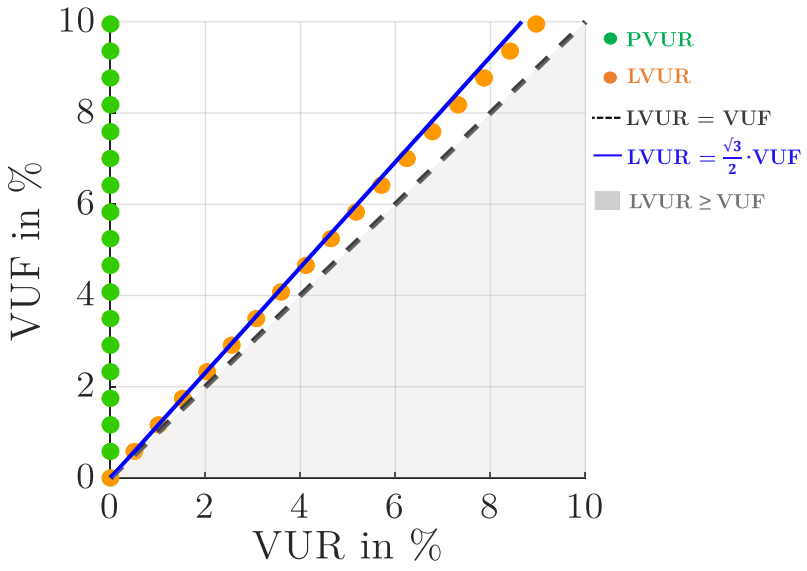

Figure 2.4: Voltage angle unbalance in phase b for -20° $\leq \phi \leq$ 20°.

We only discuss the numerical results for this case due to the complexity of the analytical expressions.

2.3.4.1 Numerical Comparison

Similar to the numerical simulations for voltage angle unbalance in phase b, we assume phase a as the reference, and consider angle deviations in phases b and c in the range $-20° \leq \phi_1,\ \phi_2 \leq 20°$, in steps of $1°$. The results are illustrated in Fig. 2.5. We again observe that PVUR is still always zero for all combinations of angle unbalance since it includes no information about phase angle unbalance. While there is no longer a direct correspondence between VUF and LVUR, we observe that the lower and upper bounds of VUF satisfy the relationships given by

$$\text{LVUR} \lesssim \text{VUF} \lesssim \left(\frac{2}{\sqrt{3}}\right) \text{LVUR}, \tag{2.28}$$

where the upper bound was derived in (2.27).

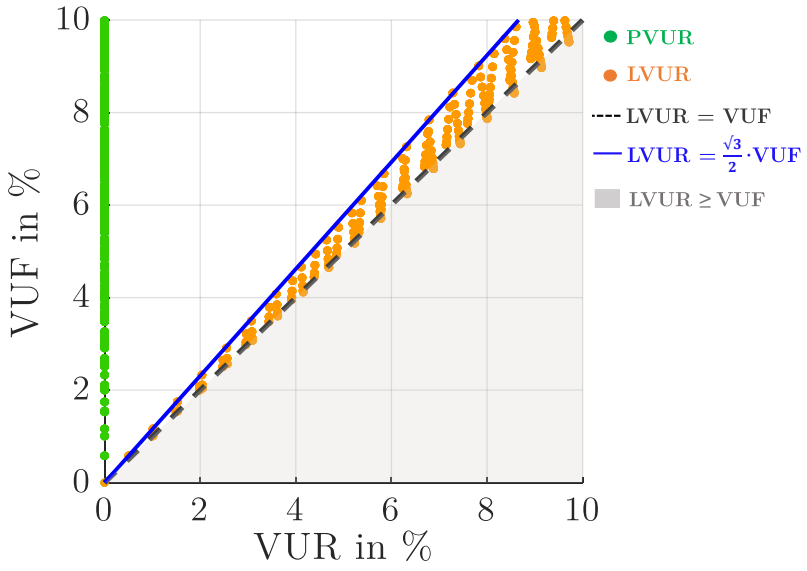

Figure 2.5: Voltage angle unbalance in phases b and c for -20° $\leq \phi_1, \phi_2 \leq$ 20°.

2.3.5 Voltage Magnitude and Angle Unbalance

Finally, we consider the most general case where the unbalance occurs due to asymmetries in both voltage magnitudes and angles. We first analyze the case with unbalanced voltage magnitude xv_{P} and asymmetrical angle displacement ϕ in phase b as shown in Fig. 2.1(c). The phase-to-neutral and phase-to-phase voltage phasors in this case are

$$v^a = v_{\text{P}}\angle 0°, \qquad v^{ab} = |v^{ab}|\angle(30° \mp \gamma_1),$$
$$v^b = xv_{\text{P}}\angle -(120° \pm \phi), \qquad v^{bc} = |v^{bc}|\angle -(90° \pm \gamma_2),$$
$$v^c = v_{\text{P}}\angle 120°, \qquad v^{ca} = \sqrt{3}v_{\text{P}}\angle 150°.$$

Furthermore, we consider the situation where we have similarly defined magnitude and angle unbalance in both phases b and c. Due to the complexity of the expressions, we derive the bounds using numerical simulations only.

2.3.5.1 Numerical Comparison

To perform numerical simulations, we assume v^a as the reference voltage phasor at $1\angle 0°$ and calculate the voltage unbalance based to each definition as we vary the deviations in voltage magnitudes (from 0.8 to 1.2 in steps of 0.01) and angles (from $-20°$ to $20°$ in steps of $1°$). The results are illustrated in Fig. 2.6. The left part represents the case with unbalances in phase b only and the right part depicts the case with unbalances in both phases b and c.

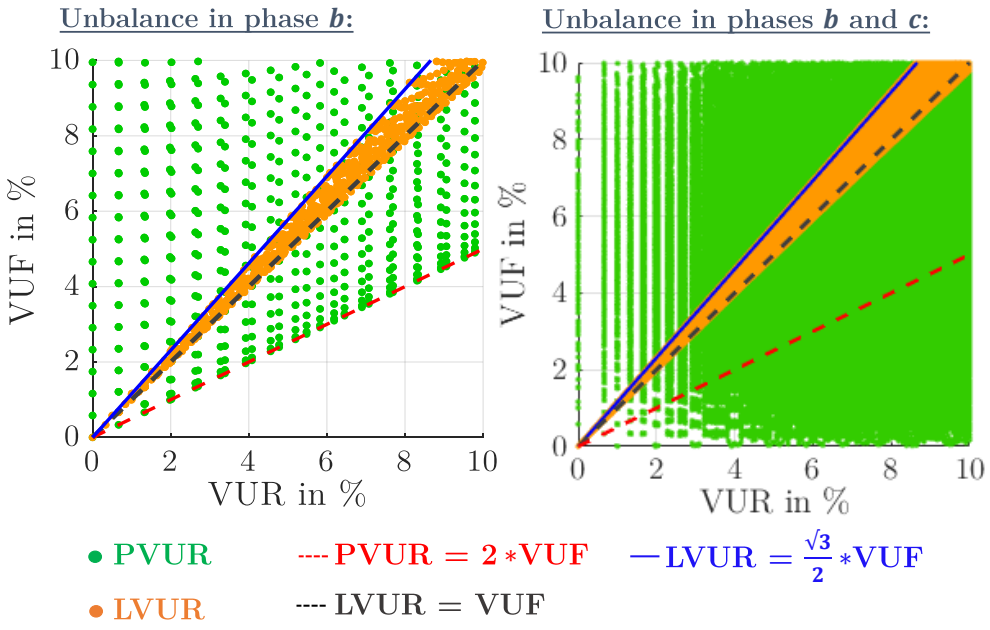

Figure 2.6: Voltage magnitude and angle unbalances for $0.8 \leq x \leq 1.2$ and $-20° \leq \phi \leq 20°$.

As discussed previously, PVUR does not detect voltage angle unbalances. Hence, Fig. 2.6 depicts a large variation of PVUR with reference to any given value of VUF. Interestingly, the relationship between LVUR and VUF is still similar to the previous cases, satisfying the bounds defined in (2.23b) or (2.27). There are some points where VUF $<$ LVUR which correspond to the extreme condition of over-voltage in one phase and under-voltage in other two phases. For the ranges of voltage magnitude deviations $0.8 \leq x_1,\, x_2 \leq 1.2$ and phase angle deviations $-20° \leq \phi_1,\, \phi_2 \leq 20°$ considered in the simulations, we never observe violations larger than 5% relative to the bounds expressed in (2.23b) or (2.27).

2.4 Main Takeaways

In this chapter, we provided a comprehensive analysis of the relationships among the three most commonly used voltage unbalance definitions using both analytical derivations and numerical simulations. The "true" definition of voltage unbalance endorsed by the IEC standard (VUF) is based on symmetrical voltage components. Although VUF captures both voltage magnitude and angle unbalance, it can be challenging to use this definition in practice due to the requirement to measure voltage angles. The other two definitions from NEMA and IEEE based on the phase-to-phase voltages (LVUR) and phase-to-neutral voltages (PVUR), respectively, are frequently used as substitutes to design electrical motors and operate the distribution system with acceptable power quality standards. To summarize:

- PVUR does not provide any information about unbalance due to phase angle asymmetries and hence, there is no clear relationship with VUF.

- LVUR can detect unbalances in both voltage magnitudes and phase angle displacement. Using the small angle approximation, we derived the lower and upper bounds [50] for the IEC definition (VUF) in terms of the NEMA definition (LVUR) as

$$\mathrm{LVUR} \lesssim \mathrm{VUF} \lesssim \left(\frac{2}{\sqrt{3}}\right) \mathrm{LVUR}.$$

For acceptable ranges of voltage magnitude (0.8 to 1.2 p.u.) and angle deviations (-20° to 20°), we observed that the violations of these bounds were below 5%.

Chapter 3

Distribution Grid Modelling

Electric power distribution is a part of the power system infrastructure that acts as an interconnection between the high-voltage, meshed transmission system and customers [63]. The distribution grid typically starts at the substation, where the incoming transmission-level voltage is stepped down to multiple primary circuits by a power transformer. These primary distribution lines are medium-voltage, radial circuits which transfer the power to local distribution transformers closer to each customer [63, 64]. The local distribution transformers further step down the voltage to secondary distribution circuits which are connected to the residential or commercial customers [63, 64].

Distribution feeders typically serve a large number of single-phase loads distributed unevenly among the three phases of the grid which make it inherently unbalanced. In addition, voltage unbalance is also introduced by the asymmetrical spacing between conductors of the three-phase overhead lines and underground cables. Due to this, traditional power-flow methods used for transmission system analysis are inadequate as they assume a perfectly balanced system and exhibit poor numerical convergence for unbalanced radial systems. In order to perform accurate analysis of the distribution feeders, it is imperative to utilize a three-phase model of all the major components. In this chapter, we describe the three-phase models of the major components which have been developed in the ”phase domain” [14]. Recall that the symmetrical component approach is a common way to analyze unbalanced three-phase power systems. In the symmetrical component approach, lines are ideally assumed to be transposed while also serving perfectly balanced loads [65]. Distribution grids typically consist of single-phase, two-phase, and untransposed three-phase lines that serve unbalanced loads [14]. This is one of the major reasons we chose to

model distribution grid components using the phase domain instead of the symmetrical component approach.

3.1 Modelling Framework and Notation

We consider a three-phase distribution grid where a set of three-phase nodes is denoted by $\mathcal{N}_0$. $\Phi = \{a, b, c\}$ represents the set of single-phase connections at each node and the set of phase-to-phase connections is defined by $\Phi_\Delta = \{ab, bc, ca\}$. Generally, we assign a reference node for voltage angle measurement which is also referred to as the slack bus. The distribution substation is typically chosen as the slack node with index $i = 0$. We define the set of three-phase nodes except the slack bus using $\mathcal{N}$ with $n = |\mathcal{N}|$. Distribution grids typically have several single and two-phase nodes. However, to simplify notation, we consider all nodes to have three phases. For the single and two-phase nodes, the corresponding entries for the missing phases are zero. The resulting total number of single-phase connections in the distribution grid is $3(n+1)$. While $\mathcal{G}$ is the set of nodes with generators, $\mathcal{L}_\mathrm{Y}$ and $\mathcal{L}_\Delta$ represent the set of nodes with wye- and delta-connected loads, respectively. The distribution grid parameters such as voltage magnitude, power, and admittance are expressed as per-unit quantities. All scalar values are denoted using small letters, while all vector counterparts and matrices are denoted using capital letters. We represent the element-wise product of two vectors using $\odot$.

The voltage at any node i can be expressed as

$$|V_i| = \begin{bmatrix} |v_i^a| \\ |v_i^b| \\ |v_i^c| \end{bmatrix}, \ \Theta_i = \begin{bmatrix} \theta_i^a \\ \theta_i^b \\ \theta_i^c \end{bmatrix}, \ |V_{\Delta,i}| = \begin{bmatrix} |v_{\Delta,i}^{ab}| \\ |v_{\Delta,i}^{bc}| \\ |v_{\Delta,i}^{ca}| \end{bmatrix}, \tag{3.1}$$

where $|V_i|, \ \theta_i \in \mathbb{R}^3$ represent the phase-to-neutral voltage magnitude and angle vectors, respectively, at every node $i \in \mathcal{N}_0$. In order to model the delta-connected loads, which will be described later in this chapter, we also consider variables for phase-to-phase voltage magnitudes $|V_{\Delta,i}| \in \mathbb{R}^3$ at every node $i \in \mathcal{N}_0$.

3.2 Distribution Lines and Cables

The determination of the impedance for overhead lines and underground cables is critical to analyze a distribution feeder. It is important to consider both the self- and mutual impedance of the conductors for an accurate model of the distribution lines or cables. A π-model is utilized to represent the series impedance along with the shunt admittance of distribution lines and cables [66] as shown in Fig. 3.1. The branch admittance matrix $Y_{ik} \in \mathbb{C}^{3\times3}$ for any three-phase branch between nodes i and k is represented by

$$Y_{ik} = \underbrace{\begin{bmatrix} z_{ik}^{aa} & z_{ik}^{ab} & z_{ik}^{ca} \\ z_{ik}^{ab} & z_{ik}^{bb} & z_{ik}^{bc} \\ z_{ik}^{ca} & z_{ik}^{bc} & z_{ik}^{cc} \end{bmatrix}^{-1}}_{Z_{ik,se}} + \underbrace{j \cdot \frac{1}{2} \begin{bmatrix} b_{ik}^{aa} & 0 & 0 \\ 0 & b_{ik}^{bb} & 0 \\ 0 & 0 & b_{ik}^{cc} \end{bmatrix}}_{Y_{ik,\text{sh}}}. \tag{3.2}$$

The diagonal elements of the series impedance matrix $Z_{ik,se}$ denote the self impedance values in each phase whereas the off-diagonal elements are the mutual impedance which account for inter-phase coupling as shown in Fig. 3.1. The modified Carson's equations can be used to calculate the self- and mutual impedances of the lines and cables [14]. The shunt admittance between the branches represented by $Y_{ik,sh}$ usually comprises of the capacitive susceptance only while conductance is ignored since it is very small [14]. In addition, we also ignore the inter-phase

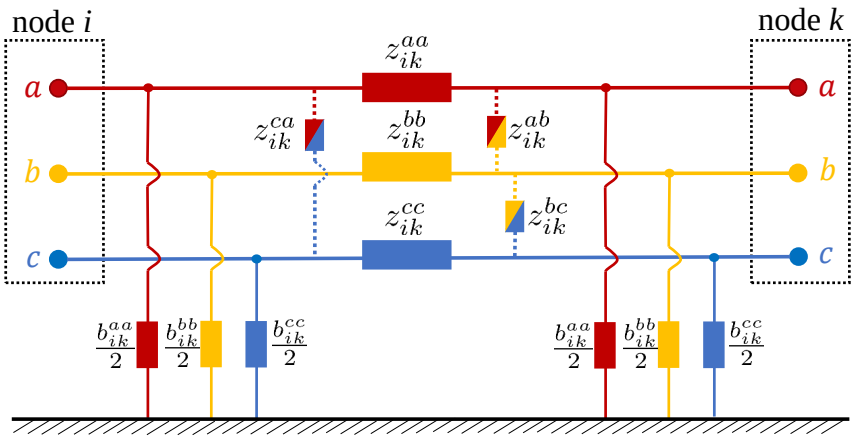

Figure 3.1: π model of a three-phase line segment.

coupling since it is negligible [67]. The principle of superposition can be employed to first calculate the voltage drop between the conductor and ground and then determine the capacitive susceptance between the two points [14].

For a four-wire system with multi-grounded neutral, we get a primitive 4×4 branch admittance matrix that also includes coupling between the neutral and different phases. This primitive 4×4 matrix can be reduced to a 3×3 phase-frame matrix shown in (3.2) using Kron reduction [68]. By employing the modified Carson's equations along with the phase-frame matrix, we get a very accurate model of the distribution lines and cables [14].

3.3 Transformer

Transformers have a significant impact on distribution grids affecting grounding methods, network losses, zero sequence currents as well as protection strategy. Three-phase transformers are typically wound on a common core and therefore, all the windings are coupled to one another [69]. Conventional transformer models used for balanced three-phase systems are no longer suitable for the unbalanced radial distribution feeders. We consider a two-winding, three-phase transformer model [69] with a primitive admittance matrix $Y_{\text{pr}} \in \mathbb{C}^{6\times6}$ expressed as

$$Y_{\text{pr}} = \begin{bmatrix} y_{\text{t}} & 0 & 0 & -y_{\text{t}} & 0 & 0 \\ 0 & y_{\text{t}} & 0 & 0 & -y_{\text{t}} & 0 \\ 0 & 0 & y_{\text{t}} & 0 & 0 & -y_{\text{t}} \\ -y_{\text{t}} & 0 & 0 & y_{\text{t}} & 0 & 0 \\ 0 & -y_{\text{t}} & 0 & 0 & y_{\text{t}} & 0 \\ 0 & 0 & -y_{\text{t}} & 0 & 0 & y_{\text{t}} \end{bmatrix} = \begin{bmatrix} Y_{\text{pp}} & Y_{\text{ps}} \\ Y_{\text{sp}} & Y_{\text{ss}} \end{bmatrix}, \tag{3.3}$$

where y_{t} is the transformer leakage admittance. Y_{pr} can be divided into four 3×3 submatrices where $Y_{\text{pp}}, Y_{\text{ss}} \in \mathbb{C}^{3\times3}$ are the primary and secondary self admittance submatrices, respectively. The mutual admittance submatrices are represented by $Y_{\text{ps}}, Y_{\text{sp}} \in \mathbb{C}^{3\times3}$. We made the following assumptions to represent Y_{pr} in (3.3):

(i) Transformer bank comprises of three single-phase transformers. Hence, all the off-diagonal elements of the $Y_{\text{pp}}, Y_{\text{ss}}, Y_{\text{ps}}, Y_{\text{sp}}$ submatrices are equal to zero. Although this assumption is not required, it simplifies the subsequent derivation.

(ii) The three sets of coils have identical characteristics with the self admittance values for primary and secondary windings as well as the couplings equal to y_{t}. Therefore, all the diagonal elements of $Y_{\text{pp}}, Y_{\text{ss}}, Y_{\text{ps}}, Y_{\text{sp}}$ are equal to $\pm y_{\text{t}}$. This assumption generally holds for realistic feeders since we ensure that the model considers the transformer leakage losses.

Fig. 3.2 illustrates a three-phase transformer connected between nodes i and k. The shunt block models core losses in the transformer. These losses can be considered as voltage-dependent loads connected to node k which will be discussed in detail in the load modelling section. The series block represents the leakage admittance matrix $Y_{\text{T}} \in \mathbb{C}^{6\times 6}$ which can be calculated using (3.3) to get

$$Y_{\text{T}} = C_{\text{tf}}^{\intercal} \cdot Y_{\text{pr}} \cdot C_{\text{tf}} = \begin{bmatrix} Y_{ii} & Y_{ik} \\ Y_{ki} & Y_{kk} \end{bmatrix}, \tag{3.4}$$

where C_{tf} is a connection matrix mapping the voltage difference across windings to the node voltages.

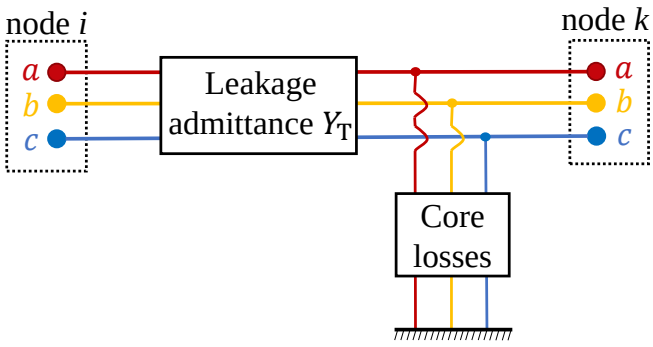

Figure 3.2: Three-phase transformer model represented by a series block and shunt block.

Typically, various transformer connections can be found in distribution grids. Table 3.1 illustrates the submatrices of Y_{T} for different IEC transformer connections [66] where

$$Y_1 = y_{\mathrm{t}} \begin{bmatrix} 1 & 0 & 0 \\ 0 & 1 & 0 \\ 0 & 0 & 1 \end{bmatrix}, \quad Y_2 = \frac{y_{\mathrm{t}}}{3} \begin{bmatrix} 2 & -1 & -1 \\ -1 & 2 & -1 \\ -1 & -1 & 2 \end{bmatrix} \quad \text{and} \quad Y_3 = \frac{y_{\mathrm{t}}}{\sqrt{3}} \begin{bmatrix} -1 & 1 & 0 \\ 0 & -1 & 1 \\ 1 & 0 & -1 \end{bmatrix}. \tag{3.5}$$

Connection		**Submatrices**			
node i	**node** k	Y_{ii}	Y_{kk}	Y_{ik}	Y_{ki}
Wye-G	Wye-G	Y_1	Y_1	-Y_1	-Y_1
Wye	Wye	Y_2	Y_2	-Y_2	-Y_2
Wye-G	Delta	Y_1	Y_2	Y_3	Y_3^{T}
Delta	Wye-G	Y_2	Y_1	Y_3^{T}	Y_3
Delta	Wye	Y_2	Y_2	Y_3^{T}	Y_3
Delta	Delta	Y_2	Y_2	-Y_2	-Y_2

Table 3.1: Admittance submatrices for most common transformer configurations. Delta, Wye and Wye-G represent the delta, ungrounded wye and grounded wye connections, respectively.

3.4 Voltage Regulator

Voltage regulation is a critical function on a distribution feeder. With varying loads connected to the feeders, it is important to maintain voltage magnitude within an acceptable level. Typically, voltage regulators are auto-transformers with adjustable turns ratio t that depend on the tap positions [66, 67, 70]. Standard voltage regulators have 32 tap positions allowing $\pm 10\%$ voltage range

which amounts to a 0.625% change per tap. The position of these taps are generally determined by a control circuit which calculates the voltage drop from the regulator to the target node whose voltage magnitude needs to be controlled. The target node is usually the node to which the output terminal of the regulator is connected or a remote node in the feeder [14].

We model voltage regulators as a special case of the transformer model with Wye-G:Wye-G connection type [67] as seen in Table 3.1, where three single-phase voltage regulators with *constant* tap ratios defined by $t_a,\ t_b,\ t_c$ for each phase are connected between nodes i and k. The regulator admittance matrix Y_{R} is then represented as

$$Y_{\text{R}} = \begin{bmatrix} {t_a}^2 \cdot y_{\text{r}} & 0 & 0 & -t_a \cdot y_{\text{r}} & 0 & 0 \\ 0 & {t_b}^2 \cdot y_{\text{r}} & 0 & 0 & -t_b \cdot y_{\text{r}} & 0 \\ 0 & 0 & {t_c}^2 \cdot y_{\text{r}} & 0 & 0 & -t_c \cdot y_{\text{r}} \\ -t_a \cdot y_{\text{r}} & 0 & 0 & y_{\text{r}} & 0 & 0 \\ 0 & -t_b \cdot y_{\text{r}} & 0 & 0 & y_{\text{r}} & 0 \\ 0 & 0 & -t_c \cdot y_{\text{r}} & 0 & 0 & y_{\text{r}} \end{bmatrix}, \tag{3.6}$$

where y_{r} is the admittance of the regulator connections between nodes i and k.

3.5 Overall System Model

By combining the major component models from (3.2)-(3.6) which include distribution lines, cables, transformers and voltage regulators, the distribution grid with $(3n + 1)$ single-phase connections can be represented using an overall nodal admittance matrix $Y \in \mathbb{C}^{(3n+1)\times(3n+1)}$ defined as

$$\begin{aligned} Y &= G + j \cdot B \\ &= \begin{bmatrix} \sum_{k=1}^{n} Y_{1k} & -Y_{12} & \dots & -Y_{1n} \\ -Y_{21} & \sum_{k=1}^{n} Y_{2k} & \dots & -Y_{2n} \\ \vdots & \vdots & \ddots & \vdots \\ -Y_{n1} & -Y_{n2} & \dots & \sum_{k=1}^{n} Y_{nk} \end{bmatrix}. \end{aligned} \tag{3.7}$$

Here, G and B corresponding to the real and imaginary part of Y are the node conductance and susceptance matrices, respectively.

3.6 Load Modelling

The loads connected to distribution grids show a voltage-dependent behavior. Therefore, we consider a polynomial load (ZIP) model [66] to represent loads as a function of the voltage magnitudes $|V_i|,$ and $|V_{\Delta,i}|$ defined in (3.1). Typically, ZIP loads comprise of a constant power (P) component which is voltage-independent along with the constant current (I) and constant impedance (Z) components which depend on voltage of the node to which the loads are connected. It must be noted here that the load models do not have any effect on the overall node admittance matrix Y discussed in the previous section. We represent complex power phasor s in rectangular form: $s = p + jq$, where p and q denote the active and reactive power components, respectively, with $j = \sqrt{-1}$. We denote the complex conjugate of current phasor i as i^*.

3.6.1 Wye-connected Loads

The active power $p^{\phi}_{\mathrm{L},i}$ and reactive power $q^{\phi}_{\mathrm{L},i}$ drawn by a wye-connected load at phase $\phi \in \Phi$ of node $i \in \mathcal{L}_{\mathrm{Y}}$ can be expressed as

$$p^{\phi}_{\mathrm{LY},i} = p^{\phi}_{\mathrm{PY},i} + p^{\phi}_{\mathrm{IY},i} \cdot |v^{\phi}_i| + p^{\phi}_{\mathrm{ZY},i} \cdot |v^{\phi}_i|^2, \tag{3.8a}$$

$$q^{\phi}_{\mathrm{LY},i} = q^{\phi}_{\mathrm{PY},i} + q^{\phi}_{\mathrm{IY},i} \cdot |v^{\phi}_i| + q^{\phi}_{\mathrm{ZY},i} \cdot |v^{\phi}_i|^2, \tag{3.8b}$$

where $p^{\phi}_{\mathrm{PY},i} + jq^{\phi}_{\mathrm{PY},i}$ is the active and reactive power of the constant power load component; $p^{\phi}_{\mathrm{IY},i} + jq^{\phi}_{\mathrm{IY},i}$ and $p^{\phi}_{\mathrm{ZY},i} + jq^{\phi}_{\mathrm{ZY},i}$ denote the active and reactive power corresponding to the constant current and constant impedance load components. Here, the actual power drawn by both the constant current and constant impedance load components depend on the phase-to-neutral voltage magnitude $|v^{\phi}_i|$. Note that the transformer core losses are also modelled as constant impedance loads using (3.8).

3.6.2 Delta-connected Loads

Similar to the model described for the wye-connected loads, the power drawn by a delta-connected load at phase $\phi_\Delta \in \Phi_\Delta$ of node $i \in \mathcal{L}_\Delta$ can be expressed as

$$p^{\phi_\Delta}_{\mathrm{L}\Delta,i} = p^{\phi_\Delta}_{\mathrm{P}\Delta,i} + p^{\phi_\Delta}_{\mathrm{I}\Delta,i} \cdot |v^{\phi_\Delta}_{\Delta,i}| + p^{\phi_\Delta}_{\mathrm{Z}\Delta,i} \cdot |v^{\phi_\Delta}_{\Delta,i}|^2, \tag{3.9a}$$

$$q^{\phi_\Delta}_{\mathrm{L}\Delta,i} = q^{\phi_\Delta}_{\mathrm{P}\Delta,i} + q^{\phi_\Delta}_{\mathrm{I}\Delta,i} \cdot |v^{\phi_\Delta}_{\Delta,i}| + q^{\phi_\Delta}_{\mathrm{Z}\Delta,i} \cdot |v^{\phi_\Delta}_{\Delta,i}|^2, \tag{3.9b}$$

where $p^{\phi_\Delta}_{\mathrm{P}\Delta,i} + jq^{\phi_\Delta}_{\mathrm{P}\Delta,i}$ is the active and reactive power of the constant power load component; $p^{\phi_\Delta}_{\mathrm{I}\Delta,i} + jq^{\phi_\Delta}_{\mathrm{I}\Delta,i}$ and $p^{\phi_\Delta}_{\mathrm{Z}\Delta,i} + jq^{\phi_\Delta}_{\mathrm{Z}\Delta,i}$ denote the active and reactive power corresponding to the constant current and constant impedance load components. Here, the actual power drawn by both the constant current and constant impedance load components depend on the phase-to-phase voltage magnitude $|v^{\phi_\Delta}_{\Delta,i}|$.

3.6.3 Shunt Capacitors

Shunt capacitor banks are generally utilized in distribution systems to aid in voltage regulation and also provide reactive power support. The capacitor banks are generally modelled as constant susceptance loads. By using (3.8), we can express a wye-connected capacitor at phase $\phi \in \Phi$ of node $i \in \mathcal{L}_\mathrm{Y}$ using

$$q^{\phi}_{\mathrm{Ycap},i} = |v^{\phi}_{i}|^2 \cdot b^{\phi}_{\mathrm{Ycap},i}, \tag{3.10}$$

where $b^{\phi}_{\mathrm{Ycap},i}$ is the constant susceptance of the capacitor. Similarly, we can use (3.9) to express a delta-connected capacitor at phase $\phi_\Delta \in \Phi_\Delta$ of node $i \in \mathcal{L}_\Delta$ with constant susceptance $b^{\phi_\Delta}_{\Delta\mathrm{cap},i}$ using

$$q^{\phi_\Delta}_{\Delta\mathrm{cap},i} = |v^{\phi_\Delta}_{\Delta,i}|^2 \cdot b^{\phi_\Delta}_{\Delta\ \mathrm{cap},i}. \tag{3.11}$$

3.7 Summary

This chapter developed models for major components of the distribution grid in the phase domain including generalized matrices for distribution lines and cables, transformers as well as

voltage regulators. One of the major features has been the implementation of a node admittance matrix that combines all the generalized matrices to model the overall network. Load models which include a combination of constant power, constant impedance, and constant current loads were developed to depict the commonly found loads in distribution grids.

Chapter 4

Three-phase Optimal Power Flow

The optimal power flow model is a well-established approach to determine the most suitable operating conditions in a balanced transmission network, typically with the objective to minimize operating cost. It is also an important tool used to improve power quality in distribution grid by coordinating various DERs and ensuring consumer voltages are within specified limits. In this chapter, we formulate the three-phase OPF problem to minimize voltage unbalance using reactive power support from the solar PV inverters.

4.1 Literature Review: Existing Methods to Mitigate Voltage Unbalance

Traditional methods to mitigate voltage unbalance include equalizing DER connections or residential load consumption between phases, which is usually done at most few times a year [5]. Furthermore, switching devices such as transformer online tap changer, voltage regulators and capacitors can be used to balance the grid. However, frequent switching of these equipment can cause failures and increase maintenance costs [71]. Other methods include installation of power electronic-based static synchronous compensators [72], which might be costly.

Inverter-based reactive power control has previously been proposed as a promising solution to mitigate unbalance due to lower investment cost and better transient performance compared to the traditional methods [73]. Solar PV inverters usually do not operate at their maximum apparent power rating throughout the day which means the additional available capacity could be utilized to absorb or inject reactive power to the grid. There are papers in the existing literature which

propose a centralized three-phase OPF approach minimizing voltage unbalance in distribution systems using solar PV inverters. In [74], an optimization problem is solved with only active power of inverters as controllable variables while reactive power is ignored. Strategies based on three-phase OPF formulation which include reactive power support are discussed in [73, 75, 76], but they use only the IEC voltage unbalance definition either as constraints or objective function in the problem formulation. The IEEE definition is used in [77] to mitigate unbalance in distribution systems with large number of solar PV systems.

Alternatively, distributed/decentralized methods have been proposed to reduce the sensing and communications effort while minimizing voltage unbalance. For example, [78] proposed an algorithm to distribute the centralized three-phase OPF problem into three single-phase sub-problems. In [77], a decentralized approach is suggested using only voltage magnitude to measure unbalance. [79] proposed a feedback control scheme that employs the Steinmetz circuit design to calculate reactive power injections of inverters using local measurements only. While these methods are computationally faster, they provide sub-optimal performance compared to the centralized three-phase OPF approach and cannot guarantee that all engineering constraints are satisfied.

Some works in the existing literature focus on integrating different approaches for distribution grids. Hierarchical control strategies which integrate centralized and distributed approaches for voltage regulation have been proposed in [20, 80, 81, 82]. However, these strategies also assume that the distribution grid is balanced or nearly balanced, making them unsuitable for mitigating voltage unbalance.

4.2 Main Contributions

In this chapter, we formulate the three-phase OPF problem to minimize voltage unbalance using reactive power support from the solar PV inverters. The OPF formulation is flexible enough to represent the various voltage unbalance definitions discussed in Chapter 2 as objective functions or constraints. For our analysis, we test the approach on two unbalanced low-voltage distribution feeders and provide an in-depth comparison of the results obtained by minimizing various voltage

unbalance definitions. Furthermore, we also evaluate the performance using critical power quality metrics such as network losses and substation power factor.

4.3 Three-phase OPF Constraints

The models for all the major components of the distribution grid have been discussed in the previous chapter. We can utilize these models to formulate various operational and physical constraints that need to be considered in order to solve the three-phase OPF problem. The three-phase OPF problem in this chapter is formulated in the polar coordinate frame. All optimization variables are denoted using **bold** symbols. Recall that all scalar values are denoted using small letters, whereas all vector counterparts and matrices are denoted using capital letters.

4.3.1 Voltage Limits

The distribution substation is assumed to be a perfectly balanced three-phase node and chosen as a reference for the measurement of voltage angles. For the substation node with index $i = 0$, the voltage is fixed at

$$|\boldsymbol{V}_0|\angle\boldsymbol{\Theta}_0 = \begin{bmatrix} 1\angle 0^\circ & 1\angle -120^\circ & 1\angle 120^\circ \end{bmatrix}^\top. \tag{4.1}$$

For any other node $i \in \mathcal{N}$ connected to phase $\phi \in \Phi$, the voltage magnitude limits can be enforced by

$$\underline{v} \leq |\boldsymbol{v}_i^\phi| \leq \overline{v}, \tag{4.2}$$

where $\underline{v}$ and $\overline{v}$ are the lower and upper voltage magnitude limits, respectively. The phase-to-phase voltage magnitude $|\boldsymbol{v}_{\Delta,i}^{\phi_\Delta}|\ \forall i \in \mathcal{N}_0,\ \phi_\Delta \in \Phi_\Delta$ is defined in terms of phase-to-neutral voltage magnitude and angle as

$$|\boldsymbol{v}_{\Delta,i}^{\phi_\Delta}|^2 = |\boldsymbol{v}_i^{\phi_1}|^2 + |\boldsymbol{v}_i^{\phi_2}|^2 - 2|\boldsymbol{v}_i^{\phi_1}||\boldsymbol{v}_i^{\phi_2}| \cdot \cos\left(\boldsymbol{\theta}_i^{\phi_1} - \boldsymbol{\theta}_i^{\phi_2}\right), \tag{4.3}$$

where $\phi_1, \phi_2 \in \Phi$ and $\phi_1 \neq \phi_2$.

4.3.2 Solar PV Inverter Limits

The primary source of flexibility in the distribution system are the solar PV inverters. We have modelled some traditional flexibility sources such as voltage regulators with tap control and capacitors with on-off control in our framework as discussed in Appendix A, but we do not consider them for any of the numerical simulations in this thesis. For a single-phase PV inverter connected to phase $\phi \in \Phi$ at node $i \in \mathcal{G}$ with maximum apparent power $|s^{\phi}_{\mathrm{G},i}|$, the controllable variable is the reactive power injection $\boldsymbol{q}^{\phi}_{\mathbf{G},i}$ and the active power output $\boldsymbol{p}^{\phi}_{\mathbf{G},i}$ is set to a constant value $p^{\phi}_{\mathrm{G},i}$ since we do not consider active power curtailment. We can express the reactive power limit of the PV inverter as $\overline{q}^{\phi}_{\mathrm{G},i} = \sqrt{|s^{\phi}_{\mathrm{G},i}|^2 - \left(p^{\phi}_{\mathrm{G},i}\right)^2}$ and constrain the inverter reactive power using

$$-\overline{q}^{\phi}_{\mathrm{G},i} \leq \boldsymbol{q}^{\phi}_{\mathbf{G},i} \leq \overline{q}^{\phi}_{\mathrm{G},i}. \tag{4.4}$$

4.3.3 Power Balance

Conservation of power must be satisfied at each node $i \in \mathcal{N}_0$ in the distribution grid. By representing the element-wise product using $\odot$, the power balance equations are expressed in terms $\boldsymbol{P}_i, \boldsymbol{Q}_i$ which denote the active and reactive power injection at node i using

$$\boldsymbol{P}_i = \boldsymbol{P}_{\mathbf{G},i} - \boldsymbol{P}_{\mathbf{L},i} = |\boldsymbol{V}_i| \odot \sum_{k \in \mathcal{N}_0} \Big[G_{ik} \odot \mathrm{C}\Big(\boldsymbol{\Theta}_{ik}\Big) + B_{ik} \odot \mathrm{S}\Big(\boldsymbol{\Theta}_{ik}\Big) \Big] \cdot |\boldsymbol{V}_k|, \tag{4.5a}$$

$$\boldsymbol{Q}_i = \boldsymbol{Q}_{\mathbf{G},i} - \boldsymbol{Q}_{\mathbf{L},i} = |\boldsymbol{V}_i| \odot \sum_{k \in \mathcal{N}_0} \Big[G_{ik} \odot \mathrm{S}\Big(\boldsymbol{\Theta}_{ik}\Big) - B_{ik} \odot \mathrm{C}\Big(\boldsymbol{\Theta}_{ik}\Big) \Big] \cdot |\boldsymbol{V}_k|, \tag{4.5b}$$

where $\boldsymbol{P}_{\mathbf{G},i}$, $\boldsymbol{Q}_{\mathbf{G},i} \in \mathbb{R}^3$ denote the active and reactive components of the substation and solar PV inverters at node i; $\boldsymbol{P}_{\mathbf{L},i}$, $\boldsymbol{Q}_{\mathbf{L},i} \in \mathbb{R}^3$ represent the active and reactive components of the load demand; $G_{ik},\ B_{ik} \in \mathbb{R}^{3\times 3}$ are the conductance and susceptance submatrices as defined in (3.7).

For a branch connecting three-phase nodes i and k, we define $\mathrm{C}\Big(\boldsymbol{\Theta}_{ik}\Big),\ \mathrm{S}\Big(\boldsymbol{\Theta}_{ik}\Big) \in \mathbb{R}^{3\times 3}$ as

$$\mathrm{C}\Big(\boldsymbol{\Theta}_{ik}\Big) = \begin{bmatrix} \cos(\boldsymbol{\theta}_i^a - \boldsymbol{\theta}_k^a) & \cos(\boldsymbol{\theta}_i^a - \boldsymbol{\theta}_k^b) & \cos(\boldsymbol{\theta}_i^a - \boldsymbol{\theta}_k^c) \\ \cos(\boldsymbol{\theta}_i^b - \boldsymbol{\theta}_k^a) & \cos(\boldsymbol{\theta}_i^b - \boldsymbol{\theta}_k^b) & \cos(\boldsymbol{\theta}_i^b - \boldsymbol{\theta}_k^c) \\ \cos(\boldsymbol{\theta}_i^c - \boldsymbol{\theta}_k^a) & \cos(\boldsymbol{\theta}_i^c - \boldsymbol{\theta}_k^b) & \cos(\boldsymbol{\theta}_i^c - \boldsymbol{\theta}_k^c) \end{bmatrix}, \tag{4.6a}$$

$$\mathrm{S}\Big(\boldsymbol{\Theta}_{ik}\Big) = \begin{bmatrix} \sin(\boldsymbol{\theta}_i^a - \boldsymbol{\theta}_k^a) & \sin(\boldsymbol{\theta}_i^a - \boldsymbol{\theta}_k^b) & \sin(\boldsymbol{\theta}_i^a - \boldsymbol{\theta}_k^c) \\ \sin(\boldsymbol{\theta}_i^b - \boldsymbol{\theta}_k^a) & \sin(\boldsymbol{\theta}_i^b - \boldsymbol{\theta}_k^b) & \sin(\boldsymbol{\theta}_i^b - \boldsymbol{\theta}_k^c) \\ \sin(\boldsymbol{\theta}_i^c - \boldsymbol{\theta}_k^a) & \sin(\boldsymbol{\theta}_i^c - \boldsymbol{\theta}_k^b) & \sin(\boldsymbol{\theta}_i^c - \boldsymbol{\theta}_k^c) \end{bmatrix}. \tag{4.6b}$$

4.3.3.1 Delta to Wye Conversion of Loads

It is important to note that $\boldsymbol{P}_{\mathbf{L},i}$, $\boldsymbol{Q}_{\mathbf{L},i}$ in (4.5) represent power drawn by wye-connected loads. So, we need to convert the delta-connected loads defined in (3.9) to equivalent wye-connected loads before we can use them in our power balance equations. In order to do this, we first introduce rectangular components of phase-to-phase currents $\boldsymbol{i}_{\Delta\mathbf{d},i}^{\phi_\Delta},\ \boldsymbol{i}_{\Delta\mathbf{q},i}^{\phi_\Delta}\ \forall i \in \mathcal{L}_\Delta, \phi_\Delta \in \Phi_\Delta$ at the delta-connected loads as new variables in the formulation. The complex load power can be represented using

$$p_{\mathrm{L}\Delta,i}^{\phi_\Delta} + j \cdot q_{\mathrm{L}\Delta,i}^{\phi_\Delta} = v_{\Delta,i}^{\phi_\Delta} \cdot {i_{\Delta,i}^{\phi_\Delta}}^* = \Big(v_i^{\phi_1} - v_i^{\phi_2}\Big) \cdot \Big(\boldsymbol{i}_{\Delta\mathbf{d},i}^{\phi_\Delta} - j \cdot \boldsymbol{i}_{\Delta\mathbf{q},i}^{\phi_\Delta}\Big). \tag{4.7}$$

where $\phi_1, \phi_2 \in \phi$ and $\phi_1 \neq \phi_2$. The active power $p_{\mathrm{L}\Delta,i}^{\phi_\Delta}$ and reactive power $q_{\mathrm{L}\Delta,i}^{\phi_\Delta}$ drawn by the load are already functions of our optimization variables $|\boldsymbol{v}_{\Delta,i}^{\phi_\Delta}|$ as defined in (3.9). By separating the real and imaginary terms in (4.7), the equality constraints on the active power $p_{\mathrm{L}\Delta,i}^{\phi_\Delta}$ and reactive power $q_{\mathrm{L}\Delta,i}^{\phi_\Delta}$ drawn by the load can then be expressed as

$$p_{\mathrm{L}\Delta,i}^{\phi_\Delta} = \Big(|\boldsymbol{v}_i^{\phi_1}|\cos(\boldsymbol{\theta}_i^{\phi_1}) - |\boldsymbol{v}_i^{\phi_2}|\cos(\boldsymbol{\theta}_i^{\phi_2})\Big) \cdot \boldsymbol{i}_{\Delta\mathbf{d},i}^{\phi_\Delta} + \Big(|\boldsymbol{v}_i^{\phi_1}|\sin(\boldsymbol{\theta}_i^{\phi_1}) - |\boldsymbol{v}_i^{\phi_2}|\sin(\boldsymbol{\theta}_i^{\phi_2})\Big) \cdot \boldsymbol{i}_{\Delta\mathbf{q},i}^{\phi_\Delta},$$
$$q_{\mathrm{L}\Delta,i}^{\phi_\Delta} = -\Big(|\boldsymbol{v}_i^{\phi_1}|\cos(\boldsymbol{\theta}_i^{\phi_1}) - |\boldsymbol{v}_i^{\phi_2}|\cos(\boldsymbol{\theta}_i^{\phi_2})\Big) \cdot \boldsymbol{i}_{\Delta\mathbf{q},i}^{\phi_\Delta} + \Big(|\boldsymbol{v}_i^{\phi_1}|\sin(\boldsymbol{\theta}_i^{\phi_1}) - |\boldsymbol{v}_i^{\phi_2}|\sin(\boldsymbol{\theta}_i^{\phi_2})\Big) \cdot \boldsymbol{i}_{\Delta\mathbf{d},i}^{\phi_\Delta}.$$

By substituting the active and reactive power expressions for the load power derived in (3.9), we now have equality constraints for the delta-connected loads in terms of all our optimization variables $|\boldsymbol{v}_i^{\phi}|, \boldsymbol{\theta}_i^{\phi}, |\boldsymbol{v}_{\Delta,i}^{\phi_\Delta}|, \boldsymbol{i}_{\Delta\mathbf{d},i}^{\phi_\Delta}, \boldsymbol{i}_{\Delta\mathbf{q},i}^{\phi_\Delta}$.

We still need determine the per-phase power injections of the delta-connected loads so that we can use them in the power balance equations defined in (4.5). So, we next calculate the phase-to-neutral current drawn by the delta-connected loads. In order to do this, we apply Kirchhoff's current law and derive expressions for the phase-to-neutral current phasor I_i using the phase-to-phase current variables $\boldsymbol{I}^{\phi_\Delta}_{\Delta\mathbf{d},i}$, $\boldsymbol{I}^{\phi_\Delta}_{\Delta\mathbf{q},i}$ and transformation matrix Γ given by

$$I_i = \begin{bmatrix} i_i^a \\ i_i^b \\ i_i^c \end{bmatrix} = \underbrace{\begin{bmatrix} 1 & 0 & -1 \\ -1 & 1 & 0 \\ 0 & -1 & 1 \end{bmatrix}}_{\Gamma} \cdot \begin{bmatrix} \boldsymbol{i}^{ab}_{\Delta\mathbf{d},i} + j \cdot \boldsymbol{i}^{ab}_{\Delta\mathbf{q},i} \\ \boldsymbol{i}^{bc}_{\Delta\mathbf{d},i} + j \cdot \boldsymbol{i}^{bc}_{\Delta\mathbf{q},i} \\ \boldsymbol{i}^{ca}_{\Delta\mathbf{d},i} + j \cdot \boldsymbol{i}^{ca}_{\Delta\mathbf{q},i} \end{bmatrix}. \tag{4.9}$$

The final step is to derive the per-phase power drawn by the delta-connected load in terms of the optimization variables $|\boldsymbol{v}_i^\phi|, \boldsymbol{\theta}_i^\phi$. For phase a, we get

$$s^a_{\Delta\mathrm{Y},i} = v_i^a \cdot i_i^{a*} = |\boldsymbol{v}_i^a|\Big(\cos(\boldsymbol{\theta}_i^a) + j \cdot \sin(\boldsymbol{\theta}_i^a)\Big) \cdot \Big(i^a_{\mathrm{d}i} - j \cdot i^a_{\mathrm{q}i}\Big), \tag{4.10}$$

where $i^a_{\mathrm{d}i}, i^a_{\mathrm{q}i}$ are the real and imaginary components of the phase a-to-neutral current phasor i_i^a, respectively. By substituting (4.9) in (4.10), the active power $p^a_{\Delta\mathrm{Y},i}$ and reactive power $q^a_{\Delta\mathrm{Y},i}$ drawn by the delta-connected load at phase a can be expressed in terms of our optimization variables as

$$p^a_{\Delta\mathrm{Y},i} = |\boldsymbol{v}_i|^a \cos(\boldsymbol{\theta}_i^a) \cdot \Big(\boldsymbol{i}^{ab}_{\Delta\mathbf{d},i} - \boldsymbol{i}^{ca}_{\Delta\mathbf{d},i}\Big) + |\boldsymbol{v}_i|^a \sin(\boldsymbol{\theta}_i^a) \cdot \Big(\boldsymbol{i}^{ab}_{\Delta\mathbf{q},i} - \boldsymbol{i}^{ca}_{\Delta\mathbf{q},i}\Big), \tag{4.11a}$$

$$q^a_{\Delta\mathrm{Y},i} = -|\boldsymbol{v}_i|^a \cos(\boldsymbol{\theta}_i^a) \cdot \Big(\boldsymbol{i}^{ab}_{\Delta\mathbf{q},i} - \boldsymbol{i}^{ca}_{\Delta\mathbf{q},i}\Big) + |\boldsymbol{v}_i|^a \sin(\boldsymbol{\theta}_i^a) \cdot \Big(\boldsymbol{i}^{ab}_{\Delta\mathbf{d},i} - \boldsymbol{i}^{ca}_{\Delta\mathbf{d},i}\Big). \tag{4.11b}$$

The active and reactive power drawn by the delta-connected load at phases b and c can be derived using analogous expressions by following the same procedure defined in (4.9)-(4.11). Now, we can directly use (4.11) in (4.5) to represent power drawn by the delta-connected loads.

4.4 Voltage Unbalance

This section describes the formulation of different voltage unbalance metrics explained in Chapter 2 both as constraints and objective function.

4.4.1 Voltage Unbalance Factor (VUF)

Recall that $\mathrm{a} = 1\angle 120$ is used to calculate the symmetrical components defined in (2.1). The symmetrical components for critical node $i \in \mathcal{N}$ can be calculated as

$$
\begin{aligned}
&3 \cdot v_i^- = v_i^a + \mathrm{a}^2 \cdot v_i^b + \mathrm{a} \cdot v_i^c \\
&3 \cdot (\boldsymbol{v}_{\mathbf{d}i}^- + j \cdot \boldsymbol{v}_{\mathbf{q}i}^-) = |\boldsymbol{v}_i^a| \angle \boldsymbol{\theta}_i^a + |\boldsymbol{v}_i^b| \angle (\boldsymbol{\theta}_i^b - 120^\circ) + |\boldsymbol{v}_i^c| \angle (\boldsymbol{\theta}_i^c + 120^\circ) \\
&3 \cdot \begin{bmatrix} \boldsymbol{v}_{\mathbf{d}i}^- \\ \boldsymbol{v}_{\mathbf{q}i}^- \end{bmatrix} = \begin{bmatrix} \cos(\boldsymbol{\theta}_i^a) & \cos(\boldsymbol{\theta}_i^b - 120^\circ) & \cos(\boldsymbol{\theta}_i^c + 120^\circ) \\ \sin(\boldsymbol{\theta}_i^a) & \sin(\boldsymbol{\theta}_i^b - 120^\circ) & \sin(\boldsymbol{\theta}_i^c + 120^\circ) \end{bmatrix} \begin{bmatrix} |\boldsymbol{v}_i^a| \\ |\boldsymbol{v}_i^b| \\ |\boldsymbol{v}_i^c| \end{bmatrix}, \qquad (4.12a) \\
&3 \cdot v_i^+ = v_i^a + \mathrm{a} \cdot v_i^b + \mathrm{a}^2 \cdot v_i^c \\
&3 \cdot (\boldsymbol{v}_{\mathbf{d}i}^+ + j \cdot \boldsymbol{v}_{\mathbf{q}i}^+) = |\boldsymbol{v}_i^a| \angle \boldsymbol{\theta}_i^a + |\boldsymbol{v}_i^b| \angle (\boldsymbol{\theta}_i^b + 120^\circ) + |\boldsymbol{v}_i^c| \angle (\boldsymbol{\theta}_i^c - 120^\circ) \\
&3 \cdot \begin{bmatrix} \boldsymbol{v}_{\mathbf{d}i}^+ \\ \boldsymbol{v}_{\mathbf{q}i}^+ \end{bmatrix} = \begin{bmatrix} \cos(\boldsymbol{\theta}_i^a) & \cos(\boldsymbol{\theta}_i^b + 120^\circ) & \cos(\boldsymbol{\theta}_i^c - 120^\circ) \\ \sin(\boldsymbol{\theta}_i^a) & \sin(\boldsymbol{\theta}_i^b + 120^\circ) & \sin(\boldsymbol{\theta}_i^c - 120^\circ) \end{bmatrix} \begin{bmatrix} |\boldsymbol{v}_i^a| \\ |\boldsymbol{v}_i^b| \\ |\boldsymbol{v}_i^c| \end{bmatrix}, \qquad (4.12b)
\end{aligned}
$$

where $v_i^- = \boldsymbol{v}_{\mathbf{d}i}^- + j\boldsymbol{v}_{\mathbf{q}i}^-$ and $v_i^+ = \boldsymbol{v}_{\mathbf{d}i}^+ + j\boldsymbol{v}_{\mathbf{q}i}^+$ are the rectangular form representation of the negative and positive sequence voltage phasors, By using (4.12), we can express VUF at critical node i as a function of our optimization variables as

$$
\mathrm{VUF}_i = \frac{|v_i^-|}{|v_i^+|} = \sqrt{\frac{\left(\boldsymbol{v}_{\mathbf{d}i}^-\right)^2 + \left(\boldsymbol{v}_{\mathbf{q}i}^-\right)^2}{\left(\boldsymbol{v}_{\mathbf{d}i}^+\right)^2 + \left(\boldsymbol{v}_{\mathbf{q}i}^+\right)^2}}. \qquad (4.13)
$$

It is important to note here that the expression for VUF is non-convex. In order to avoid square root in the objective function, we minimize VUF by minimizing the sum of the squared VUF components across all three-phase nodes, i.e.,

$$
\min \sum_{i \in \mathcal{N}} {\mathrm{VUF}_i}^2 = \min \sum_{i \in \mathcal{N}} \frac{\left(\boldsymbol{v}_{\mathbf{d}i}^-\right)^2 + \left(\boldsymbol{v}_{\mathbf{q}i}^-\right)^2}{\left(\boldsymbol{v}_{\mathbf{d}i}^+\right)^2 + \left(\boldsymbol{v}_{\mathbf{q}i}^+\right)^2}. \qquad (4.14)
$$

We can impose constraints on the VUF at the three-phase node i by enforcing an upper bound u_{VUF}. By squaring both sides of (4.13) and rearranging terms, we get

$$\left(\boldsymbol{v}_{\mathbf{d}i}^{-}\right)^2 + \left(\boldsymbol{v}_{\mathbf{q}i}^{-}\right)^2 \leq u_{\mathrm{VUF}}^2 \cdot \left(\left(\boldsymbol{v}_{\mathbf{d}i}^{+}\right)^2 + \left(\boldsymbol{v}_{\mathbf{q}i}^{+}\right)^2\right). \tag{4.15}$$

4.4.2 Phase Voltage Unbalance Rate (PVUR)

To express PVUR at critical three-phase node $i \in \mathcal{N}$ in terms of the phase-to-neutral voltage magnitude $|\boldsymbol{V}_i|$, we first define the absolute value of voltage deviation. This can be done by including additional variables $\boldsymbol{z}_{\mathbf{P},i}^{\phi}$ at every single-phase connection, which denote the absolute voltage magnitude deviation in each phase. This leads to the following set of constraints,

$$\boldsymbol{z}_{\mathbf{P},i}^{a} \geq |\boldsymbol{v}_i^a| - v_{\mathrm{P},i}^{\mathrm{avg}},\ \boldsymbol{z}_{\mathbf{P},i}^{a} \geq -(|\boldsymbol{v}_i^a| - v_{\mathrm{P},i}^{\mathrm{avg}}), \tag{4.16a}$$

$$\boldsymbol{z}_{\mathbf{P},i}^{a} \geq |\boldsymbol{v}_i^b| - v_{\mathrm{P},i}^{\mathrm{avg}},\ \boldsymbol{z}_{\mathbf{P},i}^{b} \geq -(|\boldsymbol{v}_i^b| - v_{\mathrm{P},i}^{\mathrm{avg}}), \tag{4.16b}$$

$$\boldsymbol{z}_{\mathbf{P},i}^{c} \geq |\boldsymbol{v}_i^c| - v_{\mathrm{P},i}^{\mathrm{avg}},\ \boldsymbol{z}_{\mathbf{P},i}^{c} \geq -(|\boldsymbol{v}_i^c| - v_{\mathrm{P},i}^{\mathrm{avg}}), \tag{4.16c}$$

where $v_{\mathrm{P},i}^{\mathrm{avg}} = \frac{1}{3}(|\boldsymbol{v}_i^a| + |\boldsymbol{v}_i^b| + |\boldsymbol{v}_i^c|)$ is the average phase-to-neutral voltage magnitude as defined in (2.2). Next, we define a variable $\boldsymbol{z}_{\mathbf{P},i}$ for each node in the distribution grid. It represents the maximum relative voltage deviation across the three phases,

$$\boldsymbol{z}_{\mathbf{P},i} \geq \frac{\boldsymbol{z}_{\mathbf{P},i}^{a}}{v_{\mathrm{P},i}^{\mathrm{avg}}},\ \boldsymbol{z}_{\mathbf{P},i} \geq \frac{\boldsymbol{z}_{\mathbf{P},i}^{b}}{v_{\mathrm{P},i}^{\mathrm{avg}}} \text{ and } \boldsymbol{z}_{\mathbf{P},i} \geq \frac{\boldsymbol{z}_{\mathbf{P},i}^{c}}{v_{\mathrm{P},i}^{\mathrm{avg}}}. \tag{4.17}$$

We minimize PVUR by minimizing the sum of $\boldsymbol{z}_{\mathbf{P},i}$ across all three-phase nodes, i.e.,

$$\min \sum_{i \in \mathcal{N}} \boldsymbol{z}_{\mathbf{P},i}. \tag{4.18}$$

By defining u_{PVUR} as the specified PVUR limit, we can enforce PVUR as constraints using

$$\boldsymbol{z}_{\mathbf{P},i} \leq u_{\mathrm{PVUR}}. \tag{4.19}$$

4.4.3 Line Voltage Unbalance Rate (LVUR)

We employ a similar strategy as for PVUR to express LVUR in terms of the phase-to-phase voltage magnitude $|\boldsymbol{V}_{\Delta,i}|$. We define additional variables $\boldsymbol{z}_{\mathbf{L},i}^{\phi}$ and $\boldsymbol{z}_{\mathbf{L},i}$ for any three-phase node $i \in$

$\mathcal{N}$. This allows us to express LVUR at critical three-phase node i using following set of constraints,

$$\boldsymbol{z}^{a}_{\mathbf{L},i} \geq |\boldsymbol{v}^{ab}_{\Delta,i}| - v^{\text{avg}}_{\text{L},i},\ \boldsymbol{z}^{a}_{\mathbf{L},i} \geq -(|\boldsymbol{v}^{ab}_{\Delta,i}| - v^{\text{avg}}_{\text{L},i}), \tag{4.20a}$$

$$\boldsymbol{z}^{b}_{\mathbf{L},i} \geq |\boldsymbol{v}^{bc}_{\Delta,i}| - v^{\text{avg}}_{\text{L},i},\ \boldsymbol{z}^{b}_{\mathbf{L},i} \geq -(|\boldsymbol{v}^{bc}_{\Delta,i}| - v^{\text{avg}}_{\text{L},i}), \tag{4.20b}$$

$$\boldsymbol{z}^{c}_{\mathbf{L},i} \geq |\boldsymbol{v}^{ca}_{\Delta,i}| - v^{\text{avg}}_{\text{L},i},\ \boldsymbol{z}^{c}_{\mathbf{L},i} \geq -(|\boldsymbol{v}^{ca}_{\Delta,i}| - v^{\text{avg}}_{\text{L},i}), \tag{4.20c}$$

$$\boldsymbol{z}_{\mathbf{L},i} \geq \frac{\boldsymbol{z}^{a}_{\mathbf{L},i}}{v^{\text{avg}}_{\text{L},i}},\ \boldsymbol{z}_{\mathbf{L},i} \geq \frac{\boldsymbol{z}^{b}_{\mathbf{L},i}}{v^{\text{avg}}_{\text{L},i}} \text{ and } \boldsymbol{z}_{\mathbf{L},i} \geq \frac{\boldsymbol{z}^{c}_{\mathbf{L},i}}{v^{\text{avg}}_{\text{L},i}}, \tag{4.20d}$$

where $v^{\text{avg}}_{\text{L},i} = \frac{1}{3}(|\boldsymbol{v}^{ab}_{\Delta,i}| + |\boldsymbol{v}^{bc}_{\Delta,i}| + |\boldsymbol{v}^{ca}_{\Delta,i}|)$ is the average phase-to-phase voltage magnitude as defined in (2.4). We minimize LVUR by minimizing the sum of $\boldsymbol{z}_{\mathbf{L},i}$ across all three-phase nodes,

$$\min \sum_{i \in \mathcal{N}} \boldsymbol{z}_{\mathbf{L},i}. \tag{4.21}$$

LVUR constraints with maximum specified limit u_{LVUR} are expressed as

$$\boldsymbol{z}_{\mathbf{L},i} \leq u_{\text{LVUR}}. \tag{4.22}$$

4.5 Other Power Quality Metrics

There are other important metrics apart from voltage unbalance that a distribution system operator (DSO) must manage to operate the network efficiently.

4.5.1 Network Losses

A critical objective for DSOs is to operate the grid efficiently with minimal losses since they are a major driver for the electricity distribution cost. The network losses can be calculated as

$$p_{\text{loss}} = \sum_{i \in \mathcal{N}} \left(\boldsymbol{P}_{\mathbf{G},i} - \boldsymbol{P}_{\mathbf{L},i} \right), \tag{4.23}$$

where $\boldsymbol{P}_{\mathbf{G},i}$ and $\boldsymbol{P}_{\mathbf{L},i}$ have already been defined in (4.5) and denote the active power components of the generation and load demand at node i, respectively.

4.5.2 Power Factor

Another critical objective for the DSO is to ensure that a high power factor is maintained at the point of interconnection to the transmission system. This avoids the additional cost of acquiring the higher apparent power [83] from transmission system operators. In addition to this, it also avoids increase in investment costs due to the additional infrastructure required to distribute the excess apparent power [83]. Furthermore, higher power factor leads to lower currents flowing in the distribution network which decreases losses. The power factor at the substation node is measured as the ratio of real to apparent power given by

$$\cos\ \phi_{\text{ss}} = \frac{p^a_{\text{G},0} + p^b_{\text{G},0} + p^c_{\text{G},0}}{|s^a_{\text{G},0}| + |s^b_{\text{G},0}| + |s^c_{\text{G},0}|}, \tag{4.24}$$

where $p^a_{\text{G},0},\ p^b_{\text{G},0},\ p^c_{\text{G},0}$ and $|s^a_{\text{G},0}|,\ |s^b_{\text{G},0}|,\ |s^c_{\text{G},0}|$ are the per-phase active and apparent power generation at the substation, respectively. It is important to note that we consider power factor only for evaluation purposes and do not include it in the three-OPF formulation.

4.6 Problem Formulations

In this section, we describe the various three-phase OPF problem formulations representing typical optimization problems that might be of interest to DSOs.

4.6.1 Minimize Losses

Our first problem minimizes network losses without considering voltage unbalance. The problem formulation can be summarized as

$$\begin{aligned} &\min && \text{Network Losses : (4.23)} && \text{(P1-Loss)} \\ &\text{s.t.} && \text{System Constraints : (4.1)} - \text{(4.11)}. \end{aligned}$$

4.6.2 Minimize Voltage Unbalance

Our next problem formulations minimize voltage unbalance based on the three voltage unbalance definitions. In order to minimize VUF, we solve

$$\begin{aligned} &\min && \text{VUF}^2 : \ (4.12) - (4.14) && \text{(P2-VUF)} \\ &\text{s.t.} && \text{System Constraints} : \ (4.1) - (4.11). \end{aligned}$$

The PVUR minimization is defined by

$$\begin{aligned} &\min && \text{PVUR} : \ (4.18) && \text{(P4-PVUR)} \\ &\text{s.t.} && \text{System Constraints} : \ (4.1) - (4.11), \\ & && \text{PVUR constraints} : (4.16), \ (4.17). \end{aligned}$$

while LVUR can be minimized using

$$\begin{aligned} &\min && \text{LVUR} : \ (4.21) && \text{(P3-LVUR)} \\ &\text{s.t.} && \text{System Constraints} : \ (4.1) - (4.11), \\ & && \text{LVUR constraints} : (4.20). \end{aligned}$$

4.6.3 Minimize Losses with Voltage Unbalance Constraints

Our final problem formulation minimizes network losses with all the voltage unbalance definitions implemented as constraints,

$$\begin{aligned} &\min && \text{Network Losses} : \ (4.23) && \text{(P5-Loss}_{\text{VU}}\text{)} \\ &\text{s.t.} && \text{System Constraints} : \ (4.1) - (4.11), \\ & && \text{VUF constraints} : (4.12), \ (4.15), \\ & && \text{PVUR constraints} : (4.16), \ (4.17), \ (4.19), \\ & && \text{LVUR constraints} : (4.20), \ (4.22). \end{aligned}$$

4.7 Software Implementation

The three-phase OPF problems discussed in the previous section were implemented in Julia which is an open-source programming language with math-friendly syntax and excels at numerical

computing [25]. In addition to this, we employed the JuMP [26] package embedded in Julia and used the solver Ipopt [84] to solve the non-convex and nonlinear optimization problems.

Our main source of distribution grid data is GridLAB-D which generates the following files for a given distribution feeder:

(i) `data.xml`: This file contains the topology of the distribution feeder which includes information about the nodes as well as details about loads, generators connected to the feeder.

(ii) `z_dump.xml`: All information about the series and shunt impedance of branches required to construct the overall nodal admittance matrix Y are included in this file.

For our implementation, the first step was to build a flexible data parser that is able to read the models of all major distribution grid components designed in GridLAB-D and convert this network data into MATPOWER [85] format matrices. These matrices will then be used as inputs to the three-phase OPF implementation in Julia. Fig. 4.1 illustrates a flow diagram for the data parser and Table 4.1 summarizes all the matrices generated by the data parser.

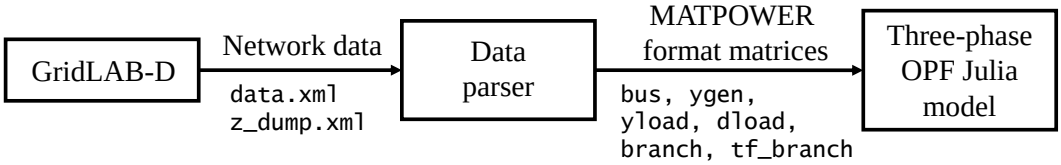

Figure 4.1: Data parser for GridLAB-D to Julia conversion.

In order to benchmark the three-phase OPF implementation with GridLAB-D, we utilized the matrices generated by the data parser and first solved an optimization problem with only one set of constraints representing the power balance equations defined in (4.5). The solution obtained in Julia was benchmarked against the power flow solution from GridLAB-D. Both solutions were similar which ensured that the Julia model developed using matrices generated by the data parser along with the models of distribution grid components defined in (3.2)-(3.11) are consistent with the GridLAB-D model.

Notation	Description
`node`	node type, voltage limits, GridLAB-D voltage solution
`yload`	location, ZIP components for wye-connected loads
`dload`	location, ZIP components for delta-connected loads
`branch`	location, series and shunt impedance of branches
`tf_branch`	location, impedance, and configurations of transformers
`ygen`	location, inverter limits, GridLAB-D power solution

Table 4.1: MATPOWER format matrices generated by data parser.

4.8 Case Study Overview

In the next two sections, we perform various analyses to evaluate the performance of our proposed method:

- Section 4.9 investigates the performance of the approach on a small **IEEE 13-node feeder**. More specifically, we want to compare the solutions obtained by minimizing voltage unbalance using the three different metrics as well as the overall network losses.
- After evaluating the performance of the method on a small test case, Section 4.10 describes the results obtained for a large **PNNL taxonomic feeder: R2-12-47-2**. The goal is to determine if the three-phase OPF formulation can be used to analyze realistically sized distribution feeders.

For our analysis, we solve the five optimization problems: (P1-Loss), (P2-VUF), (P3-LVUR), (P4-PVUR) and (P5-Loss$_{\mathrm{VU}}$) defined in the previous section. In problem (P5-Loss$_{\mathrm{VU}}$), we set the voltage unbalance limits to $u_{\mathrm{VUF}} = u_{\mathrm{PVUR}} = 0.02$ and $u_{\mathrm{LVUR}} = 0.03$.

4.9 Case Study I: IEEE 13-node Feeder

Fig. 4.2 illustrates the modified IEEE 13-node feeder with 15 single-phase solar PV systems at seven nodes as shown by the houses. The maximum apparent power rating of each solar PV inverter is 50 kVA. We define the PV penetration level as ratio of total PV generation (in kW) to the total rated load (in kW). For this test case, the the active power injected by the 15 solar PV inverters was chosen such that PV penetration level is 35%.

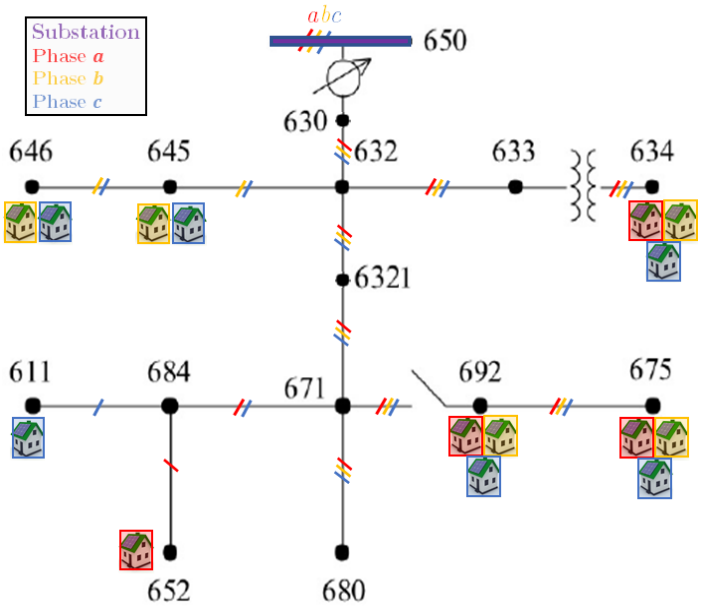

Figure 4.2: Modified IEEE-13 node feeder.

Fig. 4.3 illustrates the average and maximum values of the different voltage unbalance metrics for the solution of each optimization problem. The average unbalance is calculated as the ratio of the sum of voltage unbalance at all three-phase nodes to the number of three-phase nodes. The maximum voltage unbalance level is the highest level among all the three-phase nodes of the feeder. The green dashed line represents the voltage unbalance limit specified by IEC and IEEE standards for VUF and PVUR, respectively. The NEMA standard for LVUR has a higher limit of 3% that is never violated and therefore, not shown in Fig. 4.3. Other performance metrics such as network losses, substation power factor ($\cos \phi_{ss}$) are summarized in Fig. 4.4 along with the average reactive

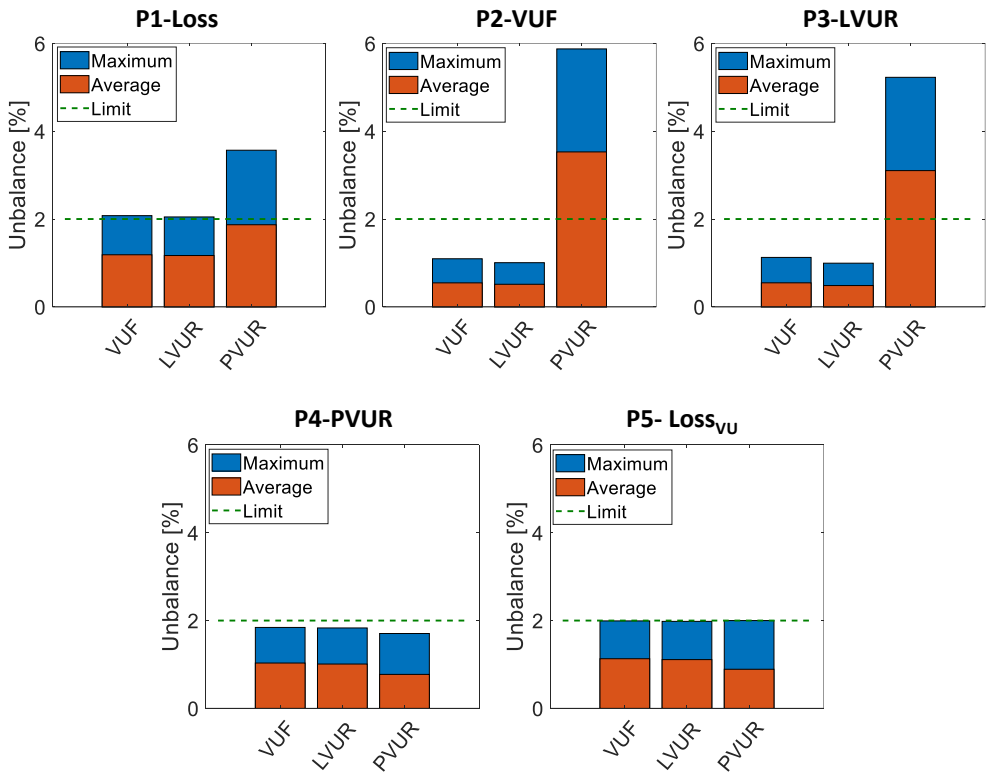

Figure 4.3: IEEE-13 node feeder results. We show the values of the different voltage unbalance metrics for each of the considered optimization problem formulations.

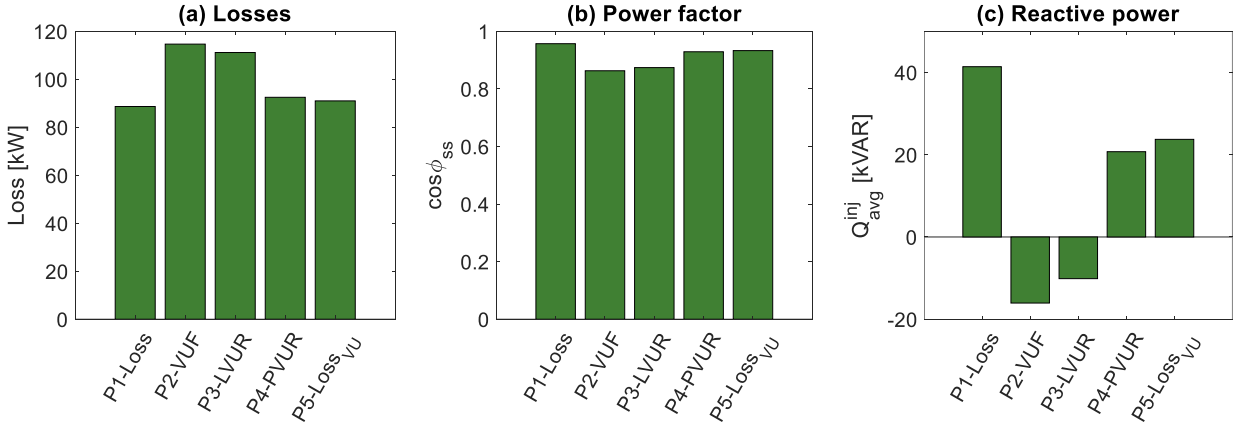

Figure 4.4: IEEE-13 node feeder results for network losses, substation power factor and average reactive power injection.

power injections ($Q_{\text{avg}}^{\text{inj}}$) which is calculated as the ratio of the sum of reactive power injections of all solar PV inverters to the number of solar PV inverters.

We observe from the results in Fig. 4.3 that minimizing network losses leads to an operating condition where PVUR unbalance limit is violated. This emphasizes the need to consider voltage unbalance when optimizing system operations. We further observe in Fig. 4.3 and Fig. 4.4 that there is a strong relationship between VUF and LVUR since the resulting values for VUF and LVUR are similar when we minimize losses or any of the voltage unbalance metrics. Another significant observation is that PVUR in Fig. 4.3 considerably increases when VUF or LVUR is minimized. Hence, we can conclude that minimizing one voltage unbalance definition may result in violation of another voltage unbalance definition.

By comparing the simulation results for problem (P1-Loss) with the results for problems (P2-VUF) and (P3-LVUR) in Fig. 4.4, we observe that the average reactive power injection is negative when VUF or LVUR is minimized. This illustrates that the solar PV inverters are absorbing reactive power from the grid. This also explains the reduction in power factor and increase in losses since the substation needs to supply the additional reactive power to the grid to satisfy the power balance equation in (4.5). On the contrary, the average reactive power injection for problem (P4-PVUR) is positive, resulting in higher power factor at the substation with lower network losses.

Finally, we analyze the results for problem (P5-Loss$_{\text{VU}}$), which minimizes losses subject to voltage unbalance constraints, in Fig. 4.4. We conclude that it is possible to find a solution which ensures that the maximum values of all the unbalance metrics are within acceptable limits, while incurring negligible increase in the network losses.

4.10 Case Study II: PNNL Taxonomic Feeder- R2-12-47-2

The R2-12-47-2 feeder shown in Fig. 4.5 consists of $n = 646$ nodes which represents a moderately populated suburban area mainly comprised of single family homes and small commercial loads [86]. The colored dots indicate solar PV inverters connected to 385 single-phase nodes in the feeder. Each inverter has a maximum rating of 10 KVA with the active power injection chosen to achieve a PV penetration level of 50% of the total rated load.

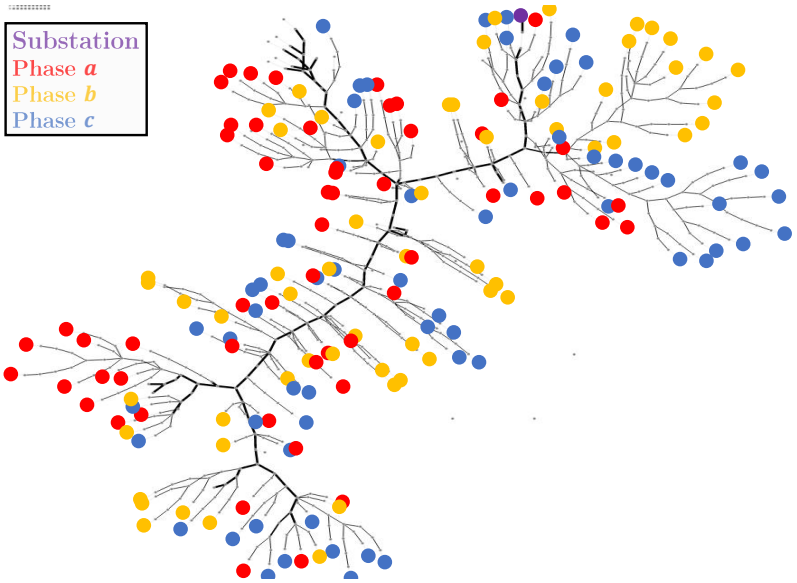

Figure 4.5: Modified R2-12-47-2 taxonomic feeder visualized using [1].

Fig. 4.6 shows the average voltage unbalance results for all cases and Fig. 4.7 illustrates the results for network losses, substation power factor as well as average reactive power injections. Different from the IEEE-13 node results, the base case solution (P0-Base$_{\text{PF}}$) is not computed by solving the three-phase OPF problem, but by running the power flow in GridLAB-D using the Newton-Raphson method.

We observe from the results in Fig. 4.6 and Fig. 4.7 that minimizing any of the voltage unbalance metrics gives rise to similar results. In comparison to the base case, there is considerable reduction in voltage unbalance as well as losses. The substation power factor decreases because the average reactive power injection is negative for all cases minimizing the voltage unbalance metrics, as illustrated in Fig. 4.7.

Finally, we compare the results of problem (P5-Loss$_{\text{VU}}$) in Fig. 4.6 and Fig. 4.7 with other cases. Since the average reactive power for (P5-Loss$_{\text{VU}}$) is positive, the network losses are significantly lower which also leads to a higher power factor. All the voltage unbalance metrics are lower than the acceptable limits, highlighting that minimizing losses is sufficient to ensure that voltage unbalance limits are never violated in this case.

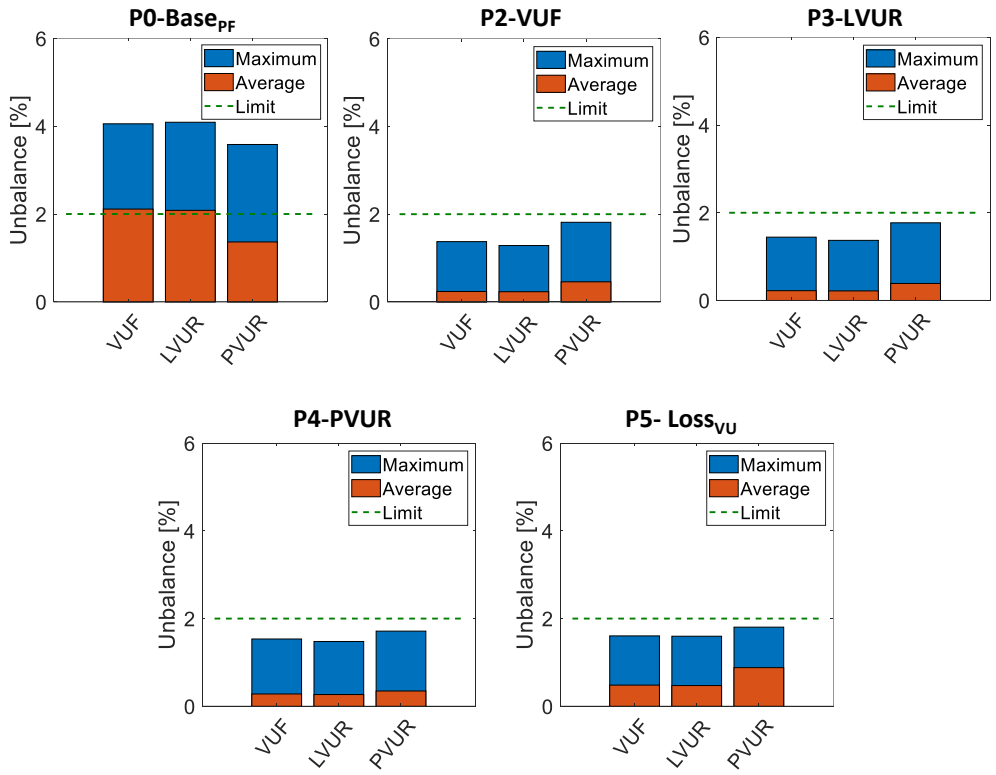

Figure 4.6: Taxonomic feeder: R2-12-47-2 results for voltage unbalance.

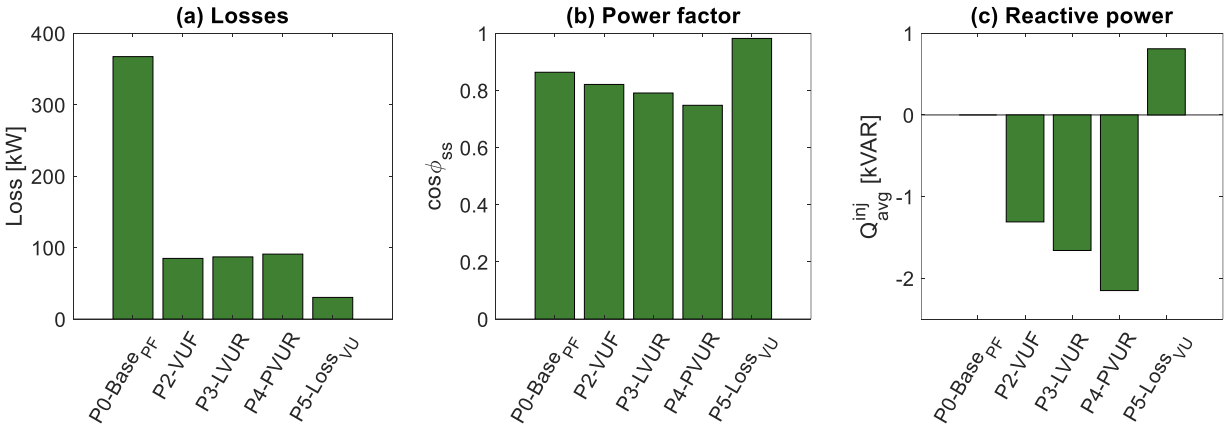

Figure 4.7: R2-12-47-2 feeder results for network losses, substation power factor and average reactive power injection.

4.11 Summary

In this chapter, we presented a full three-phase AC OPF formulation, which we extended with the different voltage unbalance definitions [47]. The case studies showed that care must be taken when minimizing voltage unbalance. To summarize the main observations from our simulation results:

- For the IEEE 13-node test feeder, we observed that minimizing VUF and LVUR led to similar results, but the PVUR value violated acceptable limits.
- Our results for the larger taxonomic distribution feeder were slightly different and we observed that minimizing any of the voltage unbalance metrics led to similar results along with a reduction in losses relative to the base case.
- The results obtained for both test feeders when minimizing network losses subject to the voltage unbalance constraints demonstrated that it is possible obtain a solution with low losses without violating any of the voltage unbalance limits.

Chapter 5

Scalable Implementation of Three-phase Optimal Power Flow

We have shown in Chapter 4 that considerable reduction in voltage unbalance can be achieved by using the three-phase OPF approach. Recall that the optimization problem is non-convex and nonlinear which is challenging to solve especially for large, realistic distribution grids. One of the major challenges with the three-phase OPF approach is computation time. Table 5.1 shows the computation time for test feeders with varying sizes when we solve the optimization problem OPF_{opt} minimizing VUF at critical node $x \in \mathcal{N}$ as summarized in the next page.

Test case	**IEEE-13**	**R1-12.47-3**	**R2-12.47-2**	**R1-12.47-1**
Single-phase connections	40	163	820	2204
Computation time	$<$2 sec	$<$20 sec	$<$20 min	$>$120 min

Table 5.1: Computation time to solve three-phase OPF for various test feeders. All simulations were run on a Windows 10 PC with 2.60 GHz Intel Xeon processor and 64 GB RAM.

$$\min \text{VUF}_x^2 = \frac{\left(\boldsymbol{v}_{\mathbf{d}x}^-\right)^2 + \left(\boldsymbol{v}_{\mathbf{q}x}^-\right)^2}{\left(\boldsymbol{v}_{\mathbf{d}x}^+\right)^2 + \left(\boldsymbol{v}_{\mathbf{q}x}^+\right)^2} \tag{OPF}$$

$$\text{s.t. } |\boldsymbol{V}_0| \angle \boldsymbol{\Theta}_0 = \begin{bmatrix} 1\angle 0^\circ & 1\angle -120^\circ & 1\angle 120^\circ \end{bmatrix}^\top,$$

$$\underline{v} \leq |\boldsymbol{v}_i^\phi| \leq \overline{v}, \qquad \forall i \in \mathcal{N}, \phi \in \Phi,$$

$$-\overline{q}_{\mathrm{G},l}^\phi \leq \boldsymbol{q}_{\mathbf{G},l}^\phi \leq \overline{q}_{\mathrm{G},l}^\phi, \qquad \forall l \in \mathcal{G}, \phi \in \Phi,$$

$$\boldsymbol{P}_{\mathbf{G},i} - \boldsymbol{P}_{\mathbf{L},i} = |\boldsymbol{V}_i| \odot \sum_{k \in \mathcal{N}_0} \left[G_{ik} \odot \mathrm{C}\Big(\boldsymbol{\Theta}_{ik}\Big) + B_{ik} \odot \mathrm{S}\Big(\boldsymbol{\Theta}_{ik}\Big) \right] \cdot |\boldsymbol{V}_k|, \quad \forall i \in \mathcal{N}_0,$$

$$\boldsymbol{Q}_{\mathbf{G},i} - \boldsymbol{Q}_{\mathbf{L},i} = |\boldsymbol{V}_i| \odot \sum_{k \in \mathcal{N}_0} \left[G_{ik} \odot \mathrm{S}\Big(\boldsymbol{\Theta}_{ik}\Big) - B_{ik} \odot \mathrm{C}\Big(\boldsymbol{\Theta}_{ik}\Big) \right] \cdot |\boldsymbol{V}_k|, \quad \forall i \in \mathcal{N}_0.$$

Apart from the power balance equations and lower voltage limits which can yield feasible spaces that are non-convex, the expression for VUF is also non-convex and therefore, solving OPF_{opt} can be challenging. We observe in Table 5.1 that OPF can be solved in less than 1-minute for small test cases (i.e. IEEE-13 node, R1-12.47-3 feeder). For larger, realistic test cases such as the R1-12.47-1 taxonomic feeder, the computation time is more than two hours. In practice, OPF needs to be solved frequently to consider the time-varying load and PV generation and the delay associated with computation time to solve OPF can have an impact on the performance of this approach.

5.1 Literature Review: Existing Methods to Improve Computation Time

Most conventional techniques proposed in existing literature to reduce computational complexity are based on approximations and convex relaxations of the power balance equations. The DC power flow approximation [87, 88] is not applicable for distribution grids since the voltage magnitudes are usually not close to 1 p.u. and resistance of distribution lines are significant. Several improvements over the DC power flow approximation have been discussed in [89, 90] which extends the LinDistFlow model for unbalanced distribution grids. The power balance equations were approximated in [89, 90] by ignoring the line losses. In addition to this, the ratio of voltage phasors at different phases was also approximated to a constant value, which might not be

a suitable approach when trying to minimize voltage unbalance. An unbalanced OPF approach was proposed in [21] to optimize load shedding and the optimization problem was solved using a quasi-Newton method coupled with OpenDSS to calculate the three-phase power flow. Convex relaxation techniques using semidefinite programming (SDP) have been proposed in [24, 91, 92] which converge to globally optimal solutions in many practical cases. However, the computation time is still large and the solutions might not be feasible for the original problem with nonlinear power balance equations. In [92], the results indicated that the semidefinite relaxation is not tight for distributions grids with delta-connected loads. In order to obtain good quality solutions, it was necessary to assume nearly balanced voltages which make these relaxations unsuitable for analysis of voltage unbalance. Other relaxation techniques using second order cone programming (SOCP) have been employed for balanced distribution grids in [93, 94].

5.2 Main Contributions

To solve the OPF problem related to voltage unbalance that is challenging to address via existing approximations and relaxation, we formulate the optimization problem based on linear power flow models that are used as part of a successive approximation approach. This method not only provides AC feasible solutions upon convergence, but can also be used as a direct replacement of the nonlinear AC power balance equations to obtain an approximate solution. In this chapter, we develop three linearized methods based on first-order Taylor expansion, fixed-point equation and forward-backward sweep. They provide good solutions with significant computational benefits when solving the OPF problem for realistic distribution feeders with components such as ZIP loads or delta-connected components. We test the three strategies using a large taxonomic feeder R1-12.47-1 to compare the performance in terms of voltage unbalance reduction, violations of voltage limits and computation time. We benchmark our methods against Lin3DistFlow [90] because it is one of the most widely used linear models for distribution grid analysis. In the next few sections, we describe the successive approximation approach and also discuss the different methods to linearize the power balance equations.

5.3 Successive Approximation Approach

The general approach for all three strategies is to employ a successive approximation method [95] as shown in Fig. 5.1. The iterative approach is carried out according to the following steps:

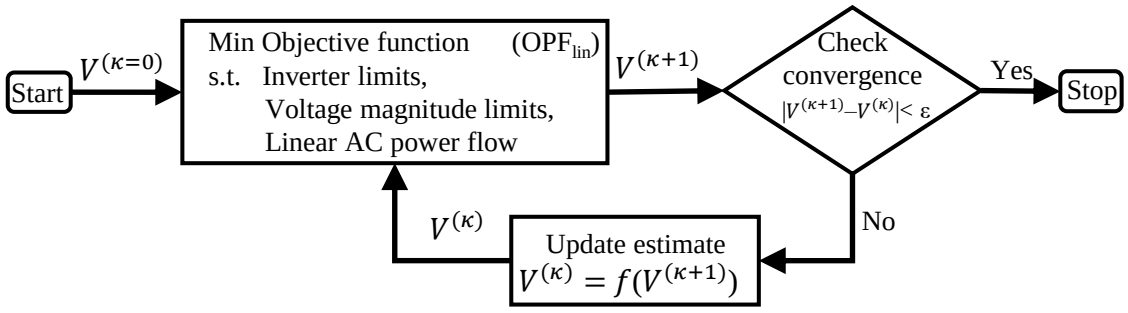

Figure 5.1: Flow diagram for the iterative approach using successive approximation.

1) *Initialization:* Set iteration count to $\kappa = 0$ and start with an initial voltage estimate $V^{(\kappa=0)}$.

2) *Solve OPF:* Solve a simplified optimization problem OPF_{lin} that is similar to OPF_{opt} except that the nonlinear power flow equations are replaced by their linear approximations derived using the voltage estimate $V^{(\kappa)}$.

3) *Check convergence:* Terminate if the deviation between the new voltage estimate $V^{(\kappa+1)}$ and initial voltage estimate $V^{(\kappa)}$ is below specified tolerance ϵ.

4) *Update voltage estimate:* If the stopping criterion is not satisfied, update the voltage estimate and iteration count to $\kappa = \kappa + 1$ and repeat steps 2) and 3).

It is important to note that the only simplification to the OPF problem in step 2) is to linearize the AC power balance equations. The problem still includes nonlinear objective function which will be described in the subsequent section. Hence, we cannot guarantee that this approach converges to an optimal solution. However, the iterative method is guaranteed to provide a feasible solution upon convergence. As shown in Fig. 5.1, we utilize $f(V^{(\kappa+1)})$ in step 4) to update the voltage estimate which we will discuss in more detail in the next few sections.

5.3.1 Objective Function

We will now describe the three objective functions that will be used to compare the performance of the linear approximations. Recall that optimization variables are denoted using **bold** symbols, scalar values are denoted using small letters, and their vector counterparts and matrices are denoted using capital letters.

5.3.1.1 Voltage Unbalance

Since VUF is considered to be the true definition of voltage unbalance, we only use VUF defined in (4.14) to measure voltage unbalance in this chapter. We saw in Chapter 4 that minimizing VUF can lead to higher network losses due to excessive absorption of reactive power by inverters. Furthermore, the optimization algorithm can sometimes identify solutions that would require large reactive power injections from the PV systems. Such solutions are less desirable than solutions with smaller reactive power injections and, in some cases, they also lead to convergence problems for the algorithm. To promote solutions with moderate reactive power injections and faster convergence, we add a penalty on the reactive power injections to our objective function (4.14),

$$\min {\text{VUF}_x}^2 + Q_{\text{pen}} = \min \frac{\left(\boldsymbol{v}_{\mathbf{d}x}^{-}\right)^2 + \left(\boldsymbol{v}_{\mathbf{q}x}^{-}\right)^2}{\left(\boldsymbol{v}_{\mathbf{d}x}^{+}\right)^2 + \left(\boldsymbol{v}_{\mathbf{q}x}^{+}\right)^2} + w \sum_{i \in \mathcal{G}} \sum_{\phi \in \Phi} \left(\boldsymbol{q}_{\mathbf{G},i}^{\phi}\right)^2, \tag{5.1}$$

where w is a scalar weighting factor, which we choose to be small to ensure that higher priority is given to minimizing VUF. A larger w will reduce the reactive power injections from PV systems and promote convergence of the algorithm, but may also increase the resulting VUF.

5.3.1.2 Substation Power

A critical objective for the DSO is to minimize active power drawn at the point of interconnection with the transmission system (i.e. the substation) to avoid investment costs due to the additional infrastructure required to distribute the excess power [83]. The overall active power at the substation is given by

$$\min p_{\text{ss}} = \min \sum_{\phi \in \Phi} \boldsymbol{p}_{\mathbf{G},0}^{\phi}, \tag{5.2}$$

where $\boldsymbol{p}^{\phi}_{\mathbf{G},0}$ is the per-phase active power generation at substation which can be expressed as a function of our voltage variables using (4.5a).

5.3.1.3 Network Losses

As discussed in the previous chapter, active power loss in the network is one of the major drivers for the cost of electricity distribution. Similar to (4.23), we calculate network losses using

$$\min p_{\text{loss}} = \min \sum_{i \in \mathcal{N}} \left(\boldsymbol{P}_{\mathbf{G},i} - \boldsymbol{P}_{\mathbf{L},i} \right), \tag{5.3}$$

where $\boldsymbol{P}_{\mathbf{G},i}$ and $\boldsymbol{P}_{\mathbf{L},i}$ have already been defined in (4.5) and denote the active power components of the generation and load demand at node i, respectively. Note that minimizing active power at substation using (5.2) might not lead to minimal losses since we consider voltage dependent ZIP loads in our formulation.

Now that we have defined the different objective functions, we summarize the nonlinear TP-OPF problem as

$$\begin{aligned}
&\text{min VUF (5.1) or } p_{\text{ss}} \text{ (5.2) or } p_{\text{loss}} \text{ (5.3)} && (\text{OPF}_{\text{opt}})\\
&\text{s.t. } |\boldsymbol{V}_0| \angle \boldsymbol{\Theta}_0 = \begin{bmatrix} 1\angle 0^\circ & 1\angle -120^\circ & 1\angle 120^\circ \end{bmatrix}^\top,\\
&\quad \underline{v} \leq |\boldsymbol{v}_i^{\phi}| \leq \overline{v}, && \forall i \in \mathcal{N}, \phi \in \Phi,\\
&\quad -\overline{q}^{\phi}_{\text{G},l} \leq \boldsymbol{q}^{\phi}_{\mathbf{G},l} \leq \overline{q}^{\phi}_{\text{G},l}, && \forall l \in \mathcal{G}, \phi \in \Phi,\\
&\quad \boldsymbol{P}_{\mathbf{G},i} - \boldsymbol{P}_{\mathbf{L},i} = |\boldsymbol{V}_i| \odot \sum_{k \in \mathcal{N}_0} \left[G_{ik} \odot \mathrm{C}\Big(\boldsymbol{\Theta}_{ik}\Big) + B_{ik} \odot \mathrm{S}\Big(\boldsymbol{\Theta}_{ik}\Big) \right] \cdot |\boldsymbol{V}_k|, \quad \forall i \in \mathcal{N}_0,\\
&\quad \boldsymbol{Q}_{\mathbf{G},i} - \boldsymbol{Q}_{\mathbf{L},i} = |\boldsymbol{V}_i| \odot \sum_{k \in \mathcal{N}_0} \left[G_{ik} \odot \mathrm{S}\Big(\boldsymbol{\Theta}_{ik}\Big) - B_{ik} \odot \mathrm{C}\Big(\boldsymbol{\Theta}_{ik}\Big) \right] \cdot |\boldsymbol{V}_k|, \quad \forall i \in \mathcal{N}_0.
\end{aligned}$$

We will next describe the three linear approximations of the power flow equations used to simplify the problem OPF_{opt}.

5.4 First-order Taylor Approximation (FOT-OPF)

One way to linearize the power balance equations is to use first-order Taylor's (FOT) approximation. This technique has been used to solve the single-phase AC OPF problems for transmission systems [96] and power flow problems in distribution grids [12, 97]. In this section, we adopt the first-order Taylor's (FOT) approximation to linearize the power balance equations and describe how we incorporate the linearized equations in our iterative approach as illustrated in Fig. 5.1.

5.4.1 Notation

We combine the overall voltage variables at all nodes and denote them using

$$|\boldsymbol{V}| = \begin{bmatrix} |\boldsymbol{V}_0| \\ |\boldsymbol{V}_1| \\ \vdots \\ |\boldsymbol{V}_n| \end{bmatrix}, \ \boldsymbol{\Theta} = \begin{bmatrix} \boldsymbol{\Theta}_0 \\ \boldsymbol{\Theta}_1 \\ \vdots \\ \boldsymbol{\Theta}_n \end{bmatrix}, \tag{5.4}$$

where $|\boldsymbol{V}|, \boldsymbol{\Theta} \in \mathbb{R}^{3(n+1)}$ are vectors of the voltage magnitude and angle optimization variables, respectively. Similarly, we can denote the power injections at all nodes using

$$\boldsymbol{P} = \begin{bmatrix} \boldsymbol{P}_0 \\ \boldsymbol{P}_1 \\ \vdots \\ \boldsymbol{P}_n \end{bmatrix}, \ \boldsymbol{Q} = \begin{bmatrix} \boldsymbol{Q}_0 \\ \boldsymbol{Q}_1 \\ \vdots \\ \boldsymbol{Q}_n \end{bmatrix}, \tag{5.5}$$

where $\boldsymbol{P}, \mathbf{q} \in \mathbb{R}^{3(n+1)}$ are vectors of the active and reactive power injections, respectively. As shown in Fig. 5.1, we start with the initial estimate of the voltage phasor $V^{(0)} \in \mathbb{C}^{3(n+1)}$ which is typically a flat-start or the no-load voltage. In our case, we start with a no-load voltage and run a three-phase power flow until convergence. The power flow solution is considered as the initial voltage estimate $V^{(0)}$. We denote $P^{(0)}, Q^{(0)} \in \mathbb{R}^{3(n+1)}$ as the vectors of the active and reactive

power injections calculated using the initial voltage estimate $V^{(0)} = |V^{(0)}|\angle\Theta^{(0)}$ where

$$|V^{(0)}| = \begin{bmatrix} |V_0^{(0)}| \\ |V_1^{(0)}| \\ \vdots \\ |V_n^{(0)}| \end{bmatrix},\ \Theta^{(0)} = \begin{bmatrix} \Theta_0^{(0)} \\ \Theta_1^{(0)} \\ \vdots \\ \Theta_n^{(0)} \end{bmatrix},\ P^{(0)} = \begin{bmatrix} P_0^{(0)} \\ P_1^{(0)} \\ \vdots \\ P_n^{(0)} \end{bmatrix},\ Q^{(0)} = \begin{bmatrix} Q_0^{(0)} \\ Q_1^{(0)} \\ \vdots \\ Q_n^{(0)} \end{bmatrix}. \tag{5.6}$$

Here, $|V^{(0)}|, \Theta^{(0)} \in \mathbb{R}^{3(n+1)}$ are the voltage magnitude and angle vectors of the initial estimate $V^{(0)}$, respectively.

5.4.2 Linearized Power Balance Equations

The power balance equations in (4.5) can be linearized using the first-order Taylor's approximation and the power injections $\boldsymbol{P}, \boldsymbol{Q} \in \mathbb{R}^{3(n+1)}$ can be expressed as

$$\begin{bmatrix} \boldsymbol{P} \\ \boldsymbol{Q} \end{bmatrix} = \begin{bmatrix} \boldsymbol{P_G} - P_{\mathrm{L}}^{(\kappa)} \\ \boldsymbol{Q_G} - Q_{\mathrm{L}}^{(\kappa)} \end{bmatrix} = \begin{bmatrix} P^{(\kappa)} \\ Q^{(\kappa)} \end{bmatrix} + J(V^{(\kappa)}) \cdot \begin{bmatrix} |\boldsymbol{V}| - |V^{(\kappa)}| \\ \boldsymbol{\Theta} - \Theta^{(\kappa)} \end{bmatrix}, \tag{5.7}$$

where $\boldsymbol{P_G}, \boldsymbol{Q_G} \in \mathbb{R}^{3(n+1)}$ are the active and reactive power generation vectors; $P_{\mathrm{L}}^{(\kappa)}, Q_{\mathrm{L}}^{(\kappa)} \in \mathbb{R}^{3(n+1)}$ are the estimates of active and reactive power drawn by the ZIP loads; $P^{(\kappa)}, Q^{(\kappa)} \in \mathbb{R}^{3(n+1)}$ are the estimates of active and reactive power injections. The Jacobian matrix $J \in \mathbb{R}^{6(n+1)\times 6(n+1)}$ represents the partial derivatives [98] of the nonlinear power flow equations defined

in (4.5). It has the form

$$J(\boldsymbol{V}) = \left[\begin{array}{ccc|ccc} \frac{\delta \boldsymbol{p}_0^a}{\delta|\boldsymbol{v}_0^a|} & \cdots & \frac{\delta \boldsymbol{p}_0^a}{\delta|\boldsymbol{v}_n^c|} & \frac{\delta \boldsymbol{p}_0^a}{\delta \boldsymbol{\theta}_0^a} & \cdots & \frac{\delta \boldsymbol{p}_0^a}{\delta \boldsymbol{\theta}_n^c} \\ \vdots & \ddots & \vdots & \vdots & \ddots & \vdots \\ \frac{\delta \boldsymbol{p}_n^c}{\delta|\boldsymbol{v}_0^a|} & \cdots & \frac{\delta \boldsymbol{p}_n^c}{\delta|\boldsymbol{v}_n^c|} & \frac{\delta \boldsymbol{p}_n^c}{\delta \boldsymbol{\theta}_0^a} & \cdots & \frac{\delta \boldsymbol{p}_n^c}{\delta \boldsymbol{\theta}_n^c} \\ \hline \frac{\delta \boldsymbol{q}_0^a}{\delta|\boldsymbol{v}_0^a|} & \cdots & \frac{\delta \boldsymbol{q}_0^a}{\delta|\boldsymbol{v}_n^c|} & \frac{\delta \boldsymbol{q}_0^a}{\delta \boldsymbol{\theta}_0^a} & \cdots & \frac{\delta \boldsymbol{q}_0^a}{\delta \boldsymbol{\theta}_n^c} \\ \vdots & \ddots & \vdots & \vdots & \ddots & \vdots \\ \frac{\delta \boldsymbol{q}_n^c}{\delta|\boldsymbol{v}_0^a|} & \cdots & \frac{\delta \boldsymbol{q}_n^c}{\delta|\boldsymbol{v}_n^c|} & \frac{\delta \boldsymbol{q}_n^c}{\delta \boldsymbol{\theta}_0^a} & \cdots & \frac{\delta \boldsymbol{q}_n^c}{\delta \boldsymbol{\theta}_n^c} \end{array}\right]. \tag{5.8}$$

The partial derivatives defined in (5.8) are functions of our optimization variables $|\boldsymbol{V}|, \boldsymbol{\Theta}$ as summarized in Tables. 5.2 and 5.3. The Jacobian matrix $J(V^{(\kappa)})$ in (5.7) can be calculated using the voltage estimate $V^{(\kappa)}$ by substituting $|\boldsymbol{V}| = |V^{(\kappa)}|$ and $\boldsymbol{\Theta} = \Theta^{(\kappa)}$ in Tables. 5.2 and 5.3. In addition, we also require the nodal admittance matrix $Y = |Y|\angle\Psi$, where $|Y|, \Psi \in \mathbb{R}^{3(n+1)\times 3(n+1)}$ are the magnitude and angle components, respectively.

To determine $P^{(\kappa)}, Q^{(\kappa)}$ in (5.7), we substitute $|\boldsymbol{V}| = |V^{(\kappa)}|$ and $\boldsymbol{\theta} = \theta^{(\kappa)}$ in (4.5) to calculate the initial power injections $P_i^{(\kappa)},\ Q_i^{(\kappa)}$ at node $i \in \mathcal{N}_0$ given by

$$P_i^{(\kappa)} = |V_i^{(\kappa)}| \odot \sum_{k\in\mathcal{N}_0} \left[G_{ik} \odot \mathrm{C}\left(\Theta_{ik}^{(\kappa)}\right) + B_{ik} \odot \mathrm{S}\left(\Theta_{ik}^{(\kappa)}\right)\right] \cdot |V_k^{(\kappa)}|, \tag{5.9a}$$

$$Q_i^{(\kappa)} = |V_i^{(\kappa)}| \odot \sum_{k\in\mathcal{N}_0} \left[G_{ik} \odot \mathrm{S}\left(\Theta_{ik}^{(\kappa)}\right) - B_{ik} \odot \mathrm{C}\left(\Theta_{ik}^{(\kappa)}\right)\right] \cdot |V_k^{(\kappa)}|, \tag{5.9b}$$

where $|V_i^{(\kappa)}|, |V_k^{(\kappa)}|$ are the magnitude components of the initial voltage estimate. $\mathrm{C}\left(\Theta_{ik}^{(\kappa)}\right)$ and $\mathrm{S}\left(\Theta_{ik}^{(\kappa)}\right)$ are calculated from (4.6) using the angle components $\Theta_i^{(\kappa)}, \Theta_k^{(\kappa)}$ of the initial voltage estimate.

$\boldsymbol{\delta}$	$\boldsymbol{i = k}$
$\frac{\delta \boldsymbol{p}_i^{\phi_i}}{\delta \lvert \boldsymbol{v}_k^{\phi_k} \rvert}$	$\lvert \boldsymbol{v}_i^{\phi_i} \rvert \cdot \lvert y_{ii}^{\phi_i \phi_i} \rvert \cos \psi_{ii}^{\phi_i \phi_i} + \sum_{k \in \mathcal{N}_0} \sum_{\phi_k \in \Phi} \lvert \boldsymbol{v}_k^{\phi_k} \rvert \cdot \lvert y_{ik}^{\phi_i \phi_k} \rvert \cos \left(\boldsymbol{\theta}_i^{\phi_i} - \boldsymbol{\theta}_k^{\phi_k} - \psi_{ik}^{\phi_i \phi_k} \right)$
$\frac{\delta \boldsymbol{p}_i^{\phi_i}}{\delta \boldsymbol{\theta}_k^{\phi_k}}$	$-\lvert \boldsymbol{v}_i^{\phi_i} \rvert \sum_{\substack{k \in \mathcal{N}_0, \\ k \neq i}} \sum_{\phi_k \in \Phi} \lvert \boldsymbol{v}_k \rvert \cdot \lvert y_{ik}^{\phi_i \phi_k} \rvert \sin \left(\boldsymbol{\theta}_i^{\phi_i} - \boldsymbol{\theta}_k^{\phi_k} - \psi_{ik}^{\phi_i \phi_k} \right)$
$\frac{\delta \boldsymbol{q}_i^{\phi_i}}{\delta \lvert \boldsymbol{v}_k^{\phi_k} \rvert}$	$-\lvert \boldsymbol{v}_i^{\phi_i} \rvert \cdot \lvert y_{ii}^{\phi_i \phi_i} \rvert \sin \psi_{ii}^{\phi_i \phi_i} + \sum_{k \in \mathcal{N}_0} \sum_{\phi_k \in \Phi} \lvert \boldsymbol{v}_k \rvert \cdot \lvert y_{ik}^{\phi_i \phi_k} \rvert \sin \left(\boldsymbol{\theta}_i^{\phi_i} - \boldsymbol{\theta}_k^{\phi_k} - \psi_{ik}^{\phi_i \phi_k} \right)$
$\frac{\delta \boldsymbol{q}_i^{\phi_i}}{\delta \boldsymbol{\theta}_k^{\phi_k}}$	$\lvert \boldsymbol{v}_i^{\phi_i} \rvert \sum_{\substack{k \in \mathcal{N}_0, \\ k \neq i}} \sum_{\phi_k \in \Phi} \lvert \boldsymbol{v}_k^{\phi_k} \rvert \cdot \lvert y_{ik}^{\phi_i \phi_k} \rvert \cos \left(\boldsymbol{\theta}_i^{\phi_i} - \boldsymbol{\theta}_k^{\phi_k} - \psi_{ik}^{\phi_i \phi_k} \right)$

Table 5.2: Diagonal entries of Jacobian matrix $J(\boldsymbol{V})$ with $i, k \in \mathcal{N},\ \phi_i, \phi_k \in \Phi$. The nodal admittance matrix is $Y = |Y| \angle \Psi$.

$\boldsymbol{\delta}$	$\boldsymbol{i \neq k}$
$\frac{\delta \boldsymbol{p}_i^{\phi_i}}{\delta \lvert \boldsymbol{v}_k^{\phi_k} \rvert}$	$\lvert \boldsymbol{v}_i^{\phi_i} \rvert \cdot \lvert y_{ik}^{\phi_i \phi_k} \rvert \cos \left(\boldsymbol{\theta}_i^{\phi_i} - \boldsymbol{\theta}_k^{\phi_k} - \psi_{ik}^{\phi_i \phi_k} \right)$
$\frac{\delta \boldsymbol{p}^{\phi_i}}{\delta \boldsymbol{\theta}_k^{\phi_k}}$	$\lvert \boldsymbol{v}_i^{\phi_i} \rvert \cdot \lvert \boldsymbol{v}_k^{\phi_k} \rvert \cdot \lvert y_{ik}^{\phi_i \phi_k} \rvert \sin \left(\boldsymbol{\theta}_i^{\phi_i} - \boldsymbol{\theta}_k^{\phi_k} - \psi_{ik}^{\phi_i \phi_k} \right)$
$\frac{\delta \boldsymbol{q}_i^{\phi_i}}{\delta \lvert \boldsymbol{v}_k^{\phi_k} \rvert}$	$\lvert \boldsymbol{v}_i^{\phi_i} \rvert \cdot \lvert y_{ik}^{\phi_i \phi_k} \rvert \sin \left(\boldsymbol{\theta}_i^{\phi_i} - \boldsymbol{\theta}_k^{\phi_k} - \psi_{ik}^{\phi_i \phi_k} \right)$
$\frac{\delta \boldsymbol{q}_i^{\phi_i}}{\delta \boldsymbol{\theta}_k^{\phi_k}}$	$-\lvert \boldsymbol{v}_i^{\phi_i} \rvert \cdot \lvert \boldsymbol{v}_k^{\phi_k} \rvert \cdot \lvert y_{ik}^{\phi_i \phi_k} \rvert \cos \left(\boldsymbol{\theta}_i^{\phi_i} - \boldsymbol{\theta}_k^{\phi_k} - \psi_{ik}^{\phi_i \phi_k} \right)$

Table 5.3: Off-diagonal entries of Jacobian matrix $J(\boldsymbol{V})$ with $i, k \in \mathcal{N},\ \phi_i, \phi_k \in \Phi$. The nodal admittance matrix is $Y = |Y| \angle \Psi$.

It is important to note that the linearized power balance equations in (5.7) include $P_{\mathrm{L}}^{(\kappa)}, Q_{\mathrm{L}}^{(\kappa)}$ which represent expressions for voltage dependent wye- and delta-connected loads as defined in (3.8) and (3.9), respectively. In the next subsections, we simplify these expressions to constant values using the initial voltage estimate $V^{(\kappa)}$.

5.4.2.1 Wye-connected Loads

When solving power flows with voltage-dependent loads, it is common to approximate the load demand using a zero-order approximation. We employ the same approximation in the optimization framework by using the initial voltage magnitude estimate $|V^{(\kappa)}|$ in (3.8) to compute the approximate load demand. For a wye-connected load at phase $\phi \in \Phi$ of node $i \in \mathcal{L}_{\mathrm{Y}}$, we substitute $|\boldsymbol{v}_i^{\phi}| = |v_i^{\phi(\kappa)}|$ in (3.8) to get

$$p_{\mathrm{LY},i}^{\phi(\kappa)} = p_{\mathrm{PY},i}^{\phi} + p_{\mathrm{IY},i}^{\phi} \cdot |v_i^{\phi(\kappa)}| + p_{\mathrm{ZY},i}^{\phi} \cdot |v_i^{\phi(\kappa)}|^2, \tag{5.10a}$$

$$q_{\mathrm{LY},i}^{\phi(\kappa)} = q_{\mathrm{PY},i}^{\phi} + q_{\mathrm{IY},i}^{\phi} \cdot |v_i^{\phi(\kappa)}| + q_{\mathrm{ZY},i}^{\phi} \cdot |v_i^{\phi(\kappa)}|^2. \tag{5.10b}$$

We observe in (5.10) that the active and reactive power demand are constant values and not a function of our optimization variable $|\boldsymbol{v}_i^{\phi}|$. Note that the load demand is recalculated in each iteration of the successive approximation approach based on the updated voltage estimate. It is possible to use a first-order approximation (which is a linear function of the voltage magnitude variable $|\boldsymbol{v}_i^{\phi}|$) instead of the zero-order approximation to get a slightly better accurate model of the load demand at every iteration of the successive approximation approach. However, recall that the iterative approach converges only when the deviation between the voltage at the current iteration and previous voltage estimate is very small. Hence, the first-order approximation essentially reduces to a zero-order approximation when the voltage steps taken by the iterative process is very small.

5.4.2.2 Delta-connected Loads

Similar to the wye-connected loads, we can employ the zero-order approximation in (3.9) to calculate the approximate load demand. Using the first-order approximation in this case will require inclusion of nonlinear constraints defining the relationship between phase-to-phase and

phase-to-neutral voltage magnitudes as described in (4.3). To avoid this, we can use the zero-order approximation and express the demand for a delta-connected load at phase $\phi_\Delta \in \{ab, bc, ca\}$ of node $i \in \mathcal{L}_\Delta$ using

$$p_{\mathrm{L}\Delta,i}^{\phi_\Delta(\kappa)} = p_{\mathrm{P}\Delta,i}^{\phi_\Delta} + p_{\mathrm{I}\Delta,i}^{\phi_\Delta} \cdot |v_{\Delta,i}^{\phi_\Delta(\kappa)}| + p_{\mathrm{Z}\Delta,i}^{\phi_\Delta} \cdot |v_{\Delta,i}^{\phi_\Delta(\kappa)}|^2, \tag{5.11a}$$

$$q_{\mathrm{L}\Delta,i}^{\phi_\Delta(\kappa)} = q_{\mathrm{P}\Delta,i}^{\phi_\Delta} + q_{\mathrm{I}\Delta,i}^{\phi_\Delta} \cdot |v_{\Delta,i}^{\phi_\Delta(\kappa)}| + q_{\mathrm{Z}\Delta,i}^{\phi_\Delta} \cdot |v_{\Delta,i}^{\phi_\Delta(\kappa)}|^2, \tag{5.11b}$$

$$\text{where } |v_{\Delta,i}^{\phi_\Delta(\kappa)}|^2 = |v_i^{\phi_1(\kappa)}|^2 + |v_i^{\phi_2(\kappa)}|^2 - 2|v_i^{\phi_1(\kappa)}||v_i^{\phi_2(\kappa)}| \cdot \cos\left(\theta_i^{\phi_1(\kappa)} - \theta_i^{\phi_2(\kappa)}\right), \tag{5.11c}$$

with $\phi_1, \phi_2 \in \{a, b, c\}$ and $\phi_1 \neq \phi_2$. Recall that we converted the delta-connected loads to equivalent wye-connected loads in (4.7)-(4.11) by introducing the phase-to-phase current variables $\boldsymbol{i}_{\Delta\mathbf{d},i}^{\phi_\Delta}$, $\boldsymbol{i}_{\Delta\mathbf{q},i}^{\phi_\Delta}$ $\forall i \in \mathcal{L}_\Delta, \phi_\Delta \in \{ab, bc, ca\}$. Since the complex power defined in (4.7) simplifies to a constant value, no current variables are required and we can directly compute the initial phase-to-phase current phasor $i_{\Delta,i}^{\phi_\Delta(\kappa)}$ using

$$i_{\Delta,i}^{\phi_\Delta(\kappa)^*} = \frac{p_{\mathrm{L}\Delta,i}^{\phi_\Delta(\kappa)} + j \cdot q_{\mathrm{L}\Delta,i}^{\phi_\Delta(\kappa)}}{\left(v_i^{\phi_1(\kappa)} - v_i^{\phi_2(\kappa)}\right)}. \tag{5.12}$$

By following the same procedure defined in (4.9) to get the initial phase-to-neutral current phasor $I_i^{(\kappa)} = \Gamma \cdot I_{li}^{(\kappa)}$, we can calculate the complex power $S_{\Delta\mathrm{Y},i}^{(\kappa)}$ drawn by the delta-connected load using

$$S_{\Delta\mathrm{Y},i}^{(\kappa)} = \begin{bmatrix} s_{\Delta\mathrm{Y},i}^a \\ s_{\Delta\mathrm{Y},i}^b \\ s_{\Delta\mathrm{Y},i}^c \end{bmatrix} = \underbrace{\begin{bmatrix} v_i^a \\ v_i^b \\ v_i^c \end{bmatrix}}_{V_i^{(\kappa)}} \odot \underbrace{\begin{bmatrix} i_{i0}^{a\,*} \\ i_{i0}^{b\,*} \\ i_{i0}^{c\,*} \end{bmatrix}}_{I_i^{(\kappa)*}}. \tag{5.13}$$

Similar to the power demand derived in (5.10) for wye-connected loads, we observe that $S_{\Delta\mathrm{Y},i}^{(\kappa)}$ is also a constant value and not a function of our optimization variables $|\boldsymbol{v}_i^\phi|, |\boldsymbol{v}_{\Delta,i}^{\phi_\Delta}|$. We can directly use the real and imaginary components of $S_{\Delta\mathrm{Y},i}^{(\kappa)}$ to represent power drawn by the delta-connected loads in (5.7). Similar to the wye-connected loads, note that the load demand is recalculated in each iteration of the successive approximation approach using the updated voltage estimate.

5.4.3 Iterative Approach

As discussed in the beginning of the chapter and illustrated in Fig. 5.1, we employ an iterative approach to ensure our solutions are AC feasible and close to the optimal solution. The iterative approach using first-order Taylor approximation (FOT-OPF) is executed as per the following steps:

1) *Initialization:* Run a power flow until convergence from a flat-start. The solution obtained by solving power flow is the initial voltage estimate $V^{(\kappa=0)}$.

2) *Solve OPF:* Solve a simplified optimization problem OPF_{FOT} which utilizes the initial voltage estimate $V^{(\kappa)}$ to linearize the power flow equations using FOT series approximation. The solution of the optimization problem is the new estimate is $V^{(\kappa+1)}$.

$$
\begin{aligned}
&\text{min} \quad \text{VUF (5.1) or } p_{\text{ss}} \text{ (5.2) or } p_{\text{loss}} \text{ (5.3)} && (\text{OPF}_{\text{FOT}})\\
&\text{s.t.} \quad |\boldsymbol{V}_0|\angle\boldsymbol{\Theta}_0 = \begin{bmatrix} 1\angle 0^\circ & 1\angle -120^\circ & 1\angle 120^\circ \end{bmatrix}^\top,\\
&\qquad \underline{v} \le |\boldsymbol{v}_i^\phi| \le \overline{v}, && \forall i \in \mathcal{N}, \phi \in \Phi,\\
&\qquad -\overline{q}_{\text{G},l}^{\phi} \le \boldsymbol{q}_{\text{G},l}^{\phi} \le \overline{q}_{\text{G},l}^{\phi}, && \forall l \in \mathcal{G}, \phi \in \Phi,\\
&\qquad \begin{bmatrix} \boldsymbol{P} \\ \boldsymbol{Q} \end{bmatrix} = \begin{bmatrix} \boldsymbol{P}_{\mathbf{G}} - P_{\text{L}}^{(\kappa)} \\ \boldsymbol{Q}_{\mathbf{G}} - Q_{\text{L}}^{(\kappa)} \end{bmatrix} = \begin{bmatrix} P^{(\kappa)} \\ Q^{(\kappa)} \end{bmatrix} + J(V^{(\kappa)}) \cdot \begin{bmatrix} |\boldsymbol{V}| - |V^{(\kappa)}| \\ \boldsymbol{\Theta} - \Theta^{(\kappa)} \end{bmatrix}.
\end{aligned}
$$

3) *Check convergence:* Terminate if $\sum_{i \in \mathcal{N}} |V_i^{(\kappa+1)} - V_i^{(\kappa)}|$ is below specified tolerance ϵ.

4) *Update voltage estimate:* If the stopping criterion is not satisfied, run a power flow until convergence using $V^{(\kappa+1)}$ as the initial point. Update the voltage estimate $V^{(\kappa)} = V^{(\kappa+1)}$ and increase the iteration count to $\kappa = \kappa + 1$ and return to step 2).

5.5 Fixed-point Linearization (FP-OPF)

Another way to improve scalability of the three-phase OPF problem would be to utilize the fixed-point interpretation of the power balance equations. This method has been used in [12, 99] to solve power flow for unbalanced distribution grids. In this section, we incorporate the fixed-point

equations into our three-phase OPF framework and employ an iterative approach similar to the FOT-OPF method. We will first introduce the fixed-point linearization of the power balance equations and then discuss the modifications necessary to integrate this approach into our optimization framework.

5.5.1 Linearized Power Balance Equations

In order to express the fixed-point interpretation of the nonlinear power balance equations, we can split the nodal admittance matrix Y defined in (3.7) into four submatrices given by

$$Y = \begin{bmatrix} Y_{00} & Y_{0\mathrm{L}} \\ Y_{\mathrm{L}0} & Y_{\mathrm{LL}} \end{bmatrix}. \tag{5.14}$$

Here, $Y_{00} \in \mathbb{C}^{3\times 3}$ represents the submatrix corresponding to the slack node (i.e. substation) and $Y_{\mathrm{LL}} \in \mathbb{C}^{3n\times 3n}$ denotes the submatrix of the entire network ignoring the slack node. $Y_{0\mathrm{L}} \in \mathbb{C}^{3\times 3n}$, $Y_{\mathrm{L}0} \in \mathbb{C}^{3n\times 3}$ are the other submatrices of Y.

Next, we split the complex power injections at all nodes except the substation node with index 0 into wye-connected injections $S_{\mathrm{Y}} \in \mathbb{C}^{3n}$ and delta-connected injections $S_{\Delta} \in \mathbb{C}^{3n}$, which can be defined as

$$S_{\mathrm{Y}} = \begin{bmatrix} S_{\mathrm{Y},1} \\ S_{\mathrm{Y},2} \\ \vdots \\ S_{\mathrm{Y},n} \end{bmatrix} = \underbrace{\begin{bmatrix} S_{\mathrm{GY},1} \\ S_{\mathrm{GY},2} \\ \vdots \\ S_{\mathrm{GY},n} \end{bmatrix}}_{S_{\mathrm{GY}}} - \underbrace{\begin{bmatrix} S_{\mathrm{LY},1} \\ S_{\mathrm{LY},1} \\ \vdots \\ S_{\mathrm{LY},n} \end{bmatrix}}_{S_{\mathrm{LY}}}, \; S_{\Delta} = \begin{bmatrix} S_{\Delta,1} \\ S_{\Delta,2} \\ \vdots \\ S_{\Delta,n} \end{bmatrix} = \underbrace{\begin{bmatrix} S_{\mathrm{G}\Delta,1} \\ S_{\mathrm{G}\Delta,2} \\ \vdots \\ S_{\mathrm{G}\Delta,n} \end{bmatrix}}_{S_{\mathrm{G}\Delta}} - \underbrace{\begin{bmatrix} S_{\mathrm{L}\Delta,1} \\ S_{\mathrm{L}\Delta,2} \\ \vdots \\ S_{\mathrm{L}\Delta,n} \end{bmatrix}}_{S_{\mathrm{L}\Delta}}, \tag{5.15}$$

where $S_{\mathrm{Y},i} \in \mathbb{C}^3$ represent the power injections at node i corresponding to wye-connected sources $S_{\mathrm{GY},i}$ and loads $S_{\mathrm{LY},i}$. Similarly, $S_{\Delta,i} \in \mathbb{C}^3$ denote the power injections at node i corresponding to delta-connected sources $S_{\mathrm{G}\Delta,i}$ and loads $S_{\mathrm{L}\Delta,i}$. We also define a transformation block diagonal matrix $H \in \mathbb{Z}^{3n\times 3n}$ to convert the delta-connected injections to equivalent wye-connected injections,

which is defined by

$$H = \begin{bmatrix} \Gamma & 0 & \dots \\ \vdots & \ddots & \dots \\ 0 & \dots & \Gamma \end{bmatrix}, \text{ where } \Gamma = \begin{bmatrix} 1 & -1 & 0 \\ 0 & 1 & -1 \\ -1 & 0 & 1 \end{bmatrix}. \tag{5.16}$$

Similar to the FOT-OPF approach, we start with an initial estimate of the voltage phasor $V^{(\kappa)}$ which allows us to express the fixed-point equation [12] as

$$\begin{aligned} |\boldsymbol{V}|\angle\boldsymbol{\Theta} &= f(V^{(\kappa)}, S_{\mathrm{Y}}, S_{\Delta}) \\ &= \underbrace{-Y_{\mathrm{LL}}^{-1} Y_{\mathrm{L0}}(|\boldsymbol{V}_0|\angle\boldsymbol{\theta}_0)}_{W} + Y_{\mathrm{LL}}^{-1}\Big(\mathrm{diag}(V^{(\kappa)^*})^{-1} S_{\mathrm{Y}}^* + H^{\top}\mathrm{diag}(HV^{(\kappa)^*})^{-1} S_{\Delta}^*\Big), \end{aligned} \tag{5.17}$$

where $|\boldsymbol{V}|\angle\boldsymbol{\Theta}$ is the voltage phasor expressed in terms of our optimization variables defined in (5.4) and $|\boldsymbol{V}_0|\angle\boldsymbol{\Theta}_0$ is the voltage phasor at substation node. Since our voltage variables at the substation node are fixed, we refer to $W = -Y_{\mathrm{LL}}^{-1} Y_{\mathrm{L0}} V_0$ as the no-load voltage phasor and use it as the initial voltage estimate $V^{(\kappa)}$ for this method. It is important to note in (5.17) that the inverse of Y_{LL} exists for most practical distribution grids [99, 100]. By rearranging and equating the real and imaginary terms, we can rewrite (5.17) as

$$\Re\{V\} = \Re\Big\{Z_1\Big\} + \Re\Big\{Z_2\Big\} \cdot \boldsymbol{P}_{\mathbf{Y}} + \Im\Big\{Z_2\Big\} \cdot \boldsymbol{Q}_{\mathbf{Y}}, \tag{5.18a}$$

$$\Im\{V\} = \Im\Big\{Z_1\Big\} + \Im\Big\{Z_2\Big\} \cdot \boldsymbol{P}_{\mathbf{Y}} - \Re\Big\{Z_2\Big\} \cdot \boldsymbol{Q}_{\mathbf{Y}}, \tag{5.18b}$$

$$\text{where } Z_1 = -W + Y_{\mathrm{LL}}^{-1} H^{\top}\mathrm{diag}(HV^{(\kappa)^*})^{-1} S_{\Delta}^*, \text{ and } Z_2 = Y_{\mathrm{LL}}^{-1}\mathrm{diag}(V^{(\kappa)^*})^{-1}.$$

Here, Z_2 is fixed and Z_1 is also a constant term since S_{Δ} represents only the power drawn by delta-connected loads $S_{\mathrm{L}\Delta}$ as we do not consider delta-connected sources. We can calculate $S_{\mathrm{L}\Delta}$ using the initial voltage estimate $V^{(\kappa)}$ and by following the same steps defined in (5.11)-(5.13) for the FOT-OPF approach. Similarly, we can also calculate the power drawn by wye-connected loads S_{LY} using $V^{(\kappa)}$ and by repeating the procedure defined in (5.10) for the FOT-OPF approach. Furthermore, we know that the real component of S_{Y} which is $\boldsymbol{P}_{\mathbf{Y}} = \boldsymbol{P}_{\mathbf{GY}} - P_{\mathrm{LY}}$ is also constant since the active power of solar PV inverters $\boldsymbol{P}_{\mathbf{GY}}$ is fixed. This means that $\boldsymbol{Q}_{\mathbf{Y}} = \boldsymbol{Q}_{\mathbf{GY}} - Q_{\mathrm{LY}}$ which is the imaginary component of S_{Y} and includes our controllable variables (i.e. the reactive

power injections of solar PV inverters) in $\boldsymbol{Q}_{\mathbf{GY}}$ is the only unknown part in the right-hand side of (5.18) and makes it a set of linear expressions.

It is important to note the left-hand side expressions of (5.18) are linear in rectangular coordinate frame and hence, (5.18) represents a set of linear equality constraints. So, we implement this approach in the rectangular coordinate frame. In the next few subsections, we will discuss the notation and constraints that need to be reformulated in the rectangular coordinate frame.

5.5.2 Notation

We replace our polar coordinate frame voltage variables $|\boldsymbol{V}_i|,\ \boldsymbol{\Theta}_i$ defined in (3.1) for a three-phase node $i \in \mathcal{N}_0$ node with the variables defined by

$$\boldsymbol{V}_{\mathbf{d}i} = \begin{bmatrix} \boldsymbol{v}_{\mathbf{d}i}^{a} \\ \boldsymbol{v}_{\mathbf{d}i}^{b} \\ \boldsymbol{v}_{\mathbf{d}i}^{c} \end{bmatrix},\ \boldsymbol{V}_{\mathbf{q}i} = \begin{bmatrix} \boldsymbol{v}_{\mathbf{q}i}^{a} \\ \boldsymbol{v}_{\mathbf{q}i}^{b} \\ \boldsymbol{v}_{\mathbf{q}i}^{c} \end{bmatrix}, \tag{5.19}$$

where $\boldsymbol{V}_{\mathbf{d}i}, \boldsymbol{V}_{\mathbf{q}i} \in \mathbb{R}^3$ represent the real and imaginary components of the phase-to-neutral voltage phasor at node i, respectively. We can combine the overall voltage variables at all nodes except the substation node and denote them using

$$\boldsymbol{V}_{\mathbf{d}} = \begin{bmatrix} \boldsymbol{V}_{\mathbf{d}1} \\ \boldsymbol{V}_{\mathbf{d}2} \\ \vdots \\ \boldsymbol{V}_{\mathbf{d}n} \end{bmatrix},\ \boldsymbol{V}_{\mathbf{q}} = \begin{bmatrix} \boldsymbol{V}_{\mathbf{q}1} \\ \boldsymbol{V}_{\mathbf{q}2} \\ \vdots \\ \boldsymbol{V}_{\mathbf{q}n} \end{bmatrix}, \tag{5.20}$$

where $\boldsymbol{V}_{\mathbf{d}}, \boldsymbol{V}_{\mathbf{q}} \in \mathbb{R}^{3n}$ are vectors of the real and imaginary components of the phase-to-neutral voltage, respectively. The initial voltage estimate in rectangular form is defined as $V^{(\kappa)} = V_{\mathrm{d}}^{(\kappa)} + jV_{\mathrm{q}}^{(\kappa)}$ where

$$V_{\mathrm{d}}^{(\kappa)} = \begin{bmatrix} V_{\mathrm{d}1}^{(\kappa)} \\ V_{\mathrm{d}2}^{(\kappa)} \\ \vdots \\ V_{\mathrm{d}n}^{(\kappa)} \end{bmatrix},\ V_{\mathrm{q}}^{(\kappa)} = \begin{bmatrix} V_{\mathrm{q}1}^{(\kappa)} \\ V_{\mathrm{q}2}^{(\kappa)} \\ \vdots \\ V_{\mathrm{q}n}^{(\kappa)} \end{bmatrix}. \tag{5.21}$$

Here, $V_{\mathrm{d}}^{(\kappa)}, V_{\mathrm{q}}^{(\kappa)} \in \mathbb{R}^{3n}$ are the real and imaginary components of the initial estimate $V^{(\kappa)}$, respectively. We can now rewrite (5.18) in terms of our new optimization variables $\boldsymbol{V}_{\mathbf{d}}, \boldsymbol{V}_{\mathbf{q}}$ to get the linearized power balance equations defined as

$$\boldsymbol{V}_{\mathbf{d}} = \Re\Big\{Z_1\Big\} + \Re\Big\{Z_2\Big\} \cdot \boldsymbol{P}_{\mathbf{Y}} + \Im\Big\{Z_2\Big\} \cdot \boldsymbol{Q}_{\mathbf{Y}}, \tag{5.22a}$$

$$\boldsymbol{V}_{\mathbf{q}} = \Im\Big\{Z_1\Big\} + \Im\Big\{Z_2\Big\} \cdot \boldsymbol{P}_{\mathbf{Y}} - \Re\Big\{Z_2\Big\} \cdot \boldsymbol{Q}_{\mathbf{Y}}, \tag{5.22b}$$

where Z_1, Z_2 have already been defined in (5.18). Now that we have the linearized power balance equations in the rectangular form, we also need to modify the voltage limits and expression for VUF since they depend on the voltage variables. On the contrary, we do not need to reformulate the inverter limits defined in (4.4) since our controllable variables $\boldsymbol{q}_{\mathbf{G},i}^{\phi}$ denoting the reactive power injection of single-phase solar PV inverters connected to phase ϕ at node i are unchanged. Next, we will implement the voltage limits and VUF expressions in the rectangular coordinate frame.

5.5.3 Voltage Limits

With substation node chosen as a balanced reference node, the voltage is fixed at

$$\boldsymbol{V}_{\mathbf{d}0} + j \cdot \boldsymbol{V}_{\mathbf{q}0} = \begin{bmatrix} e^{j0^\circ} & e^{-j120^\circ} & e^{j120^\circ} \end{bmatrix}^\top. \tag{5.23}$$

For every other node $i \in \mathcal{N}$ connected to phase $\phi \in \Phi$, the voltage limits can be represented by nonlinear constraints as

$$\underline{v}^2 \leq \left(\boldsymbol{v}_{\mathbf{d}i}^{\phi}\right)^2 + \left(\boldsymbol{v}_{\mathbf{q}i}^{\phi}\right)^2 \leq \overline{v}^2. \tag{5.24}$$

5.5.4 Voltage Unbalance

Recall that $\mathrm{a} = 1\angle 120^\circ = -0.5 + j0.87$ is used to calculate the symmetrical components defined in (2.1). The symmetrical components for critical node x can be represented in rectangular

coordinates as

$$
\begin{aligned}
3 \cdot v_x^- &= 3 \cdot (\boldsymbol{v}_{\mathbf{d}x}^- + j \cdot \boldsymbol{v}_{\mathbf{q}x}^-) = v_x^a + \mathrm{a}^2 \cdot v_x^b + \mathrm{a} \cdot v_x^c \\
&= \Big(\boldsymbol{v}_{\mathbf{d}x}^a + j\boldsymbol{v}_{\mathbf{q}x}^a\Big) + \Big(-0.5 - j0.87\Big)\Big(\boldsymbol{v}_{\mathbf{d}x}^b + j\boldsymbol{v}_{\mathbf{q}x}^b\Big) + \Big(-0.5 + j0.87\Big)\Big(\boldsymbol{v}_{\mathbf{d}x}^c + j\boldsymbol{v}_{\mathbf{q}x}^c\Big)
\end{aligned}
$$

$$
3 \cdot \begin{bmatrix} \boldsymbol{v}_{\mathbf{d}x}^- \\ \boldsymbol{v}_{\mathbf{q}x}^- \end{bmatrix} = \begin{bmatrix} 1 & -0.5 & -0.5 \\ 0 & -0.87 & 0.87 \end{bmatrix} \begin{bmatrix} \boldsymbol{v}_{\mathbf{d}x}^a \\ \boldsymbol{v}_{\mathbf{d}x}^b \\ \boldsymbol{v}_{\mathbf{d}x}^c \end{bmatrix} + \begin{bmatrix} 0 & 0.87 & -0.87 \\ 1 & -0.5 & -0.5 \end{bmatrix} \begin{bmatrix} \boldsymbol{v}_{\mathbf{q}x}^a \\ \boldsymbol{v}_{\mathbf{q}x}^b \\ \boldsymbol{v}_{\mathbf{q}x}^c \end{bmatrix}, \tag{5.25a}
$$

$$
\begin{aligned}
3 \cdot v_x^+ &= 3 \cdot (\boldsymbol{v}_{\mathbf{d}x}^+ + j \cdot \boldsymbol{v}_{\mathbf{q}x}^+) = v_x^a + \mathrm{a} \cdot v_x^b + \mathrm{a}^2 \cdot v_x^c \\
&= \Big(\boldsymbol{v}_{\mathbf{d}x}^a + j\boldsymbol{v}_{\mathbf{q}x}^a\Big) + \Big(-0.5 + j0.87\Big)\Big(\boldsymbol{v}_{\mathbf{d}x}^b + j\boldsymbol{v}_{\mathbf{q}x}^b\Big) + \Big(-0.5 - j0.87\Big)\Big(\boldsymbol{v}_{\mathbf{d}x}^c + j\boldsymbol{v}_{\mathbf{q}x}^c\Big)
\end{aligned}
$$

$$
3 \cdot \begin{bmatrix} \boldsymbol{v}_{\mathbf{d}x}^+ \\ \boldsymbol{v}_{\mathbf{q}x}^+ \end{bmatrix} = \begin{bmatrix} 1 & -0.5 & -0.5 \\ 0 & 0.87 & -0.87 \end{bmatrix} \begin{bmatrix} \boldsymbol{v}_{\mathbf{d}x}^a \\ \boldsymbol{v}_{\mathbf{d}x}^b \\ \boldsymbol{v}_{\mathbf{d}x}^c \end{bmatrix} + \begin{bmatrix} 0 & -0.87 & 0.87 \\ 1 & -0.5 & -0.5 \end{bmatrix} \begin{bmatrix} \boldsymbol{v}_{\mathbf{q}x}^a \\ \boldsymbol{v}_{\mathbf{q}x}^b \\ \boldsymbol{v}_{\mathbf{q}x}^c \end{bmatrix}, \tag{5.25b}
$$

where $v_x^- = \boldsymbol{v}_{\mathbf{d}x}^- + j\boldsymbol{v}_{\mathbf{q}x}^-$ and $v_x^+ = \boldsymbol{v}_{\mathbf{d}x}^+ + j\boldsymbol{v}_{\mathbf{q}x}^+$ are the rectangular form representation of the negative and positive sequence voltage phasors, respectively. We can substitute the expressions for rectangular components derived using (5.25) in (5.1) to express the objective function minimizing voltage unbalance.

5.5.5 Iterative Approach

Similar to the FOT-OPF iterative approach, we replace the nonlinear power balance equations in OPF_{opt} defined at the beginning of this chapter with the linearized equations derived using the fixed-point interpretation. As illustrated in Fig. 5.1, the iterative approach using fixed-point linearization (FP-OPF) is carried out according to the following steps:

1) *Initialization:* Start with no-load voltage $W = V^{(\kappa=0)}$.

2) *Solve OPF:* Solve a simplified optimization problem OPF_{FP} which utilizes the initial voltage estimate $V^{(\kappa)}$ to linearize the power flow equations using FP interpretation. The solution of the

optimization problem is the new estimate is $V^{(\kappa+1)}$.

$$
\begin{aligned}
&\min \;\; \text{VUF (5.1) or } p_{\text{ss}} \text{ (5.2) or } p_{\text{loss}} \text{ (5.3)} && (\text{OPF}_{\text{FP}})\\
&\text{s.t.} \;\; \boldsymbol{V}_{\mathbf{d}0} + j \cdot \boldsymbol{V}_{\mathbf{q}0} = \begin{bmatrix} e^{j0^\circ} & e^{-j120^\circ} & e^{j120^\circ} \end{bmatrix}^\top,\\
&\qquad \underline{v}^2 \leq \left(\boldsymbol{v}_{\mathbf{d}i}^{\phi}\right)^2 + \left(\boldsymbol{v}_{\mathbf{q}i}^{\phi}\right)^2 \leq \overline{v}^2, && \forall i \in \mathcal{N}, \phi \in \Phi,\\
&\qquad -\overline{q}_{\text{G},l}^{\phi} \leq \boldsymbol{q}_{\mathbf{G},l}^{\phi} \leq \overline{q}_{\text{G},l}^{\phi}, && \forall l \in \mathcal{G}, \phi \in \Phi,\\
&\qquad \boldsymbol{V}_{\mathbf{d}} = \Re\Big\{Z_1\Big\} + \Re\Big\{Z_2\Big\} \cdot \boldsymbol{P}_{\mathbf{Y}} + \Im\Big\{Z_2\Big\} \cdot \boldsymbol{Q}_{\mathbf{Y}},\\
&\qquad \boldsymbol{V}_{\mathbf{q}} = \Im\Big\{Z_1\Big\} + \Im\Big\{Z_2\Big\} \cdot \boldsymbol{P}_{\mathbf{Y}} - \Re\Big\{Z_2\Big\} \cdot \boldsymbol{Q}_{\mathbf{Y}}.
\end{aligned}
$$

3) *Check convergence:* Terminate if $\sum_{i \in \mathcal{N}} |V_i^{(\kappa+1)} - V_i^{(\kappa)}|$ is below specified tolerance ϵ.

4) *Update voltage estimate:* If the stopping criterion is not satisfied, directly update the voltage estimate $V^{(\kappa)} = V^{(\kappa+1)}$ and increase the iteration count to $\kappa = \kappa + 1$ and return to step 2).

5.6 Forward-Backward Sweep Linearization (FBS-OPF)

The forward-backward sweep (FBS) is an iterative power flow solution approach which exploits the radial topology of distribution grids [14]. It has already been utilized in three-phase OPF formulations [75, 101, 102] due to the easy mathematical formulation which gives rise to three-phase OPF problems that can be efficiently solved. In [75], an iterative FBS approach is employed to reducing voltage unbalance by enforcing limits on the negative sequence voltage. While [101] focuses on solving a multi-period optimal power flow problem to determine optimal placement and size of storage in low voltage networks, [102] proposes a chance-constrained OPF with objective to minimize network losses and cost of DER control. All three papers [75, 101, 102] test their implementation on a small European LV feeder [103] with constant power loads and the extension to a more general case including ZIP loads with both wye- and delta-connections are not presented.

In this section, we replace the nonlinear power balance equations in our three-phase OPF framework with a single iteration of the FBS approach. Similar to the previous two methods, we will

solve the simplified optimization problem iteratively to obtain AC feasible solutions. A single iteration of the FBS approach comprises of:

- *Backward sweep* to calculate the current injections at every node using the initial voltage estimate $V^{(\kappa)}$ and determine the branch currents by applying Kirchoff's current law (KCL)
- *Forward sweep* to update the voltage at all nodes by using the branch currents calculated from the backward sweep and applying Kirchoff's voltage law (KVL)

The next subsection provide a detailed description of the backward and forward sweep implementation.

5.6.1 Linearized Power Balance Equations

Similar to the FP-OPF method, we implement this method in the rectangular coordinate frame so that the power balance equations can be expressed in a linear form. Our initial voltage estimate for this method is the no-load voltage $W = V^{(\kappa)} = V_{\mathrm{d}}^{(\kappa)} + jV_{\mathrm{q}}^{(\kappa)}$ which can be calculated using (5.17).

5.6.1.1 Backward Sweep

As mentioned previously, we start with a backward sweep to calculate the branch currents. This step is referred to as backward sweep since we start calculating current injections at the remote terminal nodes and move towards the root node which is the substation. We denote the real and imaginary components of branch currents flowing between intermediate node $k \in \mathcal{N}$ and terminal node $i \in \mathcal{N}$ using $\boldsymbol{I}_{\mathbf{d},ki}, \boldsymbol{I}_{\mathbf{q},ki} \in \mathbb{R}^3$. Since these branches are located at the end of the feeder, it must be noted that the branch current will be equal to the current injections at the terminal node i, which are represented by $I_{\mathrm{d}i}, I_{\mathrm{q}i} \in \mathbb{R}^3$ in the rectangular form. So, we express the current injections at the terminal node i by using the real and imaginary components of the initial voltage

estimate $V_{\mathrm{d}i}^{(\kappa)}, V_{\mathrm{q}i}^{(\kappa)} \in \mathbb{R}^3$ at node i and representing the element-wise division using $\oslash$ to get

$$\begin{aligned} I_i = I_{ki} &= S_i^* \oslash V_i^{(\kappa)^*} \\ I_{\mathrm{d}i} + jI_{\mathrm{q}i} = \boldsymbol{I}_{\mathbf{d},ki} + j\boldsymbol{I}_{\mathbf{q},ki} &= (\boldsymbol{P}_i - j\boldsymbol{Q}_i) \oslash (V_{\mathrm{d}i}^{(\kappa)} - jV_{\mathrm{q}i}^{(\kappa)}), \end{aligned} \tag{5.26}$$

where $\boldsymbol{P}_i = \boldsymbol{P}_{\mathbf{G},i} - P_{\mathrm{L},i}$ and $\boldsymbol{Q}_i = \boldsymbol{Q}_{\mathbf{G},i} - Q_{\mathrm{L},i}$ are the active and reactive power components of the complex power injection S_i, respectively. The load components $P_{\mathrm{L},i}, Q_{\mathrm{L},i}$ are constant and calculated by using the initial voltage estimate $V^{(\kappa)}$ and following the same procedure explained in (5.10)-(5.13) for the FOT-OPF method. Furthermore, $\boldsymbol{P}_{\mathbf{G},i}$ is also fixed since it represents the active power injections of solar PV inverters. Our controllable variable $\boldsymbol{q}_{\mathbf{G},i}^{\phi}$ will be show up in (5.26) as a part of $\boldsymbol{Q}_i$ and more specifically $\boldsymbol{Q}_{\mathbf{G},i}$, when the terminal node i has a solar PV inverter connected at phase $\phi \in \Phi$. We can rewrite (5.26) by equating the real and imaginary parts as

$$\boldsymbol{I}_{\mathbf{d},ki} = I_{\mathrm{d}i} = \left(\boldsymbol{P}_i \odot V_{\mathrm{d}i}^{(\kappa)} + \boldsymbol{Q}_i \odot V_{\mathrm{q}i}^{(\kappa)}\right) \oslash \left(V_{\mathrm{d}i}^{(\kappa)^2} + V_{\mathrm{q}i}^{(\kappa)^2}\right), \tag{5.27a}$$

$$\boldsymbol{I}_{\mathbf{q},ki} = I_{\mathrm{q}i} = \left(\boldsymbol{P}_i \odot V_{\mathrm{q}i}^{(\kappa)} - \boldsymbol{Q}_i \odot V_{\mathrm{d}i}^{(\kappa)}\right) \oslash \left(V_{\mathrm{d}i}^{(\kappa)^2} + V_{\mathrm{q}i}^{(\kappa)^2}\right). \tag{5.27b}$$

For all other branches connecting nodes $m \in \mathcal{N}_0$ and k, we can apply KCL to get

$$\boldsymbol{I}_{\mathbf{d},mk} = I_{\mathrm{d}k} + \sum_{i \in \mathcal{N}_k} \boldsymbol{I}_{\mathbf{d},ki}, \tag{5.28a}$$

$$\boldsymbol{I}_{\mathbf{q},mk} = I_{\mathrm{q}k} + \sum_{i \in \mathcal{N}_k} \boldsymbol{I}_{\mathbf{q},ki}, \tag{5.28b}$$

where $\mathcal{N}_k$ is the set of downstream nodes connected to node k. By substituting (5.27) in (5.28), we now have linear expressions for all the branch currents in terms of our controllable variables $\boldsymbol{q}_{\mathbf{G},i}^{\phi}$. Next, we will implement the forward sweep to complete one single iteration of the FBS approach.

5.6.1.2 Forward Sweep

After all the branch currents are calculated using the backward sweep, we apply KVL to perform a forward sweep. This step is referred to as forward sweep since we start with the root node and move towards the remote terminal nodes. Recall that the voltage at the root node (i.e. substation) denoted by $V_0 = \boldsymbol{V}_{\mathbf{d}0} + j\boldsymbol{V}_{\mathbf{q}0}$ is fixed. Based on the ordering of the nodes in the system, we

first update the voltage at node $m \in \mathcal{N}_0$ which is connected to the root node using

$$\begin{aligned} V_m &= A_{0m} \cdot V_0 - Z_{0m} \cdot I_{0m} \\ \boldsymbol{V}_{\mathbf{d}m} + j\boldsymbol{V}_{\mathbf{q}m} &= A_{0m} \cdot (\boldsymbol{V}_{\mathbf{d}0} + j\boldsymbol{V}_{\mathbf{q}0}) - \underbrace{Z_{0m} \cdot (\boldsymbol{I}_{\mathbf{d},0m} + j\boldsymbol{I}_{\mathbf{q},0m})}_{V_{0m}}, \end{aligned} \tag{5.29}$$

where $V_m = \boldsymbol{V}_{\mathbf{d}m} + j\boldsymbol{V}_{\mathbf{q}m}$ is the voltage at node m. $Z_{0m} \in \mathbb{C}^{3\times3}$ is the series branch impedance matrix for branch connecting the substation and node m as defined in (3.2). It is important to note here that the shunt admittance of all the branches are not ignored and instead modelled as constant impedance loads using (5.10). Hence, we only need to use the series branch impedance matrix in the forward sweep to calculate the voltage drop V_{0m} across the branch connecting the substation and node m. The voltage transformation matrix $A_{0m} \in \mathbb{R}^{3\times3}$ is usually an identity matrix for branches corresponding to distribution lines and cables. For transformers and voltage regulators, A_{0m} can be calculated using the "ABCD" matrix definitions in [14]. The rectangular components of current $\boldsymbol{I}_{\mathbf{d},0m}, \boldsymbol{I}_{\mathbf{q},0m}$ flowing in the branch connecting the substation and node m has already been calculated during the backward sweep as defined in (5.28). By separating and equating the real and imaginary terms in (5.29), we get

$$\boldsymbol{V}_{\mathbf{d}m} = A_{0m} \cdot \boldsymbol{V}_{\mathbf{d}1} - \Re\{V_{0m}\}, \tag{5.30a}$$

$$\boldsymbol{V}_{\mathbf{q}m} = A_{0m} \cdot \boldsymbol{V}_{\mathbf{q}1} - \Im\{V_{0m}\}. \tag{5.30b}$$

In general, the forward sweep equation for any downstream node k connected to upstream node m can be expressed as

$$\boldsymbol{V}_{\mathbf{d}k} = A_{mk} \cdot \boldsymbol{V}_{\mathbf{d}m} - \Re\{V_{mk}\}, \tag{5.31a}$$

$$\boldsymbol{V}_{\mathbf{q}k} = A_{mk} \cdot \boldsymbol{V}_{\mathbf{q}m} - \Im\{V_{mk}\}, \tag{5.31b}$$

$$\text{where } V_{mk} = Z_{mk} \cdot (\boldsymbol{I}_{\mathbf{d},mk} + j\boldsymbol{I}_{\mathbf{q},mk}),$$

and $V_k = \boldsymbol{V}_{\mathbf{d}k} + j\boldsymbol{V}_{\mathbf{q}k}$ is the voltage at node k. $Z_{mk} \in \mathbb{C}^{3\times3}$ is the series branch impedance matrix for branch mk with voltage drop V_{mk}. We now have linear expressions for all the node voltages in terms of our optimization variables. We can replace the nonlinear power balance equations in OPF with (5.28) and (5.31), which are a set of linear constraints.

5.6.2 Iterative Approach

Since this method was implemented in the rectangular coordinate frame, we can reuse the voltage constraints as well as the inverter limits defined for the FP-OPF approach and replace the power balance equations with the backward and forward sweep equations. Similar to the previous methods, we employ an the iterative approach using the forward-backward sweep (FBS-OPF) according to the following steps:

1) *Initialization:* Start with no-load voltage $W = V^{(\kappa=0)}$.

2) *Solve OPF:* Solve a simplified optimization problem OPF_{FBS} which utilizes the initial voltage estimate $V^{(\kappa)}$ to linearize the power flow equations using FP interpretation. The solution of the optimization problem is the new estimate is $V^{(\kappa+1)}$.

$$\text{min VUF (5.1) or } p_{\text{ss}} \text{ (5.2) or } p_{\text{loss}} \text{ (5.3)} \qquad (\text{OPF}_{\text{FBS}})$$

$$\text{s.t. } \boldsymbol{V}_{\mathbf{d}0} + j \cdot \boldsymbol{V}_{\mathbf{q}0} = \begin{bmatrix} e^{j0^\circ} & e^{-j120^\circ} & e^{j120^\circ} \end{bmatrix}^\top,$$

$$\underline{v}^2 \leq \left(\boldsymbol{v}_{\mathbf{d}i}^{\phi}\right)^2 + \left(\boldsymbol{v}_{\mathbf{q}i}^{\phi}\right)^2 \leq \overline{v}^2, \qquad \forall i \in \mathcal{N}, \phi \in \Phi,$$

$$-\overline{q}_{\text{G},l}^{\phi} \leq \boldsymbol{q}_{\mathbf{G},l}^{\phi} \leq \overline{q}_{\text{G},l}^{\phi}, \qquad \forall l \in \mathcal{G}, \phi \in \Phi,$$

$$\boldsymbol{I}_{\mathbf{d},mk} = I_{\text{d}k} + \sum_{i \in \mathcal{N}_k} \boldsymbol{I}_{\mathbf{d},ki}, \; \boldsymbol{I}_{\mathbf{q},mk} = I_{\text{q}k} + \sum_{i \in \mathcal{N}_k} \boldsymbol{I}_{\mathbf{q},ki}, \qquad \forall m \in \mathcal{N}_0, k \in \mathcal{N},$$

$$\boldsymbol{V}_{\mathbf{d}k} = A_{mk} \cdot \boldsymbol{V}_{\mathbf{d}m} - \Re\{V_{mk}\}, \; \boldsymbol{V}_{\mathbf{q}k} = A_{mk} \cdot \boldsymbol{V}_{\mathbf{q}m} - \Im\{V_{mk}\}, \qquad \forall m \in \mathcal{N}_0, k \in \mathcal{N}.$$

3) *Check convergence:* Terminate if $\sum_{i \in \mathcal{N}} |V_i^{(\kappa+1)} - V_i^{(\kappa)}|$ is below specified tolerance ϵ.

4) *Update voltage estimate:* If the stopping criterion is not satisfied, directly update the voltage estimate $V^{(\kappa)} = V^{(\kappa+1)}$ and increase the iteration count to $\kappa = \kappa + 1$ and return to step 2).

5.7 Linear Benchmark- LinDist3Flow

The LinDist3Flow model from [89] proposes a linear approximation of the AC power flow equations for unbalanced distribution grids. In this chapter, we utilize the LinDist3Flow model as a benchmark for the approximate solutions obtained after the first iteration.

5.7.1 Linearized Power Balance Equations

Following [89], we initially calculate the power flow S_{ik} through the branch connecting upstream node $i \in \mathcal{N}_0$ and downstream node $k \in \mathcal{N}$ similar to the backward sweep using

$$S_{ik} = \boldsymbol{P}_{ik} + j\boldsymbol{Q}_{ik} = \underbrace{(\boldsymbol{P}_k + j\boldsymbol{Q}_k)}_{S_k} + \sum_{l \in \mathcal{N}_k} \underbrace{(\boldsymbol{P}_l + j\boldsymbol{Q}_l)}_{S_l}, \tag{5.32}$$

where S_k, S_l are power injections at node k and l, respectively. It is important to note that (5.32) only considers power injections at all nodes in the network and ignores network line losses since they involve nonlinear terms.

Next, we define a new optimization variable $\boldsymbol{y}_i^{\phi} = (\boldsymbol{v}_{\mathbf{d}i}^{\phi})^2 + (\boldsymbol{v}_{\mathbf{q}i}^{\phi})^2$ at any node $i \in \mathcal{N}_0$ connected to phase $\phi \in \Phi$. So, the voltage magnitude constraints at the substation becomes

$$\boldsymbol{Y}_0 = \begin{bmatrix} \boldsymbol{y}_0^a & \boldsymbol{y}_0^b & \boldsymbol{y}_0^c \end{bmatrix}^{\top} = \begin{bmatrix} 1 & 1 & 1 \end{bmatrix}^{\top}. \tag{5.33}$$

For any other node i connected to phase ϕ, the voltage magnitude is bounded by

$$\underline{v}^2 \leq \boldsymbol{y}_i^{\phi} \leq \overline{v}^2. \tag{5.34}$$

We next use the KVL equation defined for a branch connecting upstream node i to downstream node k and square both sides. By ignoring the higher order term corresponding to the square of the voltage drop across the branch, we get

$$\boldsymbol{Y}_i = \boldsymbol{Y}_k + 2 \cdot \Re\{\Gamma_k \odot Z_{ik}^* \cdot S_{ik}\} \tag{5.35a}$$

$$= \boldsymbol{Y}_k + 2 \cdot \Gamma_k \odot \Re\{Z_{ik}^*\} \cdot \boldsymbol{P}_{ik} + 2 \cdot \Gamma_k \odot \Im\{Z_{ik}^*\} \cdot \boldsymbol{Q}_{ik}, \tag{5.35b}$$

where $\Gamma_k \in \mathbb{C}^{3\times 3}$ is a square matrix denoting the ratio of voltage between different phases defined as

$$\Gamma_k = \begin{bmatrix} 1 & \gamma_k^{ab} & \gamma_k^{ac} \\ \gamma_k^{ba} & 1 & \gamma_k^{bc} \\ \gamma_k^{ca} & \gamma_k^{cb} & 1 \end{bmatrix} = \begin{bmatrix} 1 & v_k^a (v_k^b)^{-1} & v_k^a (v_k^c)^{-1} \\ v_k^b (v_k^a)^{-1} & 1 & v_k^b (v_k^c)^{-1} \\ v_k^c (v_k^a)^{-1} & v_k^c (v_k^b)^{-1} & 1 \end{bmatrix}. \tag{5.36}$$

For (5.35) to be linear, Γ_k is assumed constant and simplifies to

$$\Gamma_k = \begin{bmatrix} 1 & 1\angle 120^\circ & 1\angle -120^\circ \\ 1\angle -120^\circ & 1 & 1\angle 120^\circ \\ 1\angle 120^\circ & 1\angle -120^\circ & 1 \end{bmatrix}. \tag{5.37}$$

The LinDist3Flow problem can be summarized as

$$\begin{aligned}
\min \quad & \text{VUF (5.1) or } p_{\text{ss}} \text{ (5.2) or } p_{\text{loss}} \text{ (5.3)} && && (\text{OPF}_{\text{LDF}}) \\
\text{s.t.} \quad & \boldsymbol{Y}_0 = \begin{bmatrix} 1 & 1 & 1 \end{bmatrix}^\top, \\
& \underline{v}^2 \leq \boldsymbol{y}_i^\phi \leq \overline{v}^2, && && \forall i \in \mathcal{N}, \phi \in \Phi, \\
& -\overline{q}_{\text{G},l}^\phi \leq \boldsymbol{q}_{\mathbf{G},l}^\phi \leq \overline{q}_{\text{G},l}^\phi, && && \forall l \in \mathcal{G}, \phi \in \Phi, \\
& \boldsymbol{Y}_i = \boldsymbol{Y}_k + 2 \cdot \Gamma_k \odot \Re\{Z_{ik}^*\} \cdot \boldsymbol{P}_{ik} + 2 \cdot \Gamma_k \odot \Im\{Z_{ik}^*\} \cdot \boldsymbol{Q}_{ik}, && && \forall i \in \mathcal{N}_0, k \in \mathcal{N}.
\end{aligned}$$

5.8 Summary

Table 5.4 summarizes all three scalable methods discussed in this chapter along with the original approach to solve OPF as discussed in the beginning of this chapter and the LinDist3Flow benchmark method described in the previous section. Recall that while the scalable methods cannot guarantee convergence to an optimal solution, they are able to obtain solutions that are AC feasible. Some key observations when comparing the computational complexity and solution quality of all three scalable methods include:

- *First-order Taylor approximation:* The FOT-OPF approach provides the best approximation accuracy around the initial voltage estimate $V^{(\kappa)}$, which means it is a good approach if local behavior is of interest [12]. Each iteration of this method involves calculation of the Jacobian matrix J, which could be a computationally expensive step for large systems.

- *Fixed-point linearization:* The fixed-point equations at each iteration can be interpreted as an interpolation between two solutions (i.e. initial voltage estimate $V^{(\kappa)}$ and FP-OPF solution $V^{(\kappa+1)}$). So, it might lead to a better approximation if a less local behavior is of

interest [12]. This strategy has a computational advantage over FOT-OPF method since it does not require calculation of the Jacobian matrix J provided that the nodal admittance matrix Y is precalculated in advance. However, it is also necessary to recalculate Y if there are any topology changes in the feeder (E.g. regulator tap switching).

- *Forward-backward sweep:* Both the FOT-OPF and FP-OPF methods do not exploit the radial nature of distribution grids. Hence, these methods are still computationally heavy to solve. On the contrary, the FBS-OPF method does not involve the time-consuming step of calculating large matrices such as J or Y. Similar to the other two methods, this method does not guarantee convergence to an optimal solution, but is computationally tractable to determine AC feasible solutions.

Abbreviation	**Description**
TP-OPF	Conventional approach solving OPF_{opt} by using nonlinear power balance equations
FOT-OPF	Iterative approach solving OPF_{FOT} with power balance equations linearized using first-order Taylor's approximation
FP-OPF	Iterative approach solving OPF_{FP} with power balance equations linearized using fixed-point equation
FBS-OPF	Iterative approach solving OPF_{FBS} with power balance equations replaced by forward-backward sweep equations
LinDist3Flow	Benchmark approach solving OPF_{LDF} with power balance equations replaced by three-phase version of the LinDistFlow model

Table 5.4: Summary of different methods to solve three-phase OPF.

5.9 Case Study Setup

For our analysis, the performance of each method shown in Table 5.4 was evaluated using a large test case based on one of the taxonomic distribution feeders from Pacific Northwest National Laboratory (PNNL) [104]. To do this, we consider three different objective functions:

1) C1-P_{ss}: Minimize active power at substation using (5.2)

2) C2-P_{loss}: Minimize network losses using (5.3)

3) C3-VUF: Minimize voltage unbalance at a critical three-phase node (e.g., a node with a three-phase motor load) using (5.1)

5.9.1 Feeder Description

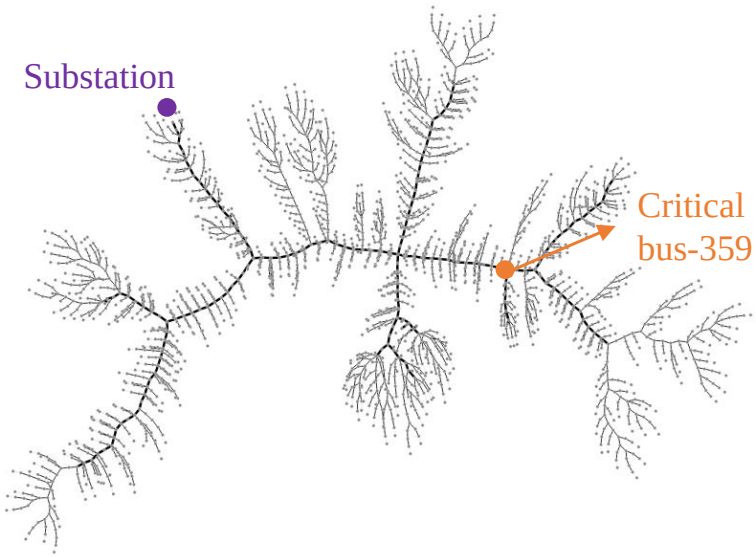

Figure 5.2: Modified taxonomy feeder R1-12.47-1 visualized using [1].

The R1-12-47-1 feeder shown in Fig. 5.2 comprises of $n = 1833$ nodes with 2204 single-phase connections. It represents a moderately populated suburban and rural area composed of single family homes and light commercial loads [86]. The feeder was modified to include 598 houses with solar PV systems (265 at phase a, 150 at phase b and 183 at phase c). The voltage magnitude

limits at all single-phase connections is set to $\underline{v} = 0.9$ p.u. and $\overline{v} = 1.1$ p.u. For C3-VUF, we choose a three-phase node (shown by the orange dot in Fig. 5.2) far away from the substation to which critical three-phase equipment such as induction motor is connected.

5.9.2 Measurement Data

We solve the OPF for multiple time instances in a day. For our numerical experiments, we use realistic measurement data for the load power and solar PV injections of each of the 598 houses. The solar PV active power generation is simulated based on 1-minute irradiance data from the National Renewable Energy Laboratory's Measurement and Instrumentation Data Center [105]. Fig. 5.3a illustrates the six different PV profiles used to model the active power injections of the solar PV systems. The maximum apparent power capacity of each solar PV inverter is 20 kVA. Furthermore, we also use actual 1-minute residential load data from Pecan Street [106]. Fig. 5.3b represents 30 unique load profiles modelling electric vehicle charging behavior as well as HVAC, refrigerator and other appliance use.

We assume that load and PV generation remain constant within the 1-minute interval. The overall number of time steps over the day by using the 1-minute resolution load and PV data is $T = 1440$.

5.9.3 Investigations

In the next two sections, we describe the results of the numerical experiments and provide a detailed comparison of the performance of all the methods listed in Table. 5.4.

- Section 5.10 evaluates **performance of the three iterative approaches** and compares them with the nonlinear TP-OPF and Lin3DistFlow formulations. More specifically, we assess the solution quality, computation time and linearization accuracy of all three methods.

- Section 5.11 discusses the results obtained for time-based simulations in a realistic setting. We examine the **impact of time delays and limited measurements** on the performance of the iterative methods.

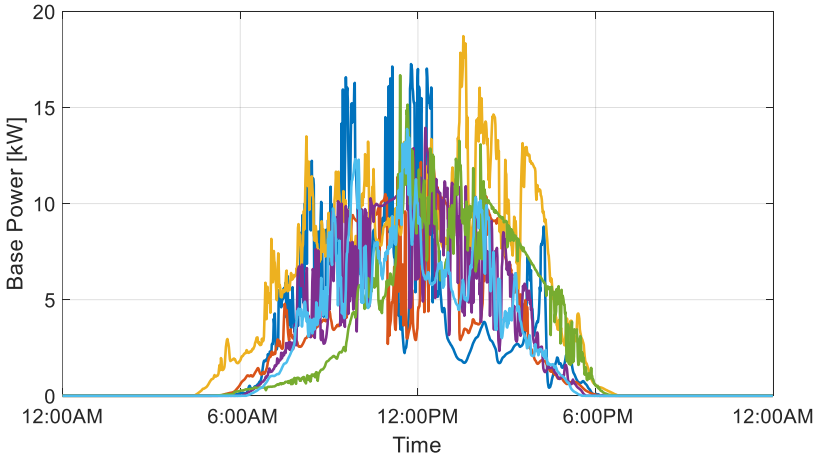

(a) Solar PV active power

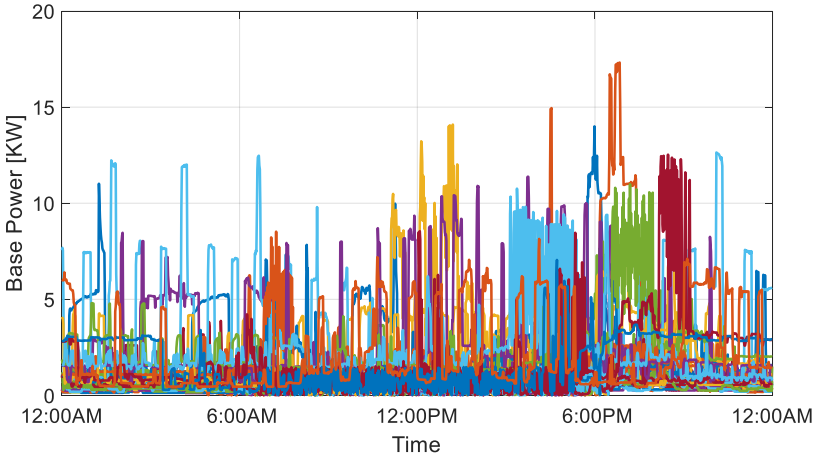

(b) Residential load

Figure 5.3: Actual 1-minute resolution measurement data. (a) Solar PV active power profile from NREL (b) Residential load profile from Pecan Street.

5.10 Case Study I: Performance Evaluation of Scalable Methods

We first solve the OPF for multiple time instances to compare the performance of the three iterative approaches using linear power flow models with the benchmark TP-OPF formulation. We also compare quality of the approximate solutions obtained after one iteration with the solution obtained using Lin3DistFlow.

5.10.1 Performance Comparison with TP-OPF

We start by running simulations for a single time instance and benchmark the performance of all three iterative methods against the conventional TP-OPF. Recall that the PV penetration level is defined as the ratio of total PV generation (in kW) to the overall rated load (in kW). For this case study, we choose the active power injected by each PV inverter such that the PV penetration level is 50%.

5.10.1.1 Objective Value

Table 5.5 shows the results of the objective value when solving the three cases. The initial objective value is obtained by running a power flow with zero reactive power injections from the PV inverters. We see that all methods converge to very similar objective values. While both the network losses and substation active power are minimized by all the methods, as illustrated by the results for C1-P_{ss} and C2-P_{loss}, we also observe from the objective value for for case C3-VUF that all methods are able to reduce the VUF at node-359 to zero. Further, note that all solutions are feasible, as the iterative methods were run until convergence. This was also verified by running a power flow using the final solution of the iterative approach as the start point. For all the iterative methods, the power flow converged in one iteration to the same operating point as the initial point.

Case	**Initial (pu)**	**TP-OPF (pu)**	**FOT-OPF (pu)**	**FP-OPF (pu)**	**FBS-OPF (pu)**
C1-P_{ss}	29.44	29.17	29.16	29.17	29.17
C2-P_{loss}	2.06	1.77	1.77	1.77	1.77
C3-VUF	0.018	0	0	0	0

Table 5.5: Comparison of objective value for single time instance.

5.10.1.2 Computation Time

The total computation time for all methods is summarized in Table 5.6. Recall that TP-OPF is not solved iteratively and takes more than two hours to converge for all three cases. On the contrary, the iterative methods converge within 12 iterations with a computation time of less than 12 minutes. Furthermore, we observe that FBS-OPF exhibits the lowest computation time for all three cases. This is due to the fact that FBS-OPF exploits the radial structure of distribution grids and does not require calculation of large matrices such as the Jacobian J or nodal admittance matrix Y as explained in the previous section.

Case	**TP-OPF**	**FOT-OPF**		**FP-OPF**		**FBS-OPF**	
	min	**min**	**iter**	**min**	**iter**	**min**	**iter**
C1-P_{ss}	325.6	5.1	11	4.7	8	0.6	8
C2-P_{loss}	213.6	4.7	7	4.4	8	3.4	8
C3-VUF	130.9	6.0	12	11.8	8	0.5	8

Table 5.6: Comparison of computation time for single time instance.

The computation time shown in Table 5.6 corresponds to the time taken by Ipopt to solve the problem. If we examine the time elapsed to setup the problem that Ipopt solves, we see that the average time taken for TP-OPF for all three cases is 10 seconds. For the iterative methods, we observe that FOT-OPF takes longer time to setup (around 15 seconds) every iteration because we need to calculate the Jacobian and run a power flow until convergence to determine the initial voltage estimate. On the other hand, FP-OPF and FBS-OPF directly update the voltage estimate and as a result, take lesser average time of 8 and 5 seconds per iteration, respectively, to setup the problem.

5.10.1.3 Convergence

To further investigate the convergence for all the methods, the objective value and average reactive power injections at each iteration are shown in Fig. 5.4. A noteworthy observation is that both FP-OPF and FBS-OPF converge to identical solutions at each iteration for all cases. Furthermore, we see from the average reactive power injections that FOT-OPF finds the same solution as the benchmark TP-OPF for cases C2-P_{loss} and C3-VUF. For case C1-P_{ss} in Fig. 5.4(a), we observe that FP-OPF and FBS-OPF take large steps during the first few iterations and converge to a different solution than the TP-OPF. In addition, we also notice an oscillatory behavior in the solutions of FOT-OPF which are not seen for either FP-OPF and FBS-OPF. This behavior might be due to the fact that the FOT-OPF voltage solutions are updated in each iteration by running a power flow until convergence in step 4) of the successive approximation approach described in Section 5.3.

5.10.2 Comparison of Approximate Solutions

We next investigate the approximation accuracy of the three linearizations when they are utilized as a direct replacement for the nonlinear AC power balance equations. For this, we compare the solutions obtained after one iteration of the successive approximation approach. The solutions of the three linearizations are benchmarked against the non-iterative LinDist3Flow formulation in terms of objective value and linearization accuracy. We determine the linearization accuracy by using the following procedure:

1) We terminate the successive approximation approach after the first iteration to get the reactive power injection of PV inverters $q^{\phi}_{\text{OPF},i}\ \forall i \in \mathcal{G}, \phi \in \Phi$ and the voltage solution $V^{(1)}_{\text{OPF}} \in \mathbb{C}^n$.

2) We then set the reactive power injections of PV inverter at node i connected to phase ϕ equal to $q^{\phi}_{\text{OPF},i}$ and utilize the voltage solution $V^{(1)}_{\text{OPF}}$ as the initial starting point to run a three-phase power flow until convergence. The resulting power flow solution is $V^{(1)}_{\text{PF}} \in \mathbb{C}^n$.

3) We use the new voltage solution $V^{(1)}_{\text{PF}}$ to calculate the mean difference per node given by

$$\Delta v = \frac{\sum |V^{(1)}_{\text{OPF}} - V^{(1)}_{\text{PF}}|}{n}. \tag{5.38}$$

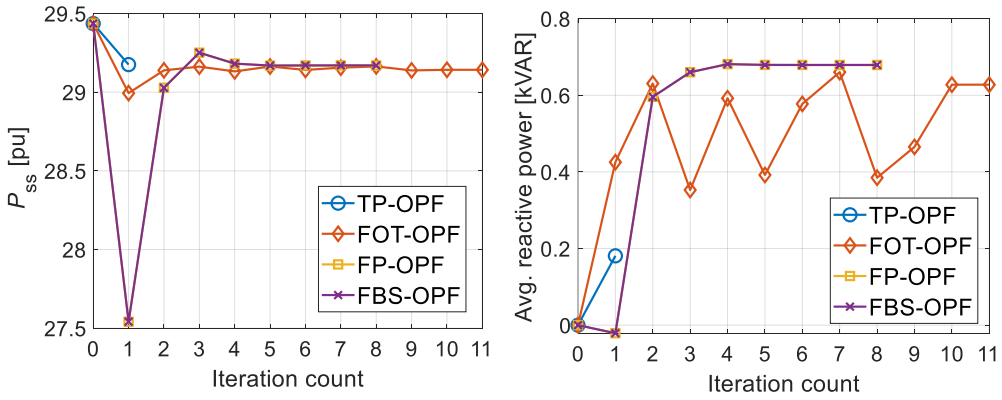

(a) C1-P_{ss}

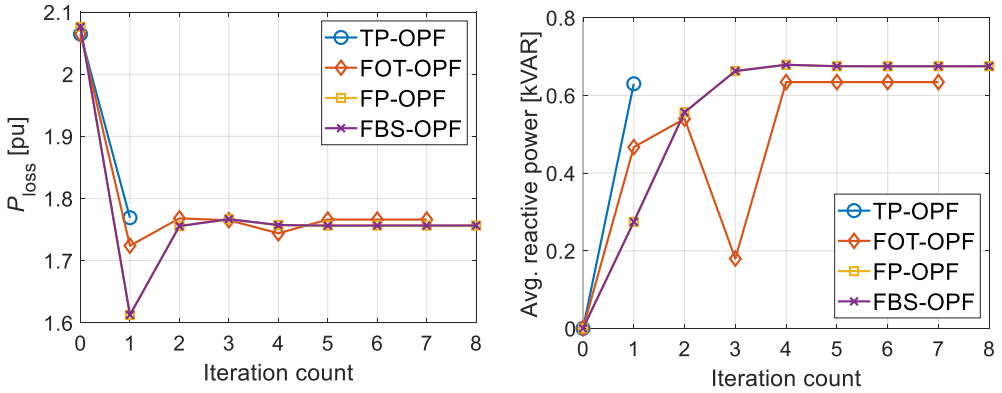

(b) C2-P_{loss}

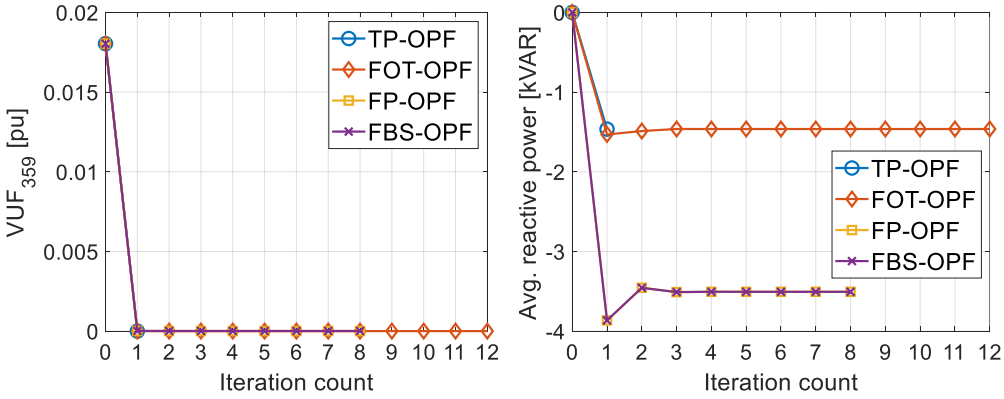

(c) C3-VUF

Figure 5.4: Convergence of objective value (left) and average reactive power injections (right) for single time instance.

The linearization accuracy Δv provides an indication of how far the voltage obtained after the first iteration of the successive approximation approach is from a feasible operating point which satisfies the nonlinear AC power flow equations.

5.10.2.1 Objective Value

Table 5.7 summarizes the objective value for the different linearizations after one iteration. We notice that the FOT-OPF provides the objective value that is closest to the final value. As expected based on the previous results, the FP-OPF and FBS-OPF provide similar solutions, with lower objective values. By comparing the results of LinDist3Flow with the other three methods, we see that objective value for cases C1-P_{ss} and C2-P_{loss} are noticeably lower. Recall that LinDist3Flow ignores line losses and as a result, underestimates the total losses in the network. Hence, it also underestimates the active power injection at the substation. Furthermore, we know that LinDist3Flow also approximates the ratio of the voltage between phases. This leads to a non-zero objective value for case C3-VUF whereas the other three methods are able to reduce the VUF to zero after the first iteration.

Case	**Initial (pu)**	**FOT-OPF (pu)**	**FP-OPF (pu)**	**FBS-OPF (pu)**	**LinDist3Flow (pu)**
C1-P_{ss}	29.44	28.99	27.54	27.54	25.28
C2-P_{loss}	2.06	1.72	1.61	1.61	0.83
C3-VUF	0.018	0	0	0	0.003

Table 5.7: Objective value after one iteration (single time instance).

5.10.2.2 Feasibility

The linearization accuracy denoted by the deviation Δv for different linear approximations is shown in Table 5.8. We notice that the FOT-OPF provides the solution with the lowest inaccuracy (i.e., the lowest Δv values). While the FP-OPF and FBS-OPF provide solutions with significantly higher inaccuracy, LinDist3Flow has the highest inaccuracy among all the methods. The better accuracy of the FOT-OPF may be because the initialization point for the FOT-OPF is a power flow solution and hence, much closer to an AC actual feasible operating point. We also observe that Δv is maximum for LinDist3Flow since the model does not consider line losses and approximates the unbalanced nature of the network. Based on the results shown in Table 5.8, we can conclude that FOT-OPF, FP-OPF and FBS-OPF exhibit better approximation accuracy than LinDist3Flow.

Case	**FOT-OPF (pu)**	**FP-OPF (pu)**	**FBS-OPF (pu)**	**LinDist3Flow (pu)**
C1-P_{ss}	0.0002	0.0073	0.0073	0.0234
C2-P_{loss}	0.0002	0.0069	0.0069	0.0231
C3-VUF	0.0001	0.0029	0.0029	0.0258

Table 5.8: linearization accuracy Δv after one iteration (single time instance).

5.10.3 Performance across Multiple Time Instances

The results from the previous section were obtained for a single time instance. In order to generalize the conclusions obtained from the previous results, we next evaluate the performance of the methods over multiple OPF instances. These instances are created by solving the OPF problem every two hours for one day (i.e. 12 time instances) with varying PV penetration levels and loading conditions by using the measurement data described in Section 5.9.2. For simplicity, we only discuss the results for case C3-VUF where the objective is to minimize voltage unbalance.

5.10.3.1 Comparison with TP-OPF

Fig. 5.5 illustrates the VUF at critical node-359 and computation time for TP-OPF as well as the three iterative methods obtained by solving for 12 multiple time instances throughout a single day. We observe that all the iterative methods are consistently able to obtain good quality solutions with the VUF at node-359 almost close to zero. During the middle of the day when PV penetration levels are high and the reactive power support is limited, we see that all the iterative methods including the benchmark TP-OPF obtain solutions with slightly higher VUF. Furthermore, we see that the iterative methods converge to a good quality solution much quicker than TP-OPF with FBS-OPF exhibiting the lowest computation time for all the 12 time instances.

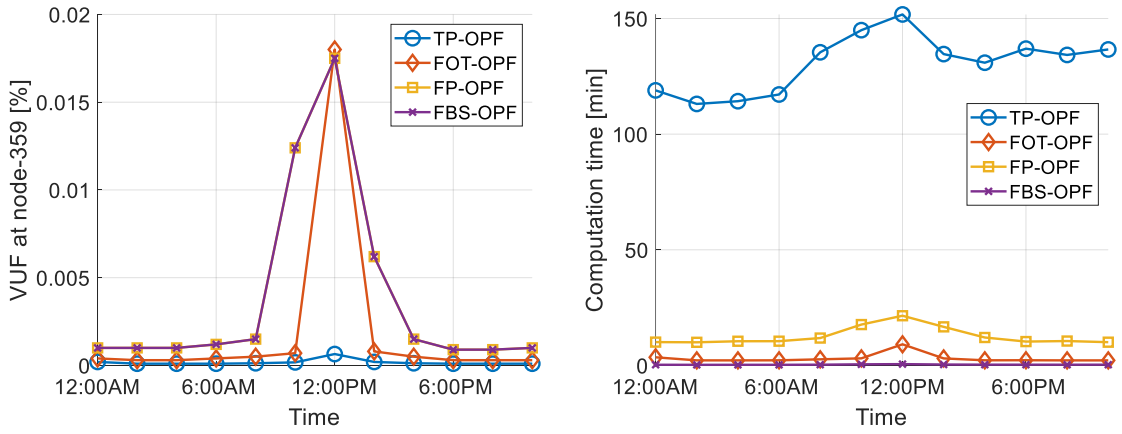

Figure 5.5: Objective value (left) and computation time (right) obtained by solving OPF every two hours in a single day.

Table 5.9 summarizes the results shown in Fig. 5.5 for TP-OPF and the three iterative methods. The average, minimum and maximum values are calculated based on the solutions obtained for 12 time instances during the entire day. The initial average, minimum and maximum VUF at node-359 obtained by solving a power flow with zero reactive power injections from the PV inverters are 1.72%, 1.66% and 1.9%, respectively. When comparing TP-OPF with the iterative methods, we see that all FOT-OPF is able to find good solutions that close to TP-OPF. In addition, the FBS-OPF always converges to a solution within 1 minute. The maximum VUF and maximum computation

time for all methods occur during midday when the PV penetration levels are high which is verified by the plots shown in Fig. 5.5.

Parameter	TP-OPF	FOT-OPF	FP-OPF	FBS-OPF
Avg. VUF_{359} (%)	0.0005	0.001	0.002	0.003
Min. VUF_{359} (%)	0.000	0.000	0.000	0.000
Max. VUF_{359} (%)	0.002	0.018	0.017	0.017
Avg. Time (min)	130.7	3.1 (7)	12.6 (8)	0.4 (8)
Min. Time (min)	113.1	2.2 (5)	10.0 (7)	0.3 (7)
Max. Time (min)	151.8	9.1 (21)	21.5 (13)	0.6 (13)

*The numbers in brackets are the no. of iterations.

Table 5.9: Summary of objective value and computation time (multiple time instances).

5.10.3.2 Comparison with LinDist3Flow

Finally, we evaluate the linearization accuracy of the iterative methods based on the solutions obtained after the first iteration of each run. Fig. 5.6 shows the VUF at critical node-359 and linearization accuracy for the three iterative methods as well as the benchmark formulation LinDist3Flow for 12 multiple time instances throughout a single day. We again observe that all the iterative methods have good linearization accuracy and are also able to consistently reduce the VUF at node-359 to almost zero whereas LinDist3Flow converges to a solution with a higher VUF and linearization accuracy. The VUF at node-359 and linearization accuracy Δv for the three linear approximations and LinDist3Flow are summarized in Table 5.10. Similar to our previous results for the single time instance, we notice that the average, minimum and maximum values of VUF at node-359 as well as deviation Δv for FOT-OPF, FP-OPF and FBS-OPF are almost 20 times lower on average compared to LinDist3Flow. Furthermore, the inaccuracy Δv is lowest for FOT-OPF verifying that the FOT approximation provides the best approximation accuracy around the initial voltage estimate.

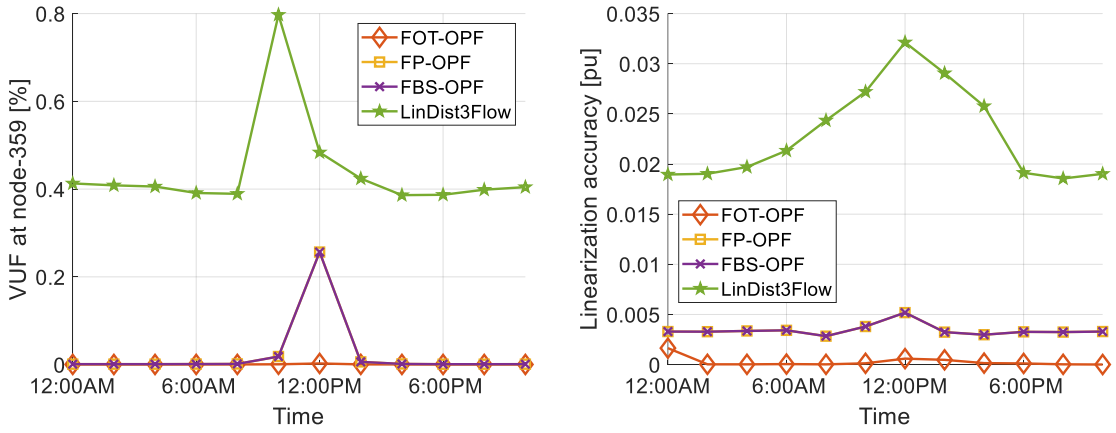

Figure 5.6: Objective value (left) and linearization accuracy (right) after one iteration of solving OPF every two hours in a single day.

Parameter	**FOT-OPF**	**FP-OPF**	**FBS-OPF**	**LinDist3Flow**
Avg. VUF_{359} (%)	0.001	0.02	0.02	0.44
Min. VUF_{359} (%)	0.000	0.00	0.00	0.39
Max. VUF_{359} (%)	0.003	0.24	0.25	0.79
Avg. Δv (pu)	0.0002	0.0034	0.0034	0.0228
Min. Δv (pu)	9.07e^{-6}	0.0028	0.0028	0.0185
Max. Δv (pu)	0.0016	0.0052	0.0052	0.0321

Table 5.10: Summary of objective value and linearization accuracy after one iteration (multiple time instances).

5.11 Case Study II: Considering Limited Measurements and Time Delays

In the previous section, we obtained results for the multiple time instances by assuming that measurement data is readily available any time during the day. Furthermore, we also assumed that the solution obtained by solving the OPF problem is instantly applied to the network at the same time instance that we receive our measurement data. However, this might not be realistic because

some of the major challenges with employing the centralized three-phase OPF approach for a realistic setting are computation time delays and extensive communication requirements which could lead to limited availability of measurement data.

In this section, we first describe a time-based simulation approach which considers realistic conditions such as limited measurement availability and time delays associated with communication as well as solving the optimization problem. We next evaluate the performance of the iterative methods in this realistic setting by running numerical experiments on the R1-12-47-1 feeder discussed in Section 5.9.1. We will also use the PV and load measurement data introduced in Section 5.9.2 for the time-based simulations. For simplicity, we will only show the results for case C3-VUF where the objective is to minimize the VUF at critical node-359. Furthermore, we compare results of FOT-OPF and FBS-OPF with the conventional TP-OPF. We do not show results for FP-OPF because it was clear from the results from the previous sections that FP-OPF and FBS-OPF converge to identical solutions.

5.11.1 Solution Timeframe

In practice, the three-phase OPF needs to be solved frequently as load and PV generation keep changing. As illustrated in Fig. 5.7, we need to consider the time-varying load and PV generation. We assume that the system data including measurements from all loads and solar PV systems connected to the distribution grid is available at regular time interval τ_{m}. Once we obtain the system data at time step t, we start solving the three-phase OPF problem. However, the corresponding reactive power set-points are available only after a time delay τ_{d} that includes both the computational time as well as the communication delay associated with acquiring measurements and sending set-points to the PV systems. If the delay τ_{d} is large, the reactive power set-points may no longer be optimal since load and especially PV generation can change quickly in real distribution systems.

It is important to note that since none of the methods listed in Table 5.4 guarantee an optimal solution, it might be difficult to assess the performance in terms of optimality of the final solution. But, it is still beneficial to compare all the methods and get a better insight on the performance of the scalable methods with reference to solving the original non-convex optimization problem

OPF. In the next subsection, we describe the various performance metrics that will be used in the time-based simulations to evaluate the performance of all the methods.

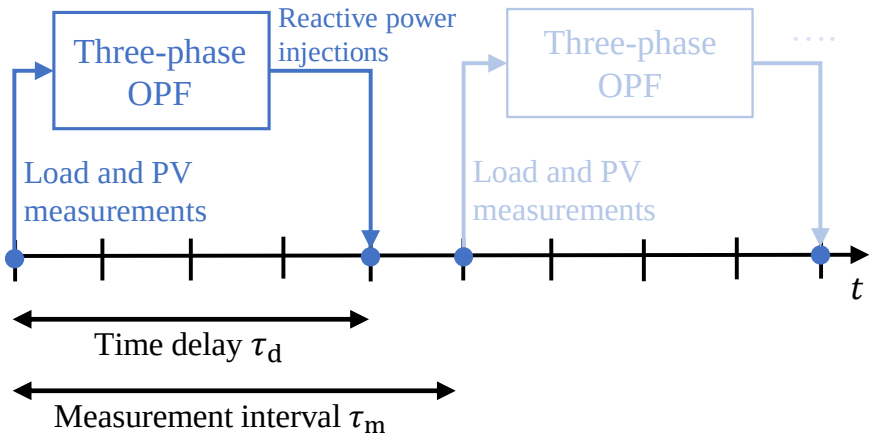

Figure 5.7: Time-based simulation approach to solve sequence of three-phase OPF problems.

5.11.2 Performance Metrics

We run simulations for a time-varying case where we solve the three-phase OPF for a given time step $t \in \mathcal{T}$ where T is the set of time steps. The total number of time-steps is denoted by $T = |\mathcal{T}|$ which is equal to 1440 in our simulations since we use 1-minute resolution data for load and PV measurements. To compare the performance of the different methods, we utilize the following performance metrics:

1) *Unbalance improvement*: Since our main objective is to minimize unbalance, we evaluate the methods based on how much reduction in VUF they can achieve. For time-varying case, the mean VUF at the critical node ($\text{VUF}_{359}^{\text{avg}}$), average ($\text{VUF}_{\text{all}}^{\text{avg}}$) and maximum ($\text{VUF}_{\text{max}}$) unbalance across all three-phase nodes over the day are compared using

$$\begin{aligned}
\text{VUF}_{359}^{\text{avg}} &= \frac{1}{T}\sum_{t=1}^{T} \text{VUF}_{359}^{t}, \\
\text{VUF}_{\text{all}}^{\text{avg}} &= \frac{1}{n \cdot T}\sum_{t=1}^{T}\sum_{i=1}^{n} \text{VUF}_{i}^{t}, \\
\text{VUF}_{\text{max}} &= \max(\text{VUF}_{i}^{t}) \;\; \forall i \in \mathcal{N}, t \in \mathcal{T}.
\end{aligned} \tag{5.39}$$

2) *Voltage limits violation*: All nodes in the distribution grid have specified voltage limits to maintain acceptable power quality standards. In addition, these limits also ensure that any device connected to the grid at these nodes are within their safe operating area and there is no damage to the equipment due to undervoltage or overvoltage conditions. Recall that the three-phase OPF is solved only at certain interval τ_{m} as shown in Fig. 5.7. During this measurement interval τ_{m}, voltage limits can be violated in the grid since we are not solving an optimization problem to enforce the voltage constraints. The voltage limits α in percent is defined as

$$\alpha = \frac{100}{3n \cdot T} \sum_{t=1}^{T} \sum_{i=1}^{n} z_i^{\phi,t}, \tag{5.40}$$

where $z_i^{\phi,t}$ is a binary variable indicating if voltage magnitude at any node i connected to phase ϕ at time step t is below the minimum limit $\underline{v}$ or above the maximum limit $\overline{v}$:

$$z_i^{\phi,t} = \begin{cases} 1, & \text{if } |v_i^{\phi,t}| < \underline{v} \text{ or } |v_i^{\phi,t}| > \overline{v}, \\ 0, & \text{otherwise.} \end{cases} \tag{5.41}$$

5.11.3 Time-based Simulation Results

We investigate the impact of measurement interval τ_{m} as well as time delay τ_{d} on performance of all the methods. Recall that load and PV data for a whole day are available at 1-minute interval as discussed in section 5.9.2. Using this data, we find that there is significant variation in the PV penetration level throughout the day. The average PV penetration level throughout the day is 45.63% with a maximum PV penetration of 199.84% occurring at 11:25 am.

5.11.3.1 Benchmark Case

We initially consider a benchmark case where we minimize unbalance at critical-node 359 throughout the day by solving the three-phase OPF problem every minute (i.e. $\tau_{\text{m}} = 1$-min) and assume that we are able to instantly use the reactive power injections calculated by solving the optimization problem without any time delay (i.e. $\tau_{\text{d}} = 0$-min). This means that the three-phase OPF problem is solved $T = 1440$ times during the whole day with the load and PV data updated every minute. Since TP-OPF takes more than two hours to converge for a single time step, we do

not have results for the benchmark case when solving the optimization problem. Hence, we will compare only the FOT-OPF and FBS-OPF for this benchmark case.

Table 5.11 summarizes the voltage unbalance results for the benchmark case (i.e. with $\tau_{\mathrm{m}} = 1$-min and $\tau_{\mathrm{d}} = 0$-min) when minimizing unbalance at node-359 for the whole day using the three scalable methods. We observe that in addition to minimizing the mean unbalance at critical node $\mathrm{VUF}_{359}^{\mathrm{avg}}$, the average unbalance $\mathrm{VUF}_{\mathrm{all}}^{\mathrm{avg}}$ and maximum unbalance $\mathrm{VUF}_{\mathrm{max}}$ across all three-phases nodes for the whole day are considerably reduced.

Method	**Unbalance (%)**		
	$\mathrm{VUF}_{359}^{\mathrm{avg}}$	$\mathrm{VUF}_{\mathrm{all}}^{\mathrm{avg}}$	$\mathrm{VUF}_{\mathrm{max}}$
Initial	1.746	1.285	2.453
FOT-OPF	0.003	0.074	0.724
FBS-OPF	0.006	0.071	0.722

Table 5.11: Simulation results for benchmark time-varying case when minimizing unbalance at node-359 for whole day using two iterative methods with $\tau_{\mathrm{m}} = 1$-min and $\tau_{\mathrm{d}} = 0$-min.

The initial VUF at node-359 obtained by solving the power flow without any control as well as the VUF at node-359 throughout the day for both iterative methods is illustrated in Fig. 5.8a. We observe that PV penetration levels have higher impact on unbalance compared to load variations since the initial VUF at node-359 (shown by blue line) violates the 2% limit during midday when PV penetration levels are high. Both iterative methods are able to reduce VUF at node-359 throughout the day to almost zero except for some time steps during midday, as shown by the zoomed plot in Fig. 5.8a, when the PV penetration levels are high. Fig. 5.8b illustrates the average reactive power injections throughout the day for the scalable methods. While the average reactive power injections are almost identical for both FOT-OPF and FBS-OPF during midday (between 12-3pm) when the PV penetration level is high, the results for FBS-OPF show a more negative

reactive power injections throughout the rest of the day. This was also observed in the results for a single time-instance shown in Fig. 5.4 for case C3-VUF.

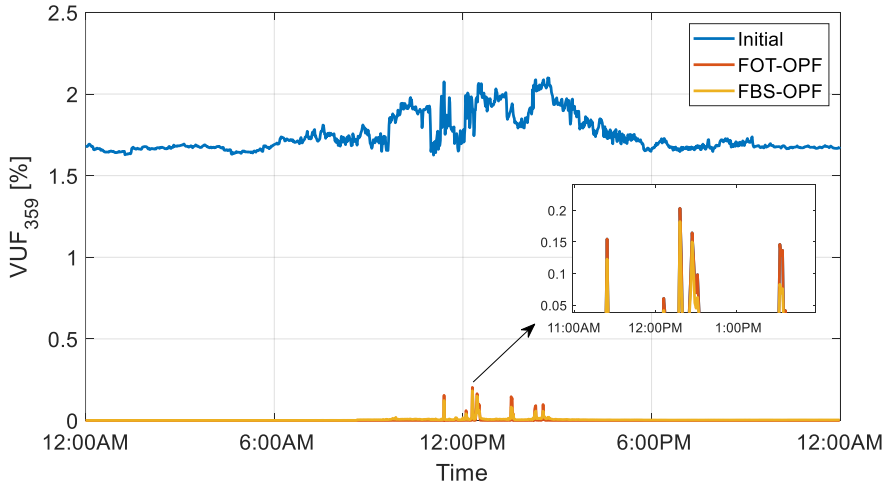

(a) VUF at critical node-359

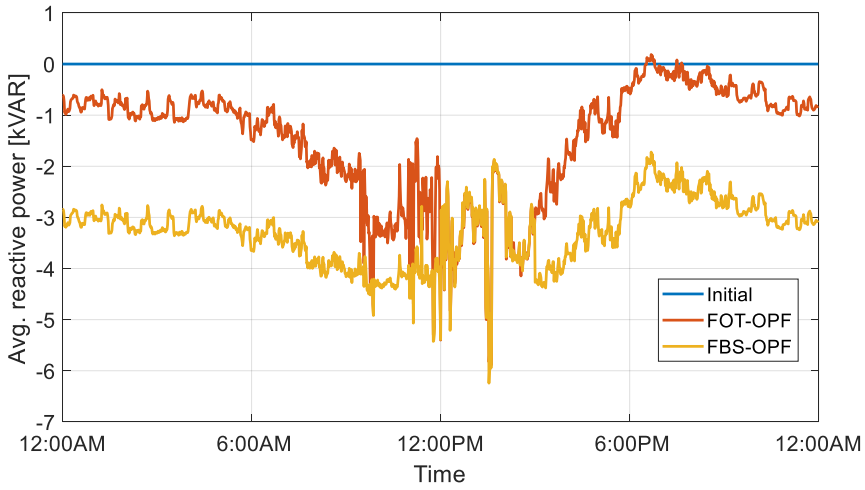

(b) Average reactive power injections

Figure 5.8: Comparison of iterative methods for the benchmark time-varying case with $\tau_{\mathrm{m}} = 1$-min and $\tau_{\mathrm{d}} = 0$-min. (a) VUF at critical node-359 (b) Average reaction power injections.

5.11.3.2 Realistic Case

Next, we investigate more realistic cases which consider computational time delay τ_{d}. In practice, the residential load and PV data for all houses might be available less frequently. Furthermore, there might be additional delay (apart from computation time) associated with acquiring the measurement as well as communication with solar PV inverters. So, we consider two realistic cases for the conventional TP-OPF as well as two scalable methods FOT-OPF and FBS-OPF with different delay and measurement intervals (i.e. $\tau_{\text{d}} = \tau_{\text{m}} =$ 15- or 120-min).

The simulation approach for the realistic case with $\tau_{\text{d}} = \tau_{\text{m}} = 15$-min is illustrated in Fig. 5.9 and described using the following steps:

1) We assume that the system data including measurements from all loads and solar PV systems connected to the distribution grid are available at time step t when we start solving the three-phase OPF.

2) The reactive power injections for all solar PV inverters calculated based on the system data at time t are available at time step $(t + 15)$ to be implemented in the system as shown in Fig. 5.9. At the same time, we acquire the new system data corresponding to time step $(t + 15)$ and start solving the three-phase OPF again.

3) During the interval between time steps t and $(t + 15)$, we solve a three-phase power flow using the updated measurement data to model the natural distribution grid behavior without any control. Recall that since we are not solving the three-phase OPF during this interval, we cannot guarantee that all engineering constraints are satisfied and hence, voltage violations might occur. In order to solve the power flow, we also need to set the reactive power injections of solar PV inverters to a fixed value. Therefore, for all the power flow calculations between time steps t and $(t + 15)$, we set the reactive power injections to values determined from the previously solved three-phase OPF using system data at time step $(t - 15)$.

Table 5.12 summarizes the unbalance and voltage violations for the realistic cases. In addition to the two iterative methods, we also consider a realistic case ($\tau_{\text{d}} = \tau_{\text{m}} = 120$-min) when solving

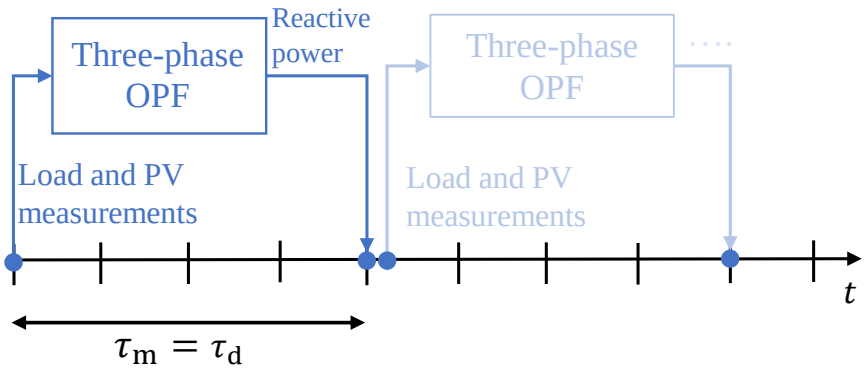

Figure 5.9: Time-based simulation approach for realistic case with $\tau_d = \tau_m$.

TP-OPF and compare the performance with the iterative methods. We see for both FOT-OPF and FBS-OPF that the mean VUF at critical node $\text{VUF}_{359}^{\text{avg}}$ and voltage violations α increase when the three-phase OPF is solved less frequently with longer delay time. This is due to the large variations of load and PV generation in the feeder which might make the reactive power injections obsolete by the time they are available as set-points for the solar PV inverters. While the voltage violations for FOT-OPF rise with increase in τ_m and τ_d, there is negligible increase in voltage violations for the FBS-OPF method. This is mostly due to the more negative reactive power injections determined by FBS-OPF which lead to lower number of overvoltages.

For a better comparison, the VUF at node-359 throughout the day for all the methods with $\tau_d = \tau_m = 120$-min is illustrated in Fig. 5.10(a). All the methods show identical improvement in the unbalance at node-359. Fig. 5.10(b) shows the minimum (dashed lines) and maximum (solid lines) voltage magnitude across all single-phase connections at each time step. The maximum voltage violations in the feeder for all the methods occur during midday mainly due to overvoltage in phase a which has the highest number of solar PV systems. In addition to this, there are some undervoltage cases that are seen during the evening mostly due to peak load. Fig. 5.10(c) illustrates the average reactive power injections throughout the day for the various methods. Different from the reactive power injections seen in Fig. 5.8(b), we see that the reactive power injections are updated after $\tau_m = 120$-min interval and hence, remain constant during the 120-min interval. We observe that the average reactive power injections for all the methods are negative throughout the

Method	**Time (min)**		**Unbalance (%)**			**Voltage**		
	τ_{m}	τ_{d}	$\text{VUF}_{359}^{\text{avg}}$	$\text{VUF}_{\text{all}}^{\text{avg}}$	VUF_{max}	α (%)	Min. (pu)	Max. (pu)
Initial	1	-	1.746	1.285	2.453	0.087	0.882	1.122
TP-OPF	120	120	0.273	0.215	2.090	3.556	0.868	1.142
FOT-OPF	15	15	0.085	0.108	2.090	1.720	0.886	1.134
	120	120	0.272	0.215	2.090	3.485	0.868	1.142
FBS-OPF	15	15	0.086	0.116	2.090	0.563	0.876	1.133
	120	120	0.276	0.220	2.090	0.419	0.857	1.130

Table 5.12: Simulation results for realistic time-varying case when minimizing unbalance at node-359 for whole day.

day with TP-OPF following an almost identical trend when compared to FOT-OPF. Similar to the reactive power injections seen in Fig. 5.8(b), the reactive power injections for FBS-OPF are more negative compared to the other methods leading to lower overvoltage cases for the FBS-OPF method as seen in Fig. 5.10(b). As a result, the voltage violations α are lower for the FP-OPF method as summarized in Table 5.12.

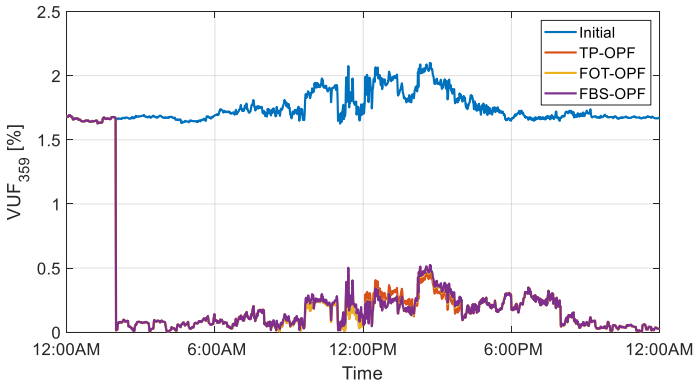

(a) VUF at critical node-359

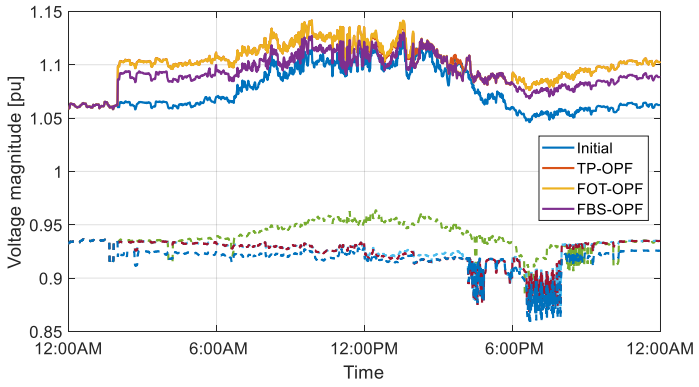

(b) Voltage magnitude across all nodes

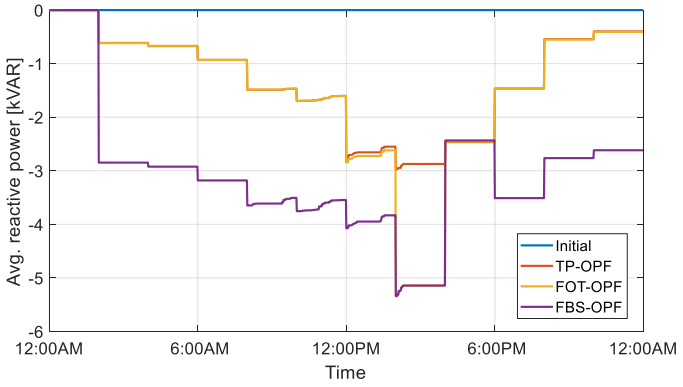

(c) Average reactive power injections

Figure 5.10: Comparison of performance metrics for the realistic time-varying case with $\tau_{\mathrm{m}} = \tau_{\mathrm{d}} =$ 120-min. (a) VUF at critical node-359 (b) Voltage magnitude across all single-phase connections (c) Average reaction power injections.

5.12 Main Takeaways

In this chapter, we presented three different scalable implementations of the three-phase AC OPF problem. We evaluated the methods by running numerical experiments on a large distribution feeder. By comparing the results of the conventional TP-OPF with all three iterative methods at a single time instance, we noticed that they converged to good quality solutions close to the local optimum obtained by solving TP-OPF, but the computation time was significantly lower. This was further validated by solving the OPF for multiple time instances. The results indicated that the iterative methods converge quickly to high-quality solutions with FBS-OPF achieving the lowest computation time. In addition, we observed that the accuracy of all three linear approximations was better than LinDist3Flow.

The results obtained from the time-based simulations for realistic cases indicated that higher time delay τ_{d} or measurement availability interval τ_{m} reduce the overall performance measured in terms of voltage unbalance reduction and voltage violations with the FBS-OPF method showing the least degradation in performance.

Chapter 6

Chance-Constrained Optimal Power Flow

The OPF problem discussed in the previous chapters is typically handled as a deterministic optimization problem on the basis of a forecasted point for the load and renewable generation. The intermittent nature of DERs and errors in load forecasting increases uncertainty in the network, while also posing considerable power quality issues such as voltage unbalance and voltage magnitude violations. While OPF provides optimal set-points, the frequency at which the set-points are updated is limited by real-time system measurements and communication delays as seen in Chapter 5. As a result, it may be critical to identify DER setpoints that ensure grid security over extended periods of time, with intervals ranging from 15 minutes (assuming good communication systems exist) to an entire season (in case low complexity is desired). Across these time horizons, there will be significant variability and uncertainty in the realization of load and DER power injections. If not appropriately accounted for, this can lead to constraint violations and high voltage unbalance in the time intervals between control set-point updates. To address this problem, we must treat the variable load and DER injections as uncertain and formulate the centralized OPF problem as a stochastic optimization problem.

6.1 Literature Review: Optimization under Uncertainty

Several types of stochastic OPF methods for distribution grids have been proposed in existing literature. This includes robust and distributionally robust methods [7, 35, 36], which aim to hedge against worst-case operating conditions, and often lead to highly conservative solutions. Other stochastic approximation techniques [34] and chance-constrained formulations [37] have also been

proposed for balanced distribution grids. These models mainly focus on voltage regulation or reducing voltage magnitude violations [7, 36] with the objectives to minimize cost of energy [35, 36, 37], deviation from a desired power injection at the distribution substation [36], or network losses [7, 34, 37]. it must also be noted that these models often leverage power flow models that exploit radial network topology of distribution grids [12, 14, 89, 93, 94], include approximations of voltage unbalance [24, 90, 91, 92], and sometimes employ successive approximation algorithms such as forward-backward sweep [75, 101, 102]. Most of these existing formulations are linear approximations [89, 90, 107] or convex relaxations [24, 91, 92, 93, 94], which typically do not converge to solutions that are AC feasible. The few methods that do consider the full, nonlinear AC power flow model [35] or converge to a solution that is AC feasible [37] generally only consider balanced, single-phase equivalent networks.

One of the major challenges for data-driven and stochastic methods in distribution grids is the uncertainty characterization. Certain assumptions such as the law of large numbers that might be true when we consider large number of customers will no longer hold for a smaller number of consumers in the case of distribution feeders, where it is hard to accurately forecast both load and DER power injections since they exhibit large variability over time. The most flexible way to model these distributions is using scenarios. However, scenario approaches may suffer from dimensionality issues due to the large number of decision variables and constraints that appear especially when using three-phase unbalanced models. Although choosing an appropriate set of samples (based on, e.g., historical data) is challenging, a chance-constrained formulation can be adopted to identify one set of control actions that can be utilized across a range of highly uncertain scenarios. This can be very useful because distribution utilities often only communicate with and control individual DERs at infrequent intervals. So the chance-constrained formulation represents a more realistic alternative to solving a deterministic problem for each uncertain scenario and identifying control set-points that need to be communicated frequently to the DERs. Another benefit of chance constraints is that they provide an intuitive trade-off between solution optimality (e.g. lowering voltage unbalance) and system robustness (i.e., reducing the number of constraint violations) by adjusting the parameter associated with the desired violation probability.

In general, chance-constrained optimization problems are challenging to solve [108], mainly because the probabilistic constraints need to be reformulated into a tractable form that can be solved by commercially available solvers. Some methods to reformulate chance constraints in applications involving distribution grids include moment-based approaches which assume Gaussian uncertainty [109] and distributionally agnostic strategies that employ e.g., scenario approaches [110], conservative convex approximations [111, 112], or data-driven robust methods [36]. While these assumptions can aid in the ability to obtain tractable reformulations of the probabilistic constraints, they are often limiting and/or inaccurate for distribution grids.

6.2 Main Contributions

In this chapter, we formulate a chance-constrained optimal power flow (CC-OPF) problem to minimize voltage unbalance while ensuring that voltage magnitude constraints and DER capacity limits are satisfied. We reformulate the problem using a data-driven, iterative approach that is computationally tractable. This method was inspired by existing approaches for transmission systems [113, 114, 115, 116] and balanced distribution grids [37]. The main idea is to define every chance constraint using its corresponding nominal constraint with the addition of a tightening term (also referred to as uncertainty margin) that accounts for uncertainty in the system. By choosing an optimal tightening term, we can obtain solutions that satisfy the chance constraints with the desired level of probability. A detailed case study is performed using real load and DER data where we test ability of the proposed approach to enforce chance constraint satisfaction. Furthermore, we investigate how properties of the uncertainty data can influence the resulting solutions.

6.3 Uncertainty Modeling

In this section, we discuss how the model of the load and PV inverters in distribution grids described in previous chapters is extended to include uncertainty. Recall that distribution grids typically have a small number of households distributed across different parts of the feeder. So, we do not see the smoothing effect that can be observed in transmission grids [14]. The PV generation

of each household as well as the load demand is highly variable, as shown by the example data in Fig. 6.1. This data is obtained from Pecan Street for a group of households in New York [106]. It is evident that forecasting the load demand can be challenging, especially due to the fact that the data does not fit any of the well described, standard probability distributions. In order to capture the probability distributions of the realistic solar PV generation and load consumption, we will directly utilize historical data (which can usually be obtained from smart meters after a delay [117]) for all the simulations in this chapter.

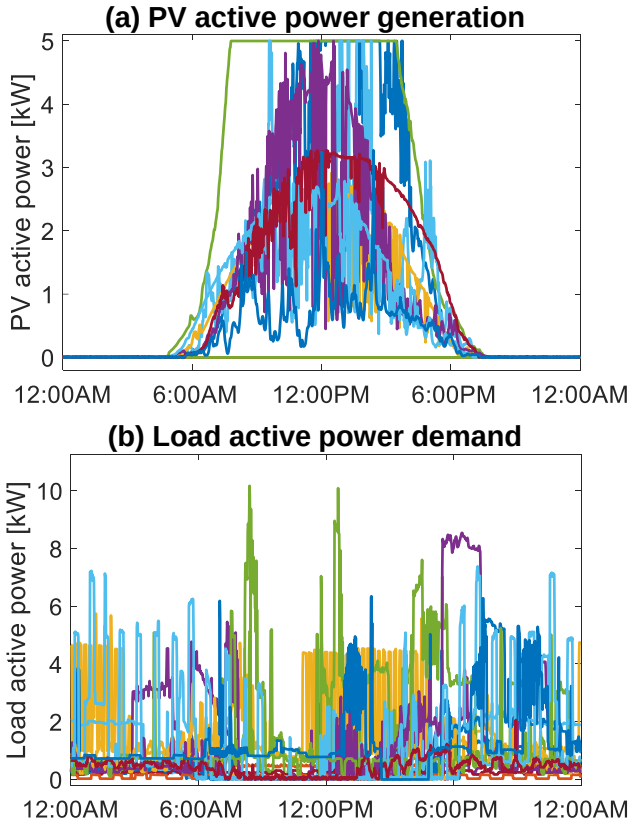

Figure 6.1: One-minute resolution Pecan Street data for 15 houses from a single day. (a) PV active power generation. (b) Load active power demand.

6.3.1 Notation

We will use the subscript ω to denote dependency on a given uncertainty realization ω. The individual realizations ω are grouped together to represent the full uncertainty data set using Ω with the total number of samples $M = |\Omega|$. Although we use radial distribution grids in our case study, the model makes no limiting assumptions of radiality and hence, we can employ the same approach to weakly-meshed or meshed distribution grid configurations. To simplify notation, we assume that there is one solar PV inverter and one load at every single-phase connection of node $i \in \mathcal{N}$. If any node connected to a phase has no source or load, we set the corresponding entries to zero. Recall that optimization variables are denoted using **bold** symbols, scalar values are denoted using small letters, and their vector counterparts and matrices are denoted using capital letters.

6.3.2 Modeling of Loads

For any node $i \in \mathcal{N}$, we represent the three-phase active and reactive power demand for a given realization ω as

$$P_{\mathrm{L},i,\omega} = \begin{bmatrix} p^a_{\mathrm{L},i,\omega} \\ p^b_{\mathrm{L},i,\omega} \\ p^c_{\mathrm{L},i,\omega} \end{bmatrix}, \; Q_{\mathrm{L},i,\omega} = \begin{bmatrix} q^a_{\mathrm{L},i,\omega} \\ q^b_{\mathrm{L},i,\omega} \\ q^c_{\mathrm{L},i,\omega} \end{bmatrix}.$$

If the reactive power demand is not known, we can assume that the loads are operating with a constant power factor $pf^{\phi}_{\mathrm{L},i}$, and the reactive power consumption then becomes

$$Q_{\mathrm{L},i,\omega} = \underbrace{\begin{bmatrix} \gamma^a_{\mathrm{L},i,\omega} \\ \gamma^b_{\mathrm{L},i,\omega} \\ \gamma^c_{\mathrm{L},i,\omega} \end{bmatrix}}_{\Gamma_{\mathrm{L},i}} \odot P_{\mathrm{L},i,\omega}, \tag{6.1}$$

where the individual entries of the constant factor $\Gamma_{\mathrm{L},i}$ are calculated using the constant power factor $pf^{\phi}_{\mathrm{L},i}$ as

$$\gamma^{\phi}_{\mathrm{L},i} = \sqrt{\frac{(1 - {pf^{\phi}_{\mathrm{L},i}}^2)}{(pf^{\phi}_{\mathrm{L},i})^2}}.$$

We express the average active power load $\bar{P}_{\mathrm{L},i}$ and reactive power load $\bar{Q}_{\mathrm{L},i}$ as the sample average across all realizations in the sample set Ω with

$$\bar{P}_{\mathrm{L},i} = \begin{bmatrix} \bar{p}^{a}_{\mathrm{L},i} \\ \bar{p}^{b}_{\mathrm{L},i} \\ \bar{p}^{c}_{\mathrm{L},i} \end{bmatrix}, \; \bar{Q}_{\mathrm{L},i} = \begin{bmatrix} \bar{q}^{a}_{\mathrm{L},i} \\ \bar{q}^{b}_{\mathrm{L},i} \\ \bar{q}^{c}_{\mathrm{L},i} \end{bmatrix},$$

where the per-phase active and reactive power values are calculated using

$$\bar{p}^{\phi}_{\mathrm{L},i} = \frac{1}{|\Omega|} \sum_{\omega \in \Omega} p^{\phi}_{\mathrm{L},i,\omega}, \tag{6.2a}$$

$$\bar{q}^{\phi}_{\mathrm{L},i} = \frac{1}{|\Omega|} \sum_{\omega \in \Omega} q^{\phi}_{\mathrm{L},i,\omega}. \tag{6.2b}$$

We define the uncertainty of the load consumption as deviation from the average value which can be expressed as

$$\delta P_{\mathrm{L},i,\omega} = P_{\mathrm{L},i,\omega} - \bar{P}_{\mathrm{L},i}, \tag{6.3a}$$

$$\delta Q_{\mathrm{L},i,\omega} = Q_{\mathrm{L},i,\omega} - \bar{Q}_{\mathrm{L},i}. \tag{6.3b}$$

6.3.3 Modeling of Solar PV Active Power Generation

Similar to the previous chapters, we assume that the utility does not perform active power curtailment and hence consider the solar PV active power generation as uncontrollable random variables. Following the load modelling procedure described in the previous section, the active power generation of the solar PV inverters $P_{\mathrm{G},i,\omega}$ under realization ω and the average generation $\bar{P}_{\mathrm{G},i}$ are defined as

$$P_{\mathrm{G},i,\omega} = \begin{bmatrix} p^{a}_{\mathrm{G},i,\omega} \\ p^{b}_{\mathrm{G},i,\omega} \\ p^{c}_{\mathrm{G},i,\omega} \end{bmatrix}, \; \bar{P}_{\mathrm{G},i} = \begin{bmatrix} \bar{p}^{a}_{\mathrm{G},i} \\ \bar{p}^{b}_{\mathrm{G},i} \\ \bar{p}^{c}_{\mathrm{G},i} \end{bmatrix}.$$

The per-phase average active power generation $\bar{p}^{\phi}_{\mathrm{G},i}$ and uncertain deviation $\delta P_{\mathrm{G},i,\omega}$ are defined similar to the loads using

$$\bar{p}^{\phi}_{\mathrm{G},i} = \frac{1}{|\Omega|} \sum_{\omega \in \Omega} p^{\phi}_{\mathrm{G},i,\omega}, \tag{6.4a}$$

$$\delta P_{\mathrm{G},i,\omega} = P_{\mathrm{G},i,\omega} - \bar{P}_{\mathrm{G},i}. \tag{6.4b}$$

6.3.4 Reactive Power Control from Solar PV Inverters

We consider that all solar PV systems connected to the distribution grid via smart inverters which provide opportunities for reactive power support as defined in the IEEE Standard 1547-2018 [118]. In this chapter, we will assume that all inverters are operating in the constant reactive power mode, where each inverter provides reactive power according to a specified set-point,

$$\boldsymbol{Q}_{\mathbf{G},i} = [\boldsymbol{q}^{a}_{\mathbf{G},i} \;\; \boldsymbol{q}^{b}_{\mathbf{G},i} \;\; \boldsymbol{q}^{c}_{\mathbf{G},i}]^{\top}.$$

This set-point is provided by the DSO and serves as a control variable in our optimization problem. Our aim is to find an optimal set-point $\boldsymbol{Q}_{\mathbf{G},i}$ that will remain the same for all the uncertainty realizations ω with the objective to minimize voltage unbalance while ensuring voltage magnitude limits are satisfied.

The active and reactive power of the PV inverter must satisfy the apparent power limits. For a single-phase PV inverter connected to phase ϕ at node i, we define the apparent power rating as $|s^{\phi}_{\mathrm{G},i}|$. The inverter reactive power $\boldsymbol{q}^{\phi}_{\mathbf{G},i}$ is then constrained by

$$\mathbb{P}_{\omega}\big((\boldsymbol{q}^{\phi}_{\mathbf{G},i})^2 + (p^{\phi}_{\mathrm{G},i,\omega})^2 \leq |s^{\phi}_{\mathrm{G},i}|\big) \geq 1 - \epsilon_q. \tag{6.5}$$

Since the active power generation $p^{\phi}_{\mathrm{G},i,\omega}$ depends in the uncertainty realizations ω, this constraint is enforced as a chance constraint where $\epsilon_q \in [0, 1]$ denotes the acceptable violation probability. This means that the reactive power set-point $\boldsymbol{q}^{\phi}_{\mathbf{G},i}$ is guaranteed to be feasible with probability $1 - \epsilon_q$.

Fig. 6.2 shows the PV inverter limit (blue dashed line), which is assumed to be a hard constraint. The reactive power is constant (orange line) with respect to the active power since we are operating in the constant reactive power mode. If the reactive power remains fixed beyond a certain value

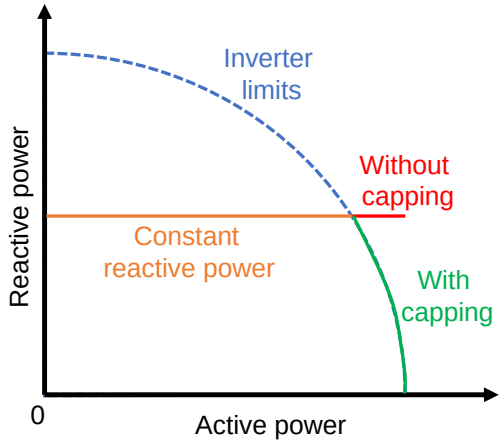

Figure 6.2: Inverter reactive power control with and without capping.

of active power generation, the PV inverter gets overloaded (red line) and operates in the region where the inverter limits are no longer satisfied. If inverter operates under overloaded conditions for long time duration, there is a high probability of premature failure of the inverter, and manual intervention might be required to avoid this situation. Therefore, we consider capping the inverter to be within the specified apparent power limits by decreasing the reactive power (green curve) as active power generation increases. This is also compliant with the IEEE Std 1547-2018 [118], which specifies that DERs should satisfy their apparent power limits. In such cases where inverter power injections are capped, the violation probability ϵ_q is interpreted as the probability that an inverter is unable to provide the desired reactive power to the grid.

6.3.5 Voltage Representation

Similar to the previous chapters, we implement the three-phase OPF in the polar coordinate frame using the phase-to-neutral voltage magnitude and angle variables at every node $i \in \mathcal{N}$. The voltage magnitudes and angles corresponding to the average power injections $\bar{P}_i,\ \bar{Q}_i$ are denoted by $|\boldsymbol{V}_i| = [|\boldsymbol{v}_i^a|\ |\boldsymbol{v}_i^b|\ |\boldsymbol{v}_i^c|]^\top$ and $\boldsymbol{\Theta}_i = [\boldsymbol{\theta}_i^a\ \ \boldsymbol{\theta}_i^b\ \ \boldsymbol{\theta}_i^c]^\top$, respectively. As the active and reactive power injections change, the voltages change as well. The voltage variables for a given realization ω is represented by $|\boldsymbol{V}_{i,\omega}| = [|\boldsymbol{v}_{i,\omega}^a|\ |\boldsymbol{v}_{i,\omega}^b|\ |\boldsymbol{v}_{i,\omega}^c|]^\top$ and $\boldsymbol{\Theta}_{i,\omega} = [\boldsymbol{\theta}_{i,\omega}^a\ \ \boldsymbol{\theta}_{i,\omega}^b\ \ \boldsymbol{\theta}_{i,\omega}^c]^\top$. Recall that the distribution substation is considered as the reference for voltage angle measurements where the

voltage is assumed to be independent of ω and remains fixed according to (4.1). All other voltage magnitudes at node $i \in \mathcal{N}$ connected to phase ϕ are constrained by

$$\mathbb{P}_\omega\big(|\boldsymbol{v}_{i,\omega}^{\phi}| \leq \overline{v}\big) \geq 1 - \epsilon_v, \tag{6.6a}$$

$$\mathbb{P}_\omega\big(|\boldsymbol{v}_{i,\omega}^{\phi}| \geq \underline{v}\big) \geq 1 - \epsilon_v. \tag{6.6b}$$

Since the voltage magnitude $|\boldsymbol{v}_{i,\omega}^{\phi}|$ depends on the uncertainty realization ω, these constraints are enforced as chance constraints with acceptable violation probability $\epsilon_v \in [0, 1]$. Note that the voltage magnitude constraints can be considered as *soft* constraints, where a violation of the constraint indicates an under- or over-voltage conditions. Soft constraint violations are generally acceptable if the magnitude and duration are quite small.

6.3.6 Power Flow

The active power injection $P_{i,\omega} \in \mathbb{R}^3$ at node $i \in \mathcal{N}$ depends on the uncertainty realization ω. It can be expressed as the sum of the average active generation $\bar{P}_{\mathrm{G},i} \in \mathbb{R}^3$ and average load $\bar{P}_{\mathrm{L},i} \in \mathbb{R}^3$ with corresponding deviations $\delta P_{\mathrm{G},i,\omega} \in \mathbb{R}^3$ and $\delta P_{\mathrm{L},i,\omega} \in \mathbb{R}^3$,

$$P_{i,\omega} = P_{\mathrm{G},i,\omega} - P_{\mathrm{L},i,\omega} = \big(\bar{P}_{\mathrm{G},i} + \delta P_{\mathrm{G},i,\omega}\big) - \big(\bar{P}_{\mathrm{L},i} + \delta P_{\mathrm{L},i,\omega}\big). \tag{6.7}$$

The reactive power injection $Q_{i,\omega} \in \mathbb{R}^3$ at node $i \in \mathcal{N}$ is modeled as the deviation between the reactive power generation of solar PV inverters $\boldsymbol{Q}_{\mathbf{G},i}$ and the reactive power load $Q_{\mathrm{L},i,\omega}$,

$$Q_{i,\omega} = \boldsymbol{Q}_{\mathbf{G},i} - Q_{\mathrm{L},i,\omega}. \tag{6.8}$$

The average active and reactive power injections at each node are then represented by

$$\bar{P}_i = \bar{P}_{\mathrm{G},i} - \bar{P}_{\mathrm{L},i}, \tag{6.9a}$$

$$\bar{Q}_i = \boldsymbol{Q}_{\mathbf{G},i} - \bar{Q}_{\mathrm{L},i}. \tag{6.9b}$$

The active power balance is maintained by the distribution substation, which injects power equal to the difference between the active power load demand and generation from PV systems for each scenario as well as any additional power needed to cover the power losses. The active power injection at the substation is considered as a decision variable $\boldsymbol{P}_{\mathbf{G},0,\omega}$.

Similarly, the reactive power balance is also guaranteed by the substation. We denote the reactive power injection at the substation as our decision variable $\boldsymbol{Q}_{\mathbf{G},0,\omega}$, which produces the difference between consumption, losses and generation.

Following [47], we can express the power flow equation at node $i \in \mathcal{N}_0$ using

$$P_{i,\omega} = |\boldsymbol{V}_{i,\omega}| \odot \sum_{k \in \mathcal{N}_0} \Big[G_{ik} \odot \mathrm{C}\big(\boldsymbol{\Theta}_{ik,\omega}\big) + B_{ik} \odot \mathrm{S}\big(\boldsymbol{\Theta}_{ik,\omega}\big) \Big] \cdot |\boldsymbol{V}_{k,\omega}|, \tag{6.10a}$$

$$Q_{i,\omega} = |\boldsymbol{V}_{i,\omega}| \odot \sum_{k \in \mathcal{N}_0} \Big[G_{ik} \odot \mathrm{S}\big(\boldsymbol{\Theta}_{ik,\omega}\big) - B_{ik} \odot \mathrm{C}\big(\boldsymbol{\Theta}_{ik,\omega}\big) \Big] \cdot |\boldsymbol{V}_{k,\omega}|, \tag{6.10b}$$

where the cosine component $\mathrm{C}(\boldsymbol{\Theta}_{ik,\omega})$ and sine component $\mathrm{S}(\boldsymbol{\Theta}_{ik,\omega})$ of the branch angle matrix $\boldsymbol{\Theta}_{ik,\omega} \in \mathbb{R}^{3\times 3}$ are given by

$$\mathrm{C}\big(\boldsymbol{\Theta}_{ik,\omega}\big) = \begin{bmatrix} \cos(\boldsymbol{\theta}^a_{i,\omega} - \boldsymbol{\theta}^a_{k,\omega}) & \cos(\boldsymbol{\theta}^a_{i,\omega} - \boldsymbol{\theta}^b_{k,\omega}) & \cos(\boldsymbol{\theta}^a_{i,\omega} - \boldsymbol{\theta}^c_{k,\omega}) \\ \cos(\boldsymbol{\theta}^b_{i,\omega} - \boldsymbol{\theta}^a_{k,\omega}) & \cos(\boldsymbol{\theta}^b_{i,\omega} - \boldsymbol{\theta}^b_{k,\omega}) & \cos(\boldsymbol{\theta}^b_{i,\omega} - \boldsymbol{\theta}^c_{k,\omega}) \\ \cos(\boldsymbol{\theta}^c_{i,\omega} - \boldsymbol{\theta}^a_{k,\omega}) & \cos(\boldsymbol{\theta}^c_{i,\omega} - \boldsymbol{\theta}^b_{k,\omega}) & \cos(\boldsymbol{\theta}^c_{i,\omega} - \boldsymbol{\theta}^c_{k,\omega}) \end{bmatrix},$$

$$\mathrm{S}\big(\boldsymbol{\Theta}_{ik,\omega}\big) = \begin{bmatrix} \sin(\boldsymbol{\theta}^a_{i,\omega} - \boldsymbol{\theta}^a_{k,\omega}) & \sin(\boldsymbol{\theta}^a_{i,\omega} - \boldsymbol{\theta}^b_{k,\omega}) & \sin(\boldsymbol{\theta}^a_{i,\omega} - \boldsymbol{\theta}^c_{k,\omega}) \\ \sin(\boldsymbol{\theta}^b_{i,\omega} - \boldsymbol{\theta}^a_{k,\omega}) & \sin(\boldsymbol{\theta}^b_{i,\omega} - \boldsymbol{\theta}^b_{k,\omega}) & \sin(\boldsymbol{\theta}^b_{i,\omega} - \boldsymbol{\theta}^c_{k,\omega}) \\ \sin(\boldsymbol{\theta}^c_{i,\omega} - \boldsymbol{\theta}^a_{k,\omega}) & \sin(\boldsymbol{\theta}^c_{i,\omega} - \boldsymbol{\theta}^b_{k,\omega}) & \sin(\boldsymbol{\theta}^c_{i,\omega} - \boldsymbol{\theta}^c_{k,\omega}) \end{bmatrix}.$$

Note that the power flow equations (4.5) are enforced for all $\omega \in \Omega$. For the remainder of the chapter, we use

$$f(|\boldsymbol{V}_{i,\omega}|, \boldsymbol{\Theta}_{i,\omega}, P_{i,\omega}, Q_{i,\omega}) = 0, \ \forall i \in \mathcal{N}_0, \ \omega \in \Omega,$$

as a shorthand representation of (6.10).

6.3.7 Objective Function

For the objective of the OPF problem, we choose to minimize voltage unbalance by using the Voltage Unbalance Factor (VUF) definition of voltage unbalance. For a three-phase node l, the square of VUF for the uncertainty realization ω is modelled as

$$\mathrm{VUF}^2_{l,\omega} = \frac{|v^-_{l,\omega}|^2}{|v^+_{l,\omega}|^2} = \frac{\big(\boldsymbol{v}^-_{\mathbf{d}l,\omega}\big)^2 + \big(\boldsymbol{v}^-_{\mathbf{q}l,\omega}\big)^2}{\big(\boldsymbol{v}^+_{\mathbf{d}l,\omega}\big)^2 + \big(\boldsymbol{v}^+_{\mathbf{q}l,\omega}\big)^2}, \tag{6.11}$$

where $\boldsymbol{v}^-_{\mathbf{d}l,\omega}, \boldsymbol{v}^-_{\mathbf{q}l,\omega}$ and $\boldsymbol{v}^+_{\mathbf{d}l,\omega}, \boldsymbol{v}^+_{\mathbf{q}l,\omega}$ denote the rectangular coordinate representation of negative sequence voltage $v^-_{l,\omega}$ and positive sequence voltage $v^+_{l,\omega}$, respectively. They can be represented as non-linear functions of the voltage variables $\boldsymbol{V}_{l,\omega}, \boldsymbol{\Theta}_{l,\omega}$ using

$$\begin{aligned}
&\boldsymbol{v}^-_{\mathbf{d}l,\omega} = \Re\{v^-_{l,\omega}\}, \boldsymbol{v}^-_{\mathbf{q}l,\omega} = \Im\{v^-_{l,\omega}\}, \text{ where} \\
&v^-_{l,\omega} = |\boldsymbol{v}^a_{l,\omega}|\angle\boldsymbol{\theta}^a_{l,\omega} + |\boldsymbol{v}^b_{l,\omega}|\angle(\boldsymbol{\theta}^b_{l,\omega} - 120^\circ) + |\boldsymbol{v}^c_{l,\omega}|\angle(\boldsymbol{\theta}^c_{l,\omega} + 120^\circ), \qquad (6.12a) \\
&\boldsymbol{v}^+_{\mathbf{d}l,\omega} = \Re(v^+_{l,\omega}), \boldsymbol{v}^+_{\mathbf{q}l,\omega} = \Im(v^+_{l,\omega}), \text{ where} \\
&v^+_{l,\omega} = |\boldsymbol{v}^a_{l,\omega}|\angle\boldsymbol{\theta}^a_{l,\omega} + |\boldsymbol{v}^b_{l,\omega}|\angle(\boldsymbol{\theta}^b_{l,\omega} + 120^\circ) + |\boldsymbol{v}^c_{l,\omega}|\angle(\boldsymbol{\theta}^c_{l,\omega} - 120^\circ). \qquad (6.12b)
\end{aligned}$$

6.4 Chance-Constrained Optimal Power Flow

The three-phase AC chance-constrained OPF problem is formulated as

$$\begin{aligned}
\min_{\boldsymbol{P}_{\mathbf{G},0}, \boldsymbol{Q}_{\mathbf{G}}, |\boldsymbol{V}|, \boldsymbol{\Theta}} \quad & \sum_{\omega\in\Omega}\sum_{l\in\mathcal{N}} \mathrm{VUF}^2_{l,\omega} && \text{(CC-OPF)} \\
\text{s.t.} \quad & f\big(|\boldsymbol{V}_{i,\omega}|, \boldsymbol{\Theta}_{i,\omega}, P_{i,\omega}, Q_{i,\omega}\big) = 0, && \forall_{i\in\mathcal{N}_0,\omega\in\Omega}, \\
& \mathbb{P}_\omega\big(|\boldsymbol{v}^\phi_{i,\omega}| \le \overline{v}\big) \ge 1-\epsilon_v, && \forall_{\phi\in\Phi,i\in\mathcal{N}}, \\
& \mathbb{P}_\omega\big(|\boldsymbol{v}^\phi_{i,\omega}| \ge \underline{v}\big) \ge 1-\epsilon_v, && \forall_{\phi\in\Phi,i\in\mathcal{N}}, \\
& \mathbb{P}_\omega\big((\boldsymbol{q}^\phi_{\mathbf{G},i})^2 + (p^\phi_{\mathrm{G},i,\omega})^2 \le |s^\phi_{\mathrm{G},i}|\big) \ge 1-\epsilon_q, && \forall_{\phi\in\Phi,i\in\mathcal{N}}, \\
& |\boldsymbol{V}_0|\angle\boldsymbol{\Theta}_0 = \begin{bmatrix} 1\angle 0^\circ & 1\angle -120^\circ & 1\angle 120^\circ \end{bmatrix}^\top,
\end{aligned}$$

where the optimization variables for each uncertainty realization $\omega \in \Omega$ are the voltage magnitudes at all nodes $|\boldsymbol{V}| \in \mathbb{R}^{3(n+1)}$, voltage angles at all nodes $\boldsymbol{\Theta} \in \mathbb{R}^{3(n+1)}$, active power generation at the substation $\boldsymbol{P}_{\mathbf{G},0} \in \mathbb{R}^3$, and reactive power generation at all nodes $\boldsymbol{Q}_{\mathbf{G}} \in \mathbb{R}^{3(n+1)}$.

Generally, we can interpret the chance constraints (6.5) and (6.6) as the probability that the DSO might need to take some real-time control actions in order to keep the system secure. There are two choices for the DSO [114]:

(i) Choosing *high* acceptable violation probabilities ϵ_q and ϵ_v puts the system at a higher risk of insecure operation. This may require frequent deployment of real-time controls, which might not always be available.

(ii) Choosing a *low* violation probability can be expensive, but the trade-off is that the system operation is safer and less prone to risk of insecure operation.

As formulated above, the CC-OPF problem is not tractable because of the chance constraints (6.5) and (6.6). While the feasible region defined by the chance constraints is non-convex, it is generally difficult to evaluate the feasibility of a solution since multi-dimensional integration is required. In addition, it is computationally expensive to enforce the power flow constraints (6.10) for all $\omega \in \Omega$, especially if the uncertainty set Ω is large. Hence, we need to reformulate these constraints into deterministic counterparts to obtain a tractable formulation that can be solved efficiently. Furthermore, our problem setting has two more complications:

(i) We do not make any distributional assumptions on the uncertainty in the problem.

(ii) We use the full, non-linear, non-convex AC power flow equations.

As a result, CC-OPF belongs to a challenging class of problems, where standard analytical reformulation techniques cannot be used. In the next section, we discuss a data driven reformulation approach to simplify the CC-OPF problem.

6.5 Analytical Reformulation

We take an iterative, data-driven approach to solve the CC-OPF problem which combines an approximate problem formulation along with sample-based evaluations to successively update the formulation, as illustrated in Fig. 6.3 [116]. Following [114, 116], we start by replacing (6.10) by a single set of deterministic power balance equations. Furthermore, we express the chance constraints (6.5) and (6.6) employing their nominal counterpart plus a constant tightening term that protects the system from risk against uncertainty. We refer to this tightening term as the uncertainty margin. By doing this, we get an approximate problem that can be solved efficiently using commercially available solvers. The candidate solution obtained by solving the approximate problem along with the available uncertainty data can be used to iteratively update the uncertainty margin. We will discuss this in more detain in the next few sections.

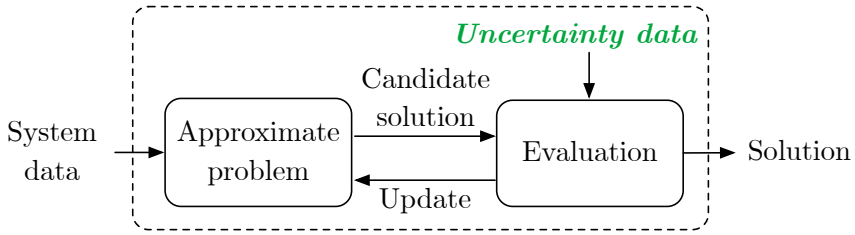

Figure 6.3: The general iterative process comprising of solving an approximate problem formulation and utilizing the results of a sample-based evaluation to update the problem formulation.

One of the primary advantages of the iterative approach is that we have decoupled the solving of the three-phase AC OPF problem from the consideration of the uncertainty. This enables us to take advantage of the available uncertainty data without adding any computational complexity associated with solving the optimization problem. Therefore, unlike other sample-based methods like the scenario method, the size of the optimization problem does not increase as more samples are used [119]. Moreover, we are now able to use the non-linear, non-convex AC power flow equations without the requirement to perform any approximations or explicit linearizations. Since we deliberately choose to utilize an approximate reformulation that is straightforward to solve, the resulting algorithm can benefit from the computational efficiency of commercially available solvers.

Accurately identifying and updating the values of the uncertainty margins is still a major challenge of using this style of deterministic reformulation. We must make sure that the uncertainty margins are large enough that the solution to the reformulated problem is feasible for the original chance constrained problem CC-OPF. Additionally, the uncertainty margins should also be small enough so that we do not obtain a very conservative result. The remainder of this section describes the main components of the iterative approach illustrated in Fig. 6.3.

6.5.1 Approximate Problem Formulation

We use a generalized approach based on [114] and reformulated the chance-constraints and power flow equations.

6.5.1.1 Nonlinear Power Flow

Instead of enforcing the power flow equations in (6.10) for all uncertainty realizations, we enforce a deterministic set of power flow equations at node $i \in \{0, \mathcal{N}\}$ which use the average power injections, $\bar{P}_i,\ \bar{Q}_i$ and corresponding voltage variables $|\boldsymbol{V}_i|, \boldsymbol{\Theta}_i$. The power balance constraints become

$$\bar{P}_i = |\boldsymbol{V}_i| \odot \sum_{k \in \mathcal{N}_0} \Big[G_{ik} \odot \mathrm{C}\big(\boldsymbol{\Theta}_{ik}\big) + B_{ik} \odot \mathrm{S}\big(\boldsymbol{\Theta}_{ik}\big) \Big] \cdot |\boldsymbol{V}_k|, \tag{6.14a}$$

$$\bar{Q}_i = |\boldsymbol{V}_i| \odot \sum_{k \in \mathcal{N}_0} \Big[G_{ik} \odot \mathrm{S}\big(\boldsymbol{\Theta}_{ik}\big) - B_{ik} \odot \mathrm{C}\big(\boldsymbol{\Theta}_{ik}\big) \Big] \cdot |\boldsymbol{V}_k|, \tag{6.14b}$$

and the shorthand representation of (6.14) is then given by

$$f(|\boldsymbol{V}_i|, \boldsymbol{\Theta}_i, \bar{P}_i, \bar{Q}_i) = 0,\ \forall i \in \mathcal{N}_0.$$

6.5.1.2 Linear Power Flow

Linear approximations of power flow equations have been widely used to reduce computational complexity as discussed already in Chapter 5. We have seen from the simulation results for larger test feeders in Chapter 5 that using the full, non-linear, non-convex AC power flow equations can lead to long computation times. Instead of formulating the deterministic power flow equations using (6.14), we can also employ one of the linear power flow models from Chapter 5. In this chapter, we have set up the problem in the polar coordinate frame. In addition, we can determine an initial voltage estimate using the average power injections with $\omega = 0$. Hence, we choose to utilize the FOT approximation to linearize the power balance equations around the operating point defined by the average power injections $\bar{P}_i,\ \bar{Q}_i$ and corresponding voltage estimates. We use

$$f_{\text{FOT}}(|\boldsymbol{V}_i|, \boldsymbol{\Theta}_i, \bar{P}_i, \bar{Q}_i) = 0,\ \forall i \in \mathcal{N}_0.$$

as the shorthand to represent the linear power flow equations defined in (5.7). Note that if the load forecasting error and variability of power injections by solar PV inverters are small, the FOT linearization approach should be able to provide accurate results.

6.5.1.3 Inverter Limits

The inverter limits represented by quadratic chance constraints in (4.4) are replaced by deterministic box constraints, which consist of a nominal limit and a tightening term. The upper and lower limits for a PV inverter at phase $\phi \in \Phi$ of node $i \in \mathcal{N}$ are computed by using the average generation $\overline{p}^{\phi}_{\mathrm{G},i}$ as

$$\overline{q}^{\phi}_{\mathrm{G},i} = \sqrt{|s^{\phi}_{\mathrm{G},i}|^2 - (\bar{p}^{\phi}_{\mathrm{G},i})^2}, \tag{6.15a}$$

$$\underline{q}^{\phi}_{\mathrm{G},i} = -\sqrt{|s^{\phi}_{\mathrm{G},i}|^2 - (\bar{p}^{\phi}_{\mathrm{G},i})^2}. \tag{6.15b}$$

The non-negative tightening terms corresponding to the upper and lower limits are represented by $\overline{\lambda}^{\phi}_{q,i}, \underline{\lambda}^{\phi}_{q,i} \in \mathbb{R}^{+}$, respectively. For notational convenience, we also define the tightenings using vectors

$$\underline{\Lambda}_q = \left[\left[\underline{\lambda}^{\phi}_{q,i}\right]^{\top}_{\phi\in\Phi}\right]^{\top}_{i\in\mathcal{N}}, \quad \overline{\Lambda}_q = \left[\left[\overline{\lambda}^{\phi}_{q,i}\right]^{\top}_{\phi\in\Phi}\right]^{\top}_{i\in\mathcal{N}}.$$

It is important to note that these tightenings can be pre-calculated because the inverter reactive power limits depend only on the apparent power and uncertain active power which are known a priori. The process is illustrated in Fig. 6.4 [48]. For example, consider the upper inverter limit where can evaluate the limit $\overline{q}^{\phi}_{\mathrm{G},i,\omega}$ for every uncertainty sample $\omega \in \Omega$ using Eq. (6.15a) with

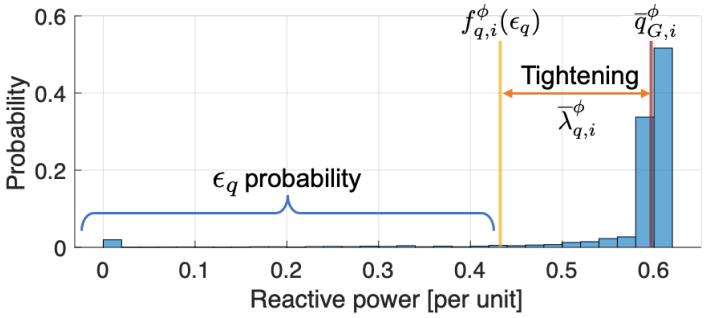

Figure 6.4: The histogram depicts the probability distribution function of an example inverter reactive power upper limit, $f^{\phi}_{q,i}(\cdot)$. The constraint tightening $\overline{\lambda}^{\phi}_{q,i}$, shown by the orange line, is given by the distance between the nominal limit $\overline{q}^{\phi}_{\mathrm{G},i}$ (brown line) and the ϵ_q quantile of the empirical distribution of the upper reactive power limit $f^{\phi}_{q,i}(\epsilon_q)$ (yellow line).

the sampled value $p_{\mathrm{G},i,\omega}$ instead of the average value $\bar{p}^{\phi}_{\mathrm{G},i}$. Once we calculate this limit for all uncertainty realizations, an empirical distribution for the upper reactive power generation limit is obtained, which we represent by $f^{\phi}_{q,i}(\cdot)$. The empirical distribution for the lower reactive power generation limit will simply be the negative, i.e., $-f^{\phi}_{q,i}(\cdot)$. Next, we identify the desired quantiles of the empirical distribution and use them to compute the constraint tightening terms. If the chance constraint on the upper reactive power limit needs to hold, the upper limit must be set to $f^{\phi}_{q,i}(\epsilon_q)$, which is equal to the ϵ_q quantile of the empirical distribution of the upper reactive power limit. To ensure the chance constraint holds, we set the appropriate uncertainty margin to the difference between the nominal inverter lower limit $\underline{q}^{\phi}_{\mathrm{G},i}$ and $f^{\phi}_{q,i}(\epsilon_q)$. Thus, the constraint tightenings for reactive power limits can be calculated as follows:

$$\overline{\lambda}^{\phi}_{q,i} = \overline{q}^{\phi}_{\mathrm{G},i} - f^{\phi}_{q,i}(\epsilon_q),$$
$$\underline{\lambda}^{\phi}_{q,i} = -f^{\phi}_{q,i}(1-\epsilon_q) - \underline{q}^{\phi}_{\mathrm{G},i}.$$

Note that the tightening values need to be calculated only once. Once they are determined, the tightenings remain fixed throughout the entirety of the iterative algorithm.

6.5.1.4 Voltage Limits

Similar to the inverter limits, we replace the chance constraints on the lower and upper voltage magnitude constraints (6.6) with the nominal limits and tightening terms, which are represented by $\overline{\lambda}^{\phi}_{v,i}, \underline{\lambda}^{\phi}_{v,i} \in \mathbb{R}^{+}$, respectively. The vector representations are

$$\underline{\lambda}_V = \left[\left[\underline{\lambda}^{\phi\in\Phi}_{V,i}\right]_{i\in\mathcal{N}}\right]^{\top},\ \overline{\lambda}_V = \left[\left[\overline{\lambda}^{\phi\in\Phi}_{V,i}\right]_{i\in\mathcal{N}}\right]^{\top}.$$

Different from the inverter limits, the voltage constraint tightenings require the solution obtained from the approximate OPF problem in order to be determined and as a result, must be calculated in every iteration and updated accordingly.

6.5.1.5 Reformulated Problem

Before we describe the reformulated problem, we must calculate the deterministic VUF by replacing the voltage variables $\boldsymbol{V}_{l,\omega}, \boldsymbol{\Theta}_{l,\omega}$ with their nominal counterparts $|\boldsymbol{V}_l|, \boldsymbol{\Theta}_l$ (corresponding to average power injections) in (6.11) and (6.12).

The deterministic approximate problem obtained by using the reformulation detailed above can be expressed as

$$
\begin{aligned}
\min_{\boldsymbol{P}_{\mathbf{G},0}, \boldsymbol{Q}_{\mathbf{G}}, |\boldsymbol{V}|, \boldsymbol{\Theta}} \quad & \sum_{l \in \mathcal{N}} \mathrm{VUF}_l^2 && \text{(CCR-OPF)} \\
\text{s.t.} \quad & f(|\boldsymbol{V}_i|, \boldsymbol{\Theta}_i, \bar{P}_i, \bar{Q}_i) = 0 \text{ or } f_{\mathrm{FOT}}(|\boldsymbol{V}_i|, \boldsymbol{\Theta}_i, \bar{P}_i, \bar{Q}_i) = 0, && \forall_{i \in \mathcal{N}_0}, \\
& |\boldsymbol{v}_i^{\phi}| \leq \overline{v} - \overline{\lambda}_{v,i}^{\phi}, && \forall_{\phi \in \Phi, i \in \mathcal{N}}, \\
& |\boldsymbol{v}_i^{\phi}| \geq \underline{v} + \underline{\lambda}_{v,i}^{\phi}, && \forall_{\phi \in \Phi, i \in \mathcal{N}}, \\
& \boldsymbol{q}_{\mathbf{G},i}^{\phi} \leq \overline{q}_{\mathrm{G},i}^{\phi} - \overline{\lambda}_{q,i}^{\phi}, && \forall_{\phi \in \Phi, i \in \mathcal{N}}, \\
& \boldsymbol{q}_{\mathbf{G},i}^{\phi} \geq \underline{q}_{\mathrm{G},i}^{\phi} + \underline{\lambda}_{q,i}^{\phi}, && \forall_{\phi \in \Phi, i \in \mathcal{N}}, \\
& \boldsymbol{V}_0 \angle \boldsymbol{\Theta}_0 = \begin{bmatrix} 1\angle 0^\circ & 1\angle -120^\circ & 1\angle 120^\circ \end{bmatrix}^\top.
\end{aligned}
$$

We represent the solution of CCR-OPF using $\mathrm{X_{sol}} = (\mathrm{P_{G,0}}, \mathrm{Q_G}, |\mathrm{V}|, \Theta)$.

6.5.2 Solution Evaluation

After solving the approximate problem (CCR-OPF) to obtain a candidate solution $\mathrm{X_{sol}}$, we can utilize the available uncertainty samples to investigate if the voltage constraint tightenings are conservative or not. To do this, we evaluate the solution $\mathrm{X_{sol}}$ by creating an empirical distribution and then perform a quantile evaluation as explained in Section 6.5.1.3 to obtain the inverter limit tightenings.

6.5.2.1 Quantile Evaluation

We start by using the candidate solution $\mathrm{X_{sol}}$ to calculate power flows (Monte Carlo simulations) for each sample in our uncertainty set. By doing this, we get empirical distributions for the voltage magnitudes around our candidate voltage solution $|\mathrm{v}_i^{\phi}|$ at node $i \in \mathcal{N}$ connected to

phase $\phi \in \Phi$. We represent this using $f^{\phi}_{v,i}(\cdot)$. Similar to the evaluation of the inverter limit tightenings, we can evaluate the voltage magnitude value at the desired quantiles by using the empirical distribution. Hence, we get the upper $1 - \epsilon_v$ and lower ϵ_v quantiles of the empirical distribution $f^{\phi}_{v,i}(\cdot)$ denoted by $f^{\phi}_{v,i}(1 - \epsilon_v)$ and $f^{\phi}_{v,i}(\epsilon_v)$, respectively.

6.5.2.2 Empirical Voltage Violation Probability Evaluation

We can also use the uncertainty samples to find the empirical violation probability of the solution X_{sol} to determine whether the chance constraint is satisfied. For example, consider the upper voltage magnitude constraint for node $i \in \mathcal{N}$ connected to phase $\phi \in \Phi$ and uncertainty samples $p^{\phi}_{\mathrm{G},i,\omega}$ and $p^{\phi}_{\mathrm{L},i,\omega}$. We define an indicator random variable $Y^{\phi}_{\overline{v},i}(\mathrm{X}_{\text{sol}}, p^{\phi}_{\mathrm{G},i,\omega}, p^{\phi}_{\mathrm{L},i,\omega}) \in \{0, 1\}$, which is equal to 0 if the upper voltage constraint holds and 1 otherwise, i.e.,

$$Y^{\phi}_{\overline{v},i}(\mathrm{X}_{\text{sol}}, p^{\phi}_{\mathrm{G},i,\omega}, p^{\phi}_{\mathrm{L},i,\omega}) = \begin{cases} 0 & \text{if } |\boldsymbol{v}^{\phi}_{i,\omega}| \leq \overline{v}, \\ 1 & \text{otherwise.} \end{cases} \tag{6.17}$$

We calculate the empirical violation probability for this constraint, denoted $\hat{E}^{\phi}_{\overline{v},i}(\mathrm{X}_{\text{sol}}) \in [0, 1]$, by taking the mean evaluated across all samples, i.e.,

$$\hat{E}^{\phi}_{\overline{v},i}(\mathrm{X}_{\text{sol}}) = \frac{1}{|\Omega|} \sum_{\omega \in \Omega} Y^{\phi}_{\overline{v},i}(\mathrm{X}_{\text{sol}}, p^{\phi}_{\mathrm{G},i,\omega}, p^{\phi}_{\mathrm{L},i,\omega}). \tag{6.18}$$

Similar evaluations can be performed to obtain the empirical violation probabilities of the voltage lower limits $\hat{E}^{\phi}_{\underline{v},i}(\mathrm{X}_{\text{sol}})$, inverter upper limits $\hat{E}^{\phi}_{\overline{q},i}(\mathrm{X}_{\text{sol}})$, and inverter lower limits $\hat{E}^{\phi}_{\underline{q},i}(\mathrm{X}_{\text{sol}})$. For a solution X_{sol}, we then define the worst case empirical violation probability for a single constraint type as the maximum empirical violation probability seen across all constraints of that type. As an example, the worst case empirical violation probability for the voltage upper limit is computed as

$$\hat{E}^{\max}_{\overline{v}}(\mathrm{X}_{\text{sol}}) = \max_{i \in \mathcal{N}, \phi \in \Phi} \{\hat{E}^{\phi}_{\overline{v},i}\}. \tag{6.19}$$

6.5.2.3 Handling of Inverter Limits

As detailed in Section 6.3.4, we consider PV inverter limits as hard constraints. Consequently, as we assess the solution X_{sol} in the evaluation step, we propose two strategies to deal with the condition when the inverter limits specified in (6.5) are violated:

(i) We allow inverters to be overloaded and observe inverter limit violations. The empirical violation probability can be calculated following the same procedure described in the previous section for voltage limits.

(ii) We cap the reactive power of inverter such that the total apparent power stays within the specified limits. Hence, no calculation of the empirical violation probability is required.

It is important to note here that the latter approach with inverter capping is a more realistic situation. Although the capping of the inverter output is challenging to model as a constraint within the approximate optimization problem, it is quite straightforward to perform this a posteriori during the solution evaluation step.

6.5.3 Iterative Quantile-based Method

Similar to the approaches proposed in [37, 113, 114], our iterative method utilizes available uncertainty samples to obtain empirical distribution functions for the voltage variables. We then follow the procedure discussed in Section 6.5.2.1 to find the desired quantiles of the empirical distribution. After doing this, we can directly calculate the tightening terms for the voltage magnitude limits. Following the approach illustrated in Fig. 6.3, the iterative quantile-based method consists of the following steps:

(1) *Initialize:* We set the iteration count to $\kappa = 0$ and fix the voltage magnitude tightenings $\overline{\Lambda}_v^{(0)}, \underline{\Lambda}_v^{(0)}$ to zero. The reactive power generation tightenings $\overline{\Lambda}_q, \underline{\Lambda}_q$ are computed as per the procedure detailed in Section 6.5.1.3.

(2) *Solve approximate problem:* We solve the simplified problem CCR-OPF using fixed tightening terms $\overline{\Lambda}_v^{(\kappa)}, \underline{\Lambda}_v^{(\kappa)}, \overline{\Lambda}_q, \underline{\Lambda}_q$ and obtain a candidate solution $X_{sol}^{(\kappa+1)}$.

(3) *Solution evaluation:* We perform the quantile evaluation discussed in Section 6.5.2.1 to determine the upper $1-\epsilon_v$ and lower ϵ_v quantiles of the empirical distribution of the voltage magnitude, $f_{v,i}^{\phi,(\kappa+1)}(1-\epsilon_v)$ and $f_{v,i}^{\phi,(\kappa+1)}(\epsilon_v)$, respectively.

(4) *Update tightenings:* We use the evaluated quantiles to update the voltage magnitude constraint tightenings,

$$\overline{\lambda}_{v,i}^{\phi} = f_{v,i}^{\phi,(\kappa+1)}(1-\epsilon_v) - |\boldsymbol{v}_i^{\phi,(\kappa+1)}|,$$
$$\underline{\lambda}_{v,i}^{\phi} = |\boldsymbol{v}_i^{\phi,(\kappa+1)}| - f_{v,i}^{\phi,(\kappa+1)}(\epsilon_v).$$

(5) *Check convergence:* We terminate when the upper and lower voltage constraint tightenings do not deviate too much from the previous iteration and converge below their respective prespecified tolerance values $\overline{\eta}_v, \underline{\eta}_v \in \mathbb{R}^+$, i.e., both

$$\max\{|\overline{\Lambda}_v^{(\kappa+1)} - \overline{\Lambda}_v^{(\kappa)}|\} \leq \overline{\eta}_v \text{ and } \max\{|\underline{\Lambda}_v^{(\kappa+1)} - \underline{\Lambda}_v^{(\kappa)}|\} \leq \underline{\eta}_v$$

must be satisfied. We return the final solution $\mathrm{X}_{\mathrm{sol}}^{(\kappa+1)}$. If not, we increase the iteration count to $\kappa = \kappa + 1$ and go back to step (2).

It is evident that the quantile-based method has some flexibility in its tightening updates because of the ability to calculate different tightenings for each of the voltage constraints separately. However, one drawback of the flexibility of the quantile-based method could be a higher chance for overfitting to the sampled uncertainty data.

6.6 Case Study Setup

In this section, we describe our case study setup where we use the IEEE 13-node radial distribution feeder [76] with realistic uncertainty data for solar PV generation and load demand to assess the performance of the iterative algorithm detailed in Section 6.5.3. Our goal is to identify reactive power set-points for the PV inverters that are valid for one full day, i.e., we assume that the distribution of possible load and solar PV values represents the power injection profiles across the whole day.

We explore how properties of the uncertainty data set (i.e., sampling procedure, number of samples, correlation between data points etc.) can have an impact on the resulting solutions. We evaluate the performance of the iterative algorithm in terms of chance constraint feasibility and objective optimality using both in- and out-of-sample evaluations. The optimization problem and algorithms are implemented in Julia [25] using JuMP [26] with the solver Ipopt [84].

6.6.1 Feeder Description

As our test system, we use the same IEEE 13-node feeder [76] described in Chapter 4, which consists of 15 houses represented as single-phase connections at seven nodes as illustrated in Fig. 4.2. In order to ensure that the generation and demand data is realistic, we utilize the same Pecan Street [106] residential data with 1-minute resolution as discussed in Section 5.9.2. This data consists of measurements from residential homes in New York, which are available for 25 full days between May 2019 and August 2019. Recall that an example of the load and solar PV profiles for a single day was shown in Fig. 6.1. We assume every house has a single-phase rooftop solar PV system with a maximum inverter rating of 100kVA (value chosen to match existing loads in the test feeder).

6.6.2 Sampling Procedure

For our numerical experiments, we divide the available data for in-sample and out-of-sample evaluations.

6.6.2.1 Out-of-sample Data

We randomly pick five days of data from the 25 day data set to be utilized for an out-of-sample evaluation. These samples remain the same across all experiments.

6.6.2.2 In-sample Data

We draw M samples from the remaining 20 days which will be used in the iterative algorithm and in-sample evaluation. We employ two types of sampling methods with different size variations to draw these M samples:

(i) *Full day samples*: We randomly pick either 1, 2 or 4 days from the set of 20 days, corresponding to $M = 1440,\ 2880,$ or 5760 data points, respectively. This data set can be interpreted as the common practice of using data from a set of "representative days". Drawing samples using this type of method could lead to data having strong correlations among subsequent time steps.

(ii) *Random samples*: All available data points from the set of 20 days are pooled together and $M = 1440,\ 2880,$ or 5760 samples are drawn randomly from the data pool. This data set assumes that the data from the 20 days defines a probability distribution of the data and we draw i.i.d. samples from this set. While this does not guarantee that all time steps in the day are represented, it most likely represents a wider variety of operating conditions since the data from more days are included.

6.6.3 Investigations

In the next four sections, we perform different analyses to analyse the performance of our proposed method and evaluate the different ways to model hard inverter limits:

- Section 6.7 examines how **different data sampling procedures** can impact the performance of our method. More specifically, we evaluate the performance of the iterative algorithm with the full day and random samples across numerous different algorithm replications, with the goal to assess which sampling procedure is more suitable.

- After identifying the most suitable sampling approach, Section 6.8 provides a **detailed description of the iterative algorithm** for one replication. We examine the resulting constraint

tightenings, voltage and inverter set points, as well as constraint violations evaluated on in- and out-of-sample data.

- Section 6.9 explores the algorithm performance when the effect of **inverter capping** is incorporated.

- Section 6.10 investigates the performance of the algorithm when **linear power flow** models are used. We evaluate if the algorithm can provide high-quality solutions with good approximation accuracy when the power flow equations are linearized.

6.7 Case Study I: Comparison of Sampling Methods

We first run numerical simulations to evaluate the performance of the quantile-based method under each of the data set sampling variations described in Section 6.6.2.2. For each of the six sampling methods (full day or random samples with $M = 1440,\ 2880,$ or 5760), we perform 10 replications, each using a different, independent sample draw. The desired chance constraint violation probability is set to $\epsilon_v = \epsilon_q = 0.05$.

6.7.1 Empirical Violation Probability

In Figs. 6.5 and 6.6, we plot the worst-case empirical violation probabilities for each constraint type (as defined in (6.19)) evaluated on both the in- and out-of-sample data, respectively. The worst-case violation probabilities for the lower voltage magnitude, upper voltage magnitude, lower inverter reactive power, and upper inverter reactive power constraints are shown in the figures using the blue, red, yellow, and purple bars, respectively. The average across the 10 replications is illustrated using the square, while the bars depict the range of worst-case violation probabilities obtained across the replications. The figures illustrate the results obtained by the quantile-based method, when using full day samples comprising of 1, 2, and 4 days (top) and $M = 1 \times 1440, 2 \times 1440$, and 4×1440 randomly drawn data points (bottom).

To evaluate if the obtained solution is feasible for the original chance-constrained problem, we first look at the in-sample violation probabilities of solutions obtained from the quantile-based

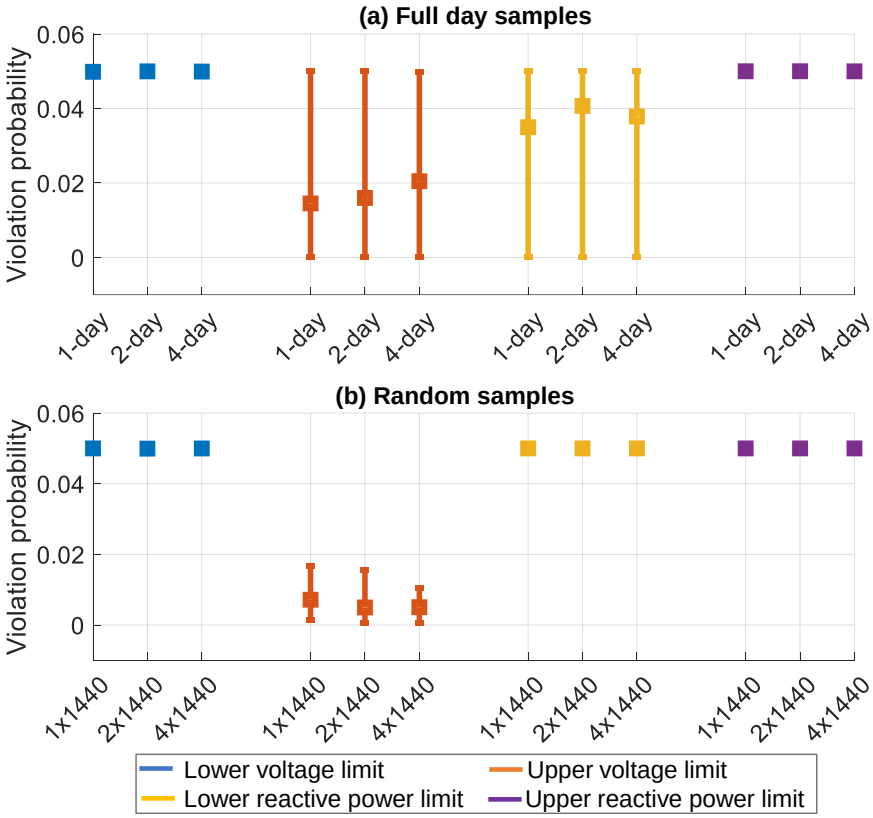

Figure 6.5: In-sample evaluation of violation probabilities for quantile-based method with different data set variations for 10 replications.

method in Fig 6.5. We see that the quantile-based method is able to limit the worst-case violation probabilities of all constraint types to the desired $\epsilon_v = \epsilon_q = 0.05$ for all cases. The quantile-based method adjusts all tightenings individually based on the quantile evaluation, and as a result, it is able to provide "fine-tuned" and less conservative tightenings for each constraint type.

In Fig. 6.6, it is obvious that the maximum violation probability across the 10 replications is considerably higher than the desired violation probabilities $\epsilon_v = \epsilon_q = 0.05$, with empirical violation probabilities up to 0.61. This demonstrates that solutions obtained from the quantile-based method is most likely infeasible to the original chance constrained problem.

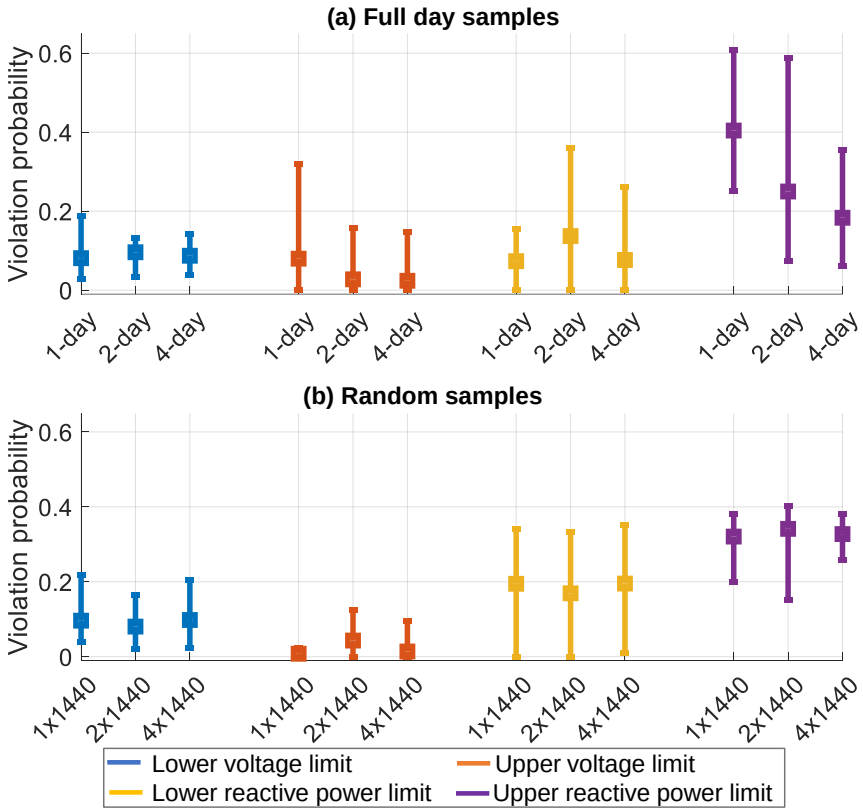

Figure 6.6: Out-of-sample evaluation of violation probabilities for quantile-based method with different data set variations for 10 replications.

6.7.2 Sampling Procedure

In Fig. 6.5, we notice that the range of worst-case probabilities is much smaller when using random samples (bottom) when compared to using full day samples (top). This most likely happens because drawing random samples leads to a data set that captures a wider range of possible uncertainty realizations.

As mentioned previously, there is a significant difference in the in- and out-of-sample violation probabilities. This suggests that the data used within the optimization algorithm (i.e., to generate the in-sample results) is not representative of the out-of-sample data, contributing to the incredibly poor results. However, we see that the solutions obtained using randomly selected samples (bottom) seem to have lower worst-case violation probabilities, verifying the fact that randomly drawn

samples may be an advantageous sampling procedure. In addition, we notice that the utilization of random samples leads to solutions with smaller ranges (i.e., less variation across replications) of violation probabilities compared to using the full-day samples.

6.7.3 VUF

We evaluate optimality of the solutions by calculating the total VUF obtained the CCR-OPF solutions. Fig. 6.7(a) shows the average, minimum, and maximum values across 10 replications of the in-sample VUF for solutions obtained by the quantile-based algorithm for different sampling methods. We also assess the solution quality on the out-of sample data by calculating the deviation between the out-of-sample VUF and in-sample VUF normalized by the in-sample VUF. The out-of-sample VUF for each replication is determined by computing the total unbalance averaged across the five evaluation days. Fig. 6.7(b) depicts the average, minimum, and maximum values across 10 replications of the normalized VUF evaluated on out-of-sample data.

By comparing the in-sample voltage unbalance results shown in Fig. 6.7(a) obtained with the full day samples (green bars) and random samples (light blue bars), we see that the VUF tends to be slightly smaller on average and fall in a narrower range when random samples are used. This is true for all sample sizes (which includes the smallest sample size set). This demonstrates that the total set of operating conditions is much better represented by randomly drawn samples rather than the full days of data.

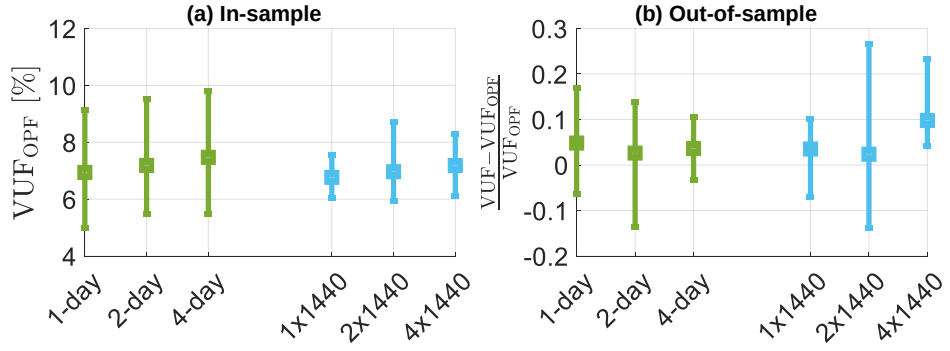

Figure 6.7: In-sample evaluation of total VUF and out-of-sample evaluation of normalized VUF for quantile-based method with different data set variations for 10 replications.

From Fig. 6.7(b), we see that the deviation in out-of-sample VUF from the in-sample VUF is higher when we use random samples (light blue bars) when compared to full day samples (green bars). This might be because the full day in-sample data is more representative of the out-of-sample data, where we also use the full day samples.

6.8 Case Study II: Detailed Results for a Single Replication

In this section, we discuss results of a single replication of the iterative algorithm. Based on the conclusions of Section 6.7, we choose to use a data set comprising of $M = 2880$ randomly sampled data points.

6.8.1 Constraint Tightenings

We first look at the constraint tightenings obtained by the quantile-based method. Fig. 6.8 illustrates the voltage magnitude set-points and constraint tightenings across all single-phase connections (left) and PV inverter reactive power set-points and constraint tightenings across all houses (right). The nominal constraints are shown using the dashed red lines, while the tightened constraints are depicted by blue lines. The tightening can be interpreted as the difference between the red dashed and the respective solid lines.

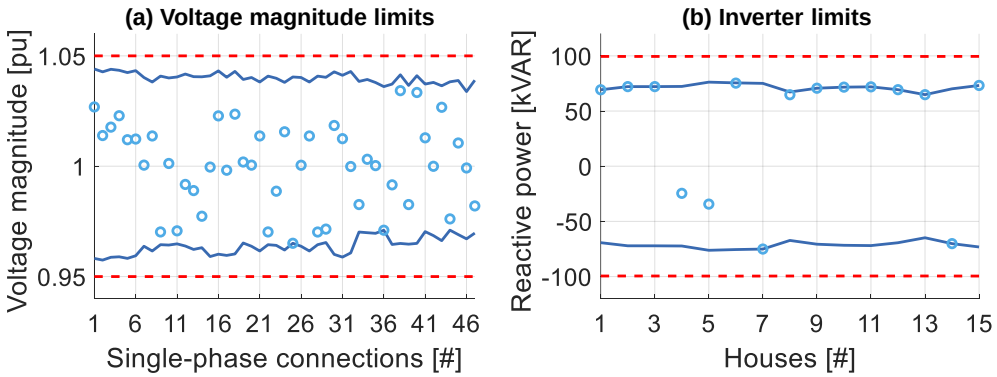

Figure 6.8: CCR-OPF solution and constraint tightenings obtained by the quantile-based method for single replication using $M = 2880$ random samples.

Consider the voltage magnitude constraints shown in Fig. 6.8(a). We first observe that the tightenings for the upper and lower voltage magnitude constraints obtained with the quantile-based method are not symmetric. This demonstrates that the probability distribution of the voltage magnitudes is asymmetric. Conversely, the inverter reactive power constraint tightenings are symmetric as expected since the probability distribution of the upper limit is equal to the negative probability distribution of the lower limit as explained in Section 6.5.1.3.

6.8.2 OPF Solutions

The VUF of the nominal solution for the quantile-based method is 6.3%. The nominal voltage magnitude and reactive power obtained with the quantile-based method is illustrated using blue circles in Fig. 6.8. When looking at the reactive power set-points obtained with the quantile-based methods in Fig. 6.8(b), we observe that most of the set-points are either equal to the maximum or minimum allowable reactive power injections. On the other hand, the voltage magnitude set-points are well within the tightened limits at most of the single-phase connections.

6.8.3 Constraint Violations by Node and Inverter

We next compare the performance of the quantile-based method in terms of constraint violations for the same replication as discussed above. To analyse the performance, we calculate the voltage magnitude and inverter apparent power for each in-sample and out-of-sample realization. Fig. 6.9 illustrates the box-whisker plots of the results for the in-sample (top) and out-of-sample (bottom) data using the quantile-based solution.

First, we compare the in-sample and out-of-sample results for the voltage magnitudes (left). The voltage magnitude violations in the in-sample evaluation (illustrated in Fig. 6.9(a)) are both larger in magnitude and also occur at a greater number of nodes compared to the out-of-sample evaluation (illustrated in Fig. 6.9(c)). We observe a similar trend when we compare the in-sample and out-of-sample constraint violations of the inverters. While the largest constraint violations are of similar magnitudes in both the in-sample and out-of-sample data, the number of nodes experiencing violations is much higher in the in-sample evaluation. Additionally, we observe that

the variability in the data for both voltage magnitudes and apparent power is higher in the in-sample compared to the out-of-sample distributions. This further verifies that the in-sample data is not representative of the out-of-sample distributions which might be due to the difference in the sampling method for the in-sample evaluation (where random samples are used) and the out-of-sample evaluation (where 5 full days of data is used). In addition, this demonstrates that it is necessity to ensure that the days used for the out-of-sample evaluation are representative of actual operating conditions.

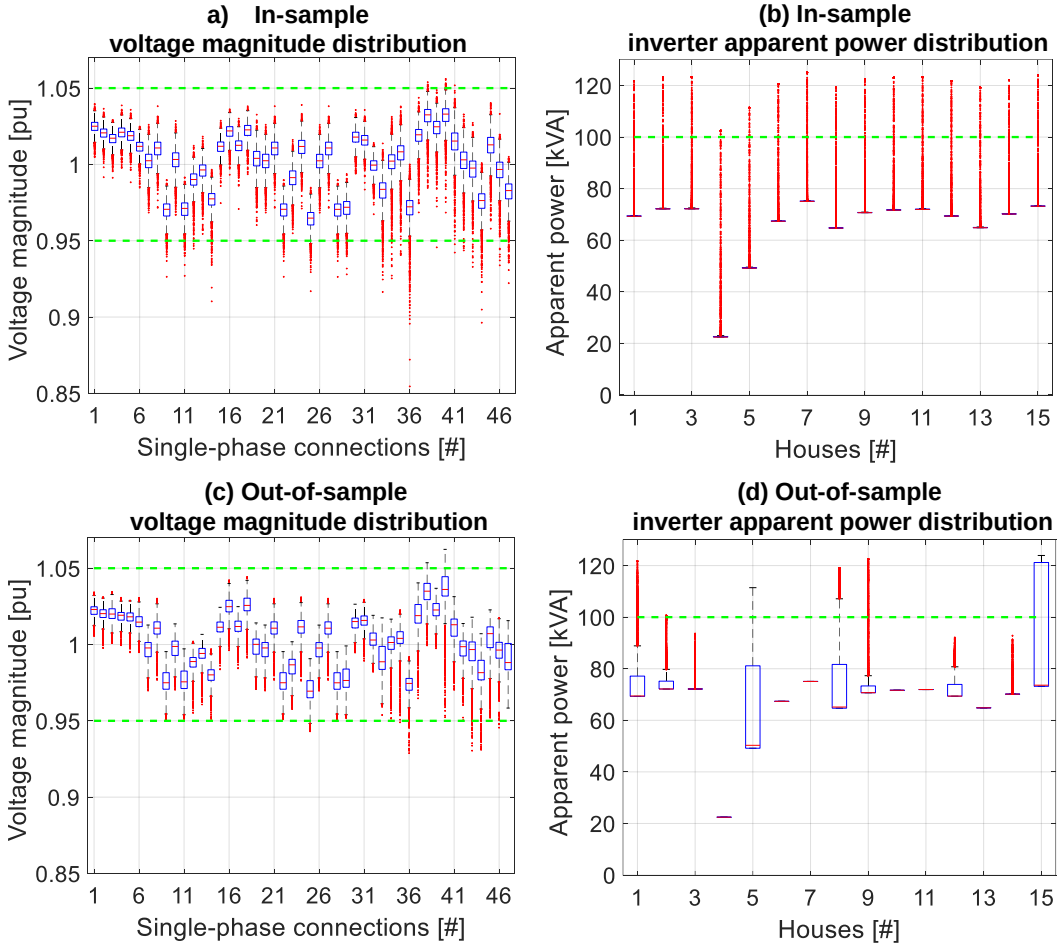

Figure 6.9: Box-whisker plots for voltage magnitude and inverter apparent power distribution calculated using Monte Carlo simulations for the quantile-based method for single replication using $M = 2880$ random samples.

6.8.4 Constraint Violations by Time of Day

We noticed above that there are significant voltage magnitude and inverter limit violations in the out-of-sample results. Because the out-of-sample evaluation is performed using full day data, we can investigate how the violations vary across the day. Fig. 6.10 illustrates violations for the quantile-based solution over time. The top plots show the percentage of single-phase connections experiencing voltage violations (left) or inverters experiencing apparent power violations (right) at each time step of the day, averaged over the five out-of-sample evaluation days. The bottom plots show the magnitude of the worst-case violation across all single-phase connections or inverters and all evaluation days at each time step.

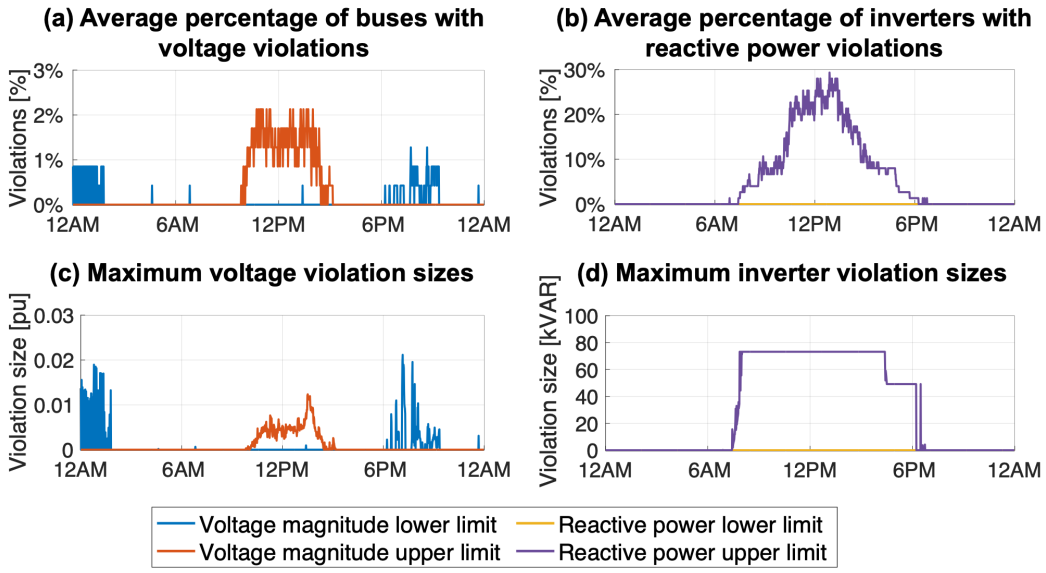

Figure 6.10: Time-series plots for out-of-sample voltage magnitude and inverter reactive power limits violations for quantile-based method for single replication using $M = 2880$ random samples.

In Fig. 6.10(a), the upper voltage violations (orange lines) usually occur during mid-day when the PV generation variability is very high. The lower voltage limit violations (blue lines) occur in the evening (mostly between 6pm and 9pm) and at night (between midnight and 2am) when the

load variability is high. However, we observe in Fig. 6.10(c) that the magnitude of the voltage magnitude violations are comparatively small, with a maximum of around 0.02 p.u.

Looking at the inverter limits in Fig. 6.10(b), we see that the quantile-based method has inverter upper limit violations (purple lines) occurring throughout the day-time when the PV generation is not zero. In contrast to the voltage violation results, the percentage of nodes experiencing violations is very high, reaching a maximum of around 30% at 1pm. The maximum magnitude of inverter upper limit violation is high in Fig. 6.10(d) at 73.2 kVAR throughout the day-time period.

6.9 Case Study III: Considering the Impact of Inverter Capping

One strategy to mitigate inverter violations is to cap the inverter reactive power injections so that they comply with the IEEE 1547-2018 standard [118]. In this section, we cap the inverter reactive power injections to their respective limits during the solution evaluation step described in Section 6.5.2. We use the same set of $M = 2880$ randomly sampled data points as in Section 6.8 and examine the impact of inverter capping on the voltage violations and total VUF.

6.9.1 Comparison of Empirical Distributions

We first examine the impact of capping the inverter reactive power injections on the voltage and inverter violations. Fig. 6.11 illustrates the voltage magnitude (left) and inverter apparent power (right) distributions for both in-sample (top) and out-of-sample (bottom) data. As expected, we do not see any inverter limit violations in Figures 6.11(b) and 6.11(d) because of the capping. When we compare the voltage distribution plots in Fig. 6.11(c) with the results obtained in Fig. 6.9(c) without capping, we observe that the violations of the upper voltage magnitude limit (at nodes 38 and 40) are lesser with smaller violation sizes for the lower voltage magnitude limit (nodes 36 and 44) for the out-of-sample data. The decrease in the number of undervoltage and overvoltages violation size is most likely because of the reduced availability of reactive power injections due to capping.

Recall that the reactive power injections are capped in the solution evaluation step. However, the reactive power limits in CCR-OPF are still tightened using the ϵ_q and $1 - \epsilon_q$ quantiles of the

empirical distribution and do not see the capping from the solution evaluation step. So, we next examine how changing ϵ_q has an impact on the constraint tightenings, resulting VUF, and out-of-sample voltage magnitude violations.

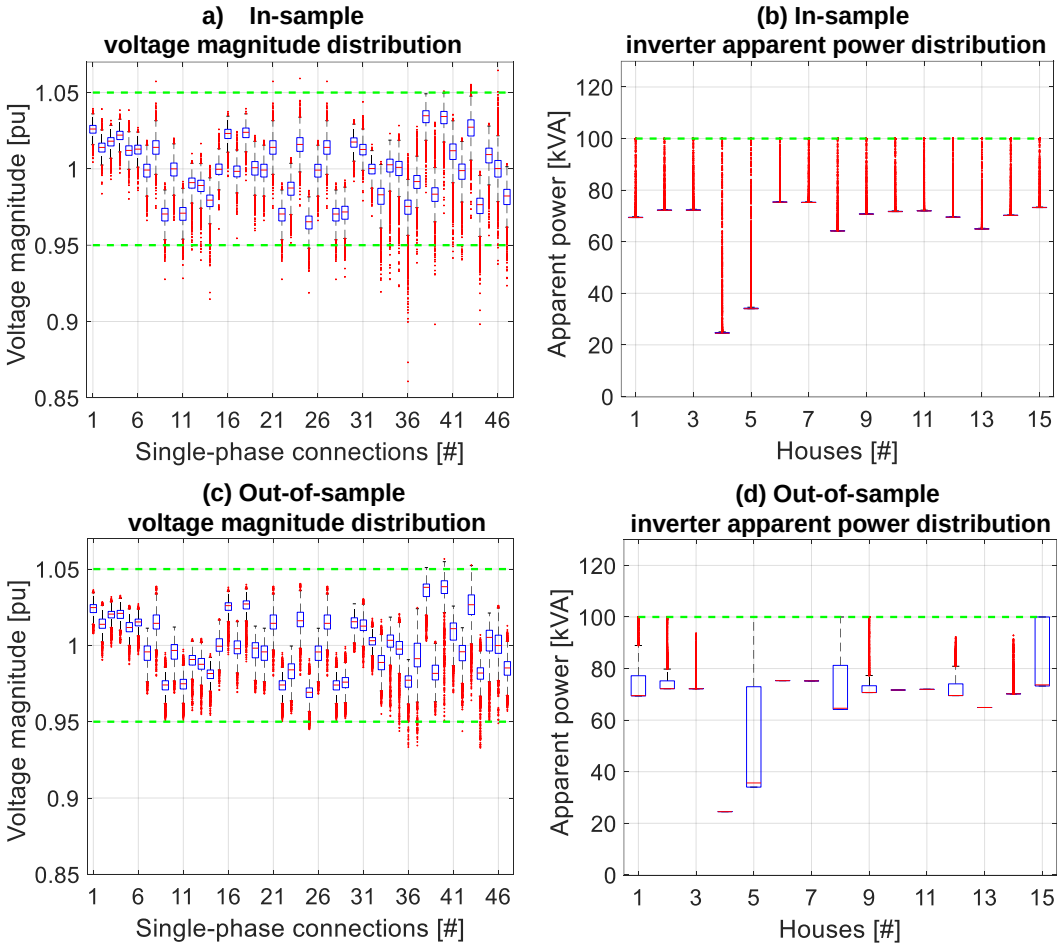

Figure 6.11: Box-whisker plots for voltage magnitude and inverter apparent power distribution calculated using Monte Carlo simulations with capping for the quantile-based method for single replication using $M = 2880$ random samples.

6.9.2 Impact of Higher Violation Probability

We evaluate the impact of using a higher desired violation for the reactive power constraints. Recall that choosing a high violation probability can be inexpensive but might put the system at

a higher risk of insecure operation. Here, we keep $\epsilon_v = 0.05$ while we set $\epsilon_q = 0.15$ in the quantile-based method with inverter capping. Fig. 6.12 compares the operating points and constraint tightenings for $\epsilon_q = 0.05$ (blue lines) and $\epsilon_q = 0.15$ (orange lines). The voltage magnitude tightenings in Fig. 6.12(a) remain almost the same since we set $\epsilon_v = 0.05$ for both cases. However, by choosing a higher violation probability $\epsilon_q = 0.15$, we achieve a wider range for the reactive power limits in Fig. 6.12(b), which almost overlap the nominal constraints (red dashed lines).

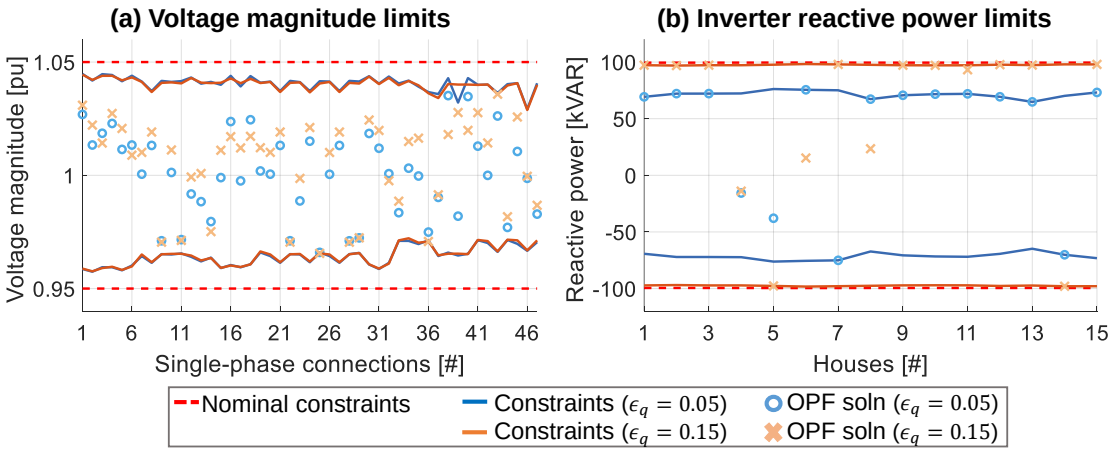

Figure 6.12: Comparison of CCR-OPF solution and constraint tightenings resulting from the quantile-based with capping for single replication using $M = 2880$ random samples with different ϵ_q.

Tables 6.1 and 6.2 show the in- and out-of-sample results for a single replication of the quantile-based method using $\epsilon_q = 0.05$ without capping (from Section 6.8), $\epsilon_q = 0.05$ with capping, and $\epsilon_q = 0.15$ with capping. All the results utilize the same sample set ($M = 2880$ randomly drawn samples). We compare the worst-case violation probabilities for all constraint types as well as the VUF. In Table 6.1, we notice that none of the in-sample violation probabilities for any of the three cases exceed 0.05. In addition, when the inverter capping is used, the violation probabilities for the inverter limits $\hat{E}^{\max}_{\underline{q}}, \hat{E}^{\max}_{\overline{q}}$ are zero as expected. By capping with $\epsilon_q = 0.05$, we see a slight increase in the VUF compared to the VUF for case without capping. This increase is most likely because of the limited reactive power support resulting from capping. By increasing $\epsilon_q = 0.15$, we

also increase the feasible space for reactive power injections, resulting in a better solution with the lowest VUF value among all three cases.

Case	$\hat{E}^{\max}_{\underline{v}}$	$\hat{E}^{\max}_{\overline{v}}$	$\hat{E}^{\max}_{\underline{q}}$	$\hat{E}^{\max}_{\overline{q}}$	VUF (%)
No capping	0.05	0.005	0.05	0.05	6.32
Capping, ϵ_q=0.05	0.05	0.007	0.0	0.0	6.61
Capping, ϵ_q=0.15	0.05	0.05	0.0	0.0	5.85

Table 6.1: In-sample results for quantile-based method with capping for single replication with 2880 random samples.

A similar trend can be seen in the out-of-sample results summarized in Table 6.2. For the case without capping, we observe that the out-of-sample violation probabilities for the inverter upper limits $\hat{E}^{\max}_{\overline{q}}$ and voltage upper limits $\hat{E}^{\max}_{\overline{v}}$ are larger than the desired violation probability of 0.05. By capping with $\epsilon_q = 0.05$, we obtain violation probabilities that are significantly below 0.05. By setting $\epsilon_q = 0.15$, we get the lowest VUF value at the cost of increasing the voltage upper limit violations.

Case	$\hat{E}^{\max}_{\underline{v}}$	$\hat{E}^{\max}_{\overline{v}}$	$\hat{E}^{\max}_{\underline{q}}$	$\hat{E}^{\max}_{\overline{q}}$	VUF (%)
No capping	0.019	0.126	0.0	0.36	6.97
Capping, ϵ_q=0.05	0.019	0.016	0.0	0.0	6.81
Capping, ϵ_q=0.15	0.018	0.029	0.0	0.0	6.21

Table 6.2: Out-of-sample results for quantile-based method with capping for single replication with 2880 random samples.

6.10 Case Study IV: Considering Linear Power Flow Models

In this section, we look at the solutions obtained when a linear power flow model is used in the CCR-OPF problem. The goal is to compare the solutions obtained by using the linearized power balance equations with the solutions determined in the previous case study section. Furthermore, it is important to note that we are adopting an iterative solution method in this chapter which lends itself naturally to the integration of the linear approximations which are used in a successive approximation approach in Chapter 5. By doing this, we can investigate how the linear approximation accuracy changes during every iteration of the quantile-based method. Note that we only employ linear power flow models to solve the approximate problem CCR-OPF. During the solution evaluation step, no linearization is used and we perform Monte Carlo simulations to calculate AC feasible operating points for each sample in the uncertainty set and create the empirical distributions. The results from Section 6.7 indicate that randomly chosen samples is the most suitable sampling method and results from Section 6.9 demonstrate that capping mitigates violations of inverter reactive power limits. Hence, for this case study, we run numerical simulations using random samples with $M = 2880$ and cap the inverter reactive power injections. We perform 10 replications, each using the same sample draw as the uncertainty data used in Section 6.7.

6.10.1 Comparison of In-sample Results

Table 6.3 summarizes the in-sample results where we compare the average, minimum and maximum values of the empirical violation probabilities for each constraint type, total VUF determined by the CCR-OPF problem and number of iterations across the 10 replications. We see that the quantile-based method limits the worst-case violation probabilities of all constraint types to the desired $\epsilon_v = 0.05$ when using either nonlinear or linear power flow equations. By comparing the in-sample voltage unbalance results, we observe that using linear approximations leads to solutions with slightly lower VUF. Another noteworthy observation is that, although the computation time of quantile-based method using linear power flow equations is small per iteration, it takes more number of iterations to converge to a solution when compared to the quantile-based method

using nonlinear power flow equations. This might be because the OPF solution of the approximate problem using linear power flow equations is not AC feasible, whereas the tightening terms calculated in the solution evaluation step are determined based on AC feasible operating points for each uncertainty realization.

Value	$\hat{E}_{\underline{v}}^{\max}$		$\hat{E}_{\overline{v}}^{\max}$		$\mathrm{VUF}_{\mathbf{OPF}}$ [%]		No. of Iter. [#]	
	Nonlin.	**FOT**	**Nonlin.**	**FOT**	**Nonlin.**	**FOT**	**Nonlin.**	**FOT**
Avg.	0.05	0.05	0.003	0.001	6.99	6.67	4	6
Min.	0.05	0.05	0.0	0.0	6.04	5.49	3	5
Max.	0.05	0.05	0.014	0.002	8.26	8.27	5	7

Table 6.3: In-sample results comparing nonlinear and linear power flow models for quantile-based method with capping using 2880 random samples for 10 replications.

To evaluate how far the solution obtained by solving the CCR-OPF problem with linear power flow equations is from an AC feasible operating point, we calculate the linearization accuracy following the procedure defined in (5.38). Our results indicate that the linearization error is small with an average deviation across 10 replications equal to 0.008 p.u. per node and the maximum deviation seen among the 10 replications is 0.015 p.u. per node.

6.10.2 Comparison of Out-of-sample Results

The out-of-sample results comparing the average, minimum and maximum values of the empirical violation probabilities for each constraint type and absolute value of the normalized VUF across the 10 replications are summarized in Table 6.4. Contrary to the results from Section 6.7, we observe that the difference between the in- and out-of-sample violation probabilities are not large when using either nonlinear or linear power flow models. While the violation probabilities for the lower voltage limits are well within 0.05, the worst-case violation probabilities of the upper voltage limits exceeds 0.05 for some of the replications. Although the number of violations are higher than expected, the violations size is small with the maximum voltage magnitude exceeding

the upper limits by 0.01 p.u. By comparing the absolute deviation in out-of-sample VUF from the in-sample VUF for the nonlinear and linear power flow models, we see that the normalized VUF is higher on average when using the linear power flow models which might be because of the linearization error.

Value	$\hat{E}_{\underline{v}}^{\max}$		$\hat{E}_{\overline{v}}^{\max}$		$\lvert\frac{\mathbf{VUF}-\mathbf{VUF_{OPF}}}{\mathbf{VUF_{OPF}}}\rvert$ [%]	
	Nonlin.	**FOT**	**Nonlin.**	**FOT**	**Nonlin.**	**FOT**
Avg.	0.007	0.006	0.085	0.084	0.081	0.097
Min.	0.000	0.000	0.019	0.015	0.019	0.023
Max.	0.022	0.021	0.154	0.156	0.249	0.297

Table 6.4: Out-of-sample results comparing nonlinear and linear power flow models for quantile-based method with capping using 2880 random samples for 10 replications.

6.10.3 Comparing Results for a Single Replication

Finally, we compare the results of a single replication of the iterative algorithm. Fig. 6.13 shows the constraint tightenings and voltage magnitude set-points across all single-phase connections (left) as well as PV inverter reactive power constraint tightenings and set-points across all houses (right). We observe from Fig. 6.8(a) that the tightenings and voltage setpoints obtained by the nonlinear and linear models are close to each other. The linearization error for this replication is 0.009 p.u. It is interesting to note that this deviation does not change much in each iteration of the algorithm. This might be due to the fact that we do not update the linearization point in each iteration and only calculate the Jacobian once at the beginning of the iterative process. By comparing the results for inverter reactive power limits in Fig. 6.8(b), we see that the most of the set-points are close to each other. This demonstrates that even though we are using the linearized power balance constraints, the iterative method is able to obtain solutions that are similar to the results obtained by the iterative method using nonlinear power flow equations.

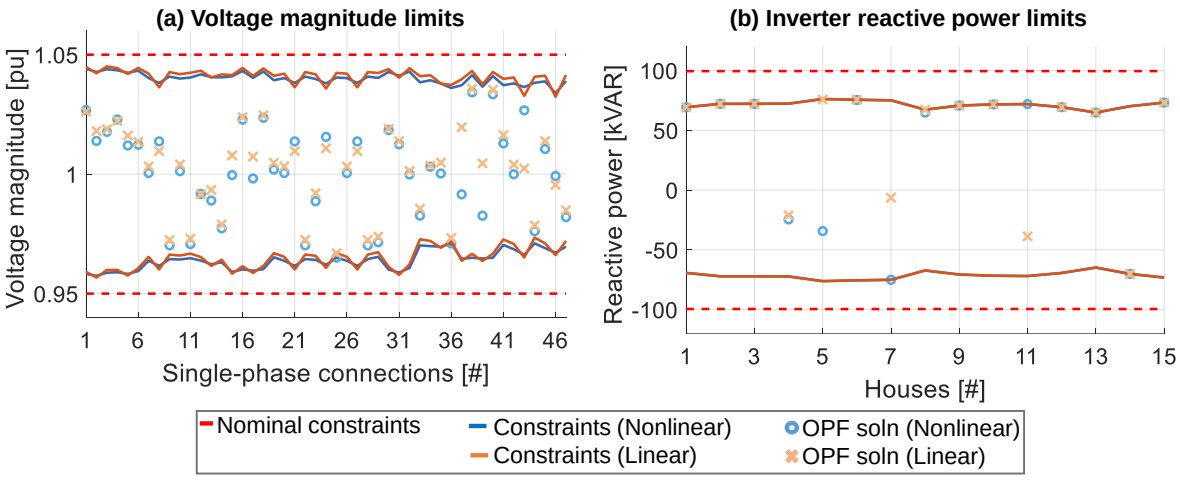

Figure 6.13: Comparison of CCR-OPF solution and constraint tightenings resulting from the quantile-based with capping for single replication using $M = 2880$ random samples with different power flow models.

6.11 Main Takeaways

In this chapter, we develop an iterative, data-driven algorithm to solve the chance-constrained AC OPF for unbalanced distribution grids. We reformulate the chance constraints to deterministic constraints which consist of a nominal constraint tightened with uncertainty margins. The optimal constraint tightenings are computed using an iterative approach that alternates between solving an approximate OPF problem with fixed tightenings and utilizing Monte Carlo simulations to update the tightening terms.

The proposed method was tested by running numerical experiments on the IEEE 13-bus test feeder using actual residential load and PV data. Our case studies show that the quantile-based method is able to enforce the chance constraints in the in-sample evaluation. The out-of-sample results were significantly improved by capping the DER inverter outputs. In addition, preliminary simulation results demonstrate that using randomly chosen samples across multiple days is the most suitable sampling procedure, as opposed to using representative full day data sets. Furthermore, we also observe that the quantile-based method obtains good quality solutions even when linear power flow models are used in the approximate problem formulation.

Chapter 7

Identifying Secure Operating Ranges for DER Control

Distribution grids are no longer being considered as passive loads in the transmission system operation. As the number of dispatchable DERs increases in distribution grids, they can provide flexibility in the form of energy services to transmission systems similar to the large-scale operating reserves. However, DERs are managed by various entities (i.e. DSOs, aggregators, individual owners) whose control objectives can be different from each other. A new framework is required to accurately model the coordination between the various entities and the interaction between transmission system and distribution grid operation in the presence of DERs. In this chapter, we assume that DERs are controlled by aggregators with no knowledge of distribution grid constraints. Our goal is to determine the aggregate power flexibility of distribution grids and identify optimal DER control actions that can be easily communicated to aggregators and transmission system operators to mitigate violations of any distribution grid constraints.

As per the recently announced FERC Order 2222 [120] in the USA, DER aggregators are allowed to participate in Independent System Operator (ISO) markets. Consider the example illustrated in Fig. 7.1 where generators and a distribution grid are connected to the transmission system. The two generators G1 and G2 can bid into the electricity market and the amount of power provided by them combined is determined by solving a transmission system dispatch problem that considers the transmission constraints expressed using $P_{\text{min}}, P_{\text{max}}$. Analogous to this, the distribution grid comprises of two DER aggregators A1 and A2, that control DERs at multiple nodes as illustrated by the red and green circles, respectively, can now bid into the electricity market. However, including the operational limits of each DER aggregator in the transmission system dispatch problem can increase the computational complexity [121, 122, 123]. One promising alternative

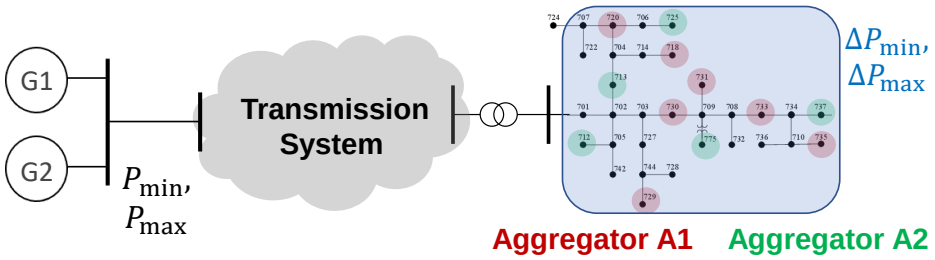

Figure 7.1: Example of transmission-distribution interaction.

to model this transmission-distribution interaction is for the DSO to identify the aggregate flexibility limits $\Delta P_{\min}, \Delta P_{\max}$ of power that can be provided from all DERs in the distribution grid combined such that no grid constraints are violated. Every DER in the distribution grid operates within a certain feasible region, which is determined by the physical and operational constraints of the distribution grid. The aggregation of these feasible regions determines the net flexibility that can be offered by the distribution grid. This aggregate feasible region defined by the limits $\Delta P_{\min}, \Delta P_{\max}$ can then be used analogous to transmission limits specified for individual lines thereby reducing the need to integrate a detailed distribution grid model in the transmission system dispatch problem.

7.1 Literature Review: Existing Methods to Find Aggregate Power Flexibility

There are numerous works in literature which focus on identifying flexibility of individual DERs [124, 125] as well as system-level aggregate power flexibility [40, 41, 42] in distribution grids. Data-driven approaches employing Monte Carlo simulations with a large number of sampling scenarios are described in [126, 127, 128] to estimate the aggregate power flexibility range. Bilevel optimization models are used to improve the interactions between DSO and aggregators in [129, 130, 131, 132] as well as interactions between end consumers and aggregators in [132, 133]. Most of these methods assume that network constraints such as voltage magnitude limits are non-binding and hence, do not consider them. However, this might not be true for large-scale aggregation of DERs where ensuring that voltage limits are not violated can be highly critical. The methods proposed in [134, 135] do consider network constraints to solve the flexibility

aggregation and feasible disaggregation problem for a single time-step in the system. Geometric approaches that consider temporally coupled constraints are discussed in [136, 137, 138], where polytope sets are utilized to describe the power flexibility of an individual DERs. The aggregate power flexibility is then determined using polytopic projection to a lower dimensional space or calculating the Minkowski sum of the polytope sets. It is important to note that most of the works mentioned above model the distribution grids using a balanced, single-phase equivalent power flow model. However, distribution grids are typically unbalanced due to untransposed lines, and asymmetrical three-phase loads [14]. To that end, [43, 44, 45, 46] employ the unbalanced three-phase network model to perform power flexibility aggregation for distribution grids.

The definition of flexibility and computation of associated flexibility regions relies on assumptions about who controls the DERs. On one hand, DERs can be controlled individually by the DSO, who can leverage these devices to both provide services to the transmission grid and manage distribution grid constraints. On the other hand, aggregators can control multiple DERs to achieve an aggregated response, possibly without awareness of their exact geographical location and without any consideration of the distribution grid constraints. In such cases, several intermediate solutions could be possible to ensure secure operation of distribution grid. For example, aggregators could control DER responses to meet their own objectives, but the DSO can override the control actions of the aggregator to ensure secure operation of the grid [139]. Another example could be for the DSO to determine and communicate secure operating ranges of individual DERs to the aggregators controlling them [125, 135]. A challenge associated with such approaches is that it requires (possibly frequent) communication between the DSO and the aggregator. Furthermore, in practice, there may be multiple aggregators in the distribution grid competing for the same capacity, and resolving the sharing of limited grid capacity in a fair manner is not a straightforward task. Hence, it can be quite challenging for the DSO to maximize (or at least check the feasibility of) the provision of DER flexibility when there is no coordination with the aggregators.

7.2 Main Contributions

All researches mentioned above assume that there is continuous communication between the DSO and aggregators to harness the full DER flexibility. To counteract the challenges of facilitating extensive communication requirements, we propose a methodology that makes such communication unnecessary. We only assume that aggregators are required to report the maximum and minimum power limits of the DERs they control to the DSO. After receiving this information from all aggregators, the DSO can then determine a secure aggregate power flexibility range such that *any* disaggregation solution (including the worst-case condition) will be feasible. This range can be communicated to the transmission system operator who may use this information to clear the market with consideration of aggregator bids. This can reduce burden on transmission resources while also ensuring that the combined bid of all aggregators participating are adequately accounted for.

By definition, the aggregate power flexibility range will be smaller if we assume a worst-case disaggregation solution, as compared with a situation in which the utility control the DERs directly. As a result, the worst-case approach could lead to conservative solutions. However, it is possible to determine rules for DER control activation that are not only easy to communicate to the aggregators, but also increase the aggregate power flexibility of the grid to the aggregator's benefit. Note that the DSO does not allocate capacity limits for individual DERs or individual DER aggregators, but instead determines total capacity limits for all DER devices combined. The individual DER aggregator capacity limits (and associated bids to provide flexibility) will be considered by the transmission system operator as part of the market clearing, which takes the distribution grid constraints as an input.

Since this decision making process is hierarchial where an upper-level authority (i.e. DSO) takes decisions based on the unknown (and thus assumed to be worst-case) responses by the lower-level entity (i.e. aggregators), it is natural to leverage a bilevel optimization framework. In this chapter, we formulate a bilevel problem that identifies the largest amount of active power capacity that can be provided to the transmission system (i.e., at the substation). The bilevel problem is

formulated with the overall objective to find the maximum allowable change in active power at the substation (relative to the current operating point) such that there are no voltage magnitude violations in the network, regardless of how this change in power injections is allocated by the aggregators among the individual DERs. This optimization problem is solved subject to several rules for DER active and reactive power control activation that can be easily communicated to aggregators. For example, one rule we impose is that the active power of all DERs must be controlled in the same way. This is practical since the benefits of the aggregate power flexibility should be shared among all the aggregators and we avoid situations where one aggregator is allowed to increase the active power while other aggregators are required to curtail active power. The upper-level problem maximizes the allowable power injections while guaranteeing that the voltage magnitudes stay within acceptable limits. The lower-level solves a three-phase OPF problem for each node in the network with objective to find the worst-case (largest or smallest) voltage magnitude in the grid, subject to the power flow constraints and rules for DER activation.

The lower-level problem of the bilevel task is similar to the formulation proposed in [140], which we extend to include the unbalanced three-phase power flow model derived in Chapter 4. As mentioned previously, the solution of the bilevel problem can be too conservative since we are looking at the worst-case conditions. To maximize the aggregate power flexibility range, we assume that DSO can provide certain rules for DER control activation (e.g. all DERs are either simultaneously increasing or decreasing their active power output) as well as reactive power setpoints to the inverters as per the IEEE Standard 1547-2018 [118]. We consider three different inverter reactive power control modes for reactive power control in this work, which include constant power factor, constant reactive power and voltage-reactive power modes. We assume that the reactive power control setpoints are provided to the DERs either through the aggregator or directly from the DSO.

In the next few sections, we provide a brief overview of bilevel optimization and then present the formulation of the bilevel problem to identify aggregate power flexibility. We then describe the analytical reformulation of the problem using linear approximations and strong duality and test the proposed approach on two unbalanced distribution feeders.

7.3 Bilevel Optimization: Theoretical Background

A bilevel problem can be defined as an optimization problem that is constrained by another optimization problem. One of the main reasons to choose a bilevel optimization approach in our work is because we have two independent decision makers i.e. the DSO and DER aggregators and each of them has their own objective and constraints. By using this approach, we are able to capture the conflicting interests of the DSO and aggregators. To better explain how to solve such a problem with hierarchical structure, we consider a sequential game based on the Stackelberg game theory [141] where two players are involved. The first player is referred to as the leader problem with the decision vector represented by $\boldsymbol{X}_{\mathbf{u}}$. The decision vector of the second player or the follower problem is denoted by $\boldsymbol{X}_{\mathbf{l}}$. From a mathematical point of view, a general bilevel problem is given by

$$\max_{\boldsymbol{X}_{\mathbf{u}}} \; f_{\mathrm{u}}(\boldsymbol{X}_{\mathbf{u}}, \hat{\boldsymbol{X}}_{\mathbf{l}}) \tag{7.1a}$$

$$\text{s.t. } g_{\mathrm{u}}(\boldsymbol{X}_{\mathbf{u}}, \hat{\boldsymbol{X}}_{\mathbf{l}}) \leq 0, \tag{7.1b}$$

$$h_{\mathrm{u}}(\boldsymbol{X}_{\mathbf{u}}, \hat{\boldsymbol{X}}_{\mathbf{l}}) = 0, \tag{7.1c}$$

$$\text{where } \hat{\boldsymbol{X}}_{\mathbf{l}} = \arg\max_{\boldsymbol{X}_{\mathbf{l}}} \; f_{\mathrm{l}}(\boldsymbol{X}_{\mathbf{u}}, \boldsymbol{X}_{\mathbf{l}}) \tag{7.1d}$$

$$\text{s.t. } g_{\mathrm{l}}(\boldsymbol{X}_{\mathbf{u}}, \boldsymbol{X}_{\mathbf{l}}) \leq 0, \tag{7.1e}$$

$$h_{\mathrm{l}}(\boldsymbol{X}_{\mathbf{u}}, \boldsymbol{X}_{\mathbf{l}}) = 0. \tag{7.1f}$$

Here, (7.1a)-(7.1c) describes the leader or the upper-level problem and (7.1d)-(7.1f) represents the follower or the the lower-level problem. It is important to note the optimal reaction of the follower is included in the decision making process of the leader in the bilevel problem. The leader problem has full knowledge of the objective and constraints of the follower problem, whereas the follower problem can only observe the decisions made by the leader problem and then optimize their own strategy. Therefore, the follower problem can be considered as an $\boldsymbol{X}_{\mathbf{u}}$-parameterized problem where the upper-level decision vector is assumed to be known and not considered as a variable. The solution pair $(X_{\mathrm{u}}, \hat{X}_{\mathrm{l}})$ where $\hat{X}_{\mathrm{l}}$ denotes the optimal response of the follower problem to the

leader problem's decision X_{u} is feasible provided that $\hat{X}_{\mathrm{l}}$ satisfies the constraints (7.1b)-(7.1c) in the upper-level problem.

Although there is considerable body of literature on solving bilevel optimization problems, the hierarchical structure of the problem introduces challenges such as disconnectedness and non-convexity [142]. Even for simple examples of bilevel optimization tasks, it has been observed that the problems are not straightforward to handle mathematically. As a result, bilevel problems are considered to be strongly NP-hard to solve [143, 144]. Some of the classical approaches to solve bilevel problems are summarized below:

- *Single-level reduction:* One of the most commonly used strategies is to reformulate the bilevel problem as a single-level problem. If the follower problem is convex, we can replace the lower-level optimization problem with its Karush-Kuhn-Tucker (KKT) conditions [145, 146, 147] or apply the strong duality theorem [148, 149, 150] for the lower-level problem. The advantage of this method is that the resulting single-level reformulation can be directly solved using state-of-the-art commercially available solvers.

- *Descent methods:* This is based on finding a descent direction in bilevel optimization that results in decrease in upper-level objective function value while ensuring that the solution is feasible [144, 151, 152]. A drawback of this approach is that finding the descent direction can be complex.

- *Penalty function methods:* This approach reformulates the problem as an unconstrained optimization task where a penalty term measures the extent of constraint violation [153, 154]. While the lower-level problem is replaced by a penalized problem, the bilevel structure is still maintained and as a result, the reduced problem is still challenging to solve.

- *Trust-region methods:* This is an iterative method where at every iteration, a model of the bilevel problem is built around the approximate solution [155, 156, 157]. If the approximation is accurate, the region is enlarged, otherwise it is reduced. Although this approach is popular due to the strong convergence properties, it can be computationally expensive since it involves solving the bilevel problem over multiple iterations.

Based on the advantages and limitations of the different approaches mentioned above, we choose to develop a linear bilevel problem which can be reformulated using the strong duality based, single-level reduction approach. We will discuss the reformulation in more detail in Section 7.5.

7.4 Problem Formulation

In this section, we describe our model of the flexibility offered by solar PV inverters and loads in the distribution grid. We then present a formulation of a bilevel optimization problem. To simplify notation, we assume that there is one solar PV inverter and one load at every single-phase connection of node $i \in \mathcal{N}$. If any node connected to a phase has no source or load, we set the corresponding entries to zero. Recall that optimization variables are denoted using **bold** symbols, scalar values are denoted using small letters, and their vector counterparts and matrices are denoted using the same capital letters.

7.4.1 Current Operating Point

Assume that we have full information about the current operating point in the grid and the full system model. At any three-phase node $i \in \mathcal{N}_0$, we know the the voltage phasor which is represented by $V_i = |V_i|\angle\Theta_i = V_{\mathrm{d}i} + j \cdot V_{\mathrm{q}i}$. Similarly, we also know the three-phase active and reactive power injections which are expressed as $P_i = [p_i^a \;\; p_i^b \;\; p_i^c]^\top$ and $Q_i = [q_i^a \;\; q_i^b \;\; q_i^c]^\top$, respectively. At any node $i \in \mathcal{N}_0$, we denote the current operating point using $V_i, P_i, Q_i \in \mathbb{R}^3$.

The power injections at node $i \in \mathcal{N}$ connected to phase $\phi \in \Phi$ are expressed as the difference between the generation and load demand using

$$p_i^\phi = p_{\mathrm{G},i}^\phi - p_{\mathrm{L},i}^\phi, \tag{7.2a}$$

$$q_i^\phi = q_{\mathrm{G},i}^\phi - q_{\mathrm{L},i}^\phi, \tag{7.2b}$$

where $p_{\mathrm{G},i}^\phi$, $q_{\mathrm{G},i}^\phi$ are the active and reactive power generation by solar PV inverters, respectively; $p_{\mathrm{L},i}^\phi$, $q_{\mathrm{L},i}^\phi$ denote the respective active and reactive load demand.

The power balance is maintained by the substation, which supplies the difference between the load and power generation as well as other losses in the grid. At the current operating point, the active and reactive power injection at the substation are denoted by $P_{\mathrm{G},0}, Q_{\mathrm{G},0} \in \mathbb{R}^3$, respectively.

7.4.2 Voltage Representation

In this chapter, the voltage variables in the bilevel problem are expressed in rectangular form. For any node $i \in \mathcal{N}_0$, the real and imaginary components of voltage are given by $\boldsymbol{V}_{\mathbf{d}i}, \boldsymbol{V}_{\mathbf{q}i} \in \mathbb{R}^3$, respectively. Recall that the fixed-point linearization method in Chapter 5 was implemented in rectangular coordinates. So, we can enforce voltage magnitude constraints at distribution substation using (5.23) defined in Chapter 5. For every other node $i \in \mathcal{N}$ connected to phase ϕ, we include additional voltage magnitude variables $|\boldsymbol{v}_i^\phi|$ in the formulation. These voltage magnitude variables are quadratic functions of the rectangular voltage variables $\boldsymbol{v}_{\mathbf{d}i}^\phi, \boldsymbol{v}_{\mathbf{q}i}^\phi$. Given the current voltage magnitude $|v_i^\phi| = \sqrt{\left(v_{\mathrm{d}i}^\phi\right)^2 + \left(v_{\mathrm{q}i}^\phi\right)^2}$, we use First-order Taylor approximation to get the following linear constraints for the voltage magnitude:

$$\left(v_{\mathrm{d}i}^\phi\right)^2 + \left(v_{\mathrm{q}i}^\phi\right)^2 + 2v_{\mathrm{d}i}^\phi \boldsymbol{v}_{\mathbf{d}i}^\phi + 2v_{\mathrm{q}i}^\phi \boldsymbol{v}_{\mathbf{q}i}^\phi = \left|v_i^\phi\right|^2 + 2|v_i^\phi||\boldsymbol{v}_i^\phi|. \tag{7.3}$$

7.4.3 Flexibility Modelling

The aggregators can offer flexibility by modifying the active power demand of controllable loads as well as the active power generation of the solar PV inverters. In this work, we only consider single-phase DER inverters since most residential solar PV systems are typically connected to single phases of distribution grids in the US. However, the modelling can be easily extended to include three-phase inverters with higher capacity and larger range of flexibility, but we defer this to future work.

7.4.3.1 Modelling of Loads

For a load at node $i \in \mathcal{N}$ connected to phase $\phi \in \Phi$, let $\Delta \boldsymbol{p}^{\phi}_{\mathbf{L},i}$ denote the controllable change in active power demand of the load from the current operating point such that

$$\underline{p}^{\phi}_{\mathrm{L},i} \leq p^{\phi}_{\mathrm{L},i} + \Delta \boldsymbol{p}^{\phi}_{\mathbf{L},i} \leq \overline{p}^{\phi}_{\mathrm{L},i}. \tag{7.4}$$

Here, $\underline{p}^{\phi}_{\mathrm{L},i}, \overline{p}^{\phi}_{\mathrm{L},i}$ represent the minimum and maximum limits for the active power load demand. We assume that the loads operate with a constant power factor $pf^{\phi}_{\mathrm{L},i}$, which means the reactive power consumption is given by

$$\boldsymbol{q}^{\phi}_{\mathbf{L},i} = \frac{\sqrt{1 - \left(pf^{\phi}_{\mathrm{L},i}\right)^2}}{pf^{\phi}_{\mathrm{L},i}} \cdot \left(p^{\phi}_{\mathrm{L},i} + \Delta \boldsymbol{p}^{\phi}_{\mathbf{L},i}\right). \tag{7.5}$$

7.4.3.2 Modeling of Solar PV Active Power Generation

Similar to the load modelling, we consider $\Delta \boldsymbol{p}^{\phi}_{\mathbf{G},i}$ as the controllable change in active power generation from the current operating point for a solar PV inverter at node $i \in \mathcal{N}$ connected to phase $\phi \in \Phi$ such that

$$\underline{p}^{\phi}_{\mathrm{G},i} \leq p^{\phi}_{\mathrm{G},i} + \Delta \boldsymbol{p}^{\phi}_{\mathbf{G},i} \leq \overline{p}^{\phi}_{\mathrm{G},i}, \tag{7.6}$$

where $\underline{p}^{\phi}_{\mathrm{G},i}, \overline{p}^{\phi}_{\mathrm{G},i}$ denote the respective minimum and maximum limits for the active power generation.

7.4.3.3 Aggregate Power Flexibility

The total active power flexibility $\Delta \boldsymbol{p}$ provided by the distribution grid can be bounded to define the secure operating range using

$$\Delta \boldsymbol{p}^{-} \leq \underbrace{\sum_{i \in \mathcal{N}} \sum_{\phi \in \Phi} \left(\Delta \boldsymbol{p}^{\phi}_{\mathbf{G},i} - \Delta \boldsymbol{p}^{\phi}_{\mathbf{L},i}\right)}_{\Delta \boldsymbol{p}} \leq \Delta \boldsymbol{p}^{+}, \tag{7.7}$$

where $\Delta \boldsymbol{p}^{-}, \Delta \boldsymbol{p}^{+}$ are the respective lower and upper limits of the aggregate power flexibility which will be provided by the substation since there are no other generators in the network apart from the

solar PV systems. Recall that the current operating point can be considered as the condition when the substation offers zero flexibility to the transmission network (i.e. $\Delta \boldsymbol{p} = 0$).

To find the limits on the aggregate power flexibility, we enforce a rule that the active power injection of each solar PV inverter as well as each load controlled by the aggregator is adjusted in the same way. The reasoning behind this rule is to ensure that limiting the aggregate response is sufficient to actually control voltage magnitude violations in the feeder. Without this rule, some DERs in one part of the feeder can arbitrarily increase their injections as long as the increases are offset by an equally large decrease in injections elsewhere. In this case, even a zero change in the overall active power injection can cause voltage violations. To model this rule in our optimization problem, we consider two cases:

(a) *Positive (+) case:* This case corresponds to finding the maximum aggregate power flexibility limit $\Delta \boldsymbol{p}^{+} \geq 0$. The active power injections at any node $i \in \mathcal{N}$ connected to phase ϕ is assumed to be greater than the current value p_i^{ϕ}. This means that the load demand is reduced and that any solar PV inverters that were not operating at full capacity at the current operating point can increase their active power injection. This gives rise to the following constraints on flexibility activation for PV generation and load:

$$\Delta \boldsymbol{p}_{\mathbf{L},i}^{\phi} \leq 0, \;\; \Delta \boldsymbol{p}_{\mathbf{G},i}^{\phi} \geq 0. \tag{7.8}$$

(b) *Negative (-) case:* This case is used to calculate the minimum aggregate power flexibility limit $\Delta \boldsymbol{p}^{-} \leq 0$. We assume that the active power injections at every node $i \in \mathcal{N}$ connected to phase ϕ is lower than the current value p_i^{ϕ}. This case gives rise to the following rules for flexibility activation from PV generation and load:

$$\Delta \boldsymbol{p}_{\mathbf{L},i}^{\phi} \geq 0, \;\; \Delta \boldsymbol{p}_{\mathbf{G},i}^{\phi} \leq 0. \tag{7.9}$$

7.4.4 Reactive Power Control from Solar PV Inverters

We assume that all solar PV inverters are smart inverters with the ability to provide reactive power control as specified in the IEEE Standard 1547-2018 [118]. To determine the reactive power

injections, which are decision variables in our optimization problem, we consider three modes in which the PV inverters can operate. For all three modes, any inverter at node $i \in \mathcal{N}$ connected to phase $\phi \in \Phi$ should not exceed the the inverter apparent power capacity $|s^{\phi}_{\mathrm{G},i}|$. Since the inverter limits are quadratic constraints, we use the circular constraint linearization method to outer approximate the feasible region using linear constraints given by

$$0 \leq p^{\phi}_{\mathrm{G},i} + \Delta \boldsymbol{p}^{\phi}_{\mathbf{G},i} \leq |s^{\phi}_{\mathrm{G},i}|, \tag{7.10a}$$

$$-|s^{\phi}_{\mathrm{G},i}| \leq \boldsymbol{q}^{\phi}_{\mathbf{G},i} \leq |s^{\phi}_{\mathrm{G},i}|, \tag{7.10b}$$

$$p^{\phi}_{\mathrm{G},i} + \Delta \boldsymbol{p}^{\phi}_{\mathbf{G},i} + \boldsymbol{q}^{\phi}_{\mathbf{G},i} \leq \sqrt{2} \cdot |s^{\phi}_{\mathrm{G},i}|, \tag{7.10c}$$

$$p^{\phi}_{\mathrm{G},i} + \Delta \boldsymbol{p}^{\phi}_{\mathbf{G},i} - \boldsymbol{q}^{\phi}_{\mathbf{G},i} \leq \sqrt{2} \cdot |s^{\phi}_{\mathrm{G},i}|. \tag{7.10d}$$

Note that it is possible to obtain a more accurate representation of the quadratic inverter constraints by including more linear constraints.

We will next describe the three inverter reactive power control modes. For each mode, the setpoints provided by the DSO are different and will be considered as the leader problem variables. All other variables in the inverter constraints are part of the follower problem. The assignment of the inverter variables to the upper-level and lower-level problems for different inverter reactive power control modes is summarized in Table 7.1 at the end of this subsection.

7.4.4.1 Constant Power Factor Mode

When the inverter is operating in this mode, the solar PV inverters operate at a constant power factor. The power factor setting can be adjusted locally or remotely as specified by the DSO. In this work, we assume that DSO provides the target power factor setting to the DERs. The reactive power injection $\boldsymbol{q}^{\phi}_{\mathbf{G},i}$ depends on the active power generation and the target power factor $pf^{\phi}_{\mathrm{G},i}$ and expressed as

$$\boldsymbol{q}^{\phi}_{\mathbf{G},i} = \boldsymbol{\gamma}^{\phi}_{\mathbf{G},i} \cdot \left(p^{\phi}_{\mathrm{G},i} + \Delta \boldsymbol{p}^{\phi}_{\mathbf{G},i} \right), \tag{7.11a}$$

$$\frac{-\sqrt{1 - \left(pf^{\phi}_{\mathrm{G},i}\right)^2}}{pf^{\phi}_{\mathrm{G},i}} \leq \boldsymbol{\gamma}^{\phi}_{\mathbf{G},i} \leq \frac{\sqrt{1 - \left(pf^{\phi}_{\mathrm{G},i}\right)^2}}{pf^{\phi}_{\mathrm{G},i}}, \tag{7.11b}$$

where $\boldsymbol{\gamma}^{\phi}_{\mathbf{G},i}$ is an upper-level variable which defined as the power ratio of the inverter.

Note that (7.11a) consist of bilinear terms involving the upper-level variables $\boldsymbol{\gamma}^{\phi}_{\mathbf{G},i}$ and lower-level variables $\Delta\boldsymbol{p}^{\phi}_{\mathbf{G},i}$. Recall that the upper-level variables are considered as parameters in the follower problem, and as a result, (7.11) is linear for the lower-level problem.

7.4.4.2 Constant Reactive Power Mode

In this mode, the reactive power injection $\boldsymbol{q}^{\phi}_{\mathbf{G},i}$ at node i connected to phase ϕ is specified by the DSO and hence, considered as an upper-level variable. The DERs are allowed to operate at any power factor in this mode as long as the power factor requirements are met at the point of interconnection to the grid. In our work, we assume that PV inverters are operating within the specified power ratio $\gamma^{\phi}_{\mathrm{G},i}$ and we enforce limits on the reactive power using

$$\boldsymbol{q}^{\phi}_{\mathbf{G},i} \geq -\gamma^{\phi}_{\mathrm{G},i} \cdot \left(p^{\phi}_{\mathrm{G},i} + \Delta\boldsymbol{p}^{\phi}_{\mathbf{G},i}\right), \tag{7.12a}$$

$$\boldsymbol{q}^{\phi}_{\mathbf{G},i} \leq \gamma^{\phi}_{\mathrm{G},i} \cdot \left(p^{\phi}_{\mathrm{G},i} + \Delta\boldsymbol{p}^{\phi}_{\mathbf{G},i}\right). \tag{7.12b}$$

7.4.4.3 Voltage-Reactive Power Mode

This mode is also commonly referred to as voltage regulation with reactive droop. The reactive power injection of the solar PV inverter is a function of the voltage magnitude, which follows a piecewise linear characteristic with the parameter values specified by the DSO. An example voltage magnitude-reactive power characteristic is illustrated in Fig. 7.2.

Consider a PV inverter at node i connected to phase ϕ with the maximum available reactive power $\overline{\boldsymbol{q}}^{\phi}_{\mathbf{G},i}$ specified by the DSO and included in our bilevel task as an upper-level decision variable. If the actual voltage magnitude $|\boldsymbol{v}^{\phi}_{i}|$ at this single-phase connection is below the minimum limit $\underline{v}$, the PV inverter injects all the available reactive power $\overline{\boldsymbol{q}}^{\phi}_{\mathbf{G},i}$. Conversely. the PV inverter absorbs the maximum reactive power when the voltage magnitude is above the maximum limit $\overline{v}$. In the grey shaded region, the reactive power can be expressed as a function of the voltage magnitude

using

$$\boldsymbol{q}^{\phi}_{\mathrm{G},i} = \overline{\boldsymbol{q}}^{\phi}_{\mathrm{G},i} - 2\overline{\boldsymbol{q}}^{\phi}_{\mathrm{G},i} \cdot \left(\frac{|\boldsymbol{v}^{\phi}_{i}| - \underline{v}}{\overline{v} - \underline{v}} \right), \tag{7.13a}$$

$$0 \leq \overline{\boldsymbol{q}}^{\phi}_{\mathrm{G},i} \leq |s^{\phi}_{\mathrm{G},i}|. \tag{7.13b}$$

It is quite challenging to model the linear piecewise equality constraints illustrated in Fig. 7.2 in an optimization problem. In our work, we assume that the inverter is operating only in the gray shaded region and hence, we can use (7.13) to determine the reactive power injections. This is a reasonable assumption since the voltage magnitude $|\boldsymbol{v}^{\phi}_{i}|$ is supposed to be within the limits $\underline{v}, \overline{v}$, which are identical to the voltage magnitude limits specified for every single-phase connection in the network as defined in (4.2). It is important to note here that the actual upper bound of the maximum available reactive power $\overline{\boldsymbol{q}}^{\phi}_{\mathrm{G},i}$ can be expressed as $|s^{\phi}_{\mathrm{G},i}|^2 - (p^{\phi}_{\mathrm{G},i} + \Delta\boldsymbol{p}^{\phi}_{\mathrm{G},i})^2$. Since this expression is quadratic, we relax the upper bound and come up with a linear constraint as defined in (7.13b).

Similar to the constant power factor mode, the reactive power constraints in (7.13a) consist of bilinear terms involving the upper-level variables $\overline{\boldsymbol{q}}^{\phi}_{\mathrm{G},i}$ and lower-level variables $|\boldsymbol{v}^{\phi}_{i}|$.

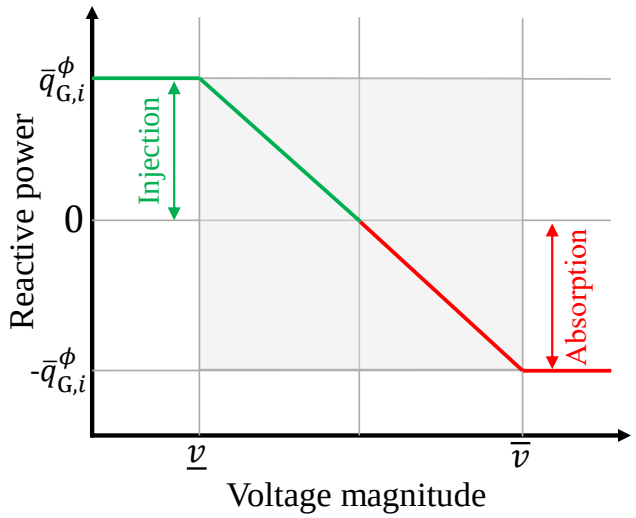

Figure 7.2: Voltage magnitude-reactive power characteristic

Reactive power mode	**Upper-level** ($\boldsymbol{X}_{\mathbf{u}}$)	**Lower-level** ($\boldsymbol{X}_{\mathbf{l}}$)
Constant power factor	$\boldsymbol{\gamma}^{\phi}_{\mathbf{G},i}$	$\Delta\boldsymbol{p}^{\phi}_{\mathbf{G},i}$, $\boldsymbol{q}^{\phi}_{\mathbf{G},i}$
Constant reactive power	$\boldsymbol{q}^{\phi}_{\mathbf{G},i}$	$\Delta\boldsymbol{p}^{\phi}_{\mathbf{G},i}$
Voltage-reactive power	$\overline{\boldsymbol{q}}^{\phi}_{\mathbf{G},i}$	$\Delta\boldsymbol{p}^{\phi}_{\mathbf{G},i}$, $\boldsymbol{q}^{\phi}_{\mathbf{G},i}$, $\lvert\boldsymbol{v}^{\phi}_{i}\rvert$

Table 7.1: Assignment of inverter variables to the bilevel problem for different inverter reactive power control modes.

7.4.5 Power Flow

We can use any of the linear power flow models described in Chapter 5 to enforce power balance constraints in our bilevel problem. We choose the fixed-point linear power flow model described in Section 5.5 because it exhibits better global approximation accuracy when compared to the first-order Taylor approximation and provides the same solutions as the forward-backward sweep model.

7.4.6 Bilevel Optimization Problem

The main objective of the bilevel problem is to find the maximum range of aggregate power flexibility while ensuring that the grid is secure even in the worst-case conditions. In this section, we first discuss the bilevel problem formulation where inverters are operating in constant power factor mode and DSO controls the power ratio $\boldsymbol{\gamma}^{\phi}_{\mathbf{G},i}$ of each inverter. The upper-level variable vector $\boldsymbol{X}_{\mathbf{u}}$ and lower-level variable vector $\boldsymbol{X}_{\mathbf{l}}$ of the bilevel problem is denoted by

$$\begin{aligned}
\boldsymbol{X}_{\mathbf{u}} &:= \{\Delta\boldsymbol{p}^{+}, \Delta\boldsymbol{p}^{-}, \boldsymbol{\gamma}^{\phi}_{\mathbf{G},i} \forall_{\phi\in\Phi, i\in\mathcal{N}}\}, \\
\boldsymbol{X}_{\mathbf{l}} &:= \left\{\{\boldsymbol{v}^{\phi}_{\mathbf{d}i}, \boldsymbol{v}^{\phi}_{\mathbf{q}i}, |\boldsymbol{v}^{\phi}_{i}|, \Delta\boldsymbol{p}^{\phi}_{\mathbf{G},i}, \Delta\boldsymbol{p}^{\phi}_{\mathbf{L},i}, \boldsymbol{q}^{\phi}_{\mathbf{L},i}, \boldsymbol{q}^{\phi}_{\mathbf{G},i}\}_{\forall_{\phi\in\Phi, i\in\mathcal{N}}}\right\}.
\end{aligned} \tag{7.14}$$

Recall that we define a positive and negative case in Section 7.4.3.3 to enforce rules on how all aggregators are required to control the DER power injections in the same way. The aggregate power flexibility and inverter setpoints determined by the bilevel problem must be applicable for both the

cases and hence, we only need one set of the upper-level variables $\boldsymbol{X}_{\mathrm{u}}$ that is shared by both cases. On the other hand, the worst-case conditions determined for the positive case can be different from the worst-case conditions seen for the negative case because the rules for power injections are not the same. Furthermore, we determine the worst-case conditions at every single-phase connection in the network by finding the minimum and maximum voltage magnitude achievable at that connection. Again, these operating conditions will be different for the positive and negative cases. As a result, we need to consider four sets of lower-level variables $\underline{\boldsymbol{X}}_{\mathrm{l}}^{+}, \underline{\boldsymbol{X}}_{\mathrm{l}}^{-}, \overline{\boldsymbol{X}}_{\mathrm{l}}^{+}, \overline{\boldsymbol{X}}_{\mathrm{l}}^{-}$ which represent four different scenarios as summarized in Table 7.2. For example, scenario 1 corresponds to the positive case where the worst-case condition is determined by finding the minimum achievable voltage magnitude.

Scenario (#)	**Case**	**Voltage**	**Lower-level**
1	Positive	Min.	$\underline{\boldsymbol{X}}_{\mathrm{l}}^{+}$
2		Max.	$\overline{\boldsymbol{X}}_{\mathrm{l}}^{+}$
3	Negative	Min.	$\underline{\boldsymbol{X}}_{\mathrm{l}}^{-}$
4		Max.	$\overline{\boldsymbol{X}}_{\mathrm{l}}^{-}$

Table 7.2: Summary of lower-level problem variables corresponding to each single-phase connection in the network.

We define four sets of lower-level system constraints which depend on the follower problem variable vectors $\underline{\boldsymbol{X}}_{\mathrm{l}}^{+}, \underline{\boldsymbol{X}}_{\mathrm{l}}^{-}, \overline{\boldsymbol{X}}_{\mathrm{l}}^{+}, \overline{\boldsymbol{X}}_{\mathrm{l}}^{-}$ as

$$\mathbb{L}(\underline{\boldsymbol{X}}_{\mathrm{l}}^{+}),\ \mathbb{L}(\underline{\boldsymbol{X}}_{\mathrm{l}}^{-}),\ \mathbb{L}(\overline{\boldsymbol{X}}_{\mathrm{l}}^{+}),\ \mathbb{L}(\overline{\boldsymbol{X}}_{\mathrm{l}}^{-}) := \begin{cases} \text{Voltage constraints (7.3)}, \\ \text{Load reactive power constraints (7.5)}, \\ \text{Power flow (5.22)}. \end{cases}$$

The inverter constraints are expressed using both the leader and follower problem variables. For the inverter at node i connected to phase ϕ operating in the constant power factor mode, we can

represent four sets of inverter constraints using

$$\mathbb{I}(\boldsymbol{\gamma}^{\phi}_{\mathbf{G},i}, \underline{\boldsymbol{X}}^{+}_{\mathbf{l}}),\ \mathbb{I}(\boldsymbol{\gamma}^{\phi}_{\mathbf{G},i}, \underline{\boldsymbol{X}}^{-}_{\mathbf{l}}),\ \mathbb{I}(\boldsymbol{\gamma}^{\phi}_{\mathbf{G},i}, \overline{\boldsymbol{X}}^{+}_{\mathbf{l}}),\ \mathbb{I}(\boldsymbol{\gamma}^{\phi}_{\mathbf{G},i}, \overline{\boldsymbol{X}}^{-}_{\mathbf{l}}) := \text{Inverter constraints (7.10), (7.11).}$$

Similarly, the active power flexibility limits are defined using both the leader and follower problem variables. We denote the sets of active power flexibility constraints for the positive and negative case using

$$\mathbb{F}(\Delta\boldsymbol{p}^{+}, \Delta\boldsymbol{p}^{-}, \underline{\boldsymbol{X}}^{+}_{\mathbf{l}}),\ \mathbb{F}(\Delta\boldsymbol{p}^{+}, \Delta\boldsymbol{p}^{-}, \overline{\boldsymbol{X}}^{+}_{\mathbf{l}}) := \text{Positive case (7.7), (7.8),}$$

$$\mathbb{F}(\Delta\boldsymbol{p}^{+}, \Delta\boldsymbol{p}^{-}, \underline{\boldsymbol{X}}^{-}_{\mathbf{l}}),\ \mathbb{F}(\Delta\boldsymbol{p}^{+}, \Delta\boldsymbol{p}^{-}, \overline{\boldsymbol{X}}^{-}_{\mathbf{l}}) := \text{Negative case (7.7), (7.9).}$$

The bilevel problem to determine the aggregate power flexibility limits $\Delta\boldsymbol{p}^+, \Delta\boldsymbol{p}^-$ can be formulated as

$$
\begin{aligned}
\max_{\boldsymbol{X}_\mathrm{u}} \ & \Delta\boldsymbol{p}^+ - \Delta\boldsymbol{p}^- && \text{(P}^\pm\text{)}\\
\text{s.t. } & \underline{v} \le |\boldsymbol{v}^\phi_{i,\min}|^+, |\boldsymbol{v}^\phi_{i,\max}|^+ \le \overline{v}, && \forall_{\phi\in\Phi, i\in\mathcal{N}},\\
& \underline{v} \le |\boldsymbol{v}^\phi_{i,\min}|^-, |\boldsymbol{v}^\phi_{i,\max}|^- \le \overline{v}, && \forall_{\phi\in\Phi, i\in\mathcal{N}},\\
& \text{where } |\boldsymbol{v}^\phi_{i,\min}|^+ = \min_{\underline{\boldsymbol{X}}_\mathrm{l}^+} |\underline{\boldsymbol{v}}^\phi_i|^+, && \forall_{\phi\in\Phi, i\in\mathcal{N}},\\
& \qquad \text{s.t. System constraints } \mathbb{L}(\underline{\boldsymbol{X}}_\mathrm{l}^+),\\
& \qquad\quad \text{Inverter constraints } \mathbb{I}(\boldsymbol{\gamma}^\phi_{\mathbf{G},i}, \underline{\boldsymbol{X}}_\mathrm{l}^+),\\
& \qquad\quad \text{Flexibility constraints } \mathbb{F}(\Delta\boldsymbol{p}^+, \Delta\boldsymbol{p}^-, \underline{\boldsymbol{X}}_\mathrm{l}^+),\\
& |\boldsymbol{v}^\phi_{i,\max}|^+ = \max_{\overline{\boldsymbol{X}}_\mathrm{l}^+} |\overline{\boldsymbol{v}}^\phi_i|^+, && \forall_{\phi\in\Phi, i\in\mathcal{N}},\\
& \qquad \text{s.t. System constraints } \mathbb{L}(\overline{\boldsymbol{X}}_\mathrm{l}^+),\\
& \qquad\quad \text{Inverter constraints } \mathbb{I}(\boldsymbol{\gamma}^\phi_{\mathbf{G},i}, \overline{\boldsymbol{X}}_\mathrm{l}^+),\\
& \qquad\quad \text{Flexibility constraints } \mathbb{F}(\Delta\boldsymbol{p}^+, \Delta\boldsymbol{p}^-, \overline{\boldsymbol{X}}_\mathrm{l}^+),\\
& |\underline{\boldsymbol{v}}^\phi_{i,\min}|^- = \min_{\underline{\boldsymbol{X}}_\mathrm{l}^-} |\underline{\boldsymbol{v}}^\phi_i|^-, && \forall_{\phi\in\Phi, i\in\mathcal{N}},\\
& \qquad \text{s.t. System constraints } \mathbb{L}(\underline{\boldsymbol{X}}_\mathrm{l}^-),\\
& \qquad\quad \text{Inverter constraints } \mathbb{I}(\boldsymbol{\gamma}^\phi_{\mathbf{G},i}, \underline{\boldsymbol{X}}_\mathrm{l}^+),\\
& \qquad\quad \text{Flexibility constraints } \mathbb{F}(\Delta\boldsymbol{p}^+, \Delta\boldsymbol{p}^-, \underline{\boldsymbol{X}}_\mathrm{l}^-),\\
& |\overline{\boldsymbol{v}}^\phi_{i,\max}|^- = \max_{\overline{\boldsymbol{X}}_\mathrm{l}^-} |\overline{\boldsymbol{v}}^\phi_i|^-, && \forall_{\phi\in\Phi, i\in\mathcal{N}},\\
& \qquad \text{s.t. System constraints } \mathbb{L}(\overline{\boldsymbol{X}}_\mathrm{l}^-),\\
& \qquad\quad \text{Inverter constraints } \mathbb{I}(\boldsymbol{\gamma}^\phi_{\mathbf{G},i}, \overline{\boldsymbol{X}}_\mathrm{l}^-),\\
& \qquad\quad \text{Flexibility constraints } \mathbb{F}(\Delta\boldsymbol{p}^+, \Delta\boldsymbol{p}^-, \overline{\boldsymbol{X}}_\mathrm{l}^-).
\end{aligned}
$$

Note that for each node $i \in \mathcal{N}$ connected to phase $\phi \in \Phi$, we include four lower-level problems corresponding to the four scenarios described in Table 7.2. Hence, the total number of lower-level problems in ($P^{\pm}$) is $12n$.

7.5 Single-level Reformulation

One of the most frequently used solution method for bilevel optimization is to reformulate the problem into a single-level problem. In this section, we utilize the strong-duality theorem for the lower-level problem to perform the single-level reduction. Given that the lower-level problem has a finite optimal solution, the dual feasible set is non empty and strong duality holds for every primal and dual feasible pairs. This strong duality based reformulation does not require the use of any other additional properties or assumptions. Hence, it can be less restrictive than the KKT conditions based reformulation [158].

For simplicity of exposition, we first derive the reformulation for a setting with only one follower problem and reactive power control using a constant power factor. Then, we discuss how the reformulation generalizes to the setting with multiple follower problems and other reactive power control modes.

7.5.1 Reformulation with Single Follower Problem

Consider a reduced version of the bilevel problem $P^{\pm}$ where the objective of the upper-level problem is to determine the aggregate power flexibility limit $\Delta \boldsymbol{p}^{+}$ for the positive case only. We only consider one follower problem with the objective to find the maximum achievable voltage

magnitude at node i connected to phase ϕ. The simplified bilevel problem can be represented as

$$\begin{aligned}
&\max_{\boldsymbol{X}_{\mathrm{u}}} \ \Delta \boldsymbol{p}^{+} && (\mathrm{P}^{+})\\
&\quad \text{s.t. } |\boldsymbol{v}^{\phi}_{i,\max}|^{+} \leq \overline{v},\\
&\qquad \text{where } |\boldsymbol{v}^{\phi}_{i,\max}|^{+} = \max_{\overline{\boldsymbol{X}}^{+}_{\mathrm{l}}} |\overline{\boldsymbol{v}}^{\phi}_{i}|^{+}\\
&\qquad\qquad \text{s.t. System constraints } \mathbb{L}(\overline{\boldsymbol{X}}^{+}_{\mathrm{l}}),\\
&\qquad\qquad\quad \text{Inverter constraints } \mathbb{I}(\boldsymbol{\gamma}^{\phi}_{\mathbf{G},i}, \overline{\boldsymbol{X}}^{+}_{\mathrm{l}}),\\
&\qquad\qquad\quad \text{Flexibility constraints } \mathbb{F}(\Delta \boldsymbol{p}^{+}, \overline{\boldsymbol{X}}^{+}_{\mathrm{l}}).
\end{aligned}$$

To derive the strong duality based reformulation of the reduced problem P^{+}, we start by rewriting the bilevel problem P^{+} in a more abstract form to get

$$\begin{aligned}
&\max_{\Delta \boldsymbol{p}, \boldsymbol{\gamma}} \ \Delta \boldsymbol{p} && (7.15a)\\
&\quad \text{s.t. } \hat{\boldsymbol{x}}_{\mathrm{l}} \leq b_1, && (7.15b)\\
&\qquad \text{where } \hat{\boldsymbol{x}}_{\mathrm{l}} = \max_{\boldsymbol{x}_{\mathrm{l}}} \ \boldsymbol{x}_{\mathrm{l}} && (7.15c)\\
&\qquad\qquad \text{s.t. } a_2 \boldsymbol{x}_{\mathrm{l}} \leq b_2, && (7.15d)\\
&\qquad\qquad\quad a_3 \boldsymbol{x}_{\mathrm{l}} + d_3 \boldsymbol{\gamma} \boldsymbol{x}_{\mathrm{l}} \leq b_3, && (7.15e)\\
&\qquad\qquad\quad a_4 \boldsymbol{x}_{\mathrm{l}} + d_4 \Delta \boldsymbol{p} \leq b_4, && (7.15f)
\end{aligned}$$

where $\boldsymbol{x}_{\mathrm{l}}$ is the follower problem variable and $\boldsymbol{\gamma}, \Delta \boldsymbol{p}$ represent the upper-level variables which are considered as parameters in the lower-level problem. Therefore, the follower problem is linear in $\boldsymbol{x}_{\mathrm{l}}$ even though we have bilinear terms in (7.15e). By taking dual of the lower-level problem (7.15c)-(7.15f), we get

$$\begin{aligned}
&\min_{\boldsymbol{\lambda}} \ \begin{bmatrix} b_2 & b_3 & (b_4 - d_4 \Delta \boldsymbol{p}) \end{bmatrix} \boldsymbol{\lambda} && (7.16a)\\
&\quad \text{s.t. } \begin{bmatrix} a_2 & (a_3 + d_3 \boldsymbol{\gamma}) & a_4 \end{bmatrix} \boldsymbol{\lambda} = 1, && (7.16b)\\
&\qquad \boldsymbol{\lambda} \geq 0, && (7.16c)
\end{aligned}$$

where $\boldsymbol{\lambda}$ is the dual variable vector. For a given decision $\Delta \boldsymbol{p}$ of the leader problem, weak duality of the follower problem states that the dual objective provides an upper bound for the primal objective, i.e.

$$\boldsymbol{x}_1 \leq \begin{bmatrix} b_2 & b_3 & (b_4 - d_4 \Delta \boldsymbol{p}) \end{bmatrix} \boldsymbol{\lambda} \tag{7.17}$$

must hold for any feasible primal-dual pair $(\boldsymbol{x}_1, \boldsymbol{\lambda})$. Using the strong duality theorem, we know that the feasible primal-dual pair is the optimal solution when the objective value of the primal problem $\hat{\boldsymbol{x}}_1$ is equal to the objective value of the dual problem. This occurs when

$$\boldsymbol{x}_1 \geq \begin{bmatrix} b_2 & b_3 & (b_4 - d_4 \Delta \boldsymbol{p}) \end{bmatrix} \boldsymbol{\lambda}. \tag{7.18}$$

Consequently, we can now replace the dual of the lower-level problem (7.16) by the following set of constraints:

$$\boldsymbol{x}_1 \geq \begin{bmatrix} b_2 & b_3 & (b_4 - d_4 \Delta \boldsymbol{p}) \end{bmatrix} \boldsymbol{\lambda}, \tag{7.19a}$$

$$\begin{bmatrix} a_2 & (a_3 + d_3 \boldsymbol{\gamma}) & a_4 \end{bmatrix} \boldsymbol{\lambda} = 1, \tag{7.19b}$$

$$\boldsymbol{\lambda} \geq 0, \tag{7.19c}$$

We can use the above set of constraints and reformulate the bilevel problem (7.15) to get a single-level optimization problem given by

$$\max_{\Delta \boldsymbol{p}, \boldsymbol{\gamma}, \boldsymbol{x}_1, \boldsymbol{\lambda}} \ \Delta \boldsymbol{p} \tag{7.20a}$$

$$\text{s.t. } \boldsymbol{x}_1 \leq b_1, \tag{7.20b}$$

$$a_2 \boldsymbol{x}_1 \leq b_2, \tag{7.20c}$$

$$a_3 \boldsymbol{x}_1 + d_3 \boldsymbol{\gamma} \boldsymbol{x}_1 \leq b_3, \tag{7.20d}$$

$$a_4 \boldsymbol{x}_1 + d_4 \Delta \boldsymbol{p} \leq b_4, \tag{7.20e}$$

$$\boldsymbol{x}_1 \geq \begin{bmatrix} b_2 & b_3 & (b_4 - d_4 \Delta \boldsymbol{p}) \end{bmatrix} \boldsymbol{\lambda}, \tag{7.20f}$$

$$\begin{bmatrix} a_2 & (a_3 + d_3 \boldsymbol{\gamma}) & a_4 \end{bmatrix} \boldsymbol{\lambda} = 1, \tag{7.20g}$$

$$\boldsymbol{\lambda} \geq 0, \tag{7.20h}$$

In reality, we do not need the lower-level problem to determine the exact optimal value for $\boldsymbol{x}_\mathrm{l}$. We only need to guarantee that $\boldsymbol{x}_\mathrm{l}$ is lower than the upper bounds specified by the constraints (7.20b) which were part of the leader in the bilevel problem. Since we already have an upper bound b_1 for $\boldsymbol{x}_\mathrm{l}$, which in turn is an upper bound on the dual objective function, we can use the same bound b_1 in (7.20f) to modify the strong duality constraint. The single-level optimization problem then reduces to

$$\max_{\Delta\boldsymbol{p},\boldsymbol{\gamma},\boldsymbol{x}_\mathrm{l},\boldsymbol{\lambda}} \ \Delta\boldsymbol{p} \tag{7.21a}$$

$$\text{s.t. } a_2\boldsymbol{x}_\mathrm{l} \leq b_2, \tag{7.21b}$$

$$a_3\boldsymbol{x}_\mathrm{l} + d_3\boldsymbol{\gamma}\boldsymbol{x}_\mathrm{l} \leq b_3, \tag{7.21c}$$

$$a_4\boldsymbol{x}_\mathrm{l} + d_4\Delta\boldsymbol{p} \leq b_4, \tag{7.21d}$$

$$b_1 \geq \begin{bmatrix} b_2 & b_3 & (b_4 - d_4\Delta\boldsymbol{p}) \end{bmatrix}\boldsymbol{\lambda}, \tag{7.21e}$$

$$\begin{bmatrix} a_2 & (a_3 + d_3\boldsymbol{\gamma}) & a_4 \end{bmatrix}\boldsymbol{\lambda} = 1, \tag{7.21f}$$

$$\boldsymbol{\lambda} \geq 0. \tag{7.21g}$$

This single-level problem can now be solved using general purpose solvers. A drawback of the strong duality based reformulation is the presence of bilinear terms $\boldsymbol{\gamma} \cdot \boldsymbol{x}_\mathrm{l}$ in the primal follower problem constraint (7.21c), $\Delta\boldsymbol{p} \cdot \boldsymbol{\lambda}$ in the strong duality constraint (7.21e) and $\boldsymbol{\gamma} \cdot \boldsymbol{\lambda}$ in the dual equality constraint (7.21f) which make the problem non-convex and computationally challenging.

7.5.2 Generalization to Multiple Follower Problems

A similar approach can be used to derive the single-level reduction of $\mathrm{P}^{\pm}$ which comprises of multiple follower problems. Note that as the number of follower problems increase, we get a large optimization problem with many bilinear terms.

For lower-level problems with objectives to find the minimum achievable voltage magnitude, the primal objective value is a lower bound instead of an upper bound in the strong duality constraint. Since we already have a lower bound $\underline{v}$ for $\boldsymbol{x}_\mathrm{l}$, it is possible to modify the strong duality constraint and formulate the single-level optimization problem similar to (7.21).

7.5.3 Reformulation for Other Inverter Reactive Power Control Modes

We can choose other inverter reactive power control modes and formulate the bilevel problem and the single-level reformulated problem in the same way as described for the constant power factor mode. For the voltage-reactive power mode, the upper-level and lower-level variable vectors are defined by

$$\begin{aligned}
\boldsymbol{X}_{\mathbf{u}} &:= \{\Delta\boldsymbol{p}^{+}, \Delta\boldsymbol{p}^{-}, \overline{\boldsymbol{q}}^{\phi}_{\mathbf{G},i} \forall_{\phi\in\Phi, i\in\mathcal{N}}\}, \\
\boldsymbol{X}_{\mathbf{l}} &:= \left\{\{\boldsymbol{v}^{\phi}_{\mathbf{d}i}, \boldsymbol{v}^{\phi}_{\mathbf{q}i}, |\boldsymbol{v}^{\phi}_{i}|, \Delta\boldsymbol{p}^{\phi}_{\mathbf{G},i}, \Delta\boldsymbol{p}^{\phi}_{\mathbf{L},i}, \boldsymbol{q}^{\phi}_{\mathbf{L},i}, \boldsymbol{q}^{\phi}_{\mathbf{G},i}\}_{\forall_{\phi\in\Phi, i\in\mathcal{N}}}\right\}.
\end{aligned} \tag{7.22}$$

Recall that that we have bilinear terms in the inverter reactive power constraint, strong duality constraint as well as the dual equality constraints for the constant power factor mode. Similarly, for the voltage-reactive power mode, we get the same number of bilinear terms since the inverter constraints (7.13) are defined by product of upper-level and lower-level variables.

In case of the constant reactive power mode, the upper-level and lower-level variable vectors are given by

$$\begin{aligned}
\boldsymbol{X}_{\mathbf{u}} &:= \{\Delta\boldsymbol{p}^{+}, \Delta\boldsymbol{p}^{-}, \boldsymbol{q}^{\phi}_{\mathbf{G},i} \forall_{\phi\in\Phi, i\in\mathcal{N}}\}, \\
\boldsymbol{X}_{\mathbf{l}} &:= \left\{\{\boldsymbol{v}^{\phi}_{\mathbf{d}i}, \boldsymbol{v}^{\phi}_{\mathbf{q}i}, |\boldsymbol{v}^{\phi}_{i}|, \Delta\boldsymbol{p}^{\phi}_{\mathbf{G},i}, \Delta\boldsymbol{p}^{\phi}_{\mathbf{L},i}, \boldsymbol{q}^{\phi}_{\mathbf{L},i}\}_{\forall_{\phi\in\Phi, i\in\mathcal{N}}}\right\}.
\end{aligned} \tag{7.23}$$

Different from the other two modes, the inverter constraints (7.12) do not consist of any bilinear terms and as a result, no bilinear terms are present in the dual equality constraints. However, the upper-level inverter variable $\boldsymbol{q}^{\phi}_{\mathbf{G},i}$ shows up in a number of other constraints. Because of this, we get a large number of bilinear terms in the strong duality constraint for the constant reactive power mode.

We will next describe an iterative solution approach used to efficiently handle the bilinear terms and solve the single-level problem (7.21).

7.5.4 Iterative Solution Approach

As the number of leader problem variables or the number of follower problems in (7.15) increases, the number of bilinear terms in the single-level reformulated problem (7.21) also increase,

making it computationally expensive to solve. One way to reduce the number of bilinear terms is to decrease the number of follower problems in the bilevel problem. Typically, the voltage magnitude violations in a distribution grid occur only at a few nodes, which in turn determine the aggregate power flexibility of the system. Instead of solving the bilevel problem with $12n$ number of follower problems, we can identify the nodes where voltage violations are most likely to occur and only include the lower-level problems corresponding to these nodes in the bilevel optimization task. In this section, we use an iterative approach to identify such nodes and solve the problem efficiently. We will describe the method to solve for the single-level reformulated problem in this section. The iterative approach is summarized below and a more detailed explanation is provided in the next few subsections.

1) We solve a *worst-case problem* where we assume DSO determines the aggregate power flexibility limits $\Delta \boldsymbol{p}^{+}$, $\Delta \boldsymbol{p}^{-}$ without any DER reactive power support i.e. aggregators are free to control even the reactive power injections of the DER inverters without considering grid constraints. This means that the inverter control variables become lower-level variables and $\Delta \boldsymbol{p}^{+}$, $\Delta \boldsymbol{p}^{-}$ are the only upper-level variables. For all three inverter reactive power control modes, we have the same lower-level variables which are defined as

$$\boldsymbol{X}_{\mathrm{l}} := \left\{ \{ \boldsymbol{v}_{\mathbf{d}i}^{\phi}, \boldsymbol{v}_{\mathbf{q}i}^{\phi}, |\boldsymbol{v}_{i}^{\phi}|, \Delta \boldsymbol{p}_{\mathbf{G},i}^{\phi}, \Delta \boldsymbol{p}_{\mathbf{L},i}^{\phi}, \boldsymbol{q}_{\mathbf{L},i}^{\phi}, \boldsymbol{q}_{\mathbf{G},i}^{\phi} \}_{\forall_{\phi \in \Phi, i \in \mathcal{N}}} \right\}. \tag{7.24}$$

   By solving the worst-case problem, we can determine the node where voltage violations (i.e. either overvoltage or undervoltage) are most likely to occur and as a result, provide the lowest aggregate power flexibility range.

2) We solve an *ideal case problem* which is already defined in $\mathrm{P}^{\pm}$ where the DSO determines the setpoints for DER reactive power control along with the aggregate power flexibility limits and rest of the DER power injections are controlled by the aggregators. Instead of including all $12n$ followers, we solve a relaxed version of the problem where we only include the lower-level problems corresponding to the single-phase connection which provides the lowest aggregate power flexibility range the worst-case problem in step 1).

3) We perform a *feasibility check* to ensure that the solution of the ideal case problem mitigates voltage violations at all the nodes. To do this, we use the aggregate power flexibility range and inverter setpoints determined by solving the ideal case problem and solve only the lower-level problems defined in $\mathrm{P}^{\pm}$ to find the worst-case voltage magnitudes.

4) If all voltage magnitudes are within limits, we terminate the iterative process. Otherwise, we go back to step 2) and solve the ideal case problem again by including an additional set of follower problems corresponding to the single-phase connection that did not pass the feasibility check.

7.5.4.1 Worst Case Problem

As mentioned previously, the inverter setpoints for the different inverter reactive power control modes are not considered as leader problem variables in the worst-case problem. Instead, we assume they are determined by the aggregator and may be equal to the values that would lead to worst-case conditions occurring in the grid. These worst-case values are determined by including them in the bilevel problem as lower-level variables. This is a straightforward approach for the constant reactive power mode where the inverter constraints (7.12) are linear. However, we have bilinear terms in the inverter constraints (7.11a), (7.13a) for constant power factor and voltage-reactive power mode, respectively. To avoid these bilinear terms and ensure that we can solve the worst-case problem efficiently, we fix the inverter setpoints to one of their specified limits. For example, if the lower-level objective of the bilevel problem is to maximize voltage magnitude, the inverter setpoints for both reactive power modes are determined as follows:

- *Constant power factor mode*: We set $\boldsymbol{\gamma}^{\phi}_{\mathbf{G},i}$ for every inverter to its upper limit defined in (7.11b). This corresponds to the situation where all inverters are boosting the voltage profile in the network by injecting the full available reactive power leading to higher voltage magnitudes.

- *Voltage-reactive power mode*: We set $\overline{\boldsymbol{q}}^{\phi}_{\mathbf{G},i}$ to its lower limit defined in (7.13b). This represents the condition where inverters do not provide any reactive power support when voltage magnitude is close to or violating the upper limit $\overline{v}$.

Note that $\Delta \boldsymbol{p}^+, \Delta \boldsymbol{p}^-$ are the only variables that are shared by all the lower-level problems in the worst-case problem. Apart from that, there are no other variables or constraints linking the $12n$ follower problems. This allows us to separate the problem into individual problems for each follower specifically. We first solve $12n$ worst-case problems with one leader and one follower each to obtain $6n$ aggregate power flexibility upper limits for the positive case (with $\Delta \boldsymbol{p}^- = 0$) and $6n$ aggregate power flexibility lower limits for the negative case (with $\Delta \boldsymbol{p}^+ = 0$). Next, we sort the $6n$ upper limits in ascending order and also sort the $6n$ lower limits in the descending order. The difference between the minimum upper limit and the maximum lower limit is the lowest range of aggregate power flexibility for the network. This value should be equal to the solution obtained by solving the worst-case problem with one leader and $12n$ followers because all the follower problems are independent of each other. The total computation time to solve the $12n$ smaller worst-case problems will be much lower than the time to solve one large worst-case problem with $12n$ followers, especially when parallel computing techniques are used. Note that each of the $12n$ small worst-case problems has only one bilinear term corresponding to the product of the dual variable and upper-level variable in the strong duality constraint.

7.5.4.2 Ideal Case Problem

We have multiple upper-level variables shared by the followers of the ideal case problem $\mathrm{P}^{\pm}$ as defined in (7.14). Hence, this problem cannot be broken down into multiple bilevel problems and solved independently like the worst-case problem. To reduce computational complexity, we initially only include the two lower-level problems (one each for positive and negative cases) corresponding to the two worst-case problems that determined the lowest aggregate power flexibility range in step 1). When we only have a few follower problems, the number of bilinear terms is much lower compared to the problem with $12n$ followers. As a result, the ideal case problem can be efficiently solved to obtain the aggregate power flexibility range and inverter setpoints. Note that the subset of lower-level problems included in the ideal case bilevel problem is sequentially increased, if needed, as described in the feasibility check section.

7.5.4.3 Feasibility Check

It is not guaranteed that the solution obtained by solving the ideal case problem mitigates voltage violations at all single-phase connections in the network since we only considered two followers in the bilevel problem corresponding to one single-phase connection. Hence, we perform a feasibility check by using the aggregate power flexibility range and inverter setpoints determined by the ideal case problem and solving the lower-level problems defined in $\mathrm{P}^{\pm}$ to determine worst-case voltage magnitudes. Recall that when we solve the worst-case problems in step 1) of the iterative approach, we sort the resulting $6n$ upper-limit and lower-limit ranges in ascending and descending orders, respectively. These two lists also provides us with an order for the single-phase connections, where the connections with maximum risk of voltage violations are at the top and single-phase connections with lowest risk of voltage violations are at the bottom of the list. We utilize this ordering when we are doing the feasibility check and solve the lower-level problems sequentially starting from the top of the lists. If we observe a voltage violation, we go back to step 2) and add the followers to the ideal case problem which correspond to the single-phase connection where the voltage violation occurred and solve the problem again. We repeat this process iteratively and terminate when the feasibility check determines that all worst-case voltage magnitudes are within limits. Note that the lower-level problems are fully linear with no bilinear terms since the inverter setpoints were already determined by the ideal case problem, making them easy to solve.

7.6 Considering Impact of Limited Measurements

One of the assumptions in the previous section is that measurement data (i.e. power injections, voltage phasors) is available at all nodes in the network. As a result, we assume to have full knowledge about the current operating point of the system. However, the real-time measurements might not be available at all points in the grid since it can lead to higher cost of monitoring equipment, communication burden and privacy concerns of the end-consumers. In this section, we extend the bilevel formulation described above to include the case where the current operating

point is not known or partially known. To consider this limitation while also maintaining security of operations, we treat all unknown measurements as optimization variables in the follower of the bilevel problem. This will result in a more conservative worst-case operating condition compared to the previous case where we assumed all measurements were available. In this section, we assume that measurements are not available at any node $i \in \mathcal{N}$ and the voltage variables are denoted using $\hat{\boldsymbol{V}}_{\mathbf{d}i}, \hat{\boldsymbol{V}}_{\mathbf{q}i}, |\hat{\boldsymbol{V}}_i| \in \mathbb{R}^3$, respectively. The active and reactive power injections at node $i \in \mathcal{N}$ connected to phase ϕ at the current operating point are given by

$$\hat{\boldsymbol{p}}_i^{\phi} = \hat{\boldsymbol{p}}_{\mathbf{G},i}^{\phi} - \hat{\boldsymbol{p}}_{\mathbf{L},i}^{\phi}, \tag{7.25a}$$

$$\hat{\boldsymbol{q}}_i^{\phi} = \hat{\boldsymbol{q}}_{\mathbf{G},i}^{\phi} - \hat{\boldsymbol{q}}_{\mathbf{L},i}^{\phi}, \tag{7.25b}$$

where $\hat{\boldsymbol{p}}_{\mathbf{G},i}^{\phi}, \hat{\boldsymbol{q}}_{\mathbf{G},i}^{\phi}$ are the respective active and reactive power generation variables for solar PV inverters; $\hat{\boldsymbol{p}}_{\mathbf{L},i}^{\phi}, \hat{\boldsymbol{q}}_{\mathbf{L},i}^{\phi}$ represent the active and reactive load demand variables, respectively.

7.6.1 Load Modelling

For a load at node $i \in \mathcal{N}$ connected to phase $\phi \in \Phi$, the limits for active power demand become

$$\underline{p}_{\mathrm{L},i}^{\phi} \leq \hat{\boldsymbol{p}}_{\mathbf{L},i}^{\phi} \leq \overline{p}_{\mathrm{L},i}^{\phi}, \tag{7.26a}$$

$$\underline{p}_{\mathrm{L},i}^{\phi} \leq \hat{\boldsymbol{p}}_{\mathbf{L},i}^{\phi} + \Delta\boldsymbol{p}_{\mathbf{L},i}^{\phi} \leq \overline{p}_{\mathrm{L},i}^{\phi}. \tag{7.26b}$$

Assuming that loads operate in constant power factor $pf_{\mathrm{L},i}^{\phi}$, the reactive power consumption is

$$\hat{\boldsymbol{q}}_{\mathbf{L},i}^{\phi} = \frac{\sqrt{1 - \left(pf_{\mathrm{L},i}^{\phi}\right)^2}}{pf_{\mathrm{L},i}^{\phi}} \cdot \hat{\boldsymbol{p}}_{\mathbf{L},i}^{\phi}, \tag{7.27a}$$

$$\boldsymbol{q}_{\mathbf{L},i}^{\phi} = \frac{\sqrt{1 - \left(pf_{\mathrm{L},i}^{\phi}\right)^2}}{pf_{\mathrm{L},i}^{\phi}} \cdot \left(\hat{\boldsymbol{p}}_{\mathbf{L},i}^{\phi} + \Delta\boldsymbol{p}_{\mathbf{L},i}^{\phi}\right), \tag{7.27b}$$

where $\hat{\boldsymbol{q}}_{\mathbf{L},i}^{\phi}$ is the reactive power consumption at the current operating point.

7.6.2 Modeling of Solar PV Active Power Generation

The active power generation limits defined in (7.6) can be reformulated to include the power generation variable $\hat{\boldsymbol{p}}^{\phi}_{\mathbf{G},i}$ corresponding to the current operating point to get

$$\underline{p}^{\phi}_{\mathrm{G},i} \leq \hat{\boldsymbol{p}}^{\phi}_{\mathbf{G},i} \leq \overline{p}^{\phi}_{\mathrm{G},i}, \tag{7.28a}$$

$$\underline{p}^{\phi}_{\mathrm{G},i} \leq \hat{\boldsymbol{p}}^{\phi}_{\mathbf{G},i} + \Delta\boldsymbol{p}^{\phi}_{\mathbf{G},i} \leq \overline{p}^{\phi}_{\mathrm{G},i}. \tag{7.28b}$$

7.6.3 Inverter Constraints

The inverter limits defined in (7.10) can be reformulated to include the power generation variables $\hat{\boldsymbol{p}}^{\phi}_{\mathbf{G},i}, \hat{\boldsymbol{q}}^{\phi}_{\mathbf{G},i}$ to get

$$0 \leq \hat{\boldsymbol{p}}^{\phi}_{\mathbf{G},i} \leq |s^{\phi}_{\mathrm{G},i}|, \tag{7.29a}$$

$$-|s^{\phi}_{\mathrm{G},i}| \leq \hat{\boldsymbol{q}}^{\phi}_{\mathbf{G},i} \leq |s^{\phi}_{\mathrm{G},i}|, \tag{7.29b}$$

$$\hat{\boldsymbol{p}}^{\phi}_{\mathbf{G},i} + \hat{\boldsymbol{q}}^{\phi}_{\mathbf{G},i} \leq \sqrt{2} \cdot |s^{\phi}_{\mathrm{G},i}|, \tag{7.29c}$$

$$\hat{\boldsymbol{p}}^{\phi}_{\mathbf{G},i} - \hat{\boldsymbol{q}}^{\phi}_{\mathbf{G},i} \leq \sqrt{2} \cdot |s^{\phi}_{\mathrm{G},i}|, \tag{7.29d}$$

$$0 \leq \hat{\boldsymbol{p}}^{\phi}_{\mathbf{G},i} + \Delta\boldsymbol{p}^{\phi}_{\mathbf{G},i} \leq |s^{\phi}_{\mathrm{G},i}|, \tag{7.29e}$$

$$-|s^{\phi}_{\mathrm{G},i}| \leq \boldsymbol{q}^{\phi}_{\mathbf{G},i} \leq |s^{\phi}_{\mathrm{G},i}|, \tag{7.29f}$$

$$\hat{\boldsymbol{p}}^{\phi}_{\mathbf{G},i} + \Delta\boldsymbol{p}^{\phi}_{\mathbf{G},i} + \boldsymbol{q}^{\phi}_{\mathbf{G},i} \leq \sqrt{2} \cdot |s^{\phi}_{\mathrm{G},i}|, \tag{7.29g}$$

$$\hat{\boldsymbol{p}}^{\phi}_{\mathbf{G},i} + \Delta\boldsymbol{p}^{\phi}_{\mathbf{G},i} - \boldsymbol{q}^{\phi}_{\mathbf{G},i} \leq \sqrt{2} \cdot |s^{\phi}_{\mathrm{G},i}|. \tag{7.29h}$$

For the constant power mode, we can express the reactive power injections using

$$\hat{\boldsymbol{q}}^{\phi}_{\mathbf{G},i} = \hat{\gamma}^{\phi}_{\mathrm{G},i} \cdot \hat{\boldsymbol{p}}^{\phi}_{\mathbf{G},i}, \tag{7.30a}$$

$$\boldsymbol{q}^{\phi}_{\mathbf{G},i} = \boldsymbol{\gamma}^{\phi}_{\mathbf{G},i} \cdot \left(\hat{\boldsymbol{p}}^{\phi}_{\mathbf{G},i} + \Delta\boldsymbol{p}^{\phi}_{\mathbf{G},i}\right). \tag{7.30b}$$

where $\hat{\gamma}^{\phi}_{\mathrm{G},i}$ represents the power ratio of inverter at the current operating point. We assume that $\hat{\gamma}^{\phi}_{\mathrm{G},i}$ is specified by the DSO and hence, the value is already known. Note that the limits for $\boldsymbol{\gamma}^{\phi}_{\mathbf{G},i}$ were already defined in (7.11b).

For the constant reactive power mode, we again assume that the reactive power injections at the current operating point are known because they are controlled by the DSO and denoted by $\hat{q}^{\phi}_{\mathrm{G},i}$.

So, we replace the limits defined in (7.12) by

$$\hat{\boldsymbol{q}}^{\phi}_{\mathbf{G},i} = \hat{q}^{\phi}_{\mathrm{G},i}, \tag{7.31a}$$

$$-\gamma^{\phi}_{\mathrm{G},i} \cdot \left(\hat{\boldsymbol{p}}^{\phi}_{\mathbf{G},i} + \Delta\boldsymbol{p}^{\phi}_{\mathbf{G},i}\right) \leq \boldsymbol{q}^{\phi}_{\mathbf{G},i} \leq \gamma^{\phi}_{\mathrm{G},i} \cdot \left(\hat{\boldsymbol{p}}^{\phi}_{\mathbf{G},i} + \Delta\boldsymbol{p}^{\phi}_{\mathbf{G},i}\right). \tag{7.31b}$$

For the voltage-reactive power mode, we assume that DSO has information about the maximum available reactive power at the current operating point $\overline{\hat{q}}^{\phi}_{\mathrm{G},i}$. We still need to include additional reactive power constraints which are expressed as

$$\hat{\boldsymbol{q}}^{\phi}_{\mathbf{G},i} = \overline{\hat{q}}^{\phi}_{\mathrm{G},i} - 2\overline{\hat{q}}^{\phi}_{\mathrm{G},i} \cdot \left(\frac{|\hat{\boldsymbol{v}}^{\phi}_{i}| - \underline{v}}{\overline{v} - \underline{v}}\right). \tag{7.32}$$

Here, the voltage magnitude at current operating point $|\hat{\boldsymbol{v}}^{\phi}_{i}|$ is constrained by

$$\underline{v} \leq |\hat{\boldsymbol{v}}^{\phi}_{i}| \leq \overline{v}. \tag{7.33}$$

Furthermore, we express the relationship between $|\hat{\boldsymbol{v}}^{\phi}_{i}|$ and the rectangular form voltage variables at the current operating point $\hat{\boldsymbol{v}}^{\phi}_{\mathbf{d}i}, \hat{\boldsymbol{v}}^{\phi}_{\mathbf{q}i}$ similar to (7.3) using

$$\left(v^{\phi}_{\mathrm{d}i}\right)^2 + \left(v^{\phi}_{\mathrm{q}i}\right)^2 + 2v^{\phi}_{\mathrm{d}i}\hat{\boldsymbol{v}}^{\phi}_{\mathbf{d}i} + 2v^{\phi}_{\mathrm{q}i}\hat{\boldsymbol{v}}^{\phi}_{\mathbf{q}i} = \left|v^{\phi}_{i}\right|^2 + 2|v^{\phi}_{i}||\hat{\boldsymbol{v}}^{\phi}_{i}|, \tag{7.34}$$

where $v^{\phi}_{\mathrm{d}i}, v^{\phi}_{\mathrm{q}i}$ are the real and imaginary components of the initial voltage estimate, respectively. Note that in the previous section, we used the current operating point as the initial voltage estimate. In this case, we use the no-load solution defined in (5.17) as the initial voltage estimate for both (7.3) and (7.34).

7.6.4 Power Flow

Following (5.22) and using the no-load solution as the initial voltage estimate, we enforce the power balance constraints at the current operating point using

$$\hat{\boldsymbol{V}}_{\mathbf{d}} = \Re\Big\{Z_1\Big\} + \Re\Big\{Z_2\Big\} \cdot \hat{\boldsymbol{P}}_{\mathbf{Y}} + \Im\Big\{Z_2\Big\} \cdot \hat{\boldsymbol{Q}}_{\mathbf{Y}}, \tag{7.35a}$$

$$\hat{\boldsymbol{V}}_{\mathbf{q}} = \Im\Big\{Z_1\Big\} + \Im\Big\{Z_2\Big\} \cdot \hat{\boldsymbol{P}}_{\mathbf{Y}} - \Re\Big\{Z_2\Big\} \cdot \hat{\boldsymbol{Q}}_{\mathbf{Y}}, \tag{7.35b}$$

where $\hat{\boldsymbol{V}}_{\mathbf{d}}, \hat{\boldsymbol{V}}_{\mathbf{q}} \in \mathbb{R}^{3n}$ are vectors of the real and imaginary voltage components of the current operating point, respectively; $\hat{\boldsymbol{P}}_{\mathbf{Y}}, \hat{\boldsymbol{Q}}_{\mathbf{Y}} \in \mathbb{R}^{3n}$ denote the respective active and reactive power injections at the current operating point. Note that (5.22) also requires an initial voltage estimate and we use the same no-load voltage solution for this.

7.6.5 Bilevel Problem

In this section, we discuss the bilevel problem formulation where inverters are operating in constant power factor mode. We can follow the same procedure to formulate bilevel problems for the other inverter reactive power control modes. The upper-level and lower-level variables for the constant power factor mode are given by

$$\begin{aligned}
\boldsymbol{X}_{\mathbf{u}} &:= \{\Delta\boldsymbol{p}^{+}, \Delta\boldsymbol{p}^{-}, \boldsymbol{\gamma}^{\phi}_{\mathbf{G},i} \forall_{\phi\in\Phi, i\in\mathcal{N}}\}, \\
\boldsymbol{X}_{\mathbf{l}} &:= \left\{\{\boldsymbol{v}^{\phi}_{\mathbf{d}i}, \boldsymbol{v}^{\phi}_{\mathbf{q}i}, |\boldsymbol{v}^{\phi}_{i}|, \Delta\boldsymbol{p}^{\phi}_{\mathbf{G},i}, \Delta\boldsymbol{p}^{\phi}_{\mathbf{L},i}, \boldsymbol{q}^{\phi}_{\mathbf{L},i}, \boldsymbol{q}^{\phi}_{\mathbf{G},i}\}_{\forall_{\phi\in\Phi, i\in\mathcal{N}}}\right\}, \\
\hat{\boldsymbol{X}}_{\mathbf{l}} &:= \left\{\{\hat{\boldsymbol{v}}^{\phi}_{\mathbf{d}i}, \hat{\boldsymbol{v}}^{\phi}_{\mathbf{q}i}, |\hat{\boldsymbol{v}}^{\phi}_{k}|, \hat{\boldsymbol{p}}^{\phi}_{\mathbf{G},i}, \hat{\boldsymbol{p}}^{\phi}_{\mathbf{L},i}, \hat{\boldsymbol{q}}^{\phi}_{\mathbf{L},i}, \hat{\boldsymbol{q}}^{\phi}_{\mathbf{G},i}\}_{\forall_{\phi\in\Phi, i\in\mathcal{N}}}\right\}.
\end{aligned} \tag{7.36}$$

Note that the additional lower-level problem variables $\hat{\boldsymbol{X}}_{\mathbf{l}}$ correspond to the unknown current operating point. Furthermore, we consider the four scenarios as summarized in Table 7.2 and define four sets of lower-level variables $\underline{\boldsymbol{X}}^{+}_{\mathbf{l}}, \underline{\boldsymbol{X}}^{-}_{\mathbf{l}}, \overline{\boldsymbol{X}}^{+}_{\mathbf{l}}, \overline{\boldsymbol{X}}^{-}_{\mathbf{l}}$. However, the current operating point does not change for the four scenarios and as a result, we only need one set for $\hat{\boldsymbol{X}}_{\mathbf{l}}$.

Similar to the procedure followed in Section 7.4.6, we define an extra set of lower-level system constraints which depend on $\hat{\boldsymbol{X}}_{\mathbf{l}}$ using

$$\mathbb{L}(\hat{\boldsymbol{X}}_{\mathbf{l}}) := \begin{cases} \text{Voltage constraints (7.34)}, \\ \text{Load reactive power constraints (7.27)}, \\ \text{Power flow (7.35)}. \end{cases}$$

The four sets of inverter constraints depend on $\hat{\boldsymbol{X}}_{\mathbf{l}}$ and can be represented by

$$\left.\begin{aligned} &\mathbb{I}(\boldsymbol{\gamma}^{\phi}_{\mathbf{G},i}, \underline{\boldsymbol{X}}^{+}_{\mathbf{l}}, \hat{\boldsymbol{X}}_{\mathbf{l}}),\ \mathbb{I}(\boldsymbol{\gamma}^{\phi}_{\mathbf{G},i}, \underline{\boldsymbol{X}}^{-}_{\mathbf{l}}, \hat{\boldsymbol{X}}_{\mathbf{l}}), \\ &\mathbb{I}(\boldsymbol{\gamma}^{\phi}_{\mathbf{G},i}, \overline{\boldsymbol{X}}^{+}_{\mathbf{l}}, \hat{\boldsymbol{X}}_{\mathbf{l}}),\ \mathbb{I}(\boldsymbol{\gamma}^{\phi}_{\mathbf{G},i}, \overline{\boldsymbol{X}}^{-}_{\mathbf{l}}, \hat{\boldsymbol{X}}_{\mathbf{l}}) \end{aligned}\right\} := \text{Inverter constraints (7.29), (7.30)}.$$

It is important to note here that the lower-level variable vector $\hat{\boldsymbol{X}}_1$ is shared by all four sets.

The sets of active power flexibility constraints for the positive and negative case do not depend on $\hat{\boldsymbol{X}}_1$. So, we can use the same sets defined in Section 7.4.6 along with the above defined sets and formulate a bilevel problem similar to $\mathrm{P}^{\pm}$. The single-level reformulation of the bilevel problem can be performed using the steps described in Section 7.5.

We employ the same iterative solution approach detailed in Section 7.5.4 to solve the single-level optimization problem efficiently. It is important to note here that in step 1) of the iterative method, we solve $12n$ worst-case problems with one leader and one follower each and determine the overall aggregate power flexibility using the obtained solutions. Since the lower-level variables $\hat{\boldsymbol{X}}_1$ are also shared by the follower problems along with upper-level variables $\Delta\boldsymbol{p}^{+}, \Delta\boldsymbol{p}^{-}$, the resulting aggregate power flexibility will be more conservative than the solution determined by solving one large worst-case problem with $12n$ followers (i.e. they are no longer equal to each other). Since the solutions are more conservative, we can still use them to identify the lower-level problems that need to be included in the ideal case problem in step 2) of the iterative approach.

7.7 Case Study Overview

In the next three sections, we perform various analyses to evaluate the performance of our proposed method:

- Section 7.8 investigates the **performance of the method on a small IEEE 13-node feeder**. More specifically, we want to evaluate if our solution approach is able to find aggregate power flexibility limits and DER inverter reactive power setpoints that mitigate voltage violations throughout the grid. We also check the **accuracy of the linear power flow approximation**.

- Section 7.9 investigates whether the proposed bilevel approach **scales well for a larger PNNL taxonomic feeder: R2-12-47-2** [86].

- Section 7.10 explores the algorithm performance when **no measurements** are available at any node except the substation. Contrary to Sections 7.8 and 7.9 where we assume that the

current operating point is known, we evaluate the impact of having no knowledge of the current system state by testing the approach on the IEEE 13-node feeder.

For our analysis, we solve three optimization problems based on the three inverter reactive power control modes. The load power factor $pf^{\phi}_{\mathrm{L},i}$ at node i connected to phase ϕ is set to 0.95. For the solar PV inverters, we set the target power factor $pf^{\phi}_{\mathrm{G},i} = 0.9$ for the constant power factor mode and the target power ratio $\gamma^{\phi}_{\mathrm{G},i} = 0.48$ for the constant reactive power mode.

The bilevel optimization problem is implemented in Julia [25] and the optimization problem is solved using using JuMP [26] and Gurobi solver [159]. All simulations were run on a Windows 10 PC with 3.00 GHz Intel Xeon processor and 16 GB RAM.

7.8 Case Study I: Performance Evaluation using IEEE 13-Node Feeder

For our small test case, we use the modified IEEE 13-node feeder [76] illustrated in Fig. 4.2 with single-phase solar PV installations at seven nodes. The maximum apparent power rating of each single-phase solar PV inverter is 60 kVA. The PV penetration level, calculated as the ratio of total PV generation (in kW) to the total rated load (in kW), was chosen to be 45% for the forecasted operating point. The voltage limits are set to $\underline{v} = 0.9$ p.u. and $\overline{v} = 1.1$ p.u. The taps of the voltage regulator connecting three-phase nodes 650 and 630 are set to high values of (10,8,11) and as a result, the system is more prone to overvoltage conditions compared to undervoltage scenarios. For simplicity, we will only discuss results which focus on identifying aggregate power flexibility limits $\Delta\boldsymbol{p}^{-}, \Delta\boldsymbol{p}^{+}$ that mitigate overvoltages in the feeder (i.e. the lower-level problem objective is to maximize voltage magnitude). The maximum available aggregate power flexibility in the system, which can be determined by summing the individual bounds for load and PV inverter flexibility, is ± 1.64 MW.

7.8.1 Worst-case Aggregate Power Flexibility Limits

The first step of our iterative solution approach is to solve the worst-case problem for each single-phase connection separately and identify the location where overvoltages are most likely

going to occur. Fig. 7.3 shows the aggregate power flexibility limits obtained by solving the worst-case problem for the three inverter reactive power control modes. The orange triangles represent the solution obtained for the upper limit $\Delta \boldsymbol{p}^{+}$ and the blue triangles illustrate the solution obtained for the lower limit $\Delta \boldsymbol{p}^{-}$. We observe for the constant power factor mode that the aggregate power flexibility obtained is different for different single-phase connections. The lower limit $\Delta \boldsymbol{p}^{-}$ is equal to -1.64 MW for most of the single-phase connections. Conversely, the upper limit $\Delta \boldsymbol{p}^{-}$ is much lower than 1.64 MW indicating that the overvoltages are most likely going to occur for the positive case compared to the negative case. For the reactive power mode, the aggregate power flexibility range is equal to zero for multiple single-phase connections. This is because the reactive power constraints are less restrictive compared to the constraints defined for the constant power factor mode. On the other hand, the results for the voltage-reactive power mode indicate that the reactive power constraints are most restrictive for this mode. Therefore, we see that the aggregate power flexibility range at almost all the single-phase connections is equal to the maximum available aggregate power flexibility.

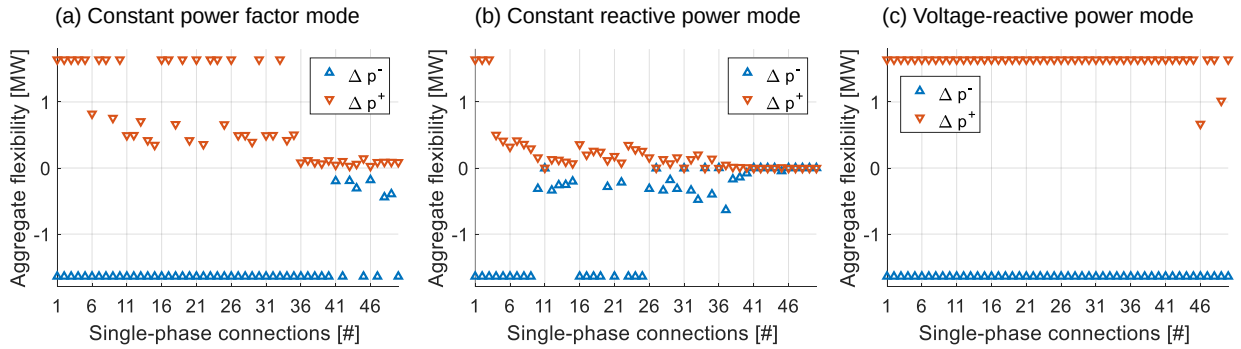

Figure 7.3: IEEE-13 node feeder results. We show the aggregate power flexibility limits obtained by solving worst-case problem for every single-phase connection with different inverter reactive power control modes.

For all three inverter reactive power control modes, the smallest aggregate power flexibility range was obtained when the lower-level problem objective was to maximize voltage magnitude at phase b of node 675 (single-phase connection #46 in Fig. 7.3). To verify this, we solved a single worst-case problem with one leader problem and multiple follower problems and the obtained

aggregate power flexibility limits are summarized in Table 7.3. We notice that the aggregate power flexibility range obtained for the different reactive power nodes is equal to the range obtained for single-phase connection #46 in Fig. 7.3. This verifies that both problems are equivalent.

It is important to note that the worst-case problem with one follower has only two bilinear terms in the single-level reformulated problem which arises due to the product of the dual variable corresponding to aggregate power flexibility constraints and either of the two upper-level variable $\Delta \boldsymbol{p}^{+}, \Delta \boldsymbol{p}^{-}$. Solvers such as Gurobi can handle this constraint efficiently using spatial branching if the number of bilinear terms are small and the average computation time to solve the worst-case problem with one follower is less than 0.07 seconds. Conversely, the computational time to solve the large worst-case problem with multiple follower problems is longer as seen in Table 7.3.

Mode	$\Delta \boldsymbol{p}^{-}$ **(MW)**	$\Delta \boldsymbol{p}^{+}$ **(MW)**	**Computation Time (sec)**
Constant power factor	-0.18	0.03	4.6
Constant reactive power	0	0	3.1
Voltage-reactive power	-1.64	0.67	3.5

Table 7.3: IEEE-13 node feeder results for aggregate power flexibility obtained by solving a single Worst-case problem for different inverter reactive power control modes.

7.8.2 Ideal Case Aggregate Power Flexibility Limits

We next solve the ideal case problem by starting with one lower-level problem corresponding to node 675 at phase b. After obtaining the inverter setpoints from the optimization, we perform a feasibility check to determine if more follower problems need to be added to the ideal case problem iteratively following the procedure described in Section 7.5.4. Table 7.4 summarizes the aggregate power flexibility limits obtained after termination of the iterative process. We observe that the

aggregate power flexibility limits are same for all inverter reactive power control modes and they are equal to the maximum available aggregate power flexibility in the system. By comparing this with the conservative limits obtained by the worst-case problem in Table 7.3, we can conclude that it is important that the DSO is able to control the reactive power settings of the inverters to maximize the amount of flexibility offered by the DERs connected to the grid.

It is interesting to note that the feasibility check is passed after only a few iterations for all the problems. While only one follower is required for the problem with inverters operating in constant reactive power mode to pass the feasibility check, we observe for the constant power factor and voltage-reactive power modes that more follower problems are required. This might be because the single-level problem for these two modes consists of bilinear terms in the dual equality constraints. On the contrary, no bilinear terms are present in the dual equality constraints of the single-level problem for the constant reactive power mode. Furthermore, Table 7.4 show the computation time to solve the ideal case problem with multiple follower problems in the last iteration. We observe that the solve time is less than a second for all three inverter reactive power modes. This indicates that the iterative approach can solve the problem efficiently and scales well for larger distribution feeders.

Mode	$\Delta \boldsymbol{p}^{-}$ **(MW)**	$\Delta \boldsymbol{p}^{+}$ **(MW)**	**No. of Iterations**	**Computation Time (sec)**
Constant power factor	-1.64	1.64	3	0.10
Constant reactive power	-1.64	1.64	1	0.05
Voltage-reactive power	-1.64	1.64	3	0.50

Table 7.4: IEEE-13 node feeder results for aggregate power flexibility obtained by solving ideal case problem for different inverter reactive power control modes.

Fig. 7.4 illustrates the inverter setpoints determined by the ideal case problem that ensure no overvoltages occur throughout the grid. For the constant power factor and constant reactive power

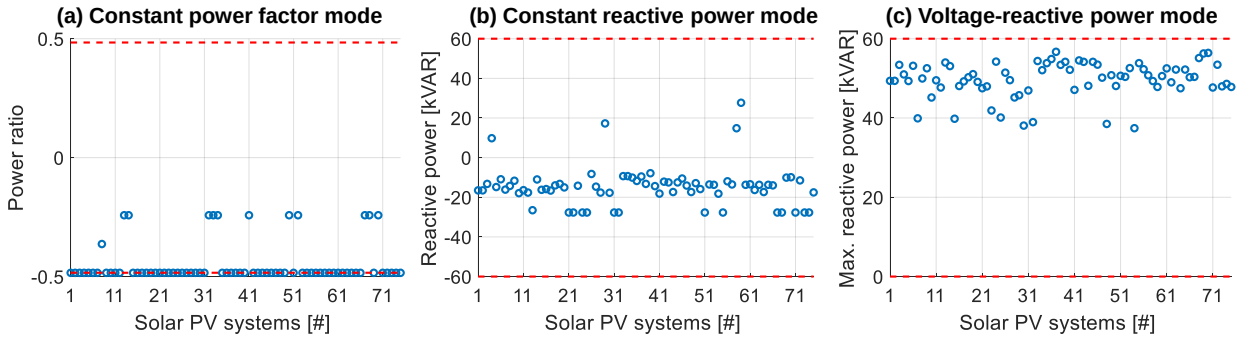

Figure 7.4: IEEE-13 node feeder results obtained by solving ideal case problem. We show the setpoints determined for different inverter reactive power control modes. The red dashed lines are maximum and minimum limits on the upper-level variables.

modes, we observe that the reactive-power injections for most of the solar PV systems are negative. This is expected since the voltage profile of the feeder is already close to the upper limit due to the high regulator tap settings and hence, absorption of the reactive power will lead to lowering of the voltage magnitudes. For the voltage-reactive power mode, it can be seen that the maximum reactive power limit is chosen very close to the apparent power limit of the inverters (red dashed line) to ensure that the total reactive power absorbed by the solar PV systems is high thereby keeping the voltage magnitudes within limits.

7.8.3 Linear Approximation Accuracy

Recall that we linearized multiple constraints in the lower-level problem of our bilevel optimization task. To analyze the accuracy of the inverter setpoints obtained by solving the linear ideal case problem, we formulate the nonlinear counterpart of the lower-level problem by making the following changes:

- Quadratic inverter constraints are utilized instead of the circular linear constraints.
- We replace the first order Taylor approximation of the relationship between the voltage variables with the quadratic constraints.

- We use the nonlinear power flow equation in rectangular form instead of the fixed-point linear power flow model.

Consequently, the nonlinear lower-level problem with objective to find worst-case maximum voltage magnitudes for the positive case can be expressed as

$$|\overline{\boldsymbol{v}}_i^{\phi}| = \max_{\boldsymbol{X}_1} |\boldsymbol{v}_i^{\phi}|, \ \forall_{\phi\in\Phi, i\in\mathcal{N}}, \tag{7.37}$$

s.t. Load reactive power : (7.5),

Aggregate power flexibility : (7.7), (7.8),

Inverter reactive power modes : (7.11) or (7.12) or (7.13),

$$(p_{\mathrm{G},i}^{\phi} + \Delta\boldsymbol{p}_{\mathbf{G},i}^{\phi})^2 + (\boldsymbol{q}_{\mathbf{G},i}^{\phi})^2 \leq |s_{\mathrm{G},i}^{\phi}|^2, \qquad \forall_{\phi\in\Phi, i\in\mathcal{N}},$$

$$|\boldsymbol{v}_i^{\phi}|^2 = \left(\boldsymbol{v}_{\mathbf{d}i}^{\phi}\right)^2 + \left(\boldsymbol{v}_{\mathbf{q}i}^{\phi}\right)^2, \qquad \forall_{\phi\in\Phi, i\in\mathcal{N}},$$

$$\boldsymbol{P}_i = \sum_{k\in\mathcal{N}_0} \boldsymbol{V}_{\mathbf{d}i} \odot \Big[G_{ik}\boldsymbol{V}_{\mathbf{d}k} - B_{ik}\boldsymbol{V}_{\mathbf{q}k}\Big] + \sum_{k\in\mathcal{N}_0} \boldsymbol{V}_{\mathbf{q}i} \odot \Big[B_{ik}\boldsymbol{V}_{\mathbf{d}k} + G_{ik}\boldsymbol{V}_{\mathbf{q}k}\Big], \qquad \forall_{i\in\mathcal{N}},$$

$$\boldsymbol{Q}_i = \sum_{k\in\mathcal{N}_0} \boldsymbol{V}_{\mathbf{d}i} \odot \Big[-B_{ik}\boldsymbol{V}_{\mathbf{d}k} - G_{ik}\boldsymbol{V}_{\mathbf{q}k}\Big] + \sum_{k\in\mathcal{N}_0} \boldsymbol{V}_{\mathbf{q}i} \odot \Big[G_{ik}\boldsymbol{V}_{\mathbf{d}k} - B_{ik}\boldsymbol{V}_{\mathbf{q}k}\Big], \ \forall_{i\in\mathcal{N}}.$$

We can formulate a similar nonlinear problem for the negative case by just replacing the aggregate power flexibility constraints (7.8) with (7.9).

We substitute the aggregate power flexibility limits determined by the ideal case problem in (7.7) and the inverter setpoints in the constraints for the inverter reactive power modes. We then solve the optimization problem for all single-phase connections to check if the resulting voltage magnitudes are within the limits. We compare the voltage magnitudes obtained by solving (7.37) with the voltage magnitudes that are obtained by solving the linear lower-level problem of our bilevel task.

Fig. 7.5 shows the worst-case voltage magnitudes obtained by solving the nonlinear and linear versions of the problem. We observe that for all three inverter reactive power control modes, the setpoints determined by the ideal case problem keep the voltage magnitudes within the limits even we solve the nonlinear problem (7.37). We note that the approximation accuracy for the constant power factor and voltage-reactive power mode is high since the nonlinear voltage magnitudes (blue circles) and linear voltage magnitudes (orange crosses) are close to each other. On

the other hand, the approximation accuracy is lower for the constant reactive power mode (maximum error ≈ 0.006 p.u.). This might be because the solution is further away from the initial operating point which was used to linearize the power flow equations in (5.22). However, we see that the fixed-point approximation is conservative for the constant reactive power mode since the voltage magnitudes determined by solving the nonlinear problem are generally lower than the voltage magnitudes obtained by the linear problem. Another noteworthy observation is that for a given single-phase connection, if we compare the worst-case voltage magnitudes obtained by all three modes, the results for the voltage-reactive power mode exhibit the lowest magnitude. This indicates that voltage-reactive power mode is the most restrictive reactive power mode among the three modes and can be used effectively to mitigate voltage violations.

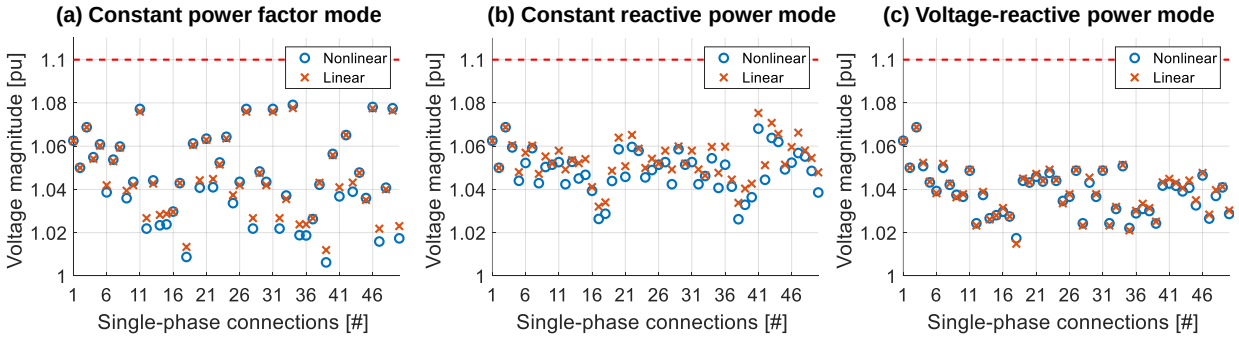

Figure 7.5: IEEE 13-node feeder results comparing the worst-case voltage magnitudes obtained by solving nonlinear and linear versions of the lower-level problem. The red dashed lines are the upper voltage magnitude limits.

7.9 Case Study II: Evaluating Scalability using Taxonomic Feeder-R2-12-47-2

We next investigate scalability of our solution method. For our larger test case, we choose the R2-12-47-2 feeder [86] shown in Fig. 4.7 which comprises of 820 single-phase connections and depicts a moderately populated suburban area with single family homes and light commercial loads [104]. Solar PV inverters are connected to all single-phase nodes in the feeder with each inverter rated at 5 KVA to achieve a PV penetration level of 20% of the total rated load. The

voltage limits for this test case are tighter and set to $\underline{v} = 0.95$ p.u. and $\overline{v} = 1.05$ p.u. The maximum available aggregate power flexibility in the system is ± 4.86 MW. In this case, we solve the bilevel problem to determine the aggregate power flexibility and inverter reactive power setpoints that mitigate both overvoltages and undervoltages in the feeder.

7.9.1 Worst-case Aggregate Power Flexibility Limits

We first look at the aggregate power flexibility limits obtained by solving the worst-case problem for every single-phase connection in the network. Different from the IEEE-13 node feeder results, we observe in Fig. 7.6 that all three inverter reactive power control modes provide an aggregate power flexibility range of zero at multiple single-phase connections in the network. Furthermore, the average computation time to solve the worst-case problem at each single-phase connections is about 2 seconds.

Since there are multiple single-phase connections with aggregate power flexibility range of zero, we randomly pick node 135 connected to phase b (#571 in Fig. 7.6) whose corresponding lower-level problems will be included in the ideal case problem.

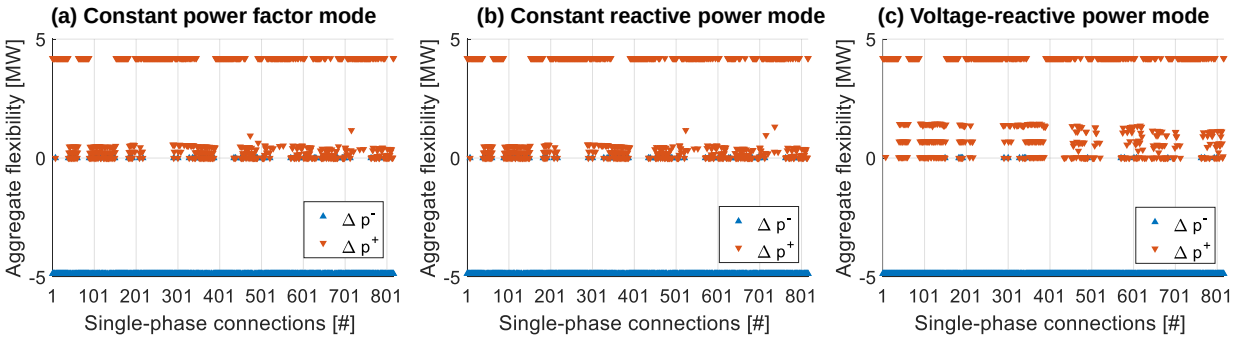

Figure 7.6: R2-12-47-2 feeder results. We show the aggregate power flexibility limits obtained by solving worst-case problem for every single-phase connection with different inverter reactive power control modes.

7.9.2 Ideal Case Aggregate Power Flexibility Limits

We compare the results obtained after termination of the iterative approach where the ideal case problem is solved repeatedly until the feasibility check is passed. Table 7.5 summarizes the obtained aggregate power flexibility limits and computation time to solve the ideal case problem at the final iteration. Similar to the IEEE 13-node results, we observe that the aggregate power flexibility limits determined for all inverter reactive power control modes are equal to the maximum available aggregate power flexibility ± 4.86 MW in the system. It is interesting to note that the feasibility check passed after the first iteration for all three inverter reactive power control modes. In addition, the computation time to solve the ideal case problem with one follower was less than a minute for all three power modes. The higher solve time for the constant reactive power mode is mostly due to the higher number of bilinear terms in the reformulated problem. It is possible to employ piecewise McCormick envelopes to relax the bilinear terms [160] and further reduce computation time, but we defer this to future work.

Mode	Δp^- **(MW)**	Δp^+ **(MW)**	**No. of Iterations**	**Computation Time (sec)**
Constant power factor	-4.86	4.86	1	10
Constant reactive power	-4.86	4.86	1	45
Voltage-reactive power	-4.86	4.86	1	30

Table 7.5: R2-12-47-2 feeder results for aggregate power flexibility obtained by solving ideal case problem for different inverter reactive power control modes.

The inverter setpoints determined by the ideal case problem for the different reactive power modes is shown in Fig. 7.7. Compared to the IEEE-13 node feeder results, most of the power ratio setpoints for the constant power factor mode are no longer close to the lower limit. Instead, we see that multiple inverters are injecting reactive power into the grid. This might be because the voltage profile of the feeder is not close to the upper limits and the lower PV penetration level

reduces the probability of overvoltages and increases the risk of undervoltages. Hence, it is not required to absorb more reactive power from the network. The inverter setpoints obtained for the reactive power mode are closer to zero compared to the lower limit which is similar to the reactive power setpoints obtained for the IEEE-13 node feeder in Fig. 7.4(b). On the other hand, for the voltage-reactive power mode, the maximum reactive power setpoints are closer to the lower limit as opposed to the IEEE-13 node results shown in Fig. 7.4(c) where the setpoints are near the upper limit. This verifies the conclusion made by looking at results for the constant power factor mode that the reactive power absorption is not required to be very high for this test case.

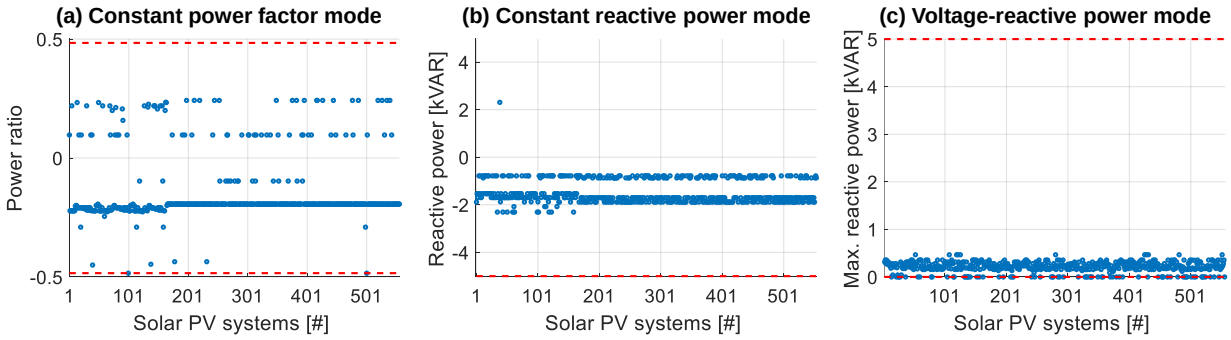

Figure 7.7: R2-12-47-2 feeder results obtained by solving ideal case problem. We show the setpoints determined for different inverter reactive power control modes. The red dashed lines are maximum and minimum limits on the upper-level variables.

7.10 Case Study III: Considering Impact of Limited Measurements

To investigate the effect of not knowing the current operating point, we use the same IEEE 13-node feeder described in Section 7.8 and focus on identifying aggregate power flexibility limits $\Delta \boldsymbol{p}^{-}, \Delta \boldsymbol{p}^{+}$ that mitigate overvoltages in the feeder. As mentioned previously, the maximum available aggregate power flexibility in the system is ± 1.64 MW.

Recall that the DER setpoints at the current operating point are assumed to be known since they are controlled by the DSO. For simplicity, we assume in this case study that the setpoints are equal to zero, i.e. $\hat{\gamma}^{\phi}_{\mathrm{G},i} = 0$ for the constant power factor mode, $\hat{q}^{\phi}_{\mathrm{G},i} = 0$ for the constant reactive

power mode and $\overline{\hat{q}}^{\phi}_{\mathrm{G},i} = 0$ for the voltage-reactive power mode. This means that the reactive power injections of all the DER inverters at the current operating point is zero for all three reactive power control modes.

7.10.1 Worst-case Aggregate Power Flexibility Limits

Fig. 7.8 illustrates the range of aggregate power flexibility obtained by solving the worst-case problem for the three inverter reactive power control modes. Different from the results in Fig. 7.3, we observe that the aggregate power flexibility range is extremely conservative since the current system state is not known and as a result, the problem finds the worst-case current operating point. Similar to the results in Section 7.8, we again choose to start solving the ideal case problem by including the followers corresponding to phase b of node 675 since the aggregate power flexibility range is zero for all three inverter reactive power control modes.

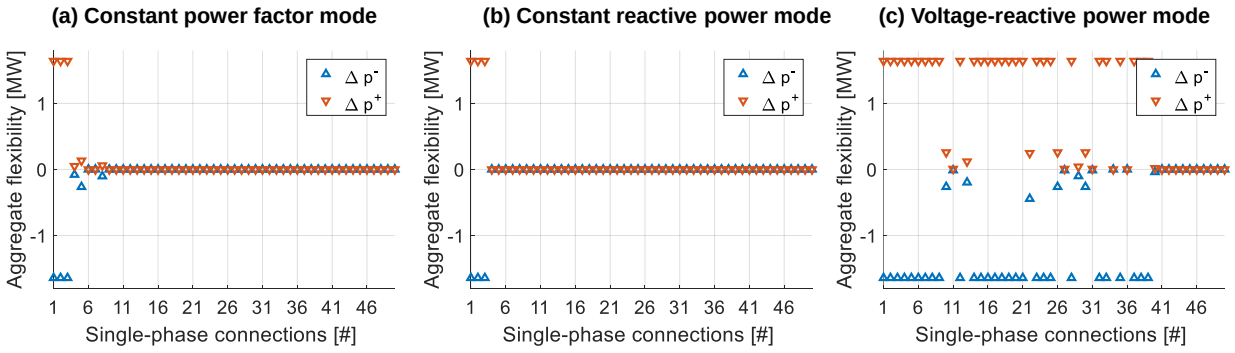

Figure 7.8: IEEE-13 node feeder results with limited measurements. We show the aggregate power flexibility limits obtained by solving worst-case problem for every single-phase connection with different inverter reactive power control modes.

7.10.2 Ideal Case Aggregate Power Flexibility Limits

Table 7.6 summarizes the final results obtained by solving the ideal case problem iteratively. We observe that it is still possible to obtain results with the maximum available aggregate power flexibility in the system. However, we see that the feasibility check is passed after a higher number

of iterations compared to the results shown in Table 7.4. Furthermore, the computation time to solve the ideal case problem with multiple follower problems in the last iteration is higher due to the larger number of variables in the optimization problem.

Mode	Δp^{-} **(MW)**	Δp^{+} **(MW)**	**No. of Iterations**	**Computation Time (sec)**
Constant power factor	-1.64	1.64	5	2.9
Constant reactive power	-1.64	1.64	6	1.5
Voltage-reactive power	-1.64	1.64	3	2.2

Table 7.6: IEEE-13 node feeder results for aggregate power flexibility obtained by solving ideal case problem with limited measurements.

Fig. 7.9 illustrates the inverter setpoints determined by solving the ideal case problem. We observe that the reactive-power injections for most of the solar PV systems are negative and the set-points are similar to the results shown in Fig. 7.4. Recall that this happens because the voltage profile of the feeder is already close to the upper limit due to the high voltage regulator tap settings and as a result, the reactive power is absorbed by PV inverters to lower the voltage profile.

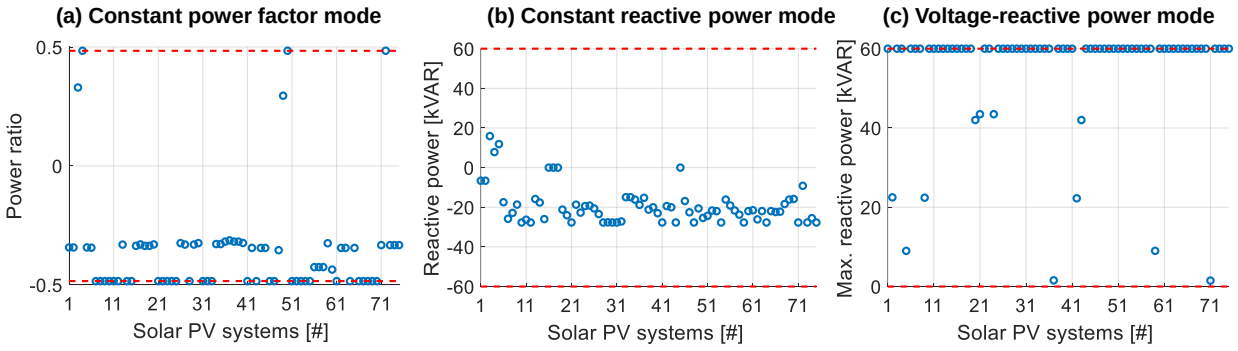

Figure 7.9: IEEE-13 node feeder results obtained by solving ideal case problem with limited measurements. We show the setpoints determined for different inverter reactive power control modes. The red dashed lines are maximum and minimum limits on the upper-level variables.

The main takeaway from the results shown above is that it is possible to identify reactive power setpoints that allow us to use the maximum available aggregate power flexibility in the system even when limited measurements are available. However, this cannot be generalized for all cases. The IEEE 13-node feeder used here is a smaller test case with a PV penetration level less that 50%. For larger and more realistically sized distribution feeders with higher PV penetration levels, it might be challenging to identify such reactive power setpoints that allows us to harness the full collective flexibility of the DERs.

7.10.3 Linear Approximation Accuracy

We finally investigate the solution quality by solving the linear and nonlinear versions of the lower-level problem using the inverter setpoints determined above. Fig. 7.10 shows the worst-case voltage magnitudes at all single-phase connections when solving the nonlinear and linear problems with limited measurements. Similar to the results shown in Fig. 7.5, we see that for all three inverter reactive power control modes, the setpoints determined by the ideal case problem maintain the voltage magnitudes within the limits even for the nonlinear case. Even though we do not use the current operating point as the initial voltage estimate in our linear power flow equations and instead use a no-load voltage estimate, the approximation accuracy is high (maximum error ≈ 0.011 p.u.) for all three inverter reactive power control modes. Different from the results in Fig. 7.5, we observe that the fixed-point approximation is no longer conservative and the voltage magnitudes determined by solving the nonlinear problem are not always lower than the voltage magnitudes obtained by the linear problem.

7.11 Main Takeaways

This chapter explores the coordination between transmission systems, distribution grids and DER aggregators. The main goal is to identify the aggregate power flexibility range provided to transmission systems without causing any constraint violations in distribution grids. We formulate

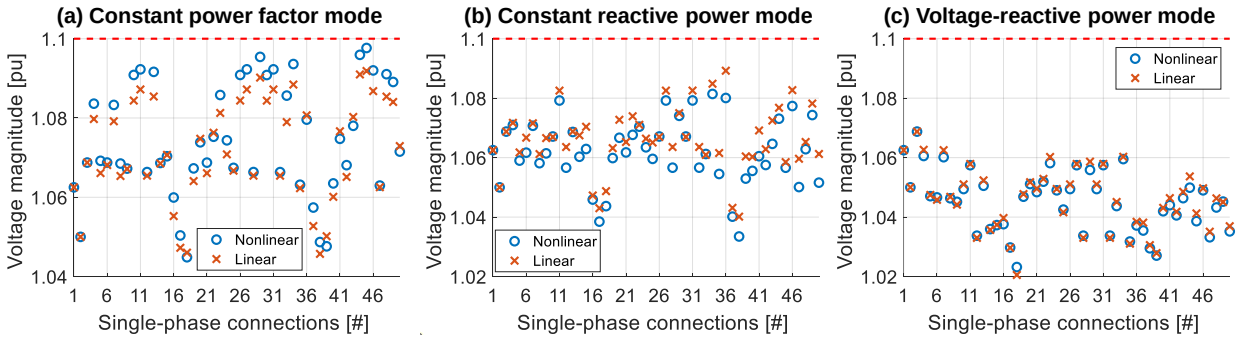

Figure 7.10: IEEE 13-node feeder results comparing the worst-case voltage magnitudes obtained by solving nonlinear and linear versions of the lower-level problem with limited measurements. The red dashed lines are the upper voltage magnitude limits.

a bilevel optimization task where the upper-level problem maximizes the aggregate power flexibility and determines the DER inverter reactive power setpoints while the lower-level problem determines the worst-case disaggregation strategy.

Our case studies demonstrate that it is important to allow the DSO to choose the DER inverter reactive power setpoints in order to utilize the maximum available flexibility in the system. These setpoints will ensure that the grid is secure even during worst-case conditions. The results for the IEEE 13-bus feeder showed that we are able to obtain high-quality solutions for the inverter setpoints by solving the single-level, strong duality based reformulated problem. We also observed that the proposed approach performs well even when limited measurements are available. Our results on the larger taxonomic feeder demonstrate that the proposed approach scales well and can be applied to large, realistic distribution feeders.

Chapter 8

Conclusions and Future Work

This thesis has introduced our approach to implementing efficient three-phase OPF formulations with the main goal to improve voltage unbalance in distribution grids and maximize the flexibility offered by distributed energy resources in response to uncertainty. In this chapter, we summarize the main conclusions that can be drawn from the work done so far. Furthermore, the work has revealed various areas of related research which require further analysis. We propose different directions for future work in this field that can build upon the unbalanced, three-phase OPF framework described in the previous chapters.

8.1 Conclusions

This sections provides a brief summary of the main contributions and conclusions of each chapter.

Chapter 1 introduced the motivation for our research work along with a literature review of the existing work that focused on analysis of distribution grids with integration of DERs. While there are some existing tools capable of performing power flow and optimal power flow analysis for distribution grids, we observed that there is a need for an optimization framework that is practical, robust and cost effective with the goal to improve power quality in large-scale, realistic distribution grids considering actual measurement data as well as variability associated with residential loads and various DER connections.

Chapter 2 discussed one of the major power quality issues in distribution grids with high penetration of DERs such as rooftop solar PV systems. In this chapter, we introduced the three most

commonly used definitions of voltage unbalance and derived the analytical relationships highlighting bounds for the maximum difference among the three definitions. The accuracy of these relationships was verified using numerical simulations. While VUF is the true definition of voltage unbalance, it requires measurement of voltage angles which is not readily available in practical distribution grids. The other two definitions (i.e. LVUR and PVUR) are widely used as substitutes for VUF since they only require voltage magnitude measurements. We were able to conclude from our analysis that PVUR has no clear relationship with VUF whereas LVUR can be used to derive lower and upper bounds on VUF.

Chapter 3 provided a detailed description of the modelling of major distribution grid components in the phase domain. We use the model in **Chapter 4** to formulate the full three-phase AC OPF problem which was extended by including the different voltage unbalance definitions as constraints or objective functions. In order to do this, we introduced additional variables and nonlinear expressions in our three-phase OPF framework making the optimization problem harder to solve when compared to the standard three-phase OPF problem. The proposed method was tested on a small feeder (i.e. IEEE 13-bus) as well as a large, realistic taxonomic feeder (i.e. R2-12-47-2). The main takeaway from the case studies was that minimizing voltage unbalance using one definition can lead to increase in network losses and/or violation of voltage unbalance limits specified by other definitions. However, we were able to demonstrate that the three-phase OPF formulation minimizing network losses subject to all the voltage unbalance constraints obtained a solution with low network losses without violating the voltage unbalance limits.

Chapter 5 acknowledged one of the challenges with the three-phase OPF approach i.e. computation time. To address this issue, we developed three different scalable implementations by linearizing the power balance equations and using an iterative approach to obtain solutions that are AC feasible and close to the optimal solution (i.e. reduce VUF at critical bus to almost zero). The main contribution of this chapter was the performance comparison of the three scalable methods in terms of voltage unbalance reduction, voltage violations and computation time. The comparison was done by performing time-based simulations for a large, realistic taxonomic feeder (i.e.

R1-12-47-1) using actual measurement data for residential loads and PV generation. Our analysis showed that all three scalable methods were able to considerably improve computation time and also obtain solutions that significantly reduced voltage unbalance. Furthermore, we observed that the overall performance of all the methods reduced if the three-phase OPF was solved less frequently. Hence, we can conclude that although solving the original optimization problem OPF might provide us optimal solutions, it is worthwhile to employ the scalable methods and obtain good, but sub-optimal solutions more frequently especially for large, realistic distribution feeders.

Chapter 6 leverages a chance-constrained optimization approach to investigate the impact of uncertainty on operation of distribution grids. We first present a chance-constrained optimal power flow problem for unbalanced distribution grids and then describe a reformulation based on constraint tightening. We employ an iterative, data-driven approach that is capable of solving the reformulation efficiently. Our case studies on the IEEE 13-bus test feeder using real PV and load measurement data indicate that the iterative quantile-based algorithm is able to enforce the chance constraints in both in- and out-of-sample evaluations. Furthermore, we observed that randomly chosen samples across multiple days is the beneficial sampling procedure compared to using full day samples. Our case study also demonstrated that the iterative method using linear power flow models performed in a similar manner compared to using the nonlinear power flow equations.

Chapter 7 develops a bilevel optimization approach to model and identify the aggregate flexibility for DERs in unbalanced distribution systems. We propose a strong duality based reformulation of the bilevel problem that can be efficiently solved using an iterative approach. Our case study results for two unbalanced distribution feeders showed that the bilevel problem provides safe operating ranges for different DER control actions which can be easily communicated to third-party aggregators controlling these devices. Moreover, the resulting aggregate flexibility range can help reduce burdens on transmission system resources while mitigating the risk of constraint violations in distribution grids.

8.2 Future Work

While the electric power system evolves towards a distributed infrastructure with increasing number of controllable nodes, there is lot of scope for research that leverage advances in optimization and control to develop frameworks for distribution grids that ensure stability, reliability, and also meet economic objectives. We have already seen that existing research work include various optimization strategies focusing on distributed control strategies or centralized methods with small test cases, simplified load models relying on approximations or relaxations of the unbalanced system model. In this section, we propose few directions for continuing the research work in this field.

8.2.1 Additional Controllable Devices

Our current three-phase OPF framework considers reactive power injections of single-phase solar PV inverters as the control variables. We have also modelled voltage regulators with tap control and capacitors with on-off switching control as described in Appendix A. There are other DER controllers and strategies to ensure efficient and reliable operation of the distribution grid while satisfying power quality standards such as

- *Three-phase PV systems:* Solar PV systems integrated in the distribution grid can also have a three-phase connection based on their rated power. For such cases, the PV inverter topology is a critical factor that must be considered when modelling the three-phase solar PV systems. While three-phase, three-wire inverters do not have the ability to inject zero-sequence currents, there are different configurations [161, 162, 163, 164] for three-phase, four wire inverters we could consider in order to apply independent per-phase control and mitigate the negative effects of unbalance. Furthermore, the active power injected by these inverters can also be considered as control variables and curtailed in extreme cases when the PV penetration levels are very high and the number of overvoltages are very high.

- *Electric vehicles and battery storage systems:* It is important to note that the above mentioned strategy can also be extended to other DERs such as electric vehicles and battery

energy storage systems. Increasing deployments of these devices make them promising candidates to overcome challenges in the distribution grid including, but not limited to, the voltage unbalance problem and multi-period implementation of the optimization problem using the scalable methods discussed in Chapter 5.

While previous work focused on controlling individual components such as three-phase PV inverters [74, 163], voltage regulators [165], electric vehicles [166] and battery storage systems [167] to improve power quality, a more comprehensive approach can be taken to extend the distribution grid modelling by including the above mentioned additional components. The main research question to address here is whether the interaction between various control strategies has an impact on the operation of the grid. This will help identify if local DER actions (such as droop control) can be utilized without violating any grid constraints or, conversely, if centralized control strategies (such as tap switching of remotely-controlled voltage regulators) are required to ensure power quality standards are maintained in the distribution grid.

8.2.2 State Estimation

One of the major assumptions in Chapter 5 is that measurement data is available at all buses to which loads are connected. However, this is not a realistic assumption as discussed in Chapter 7. Although we consider the impact of limited measurement availability in Chapter 7, we do not estimate the exact system state. So, the main research question to consider here is whether a three-phase OPF problem can be solved efficiently with limited sensors and monitoring points in the distribution grid. In such cases, we can consider state estimation for distribution grids to provide accurate real-time information of network power flow by using the limited measurement data. For transmission systems, state estimation is a matured research area with different well-known algorithms [168]. However, distribution grids do not have the same availability of measurement data or network topology as compared to transmission systems [169]. The unbalanced nature of distribution grids as well as the requirement of redundant measurement data from historical data and virtual measurement for buses with zero power injection makes state estimation complicated [170].

The distribution grid state estimation problem can be formulated using the weighted least squares or weighted least absolute value error criterion for robust state estimation. Since the presence of redundant and virtual measurement data could result in divergence issues by employing solvers similar to transmission systems for the state estimation, the convex semidefinite programming approach can be employed. This enables the state estimation problem to be solved in polynomial time with the SDP-based relaxation of non-convex constraints where virtual measurements can be handled efficiently without running into numerical issues [171]. Using this state estimation approach, the resulting voltage estimate can be used as the initial estimate to determine power injections at buses without sensors and solve the three-phase OPF problems described in Chapters 5 and 7.

8.2.3 Real-time Optimization

We have already seen that the optimization problem OPF described in the beginning of chapter 5 is nonlinear and non-convex problem which takes a long time to converge to a solution. In order to utilize this formulation as a real-time control strategy, we could improve convergence rate by identifying the binding constraints in the optimization problem. Previous work has focused on predicting the binding status of constraints [172] or decreasing the number of variables and control actions using network reduction techniques [173, 174] or choosing the most effective control actions by sensitivity analysis [175] for transmission systems. The main research question here is whether it is possible to identify the binding constraints of the three-phase OPF problem and utilize this information to generate a reduced optimization problem by ignoring the non-binding constraints. In addition to this, the measurement data such as load pattern and PV generation profile can be analyzed to investigate if there exists a direct relationship between the binding constraints and power injections in the system. Furthermore, since OPF is a non-convex problem, a good starting point might lead to better convergence rate. In our current work, we either use a flat-start or the no-load voltage as our initial operating point. One way to calculate a good initial point would be to use relaxations such as semidefinite programming [176] and solve a relaxed optimization problem. We can use the solution of this relaxed problem as a warm start for solving OPF. Although these

relaxed three-phase OPF solutions might depend on the solver and network topology, it might be a promising approach for determining a suitable starting point to solve the three-phase OPF.

8.2.4 Integration with GridLAB-D

Our main source of network data is the taxonomic feeder information included with GridLAB-D which is one of the first open source and flexible simulation platforms focusing on distribution grid modelling [17]. While GridLAB-D comprises of some the most advanced modeling techniques coupled with with high-performance algorithms for power flow studies [17], recall that it does not have any optimization capabilities or the ability to solve optimal power flow problems. Since GridLAB-D can examine the interplay between any components of a distribution grid in detail without the using approximate or reduced-order models, it might be useful to integrate our three-phase OPF framework with GridLAB-D. We already discussed earlier that the FOT-OPF method requires a power flow to be solved during each iteration and the FBS-OPF method uses a single-iteration of the forward-backward sweep. While GridLAB-D has efficient Newton-Raphson and forward-backward sweep power flow solvers, we can also integrate these solvers into the optimization framework to improve convergence time.

To the best of our knowledge, there are no existing tools to integrate GridLAB-D with Julia. However, several efforts such as open modelling framework (OMF) from National Rural Electric Cooperative Association [177] have been made to use GridLAB-D in a Python-based environment. One direction for future work could be to integrate the Julia code with GridLAB-D and use third-party open-source tools like OMF to set up an optimization framework that allows interaction with GridLAB-D. While this enables us to utilize the advanced functionalities of GridLAB-D, it also increases opportunities to make improvements and extensions which will help in standardizing the three-phase OPF framework. The integration with a common tool such as GridLAB-D will facilitate a better platform for benchmarking as well as comparison of results with other research groups.

Appendix
Conventional Flexibility Sources

While we only consider solar PV inverters as our flexibility source in the three-phase OPF problem, we can also include other traditional approaches for voltage control which include switching devices such as voltage regulators and capacitors. Note that although we have modelled these controllable devices in our framework, we use voltage regulators with constant tap-ratios as described in Section 3.4 and capacitors with fixed on-off state as discussed in Section 3.6.3 for all our numerical simulations in this thesis.

Voltage Regulator with Tap Control

In the previous chapter, we discussed the modelling of voltage regulators with constant taps. In practice, DSO can remotely change the regulator taps to control the voltage profile of the network. Consider a gang-operated, three-phase voltage regulator connected between nodes i and k. The output voltage magnitude at node k is related to the input voltage magnitude at node i as $|\boldsymbol{V}_k| = \boldsymbol{\alpha}_{ik}|\boldsymbol{V}_i|$, where $\boldsymbol{\alpha}_{ik}$ is the transformation ratio. $\boldsymbol{\alpha}_{ik}$ is a discrete variable since it ranges between 0.9 and 1.1 at integer steps of 0.625% and a mixed-integer linear programming (MILP) formulation is needed to include such variables in the optimization problem. For computational simplicity, we can approximate $\boldsymbol{\alpha}_{ik}$ as a continuous variable and model the regulator taps using

$$0.9 \cdot |\boldsymbol{V}_{\mathrm{i}}| \leq |\boldsymbol{V}_k| \leq 1.1 \cdot |\boldsymbol{V}_{\mathrm{i}}|. \tag{A.1}$$

Alternatively, the regulator can also be locally controlled if they are equipped with a line drop compensator (LDC) [14]. Consider a three-phase voltage regulator connected between the nodes i and k. By using the current I_{ik} flowing in the branch ik, the LDC regulator calculates a regulated

voltage defined by

$$V_{\text{LDC}} = V_k - Z_{\text{LDC}} \cdot \underbrace{Y_{ik} \cdot (V_i - V_k)}_{I_{ik}}, \text{ where } Z_{\text{LDC}} = R_{\text{LDC}} + j \cdot X_{\text{LDC}} \tag{A.2}$$

is the LDC impedance setting and Y_{ik} is a submatrix of the nodal admittance matrix Y. Different from the remotely-controlled regulator described previously, the LDC regulator tries to control the regulated voltage magnitude $|V_{\text{LDC}}|$ instead of the actual output voltage magnitude $|\boldsymbol{V}_k|$. To specify the voltage range for the LDC regulator, we define a reference output voltage magnitude $|V_k^{\text{ref}}|$ (bandcenter) and the bandwidth ΔV_{ik}. The LDC regulator maintains $|V_{\text{LDC}}|$ within the specified range such that

$$|V_k^{\text{ref}} - \Delta V_{ik}|^2 \leq |V_{\text{LDC}}|^2 \leq |V_k^{\text{ref}} + \Delta V_{ik}|^2. \tag{A.3}$$

We define additional variables $\boldsymbol{V}_{\mathbf{d},ik}, \boldsymbol{V}_{\mathbf{q},ik}$ in rectangular form to determine the voltage difference between nodes i and k such that

$$\begin{aligned} \boldsymbol{V}_{\mathbf{d},ik} &= |\boldsymbol{V}_i| \odot \cos(\boldsymbol{\Theta}_i) - |\boldsymbol{V}_k| \odot \cos(\boldsymbol{\Theta}_k), \\ \boldsymbol{V}_{\mathbf{q},ik} &= |\boldsymbol{V}_i| \odot \sin(\boldsymbol{\Theta}_i) - |\boldsymbol{V}_k| \odot \sin(\boldsymbol{\Theta}_k). \end{aligned} \tag{A.4}$$

By substituting these variables in (A.2) and separating the real and imaginary parts, we get

$$\begin{aligned} \Re\{V_{\text{LDC}}\} &= \boldsymbol{V}_{\mathbf{d}k} - \Re\{Z_{\text{LDC}} \cdot Y_{ik}\} \cdot \boldsymbol{V}_{\mathbf{d},ik} + \Im\{Z_{\text{LDC}} \cdot Y_{ik}\} \cdot \boldsymbol{V}_{\mathbf{q},ik}, \\ \Im\{V_{\text{LDC}}\} &= \boldsymbol{V}_{\mathbf{q}k} - \Re\{Z_{\text{LDC}} \cdot Y_{ik}\} \cdot \boldsymbol{V}_{\mathbf{q},ik} - \Im\{Z_{\text{LDC}} \cdot Y_{ik}\} \cdot \boldsymbol{V}_{\mathbf{d},ik}, \\ |V_{\text{LDC}}|^2 &= \Re\{V_{\text{LDC}}\}^2 + \Im\{V_{\text{LDC}}\}^2. \end{aligned} \tag{A.5}$$

We can substitute the above expression derived for $|V_{\text{LDC}}|^2$ in (A.3) to model the LDC regulator.

Capacitors with Switching Control

Recall that shunt capacitor banks are generally utilized in distribution systems to provide reactive power support. While we modelled capacitors as constant susceptance loads in the previous chapter, they can be switched on and off to aid in voltage regulation. Consider a wye-connected

capacitor at node i connected to phase ϕ with susceptance $b^{\phi}_{\text{Ycap},i}$. The capacitor switching action can be modelled using a binary variable $\boldsymbol{z}^{\phi}_{i}$. For computational simplicity, we can again approximate $\boldsymbol{z}^{\phi}_{i}$ as a continuous variable that ranges between 0 and 1. We define a new variable for the capacitor susceptance $\boldsymbol{b}^{\phi}_{\mathbf{Ycap},i} = \boldsymbol{z}^{\phi}_{i} \cdot b^{\phi}_{\text{Ycap},i}$ where

$$\boldsymbol{z}^{\phi}_{i} = \begin{cases} 0 & \text{if } |\boldsymbol{v}^{\phi}_{i}| \geq \overline{v}, \\ 1 & \text{if } |\boldsymbol{v}^{\phi}_{i}| \leq \underline{v}. \end{cases} \tag{A.6}$$

These if-then constraints can be modelled as

$$\text{if } \boldsymbol{z}^{\phi}_{i} = 0 \Rightarrow |\boldsymbol{v}^{\phi}_{i}| - \overline{v} \leq M \cdot (1 - \boldsymbol{z}^{\phi}_{i}) - \epsilon \cdot \boldsymbol{z}^{\phi}_{i}, \tag{A.7a}$$

$$\text{if } \boldsymbol{z}^{\phi}_{i} = 1 \Rightarrow |\boldsymbol{v}^{\phi}_{i}| - \underline{v} \geq m \cdot \boldsymbol{z}^{\phi}_{i} + \epsilon \cdot (1 - \boldsymbol{z}^{\phi}_{i}), \tag{A.7b}$$

where M, m are upper and lower bounds on $|\boldsymbol{v}^{\phi}_{i}| - \overline{v}$ and $|\boldsymbol{v}^{\phi}_{i}| - \underline{v}$, respectively, and ϵ is a small value.

Bibliography

[1] NRECA, "Open modeling framework." [Online]. Available: https://github.com/dpinney/omf

[2] M. Bollen and M. Häger, "Power quality: interactions between distributed energy resources, the grid, and other customers," *Leonardo Energy*, 2005.

[3] E. Muljadi, R. Schiferl, and T. A. Lipo, "Induction machine phase balancing by unsymmetrical thyristor voltage control," *IEEE Trans. on Industry Applications*, no. 3, pp. 669–678, 1985.

[4] A. Von Jouanne and B. Banerjee, "Assessment of voltage unbalance," *IEEE Trans. on Power Delivery*, vol. 16, no. 4, pp. 782–790, 2001.

[5] F. Shahnia, P. J. Wolfs, and A. Ghosh, "Voltage unbalance reduction in low voltage feeders by dynamic switching of residential customers among three phases," *IEEE Transactions on Smart Grid*, vol. 5, no. 3, pp. 1318–1327, 2014.

[6] K. Ma, L. Fang, and W. Kong, "Review of distribution network phase unbalance: Scale, causes, consequences, solutions, and future research direction," *CSEE Journal of Power and Energy Systems*, 2020.

[7] X. Chen, W. Wu, and B. Zhang, "Robust capacity assessment of distributed generation in unbalanced distribution networks incorporating anm techniques," *IEEE Transactions on Sustainable Energy*, vol. 9, no. 2, pp. 651–663, 2018.

[8] C. S. Cheng and D. Shirmohammadi, "A three-phase power flow method for real-time distribution system analysis," *IEEE Transactions on Power Systems*, vol. 10, no. 2, pp. 671–679, 1995.

[9] E. R. Ramos, A. G. Expósito, and G. Á. Cordero, "Quasi-coupled three-phase radial load flow," *IEEE Transactions on Power Systems*, vol. 19, no. 2, pp. 776–781, 2004.

[10] P. A. Garcia, J. L. R. Pereira, S. Carneiro, V. M. Da Costa, and N. Martins, "Three-phase power flow calculations using the current injection method," *IEEE Transactions on Power Systems*, vol. 15, no. 2, pp. 508–514, 2000.

[11] M. Abdel-Akher, K. M. Nor, and A. A. Rashid, "Improved three-phase power-flow methods using sequence components," *IEEE Transactions on power systems*, vol. 20, no. 3, pp. 1389–1397, 2005.

[12] A. Bernstein, C. Wang, E. Dall'Anese, J.-Y. Le Boudec, and C. Zhao, "Load flow in multiphase distribution networks: Existence, uniqueness, non-singularity and linear models," *IEEE Transactions on Power Systems*, vol. 33, no. 6, pp. 5832–5843, 2018.

[13] J.-H. Teng, "A direct approach for distribution system load flow solutions," *IEEE Transactions on power delivery*, vol. 18, no. 3, pp. 882–887, 2003.

[14] W. H. Kersting, *Distribution system modeling and analysis*. CRC press, 2006.

[15] D. Montenegro, M. Hernandez, and G. Ramos, "Real time OpenDSS framework for distribution systems simulation and analysis," in *2012 Sixth IEEE/PES Transmission and Distribution: Latin America Conference and Exposition (T&D-LA)*. IEEE, 2012, pp. 1–5.

[16] D. W. Gao, E. Muljadi, T. Tian, and M. Miller, "Software comparison for renewable energy deployment in a distribution network," National Renewable Energy Lab.(NREL), Golden, CO (United States), Tech. Rep., 2017.

[17] D. P. Chassin, K. Schneider, and C. Gerkensmeyer, "Gridlab-d: An open-source power systems modeling and simulation environment," in *2008 IEEE/PES Transmission and Distribution Conference and Exposition*. IEEE, 2008, pp. 1–5.

[18] H. Abdi, S. D. Beigvand, and M. La Scala, "A review of optimal power flow studies applied to smart grids and microgrids," *Renewable and Sustainable Energy Reviews*, vol. 71, pp. 742–766, 2017.

[19] M. Farivar, C. R. Clarke, S. H. Low, and K. M. Chandy, "Inverter VAR control for distribution systems with renewables," in *2011 IEEE international conference on smart grid communications (SmartGridComm)*. IEEE, 2011, pp. 457–462.

[20] B. Zhang, A. Y. Lam, A. D. Domínguez-García, and D. Tse, "An optimal and distributed method for voltage regulation in power distribution systems," *IEEE Transactions on Power Systems*, vol. 30, no. 4, pp. 1714–1726, 2014.

[21] S. Bruno, S. Lamonaca, G. Rotondo, U. Stecchi, and M. La Scala, "Unbalanced three-phase optimal power flow for smart grids," *IEEE Transactions on Industrial Electronics*, vol. 58, no. 10, pp. 4504–4513, 2011.

[22] S. Paudyal, C. A. Canizares, and K. Bhattacharya, "Optimal operation of distribution feeders in smart grids," *IEEE Transactions on Industrial Electronics*, vol. 58, no. 10, pp. 4495–4503, 2011.

[23] L. R. de Araujo, D. R. R. Penido, and F. de Alcântara Vieira, "A multiphase optimal power flow algorithm for unbalanced distribution systems," *International Journal of Electrical Power & Energy Systems*, vol. 53, pp. 632–642, 2013.

[24] E. Dall'Anese, H. Zhu, and G. B. Giannakis, "Distributed optimal power flow for smart microgrids," *IEEE Transactions on Smart Grid*, vol. 4, no. 3, pp. 1464–1475, 2013.

[25] J. Bezanson, A. Edelman, S. Karpinski, and V. Shah, "Julia: A fresh approach to numerical computing," *SIAM Review*, vol. 59, no. 1, pp. 65–98, 2017. [Online]. Available: https://doi.org/10.1137/141000671

[26] I. Dunning, J. Huchette, and M. Lubin, "JuMP: A modeling language for mathematical optimization," *SIAM Review*, vol. 59, no. 2, pp. 295–320, 2017.

[27] D. M. Fobes, S. Claeys, F. Geth, and C. Coffrin, "PowerModelsDistribution.jl: An open-source framework for exploring distribution power flow formulations," 2020.

[28] R. B. Melton, K. P. Schneider, E. Lightner, T. E. Mcdermott, P. Sharma, Y. Zhang, F. Ding, S. Vadari, R. Podmore, A. Dubey *et al.*, "Leveraging standards to create an open platform for the development of advanced distribution applications," *IEEE Access*, vol. 6, pp. 37 361–37 370, 2018.

[29] H. Zhang and P. Li, "Chance constrained programming for optimal power flow under uncertainty," *IEEE Transactions on Power Systems*, vol. 26, no. 4, pp. 2417–2424, 2011.

[30] L. Roald, F. Oldewurtel, T. Krause, and G. Andersson, "Analytical reformulation of security constrained optimal power flow with probabilistic constraints," in *2013 IEEE Grenoble Conference*. IEEE, 2013, pp. 1–6.

[31] T. Summers, J. Warrington, M. Morari, and J. Lygeros, "Stochastic optimal power flow based on conditional value at risk and distributional robustness," *International Journal of Electrical Power & Energy Systems*, vol. 72, pp. 116–125, 2015.

[32] ——, "Stochastic optimal power flow based on convex approximations of chance constraints," in *2014 Power Systems Computation Conference*. IEEE, 2014, pp. 1–7.

[33] J. Liang, D. D. Molina, G. K. Venayagamoorthy, and R. G. Harley, "Two-level dynamic stochastic optimal power flow control for power systems with intermittent renewable generation," *IEEE Transactions on Power Systems*, vol. 28, no. 3, pp. 2670–2678, 2013.

[34] V. Kekatos, G. Wang, A. J. Conejo, and G. B. Giannakis, "Stochastic reactive power management in microgrids with renewables," *IEEE Transactions on Power Systems*, vol. 30, no. 6, pp. 3386–3395, 2015.

[35] T. Soares, R. J. Bessa, P. Pinson, and H. Morais, "Active distribution grid management based on robust AC optimal power flow," *IEEE Transactions on Smart Grid*, vol. 9, no. 6, pp. 6229–6241, 2018.

[36] R. Mieth and Y. Dvorkin, "Data-driven distributionally robust optimal power flow for distribution systems," *IEEE Control Systems Letters*, vol. 2, no. 3, pp. 363–368, 2018.

[37] S. Karagiannopoulos, L. Roald, P. Aristidou, and G. Hug, "Operational planning of active distribution grids under uncertainty."

[38] L. A. Roald, "Optimization methods to manage uncertainty and risk in power systems operation," Ph.D. dissertation, ETH Zurich, 2016.

[39] E. Dall'Anese, S. S. Guggilam, A. Simonetto, Y. C. Chen, and S. V. Dhople, "Optimal regulation of virtual power plants," *IEEE Transactions on Power Systems*, vol. 33, no. 2, pp. 1868–1881, 2017.

[40] J. Silva, J. Sumaili, R. J. Bessa, L. Seca, M. A. Matos, V. Miranda, M. Caujolle, B. Goncer, and M. Sebastian-Viana, "Estimating the active and reactive power flexibility area at the TSO-DSO interface," *IEEE Transactions on Power Systems*, vol. 33, no. 5, pp. 4741–4750, 2018.

[41] X. Xu, Q. Lyu, M. Qadrdan, and J. Wu, "Quantification of flexibility of a district heating system for the power grid," *IEEE Transactions on Sustainable Energy*, vol. 11, no. 4, pp. 2617–2630, 2020.

[42] E. Polymeneas and S. Meliopoulos, "Aggregate modeling of distribution systems for multi-period OPF," in *2016 Power Systems Computation Conference (PSCC)*. IEEE, 2016, pp. 1–8.

[43] X. Chen, E. Dall'Anese, C. Zhao, and N. Li, "Aggregate power flexibility in unbalanced distribution systems," *IEEE Transactions on Smart Grid*, vol. 11, no. 1, pp. 258–269, 2019.

[44] S. Wang and W. Wu, "Aggregate flexibility of virtual power plants with temporal coupling constraints," *IEEE Transactions on Smart Grid*, vol. 12, no. 6, pp. 5043–5051, 2021.

[45] B. Cui, A. Zamzam, and A. Bernstein, "Network-cognizant time-coupled aggregate flexibility of distribution systems under uncertainties," in *2021 American Control Conference (ACC)*. IEEE, 2021, pp. 4178–4183.

[46] X. Chen and N. Li, "Leveraging two-stage adaptive robust optimization for power flexibility aggregation," *IEEE Transactions on Smart Grid*, vol. 12, no. 5, pp. 3954–3965, 2021.

[47] K. Girigoudar and L. A. Roald, "On the impact of different voltage unbalance metrics in distribution system optimization," *Electric Power Systems Research*, vol. 189, p. 106656, 2020.

[48] K. Girigoudar, A. M. Hou, and L. A. Roald, "Chance-constrained ac optimal power flow for unbalanced distribution grids," in *2022 11th Bulk Power Systems Dynamics and Control Symposium (IREP)*, 2022.

[49] K. Girigoudar and L. A. Roald, "Linearized three-phase optimal power flow models for distribution grids with voltage unbalance," in *2021 60th IEEE Conference on Decision and Control (CDC)*. IEEE, 2021, pp. 4214–4221.

[50] K. Girigoudar, D. Molzahn, and L. Roald, "On the relationships among different voltage unbalance definitions," in *North American Power Symposium (NAPS)*. IEEE, 2019.

[51] M. Karimi, H. Mokhlis, K. Naidu, S. Uddin, and A. Bakar, "Photovoltaic penetration issues and impacts in distribution network–a review," *Renewable and Sustainable Energy Reviews*, vol. 53, pp. 594–605, 2016.

[52] S.-Y. Lee and C.-J. Wu, "On-line reactive power compensation schemes for unbalanced three phase four wire distribution feeders," *IEEE Transactions on Power Delivery*, vol. 8, no. 4, pp. 1958–1965, 1993.

[53] N. C. Woolley and J. V. Milanovic, "Statistical estimation of the source and level of voltage unbalance in distribution networks," *IEEE Trans. on Power Delivery*, vol. 27, no. 3, pp. 1450–1460, 2012.

[54] *IEC 61000-2-2, EMC – Part 2-2: Environment – Compatibility Levels for Low Frequency Conducted Disturbances and Signalling in Public Low-Voltage Power Supply Systems*, 2002.

[55] "Motors and generators," ANSI/NEMA Standard MG1-1993.

[56] "IEEE Recommended Practice for Electric Power Distribution for Industrial Plants," *IEEE Standard 141-1993*, pp. 1–768, April 1994.

[57] J.-G. Kim, E.-W. Lee, D.-J. Lee, and J.-H. Lee, "Comparison of voltage unbalance factor by line and phase voltage," in *Eighth International Conference on Electrical Machines and Systems (ICEMS)*, vol. 3, 2005, pp. 1998–2001.

[58] P. Pillay and M. Manyage, "Definitions of voltage unbalance," *IEEE Power Engineering Review*, vol. 21, no. 5, pp. 50–51, 2001.

[59] A. D. Rodriguez, F. M. Fuentes, and A. J. Matta, "Comparative analysis between voltage unbalance definitions," in *Workshop on Engineering Applications-International Congress on Engineering (WEA)*, 2015.

[60] A. K. Singh, G. Singh, and R. Mitra, "Some observations on definitions of voltage unbalance," in *39th North American Power Symposium (NAPS)*, 2007, pp. 473–479.

[61] T.-H. Chen, C.-H. Yang, and N.-C. Yang, "Examination of the definitions of voltage unbalance," *International Journal of Electrical Power & Energy Systems*, vol. 49, pp. 380–385, 2013.

[62] *Electric Power Systems and Equipment- Voltage Ratings (60 Hertz)*, ANSI Standard Publication no. ANSI C84.1-1995.

[63] T. A. Short, *Electric power distribution handbook*. CRC press, 2014.

[64] A. A. Sallam and O. P. Malik, *Electric distribution systems*. John Wiley & Sons, 2018.

[65] E. Makram, M. Bou-Rabee, and A. Girgis, "Three-phase modeling of unbalanced distribution systems during open conductors and/or shunt fault conditions using the bus impedance matrix," *Electric Power Systems Research*, vol. 13, no. 3, pp. 173–183, 1987.

[66] M. Bazrafshan and N. Gatsis, "Comprehensive modeling of three-phase distribution systems via the bus admittance matrix," *IEEE Transactions on Power Systems*, vol. 33, no. 2, pp. 2015–2029, 2018.

[67] A. R. Baran Jr and T. S. Fernandes, "A three-phase optimal power flow applied to the planning of unbalanced distribution networks," *International Journal of Electrical Power & Energy Systems*, vol. 74, pp. 301–309, 2016.

[68] G. Kron, "Tensorial analysis of integrated transmission systems part i. the six basic reference frames," *Transactions of the American Institute of Electrical Engineers*, vol. 70, no. 2, pp. 1239–1248, 1951.

[69] J. A. Arrillaga and B. Harker, *Computer modelling of electrical power systems*. John Wiley & Sons, Inc., 1983.

[70] Z. Wang, D. S. Kirschen, and B. Zhang, "Accurate semidefinite programming models for optimal power flow in distribution systems," *arXiv preprint arXiv:1711.07853*, 2017.

[71] X. Liu, A. Aichhorn, L. Liu, and H. Li, "Coordinated control of distributed energy storage system with tap changer transformers for voltage rise mitigation under high photovoltaic penetration," *IEEE Transactions on Smart Grid*, vol. 3, no. 2, pp. 897–906, 2012.

[72] Y. Xu, L. M. Tolbert, J. D. Kueck, and D. T. Rizy, "Voltage and current unbalance compensation using a static VAR compensator," *IET Power Electronics*, vol. 3, no. 6, pp. 977–988, 2010.

[73] X. Su, M. A. Masoum, and P. J. Wolfs, "Optimal pv inverter reactive power control and real power curtailment to improve performance of unbalanced four-wire LV distribution networks," *IEEE Transactions on Sustainable Energy*, vol. 5, no. 3, pp. 967–977, 2014.

[74] S. Weckx, C. Gonzalez, and J. Driesen, "Reducing grid losses and voltage unbalance with PV inverters," in *2014 IEEE PES General Meeting— Conference & Exposition*. IEEE, 2014, pp. 1–5.

[75] S. Karagiannopoulos, P. Aristidou, and G. Hug, "A centralised control method for tackling unbalances in active distribution grids," in *2018 Power Systems Computation Conference (PSCC)*, 2018.

[76] K. Schneider, B. Mather, B. Pal, C.-W. Ten, G. Shirek, H. Zhu, J. Fuller, J. Pereira, L. Ochoa, L. De Araujo *et al.*, "Analytic considerations and design basis for the IEEE distribution test feeders," *IEEE Transactions on Power Systems*, vol. 33, no. 3, pp. 3181–3188, 2017.

[77] C. G. Bajo, S. Hashemi, S. B. Kjsær, G. Yang, and J. Østergaard, "Voltage unbalance mitigation in LV networks using three-phase pv systems," in *Industrial Technology (ICIT), 2015 IEEE International Conference on*. IEEE, 2015, pp. 2875–2879.

[78] S. Sun, B. Liang, M. Dong, and J. A. Taylor, "Phase balancing using energy storage in power grids under uncertainty," *IEEE Transactions on Power Systems*, vol. 31, no. 5, pp. 3891–3903, 2015.

[79] M. Yao, I. A. Hiskens, and J. L. Mathieu, "Mitigating voltage unbalance using distributed solar photovoltaic inverters," *IEEE Transactions on Power Systems*, vol. 36, no. 3, pp. 2642–2651, 2020.

[80] F. A. Viawan and D. Karlsson, "Combined local and remote voltage and reactive power control in the presence of induction machine distributed generation," *IEEE Trans. Power Systems*, vol. 22, no. 4, pp. 2003–2012, 2007.

[81] A. R. Malekpour, A. M. Annaswamy, and J. Shah, "Hierarchical hybrid architecture for volt/var control of power distribution grids," *IEEE Trans. Power Systems*, vol. 35, no. 2, pp. 854–863, 2019.

[82] Q. Zhang, K. Dehghanpour, and Z. Wang, "Distributed CVR in unbalanced distribution systems with PV penetration," *IEEE Trans. Smart Grid*, vol. 10, no. 5, pp. 5308–5319, 2018.

[83] B. J. Deaver, W. O. Radtke, W. H. Berkman *et al.*, "Method and system for providing power factor correction in a power distribution system," Sep. 28 2010, uS Patent 7,804,280.

[84] A. Wächter and L. T. Biegler, "On the implementation of a primal-dual interior point filter line search algorithm for large-scale nonlinear programming," *Math. Programming*, vol. 106, no. 1, pp. 25–57, 2006.

[85] R. D. Zimmerman, C. E. Murillo-Sánchez, and D. Gan, "Matpower: A matlab power system simulation package," *Manual, Power Systems Engineering Research Center, Ithaca NY*, vol. 1, 1997.

[86] K. P. Schneider, Y. Chen, D. P. Chassin, R. G. Pratt, D. W. Engel, and S. E. Thompson, "Modern grid initiative distribution taxonomy final report," Pacific Northwest National Lab.(PNNL), Richland, WA (United States), Tech. Rep., 2008.

[87] B. Stott, J. Jardim, and O. Alsaç, "DC power flow revisited," *IEEE Transactions on Power Systems*, vol. 24, no. 3, pp. 1290–1300, 2009.

[88] K. Purchala, L. Meeus, D. Van Dommelen, and R. Belmans, "Usefulness of DC power flow for active power flow analysis," in *IEEE Power Engineering Society General Meeting, 2005*. IEEE, 2005, pp. 454–459.

[89] M. D. Sankur, R. Dobbe, E. Stewart, D. S. Callaway, and D. B. Arnold, "A linearized power flow model for optimization in unbalanced distribution systems," *arXiv preprint arXiv:1606.04492*, 2016.

[90] D. B. Arnold, M. Sankur, R. Dobbe, K. Brady, D. S. Callaway, and A. Von Meier, "Optimal dispatch of reactive power for voltage regulation and balancing in unbalanced distribution systems," in *2016 IEEE Power and Energy Society General Meeting (PESGM)*. IEEE, 2016, pp. 1–5.

[91] J. Lavaei and S. H. Low, "Zero duality gap in optimal power flow problem," *IEEE Transactions on Power Systems*, vol. 27, no. 1, pp. 92–107, 2011.

[92] C. Zhao, E. Dall'Anese, and S. H. Low, "Convex relaxation of OPF in multiphase radial networks with delta connection," in *Proceedings of the 10th IREP*, 2017, pp. 0885–8950.

[93] R. A. Jabr, "Radial distribution load flow using conic programming," *IEEE Trans. power systems*, vol. 21, no. 3, pp. 1458–1459, 2006.

[94] L. Gan, N. Li, U. Topcu, and S. H. Low, "Exact convex relaxation of optimal power flow in radial networks," *IEEE Trans. Automatic Control*, vol. 60, no. 1, pp. 72–87, 2014.

[95] A. J. Wood, B. F. Wollenberg, and G. B. Sheblé, *Power generation, operation, and control*. John Wiley & Sons, 2013.

[96] Z. Yang, H. Zhong, Q. Xia, A. Bose, and C. Kang, "Optimal power flow based on successive linear approximation of power flow equations," *IET Generation, Transmission & Distribution*, vol. 10, no. 14, pp. 3654–3662, 2016.

[97] A. Garces, "A linear three-phase load flow for power distribution systems," *IEEE Transactions on Power Systems*, vol. 31, no. 1, pp. 827–828, 2015.

[98] J. D. Glover, M. S. Sarma, and T. Overbye, *Power system analysis & design, SI version*. Cengage Learning, 2012.

[99] C. Wang, A. Bernstein, J.-Y. Le Boudec, and M. Paolone, "Explicit conditions on existence and uniqueness of load-flow solutions in distribution networks," *IEEE Transactions on Smart Grid*, vol. 9, no. 2, pp. 953–962, 2016.

[100] S. V. Dhople, S. S. Guggilam, and Y. C. Chen, "Linear approximations to AC power flow in rectangular coordinates," in *2015 53rd Annual Allerton Conference on Communication, Control, and Computing (Allerton)*. IEEE, 2015, pp. 211–217.

[101] P. Fortenbacher, M. Zellner, and G. Andersson, "Optimal sizing and placement of distributed storage in low voltage networks," in *2016 Power Systems Computation Conference (PSCC)*. IEEE, 2016, pp. 1–7.

[102] S. Karagiannopoulos, P. Aristidou, and G. Hug, "Data-driven local control design for active distribution grids using off-line optimal power flow and machine learning techniques," *IEEE Transactions on Smart Grid*, vol. 10, no. 6, pp. 6461–6471, 2019.

[103] S. Barsali *et al.*, *Benchmark systems for network integration of renewable and distributed energy resources*, 2014.

[104] PNNL, "GridLAB-D taxonomy feeder," 2020. [Online]. Available: https://github.com/gridlab-d/Taxonomy_Feeders

[105] *NREL Measurement and Instrumentation Data Center*. [Online]. Available: https://midcdmz.nrel.gov/

[106] *Pecan Street Dataport: the world's largest energy data resource*. [Online]. Available: https://dataport.pecanstreet.org/

[107] E. Dall'Anese, K. Baker, and T. Summers, "Chance-constrained AC optimal power flow for distribution systems with renewables," *IEEE Transactions on Power Systems*, vol. 32, no. 5, pp. 3427–3438, 2017.

[108] X. Geng and L. Xie, "Data-driven decision making in power systems with probabilistic guarantees: Theory and applications of chance-constrained optimization," *Annual Reviews in Control*, vol. 47, pp. 341–363, 2019. [Online]. Available: https://www.sciencedirect.com/science/article/pii/S1367578819300306

[109] Y. Cao, Y. Tan, C. Li, and C. Rehtanz, "Chance-constrained optimization-based unbalanced optimal power flow for radial distribution networks," *IEEE Transactions on Power Delivery*, vol. 28, no. 3, pp. 1855–1864, 2013.

[110] A. Venzke, L. Halilbasic, U. Markovic, G. Hug, and S. Chatzivasileiadis, "Convex relaxations of chance constrained AC optimal power flow," *IEEE Transactions on Power Systems*, vol. 33, no. 3, pp. 2829–2841, 2018.

[111] E. Dall'Anese, K. Baker, and T. Summers, "Optimal power flow for distribution systems under uncertain forecasts," in *2016 IEEE 55th Conference on Decision and Control (CDC)*, 2016, pp. 7502–7507.

[112] K. Baker, I. E. Dall'Anese, and T. Summers, "Distribution-agnostic stochastic optimal power flow for distribution grids," in *2016 North American Power Symposium (NAPS)*, 2016, pp. 1–6.

[113] J. Schmidli, L. Roald, S. Chatzivasileiadis, and G. Andersson, "Stochastic AC optimal power flow with approximate chance-constraints," in *2016 IEEE Power and Energy Society General Meeting (PESGM)*. IEEE, 2016, pp. 1–5.

[114] L. Roald and G. Andersson, "Chance-constrained AC optimal power flow: Reformulations and efficient algorithms," *IEEE Transactions on Power Systems*, vol. 33, no. 3, pp. 2906–2918, 2017.

[115] L. A. Roald, D. K. Molzahn, and A. F. Tobler, "Power system optimization with uncertainty and AC power flow: Analysis of an iterative algorithm," in *10th IREP Symp. Bulk Power Syst. Dynamics Control*, 2017.

[116] A. M. Hou and L. A. Roald, "Chance constraint tuning for optimal power flow," in *2020 International Conference on Probabilistic Methods Applied to Power Systems (PMAPS)*. IEEE, 2020, pp. 1–6.

[117] A. Alimardani, F. Therrien, D. Atanackovic, J. Jatskevich, and E. Vaahedi, "Distribution system state estimation based on nonsynchronized smart meters," *IEEE Transactions on Smart Grid*, vol. 6, no. 6, pp. 2919–2928, 2015.

[118] D. G. Photovoltaics and E. Storage, "IEEE standard for interconnection and interoperability of distributed energy resources with associated electric power systems interfaces," *IEEE Std*, pp. 1547–2018, 2018.

[119] A. M. Hou and L. A. Roald, "Data-driven tuning for chance-constrained optimization: Two steps towards probabilistic performance guarantees," *IEEE Control Systems Letters*, vol. 6, pp. 1400–1405, 2022.

[120] FERC, "FERC order no. 2222: A new day for distributed energy resources." [Online]. Available: https://www.ferc.gov/media/ferc-order-no-2222-fact-sheet

[121] Z. Li, Q. Guo, H. Sun, and J. Wang, "Coordinated economic dispatch of coupled transmission and distribution systems using heterogeneous decomposition," *IEEE Transactions on Power Systems*, vol. 31, no. 6, pp. 4817–4830, 2016.

[122] C. Lin, W. Wu, X. Chen, and W. Zheng, "Decentralized dynamic economic dispatch for integrated transmission and active distribution networks using multi-parametric programming," *IEEE Transactions on Smart Grid*, vol. 9, no. 5, pp. 4983–4993, 2017.

[123] C. Lin, W. Wu, B. Zhang, B. Wang, W. Zheng, and Z. Li, "Decentralized reactive power optimization method for transmission and distribution networks accommodating large-scale DG integration," *IEEE Transactions on Sustainable Energy*, vol. 8, no. 1, pp. 363–373, 2016.

[124] Y. Yi and G. Verbic, "Operating envelopes under probabilistic electricity demand and solar generation forecasts," *arXiv e-prints*, pp. arXiv–2207, 2022.

[125] N. Nazir and M. Almassalkhi, "Convex inner approximation of the feeder hosting capacity limits on dispatchable demand," in *2019 IEEE 58th Conference on Decision and Control (CDC)*. IEEE, 2019, pp. 4858–4864.

[126] L. Ageeva, M. Majidi, and D. Pozo, "Analysis of feasibility region of active distribution networks," in *2019 International Youth Conference on Radio Electronics, Electrical and Power Engineering (REEPE)*. IEEE, 2019, pp. 1–5.

[127] M. Heleno, R. Soares, J. Sumaili, R. J. Bessa, L. Seca, and M. A. Matos, "Estimation of the flexibility range in the transmission-distribution boundary," in *2015 IEEE Eindhoven PowerTech*. IEEE, 2015, pp. 1–6.

[128] Z. Tan, H. Zhong, Q. Xia, C. Kang, X. S. Wang, and H. Tang, "Estimating the robust PQ capability of a technical virtual power plant under uncertainties," *IEEE Transactions on Power Systems*, vol. 35, no. 6, pp. 4285–4296, 2020.

[129] C. Zhang, Q. Wang, J. Wang, P. Pinson, J. M. Morales, and J. Østergaard, "Real-time procurement strategies of a proactive distribution company with aggregator-based demand response," *IEEE Transactions on Smart Grid*, vol. 9, no. 2, pp. 766–776, 2016.

[130] C. Zhang, Q. Wang, J. Wang, P. Pinson, and J. Østergaard, "Real-time trading strategies of proactive disco with heterogeneous dg owners," *IEEE Transactions on Smart Grid*, vol. 9, no. 3, pp. 1688–1697, 2016.

[131] P. Sheikhahmadi, S. Bahramara, A. Mazza, G. Chicco, and J. P. Catalão, "Bi-level optimization model for the coordination between transmission and distribution systems interacting with local energy markets," *International Journal of Electrical Power & Energy Systems*, vol. 124, p. 106392, 2021.

[132] S. Riaz, H. Marzooghi, G. Verbič, A. C. Chapman, and D. J. Hill, "Generic demand model considering the impact of prosumers for future grid scenario analysis," *IEEE Transactions on Smart Grid*, vol. 10, no. 1, pp. 819–829, 2017.

[133] M. Zugno, J. M. Morales, P. Pinson, and H. Madsen, "A bilevel model for electricity retailers' participation in a demand response market environment," *Energy Economics*, vol. 36, pp. 182–197, 2013.

[134] D. Lee, K. Turitsyn, D. K. Molzahn, and L. A. Roald, "Robust ac optimal power flow with robust convex restriction," *IEEE Transactions on Power Systems*, vol. 36, no. 6, pp. 4953–4966, 2021.

[135] N. Nazir and M. Almassalkhi, "Grid-aware aggregation and realtime disaggregation of distributed energy resources in radial networks," *IEEE Transactions on Power Systems*, vol. 37, no. 3, pp. 1706–1717, 2021.

[136] F. L. Müller, J. Szabó, O. Sundström, and J. Lygeros, "Aggregation and disaggregation of energetic flexibility from distributed energy resources," *IEEE Transactions on Smart Grid*, vol. 10, no. 2, pp. 1205–1214, 2017.

[137] L. Zhao, W. Zhang, H. Hao, and K. Kalsi, "A geometric approach to aggregate flexibility modeling of thermostatically controlled loads," *IEEE Transactions on Power Systems*, vol. 32, no. 6, pp. 4721–4731, 2017.

[138] H. Hao, B. M. Sanandaji, K. Poolla, and T. L. Vincent, "Aggregate flexibility of thermostatically controlled loads," *IEEE Transactions on Power Systems*, vol. 30, no. 1, pp. 189–198, 2014.

[139] S. Ross and J. Mathieu, "Strategies for network-safe load control with a third-party aggregator and a distribution operator," *IEEE Transactions on Power Systems*, vol. 36, no. 4, pp. 3329–3339, 2021.

[140] D. Molzahn and L. A. Roald, "Grid-aware versus grid-agnostic distribution system control: A method for certifying engineering constraint satisfaction," in *Proceedings of the 52nd Hawaii International Conference on System Sciences*, 2019.

[141] H. Stackelberg, *The theory of the market economy*. Oxford University Press, New York, Oxford, 1952.

[142] A. Sinha, P. Malo, and K. Deb, "A review on bilevel optimization: from classical to evolutionary approaches and applications," *IEEE Transactions on Evolutionary Computation*, vol. 22, no. 2, pp. 276–295, 2017.

[143] P. Hansen, B. Jaumard, and G. Savard, "New branch-and-bound rules for linear bilevel programming," *SIAM Journal on scientific and Statistical Computing*, vol. 13, no. 5, pp. 1194–1217, 1992.

[144] L. Vicente, G. Savard, and J. Júdice, "Descent approaches for quadratic bilevel programming," *Journal of Optimization theory and applications*, vol. 81, no. 2, pp. 379–399, 1994.

[145] J. F. Bard and J. E. Falk, "An explicit solution to the multi-level programming problem," *Computers & Operations Research*, vol. 9, no. 1, pp. 77–100, 1982.

[146] W. F. Bialas and M. H. Karwan, "Two-level linear programming," *Management science*, vol. 30, no. 8, pp. 1004–1020, 1984.

[147] J. Fortuny-Amat and B. McCarl, "A representation and economic interpretation of a two-level programming problem," *Journal of the operational Research Society*, vol. 32, no. 9, pp. 783–792, 1981.

[148] S. Dempe, V. Kalashnikov, G. A. Pérez-Valdés, and N. Kalashnykova, "Bilevel programming problems," *Energy Systems. Springer, Berlin*, vol. 10, pp. 978–3, 2015.

[149] L. P. Garcés, A. J. Conejo, R. García-Bertrand, and R. Romero, "A bilevel approach to transmission expansion planning within a market environment," *IEEE Transactions on Power Systems*, vol. 24, no. 3, pp. 1513–1522, 2009.

[150] A. Najafi, H. Falaghi, J. Contreras, and M. Ramezani, "A stochastic bilevel model for the energy hub manager problem," *IEEE Transactions on Smart Grid*, vol. 8, no. 5, pp. 2394–2404, 2016.

[151] G. Savard and J. Gauvin, "The steepest descent direction for the nonlinear bilevel programming problem," *Operations Research Letters*, vol. 15, no. 5, pp. 265–272, 1994.

[152] C. D. Kolstad and L. S. Lasdon, "Derivative evaluation and computational experience with large bilevel mathematical programs," *Journal of optimization theory and applications*, vol. 65, no. 3, pp. 485–499, 1990.

[153] E. Aiyoshi and K. Shimizu, "A solution method for the static constrained stackelberg problem via penalty method," *IEEE Transactions on Automatic Control*, vol. 29, no. 12, pp. 1111–1114, 1984.

[154] ——, "Hierarchical decentralized systems and its new solution by a barrier method." *IEEE Transactions on Systems, Man and Cybernetics*, no. 6, pp. 444–449, 1981.

[155] P. Marcotte, G. Savard, and D. Zhu, "A trust region algorithm for nonlinear bilevel programming," *Operations research letters*, vol. 29, no. 4, pp. 171–179, 2001.

[156] G. Liu, J. Han, and S. Wang, "A trust region algorithm for bilevel programing problems," *Chinese science bulletin*, vol. 43, no. 10, pp. 820–824, 1998.

[157] B. Colson, P. Marcotte, and G. Savard, "A trust-region method for nonlinear bilevel programming: algorithm and computational experience," *Computational Optimization and Applications*, vol. 30, no. 3, pp. 211–227, 2005.

[158] B. Zeng and Y. An, "Solving bilevel mixed integer program by reformulations and decomposition," *Optimization online*, pp. 1–34, 2014.

[159] Gurobi Optimization, LLC, "Gurobi Optimizer Reference Manual," 2022. [Online]. Available: https://www.gurobi.com

[160] P. M. Castro, "Tightening piecewise mccormick relaxations for bilinear problems," *Computers & Chemical Engineering*, vol. 72, pp. 300–311, 2015.

[161] P. Verdelho and G. D. Marques, "Four-wire current-regulated pwm voltage converter," *IEEE Transactions on Industrial Electronics*, vol. 45, no. 5, pp. 761–770, 1998.

[162] J. Liang, T. C. Green, C. Feng, and G. Weiss, "Increasing voltage utilization in split-link, four-wire inverters," *IEEE Transactions on Power Electronics*, vol. 24, no. 6, pp. 1562–1569, 2009.

[163] A. Gastalver-Rubio, E. Romero-Ramos, and J. M. Maza-Ortega, "Improving the performance of low voltage networks by an optimized unbalance operation of three-phase distributed generators," *IEEE Access*, vol. 7, pp. 177 504–177 516, 2019.

[164] J. M. Carrasco, L. G. Franquelo, J. T. Bialasiewicz, E. Galván, R. C. PortilloGuisado, M. M. Prats, J. I. León, and N. Moreno-Alfonso, "Power-electronic systems for the grid integration of renewable energy sources: A survey," *IEEE Transactions on industrial electronics*, vol. 53, no. 4, pp. 1002–1016, 2006.

[165] S. Taheri, M. Jalali, V. Kekatos, and L. Tong, "Fast probabilistic hosting capacity analysis for active distribution systems," *IEEE Transactions on Smart Grid*, 2020.

[166] F. K. Tuffner and M. Kintner-Meyer, "Using electric vehicles to mitigate imbalance requirements associated with an increased penetration of wind generation," in *2011 IEEE Power and Energy Society General Meeting*. IEEE, 2011, pp. 1–8.

[167] D. V. Bozalakov, M. J. Mnati, J. Laveyne, A. Van den Bossche, and L. Vandevelde, "Voltage unbalance and overvoltage mitigation by using the three-phase damping control strategy in battery storage applications," in *2018 7th International Conference on Renewable Energy Research and Applications (ICRERA)*. IEEE, 2018, pp. 753–759.

[168] A. Abur and A. G. Exposito, *Power system state estimation: theory and implementation*. CRC press, 2004.

[169] M. E. Baran, "Challenges in state estimation on distribution systems," in *2001 Power Engineering Society Summer Meeting. Conference Proceedings (Cat. No. 01CH37262)*, vol. 1. IEEE, 2001, pp. 429–433.

[170] C. Klauber and H. Zhu, "Distribution system state estimation using semidefinite programming," in *2015 North American Power Symposium (NAPS)*. IEEE, 2015, pp. 1–6.

[171] H. Zhu and G. B. Giannakis, "Power system nonlinear state estimation using distributed semidefinite programming," *IEEE Journal of Selected Topics in Signal Processing*, vol. 8, no. 6, pp. 1039–1050, 2014.

[172] A. Robson, M. Jamei, C. Ududec, and L. Mones, "Learning an optimally reduced formulation of OPF through meta-optimization," *arXiv preprint arXiv:1911.06784*, 2019.

[173] Y. Liang and D. Chen, "Fast large-scale optimal power flow analysis for smart grid through network reduction," in *2014 19th Asia and South Pacific Design Automation Conference (ASP-DAC)*. IEEE, 2014, pp. 373–378.

[174] F. Capitanescu, W. Rosehart, and L. Wehenkel, "Optimal power flow computations with constraints limiting the number of control actions," in *2009 IEEE Bucharest PowerTech*. IEEE, 2009, pp. 1–8.

[175] M. Abuella and C. Hatziadoniu, "Selection of most effective control variables for solving optimal power flow using sensitivity analysis in particle swarm algorithm," *arXiv preprint arXiv:1601.04150*, 2016.

[176] L. Gan and S. H. Low, "Convex relaxations and linear approximation for optimal power flow in multiphase radial networks," in *2014 Power Systems Computation Conference*. IEEE, 2014, pp. 1–9.

[177] F. Eldali, T. Hardy, C. Corbin, D. Pinney, and M. Javid, "Cost-benefit analysis of demand response programs incorporated in open modeling framework," in *2016 IEEE Power and Energy Society General Meeting (PESGM)*. IEEE, 2016, pp. 1–5.